# *In Situ* Studies of Pt Nanoparticles on Different Supports for Corrosion Stable PEM Fuel Cell Cathodes

Vorgelegt von
M. Sc.
Henrike Schmies
geb. in Friesoythe

Von der Fakultät II – Mathematik und Naturwissenschaften
der Technischen Universität Berlin
zur Erlangung des akademischen Grades

Doktorin der Naturwissenschaften
- Dr. rer. nat. -

genehmigte Dissertation

Promotionsausschuss:

| | |
|---|---|
| Vorsitzende: | Prof. Dr. Marga Lensen |
| Gutachter: | Prof. Dr. Peter Strasser |
| Gutachter: | Prof. Dr. Michael Bron |

Tag der wissenschaftlichen Aussprache: 18. Dezember 2018

Berlin 2019

# Danksagung

Mein besonderer Dank gilt Herrn Prof. Peter Strasser für die Bereitstellung dieses interessanten Promotionsthemas, die finanzielle Unterstützung und die persönliche Betreuung. Außerdem möchte ich mich für das Vertrauen bedanken, meine Arbeit mit großer wissenschaftlicher Freiheit und Selbstständigkeit ausführen zu dürfen.

Ich möchte mich bei Herrn Prof. Michael Bron bedanken, dass er sich bereit erklärt hat, meine Arbeit als Gutachter zu bewerten. Mein Dank geht zudem an Prof. Marga Lensen für die Übernahme des Prüfungsvorsitzes.

Des Weiteren möchte ich mich bei allen Kooperationspartnern für die Unterstützung mit verschiedensten Messmethoden, die konstruktiven Diskussionen der Ergebnisse und die erfolgreiche Zusammenarbeit bedanken. Mein besonderer Dank geht an Arno Bergmann, von dem ich unglaublich viel lernen durfte und der die Zusammenarbeit sehr inspirierend und unkompliziert gemacht hat. Ich möchte mich bei Jakub Drnec für seine zuverlässige Unterstützung bei zahlreichen Messzeiten am ESRF bedanken. Auch danke ich ganz besonders Elisabeth, Fabio, Thomas, Sören und Malte für die produktive Arbeit während auch manch schwerer (nächtlicher und zerstörerischer) Stunde an der ID31. Elisabeth und Sebastian danke ich für die gemeinsame Synthese und Analyse so manch schwarzer Pulver und eine erfolgreiche Zusammenarbeit. Ich möchte mich zudem herzlich bei Annette für die zahlreichen Messungen sowie Bestellungen und die nette Gesellschaft innerhalb und außerhalb des Labors bedanken. Außerdem möchte ich mich bei Annegret, Sabrina, Astrid, Carsten und dem ganzen Team aus der Werkstatt für eine vielseitige Unterstützung bedanken. Frau Dr. Kühl danke ich für die zahlreichen TEM Messungen und die Hilfe bei manchen nie endenden, bürokratischen Bestellvorgängen. Ein großer Dank geht auch an die ganze Kickergemeinde für extrem spannende Partien am Kickertisch. Dem ganzen Arbeitskreis danke ich für die immer großartige Stimmung, den Spaß in den Kaffeepausen und so manch feuchtfröhliche Party.

Ich bedanke mich bei allen Mitbewohnern des Büros 304 für die produktive Arbeitsatmosphäre, aber auch für willkommene Ablenkungen, die Pflege der Pflanzen und ein stets offenes Ohr bei Problemen jeglicher Art. Ich danke Nhan und Fang für die Einführung und Vorführung asiatischer Kochkünste und ich danke Vera für die unvergessliche Zeit, den Spaß während Konferenzen und Reisen und die Unterstützung in jeder Lebenslage.

Ich möchte mich ganz herzlich bei Kathrin, Paulina, Fabio, Nhan und Vera für ihre Zeit bedanken, meine Arbeit Korrektur zu lesen.

Zu guter Letzt geht mein großer Dank an meine Familie und Freunde. Vielen Dank für eure Unterstützung, ihr seid die Besten!

# Zusammenfassung

Wasserstoffbrennstoffzellen bieten als elektrochemische Energiewandler die Möglichkeit, Wasserstoff aus erneuerbaren Resourcen als saubere und emissionsarme Energiequelle für elektrische Verbraucher, wie Elektromotoren, zu nutzen. Um eine konkurrenzfähige Alternative zu heutigen Verbrennungsmotoren in der Automobilindustrie darstellen zu können, müssen aber noch verschiedenste Hindernisse überwunden werden. Im Blickfeld der Forschung sind dabei vor allem die Katalysatoren, die größtenteils aus Platin bestehen und an der Sauerstoffreduktionsseite von Niedertemperaturbrennstoffzellen zum Einsatz kommen. Neben der Maximierung der masse-basierten Aktivität dieser Katalysatoren, ist vor allem die Langlebigkeit entscheidend, um leistungsfähige Brennstoffzellen herzustellen. Dabei spielt der Katalysatorträger und sein chemisches und elektrochemisches Korrosionsverhalten unter Brennstoffzellbedingungen eine entscheidende Rolle. Hochoberflächige bis graphitisierte Kohlenstoffe sind dabei heute Stand der Technik mit ihren Vor- und Nachteilen.

Ziel dieser Arbeit ist es, den Einfluss neuartiger oxidischer oder kohlenstoffbasierter Trägermaterialien auf das elektrochemische und morphologische Stabilitätsverhalten der katalytischen Pt Nanopartikel zu untersuchen. Solche Katalysatorträger, exemplarisch dargestellt an Metalloxiden und Heteroatom-modifizierten Kohlenstoffen, wurden mit Pt Nanopartikeln dekoriert und umfangreich auf ihre physikochemischen Eigenschaften hin untersucht. Dabei kamen verschiedenste *in situ* Analysemethoden zum Einsatz, um die Katalysatorkomponenten im simulierten Brennstoffzellenbetrieb zu evaluieren und mit den Ergebnissen zum fundamentalen Wissen über Degradationsprozesse beizutragen. Es konnte gezeigt werden, dass Indium Zinn Oxid (ITO) als Trägermaterial unter simulierten Betriebsbedingungen potentialbereich-abhängige Alterung zeigt. Den Platin Nanopartikeln konnte eine exzellente strukturelle und morphologische Stabilität nachgewiesen werden. Jedoch vergiftete Trägerdegradation die Platinoberfläche auf atomarer Ebene, was folglich zu erheblichen Aktivitätsverlusten führte. Der Modifizierung von hochoberflächigen Kohlenstoffen mit Stickstoff Heteroatomen konnte ein stabilisierender Effekt auf die Pt Nanopartikel zugewiesen werden. Der modifizierte Kohlenstoff erwies sich als höchst korrosionsresistent und der Katalysator zeigte eine außerordentliche morphologische und elektrochemische Stabilität in ausgedehnten Alterungsprotokollen. Der stabilisierende Effekt konnte auf die Einführung von pyrrolischen Stickstoffgruppen an der Oberfläche zurückgeführt werden. Des weiteren wurde die elektrochemische Pt Oxidation auf verschiedenen Trägern untersucht um Rückschlüsse über mögliche Degradationmechanismen auf Basis von Oxidationsvorgängen zu erhalten.

Diese Arbeit zeigt die Wichtigkeit der Untersuchung von Pt-basierten Brennstoffzellen-katalysatoren unter simulierten Betriebsbedingungen und die Aufdeckung von Degradationsmechanismen und stabilisierenden Trägereffekten. Eine detaillierte Kenntnis auf Grundlage von tiefgreifenden Studien ist essentiell für die Weiterentwicklung effizienter Brennstoffzellen als Bestandteil einer emissionsärmeren Gesellschaft.

# Abstract

Hydrogen fuel cells offer the possibility as devices for electrochemical energy conversion to utilize hydrogen from renewable sources as a clean and low-emission energy source for electrical motors. However, to be able to represent a competitive alternative to todays internal combustion engines in the automotive sector, several difficulties have to be overcome. Especially the catalysts, that are employed at the cathode side for the oxygen reduction reaction (ORR) in low temperature fuel cells and mostly consist of the scarce metal platinum, are studied extensively. Besides maximizing mass-based activities of these catalysts, the durability is of tremendous importance for the design of efficient fuel cells. Thereby, the catalyst support and its chemical and electrochemical corrosion behavior under operating conditions plays a crucial role for the overall the stability. Nowadays, the use of graphitized and high surface area carbons as supports offer advantages as well as disadvantages.

This thesis aims at understanding the influence of alternative oxidic or carbonaceous catalyst supports on the electrochemical and morphological behavior of the catalytic Pt nanoparticles.

The use of alternative catalyst support materials is exemplified by the choice of metal oxides and modified carbons, that were decorated with Pt nanoparticles and extensively studied with regard to their physicochemical properties. Different *in situ* methods are employed to monitor the catalyst/support components under simulated fuel cell operating conditions and to contribute to the scientific knowledge on fundamental degradation processes. It could be shown that indium tin oxide (ITO) used as support degrades depending on the applied potential range under simulated operating conditions. Pt nanoparticles were found to have an excellent structural and morphological stability. However, support degradation lead to a poisoning of the Pt surface on an atomic level and consequently to activity deterioration. Modification of high surface area carbon with nitrogen heteroatoms resulted in an increased corrosion resistance and was was further proven to have a stabilizing effect on the Pt nanoparticles. The catalyst showed extraordinary morphological and electrochemical stability in long-term stress tests. This was ascribed to surface modification in the form of introduction of pyrrolic N groups as most abundant surface species. Furthermore, the electrochemical oxidation of Pt on different supports was studied by various *in situ* methods to track the structural response of the Pt nanoparticles and to draw conclusions about possible degradation pathways as a consequence of oxidation processes. Together, this work illustrates the importance of investigating Pt-based fuel cell catalysts under simulated working conditions and revealing degradation mechanisms and support-related stabilizing effects. A detailed knowledge based on profound studies is essential for the ongoing development of efficient fuel cells as part of a clean energy society.

# Table of Contents

**Danksagung** .......... I
**Zusammenfassung** .......... III
**Abstract** .......... V
**1. Introduction** .......... 1
1.1. Hydrogen Fuel Cell .......... 3
1.2. Degradation Mechanisms of supported, nanoscale Pt ORR Catalysts .......... 7
1.3. Metal Oxides as Supports for Pt Nanoparticles .......... 11
1.4. Carbon Heteroatom Modification and its Application .......... 13
1.5. Electrochemical Pt Oxidation .......... 15
**2. Motivation and Goals** .......... 17
**3. Experimental Part** .......... 19
3.1. Synthesis Procedures .......... 19
3.1.1. Pt on Indium Tin Oxide .......... 20
3.1.2. Pt on Ruthenium Titanium Oxide .......... 20
3.1.3. Pt on modified Vulcan .......... 21
3.2. Physicochemical Characterization .......... 22
3.2.1. X-ray Diffraction (XRD) .......... 23
3.2.2. Transmission Electron Microscopy (TEM) .......... 23
3.2.3. Inductively Coupled Plasma – Optical Emission Spectroscopy (ICP-OES) .......... 24
3.2.4. High-angle Annular Dark Field (HAADF) Scanning Transmission Electron Microscopy (STEM) and Energy-dispersive X-ray (EDX) Spectroscopy .......... 24
3.2.5. Elemental Analysis (EA) .......... 24
3.2.6. Nitrogen Physisorption by BET .......... 25
3.2.7. Zeta Potential (ZP) .......... 25
3.2.8. High Temperature – Differential Electrochemical Mass Spectroscopy (HT-DEMS)…. .......... 25
3.2.9. X-ray Photoelectron Spectroscopy (XPS) .......... 26
3.3. Electrochemical Characterization .......... 28
3.3.1. Preparation .......... 28
3.3.2. Activity and Stability Measurements .......... 29
3.4. *In situ* Characterization .......... 33
3.4.1. Scanning Flow Cell Inductively Coupled Plasma Mass Spectroscopy (SFC ICP-MS)…… .......... 33
3.4.2. *In situ* Electrochemical Cell and Setup .......... 33

3.4.3. High Energy X-ray Diffraction (HE-XRD) .......... 35
3.4.4. Small Angle X-ray Scattering (SAXS) .......... 37
3.4.5. X-ray Absorption Spectroscopy (XAS) .......... 40
**4. Unravelling Degradation Pathways of Oxide-Supported Pt Fuel Cell Nanocatalysts under *In Situ* Operating Conditions .......... 41**
4.1. Introduction .......... 43
4.2. Physicochemical Characterization .......... 43
4.3. Electrochemical Characterization .......... 46
4.4. XPS and STEM/EDX Results .......... 49
4.5. *In Situ* HE X-ray Investigation .......... 51
4.6. *In Situ* Pt, In and Sn Dissolution by SFC ICP-MS .......... 56
4.7. Discussion .......... 58
4.8. Conclusion .......... 63
**5. The Impact of Carbon Support Functionalization on the Electrochemical Stability of Pt Fuel Cell Catalysts .......... 65**
5.1. Introduction .......... 67
5.2. Compositional and Surface Characterization .......... 67
5.3. Analysis on Carbon Surface Functionalization by XPS .......... 69
5.4. Corrosion Behaviour by HT-DEMS .......... 72
5.5. Pt Deposition and ORR Stability .......... 73
5.6. Conclusion and Summary .......... 80
**6. On the Anisotropy of Pt Nanoparticles on Carbon- and Oxide-Support and Their Structural Response to Electrochemical Oxidation .......... 81**
6.1. Introduction .......... 83
6.2. Structure and Morphology .......... 83
6.3. Electrochemical Characterization .......... 87
6.4. *In Situ* Electrochemical Pt Oxidation .......... 89
6.5. Conclusion .......... 99
**7. Summary and Outlook .......... 101**
7.1. *In Situ* Stability Study of Pt Supported on Indium Tin Oxide .......... 101
7.2. Carbon Heteroatom Modification in Pt/C ORR Catalysts .......... 103
7.3. Electrochemical Oxidation of Pt on different Supports .......... 104
7.4. Outlook .......... 106
**8. References .......... 109**
**Appendix .......... 119**
A1 Supporting Information to Chapter 4[52] .......... 119

A2 Supporting Information to Chapter 5[71] ........ 124
A3 Supporting Information to Chapter 6 ........ 131
**List of Acronyms ........ 135**
**List of Chemicals ........ 137**
**List of Figures ........ 138**
**List of Tables ........ 143**
**List of Publications ........ 144**

# 1. Introduction

The fact that between the years 2014 and 2016 the world's carbon dioxide ($CO_2$) emissions seemed to remain on a stable level was a great achievement for todays society. However, in 2017 it was reported that $CO_2$ emissions increased again by 2 %. This was mainly due to the fact, that the observed decreasing emissions in 2017 from the US and Europe were unable to offset steadily increasing emissions from India, China and the rest of the world, resulting in an average global emission growth.[1] Furthermore, it was observed that not only $CO_2$ emissions grew, but also the coal consumption increased in 2017 related to a rising need for energy.[2]

With a current average atmospheric $CO_2$ concentration of 410.8 ppm (June 2018) this value is as high as it ever was.[3] Future trends are hard to predict due to relative large uncertainties in estimating average $CO_2$ emissions for different countries.[4] $CO_2$, as the main share of greenhouse gas emissions and one of the biggest cause for global warming, mainly arises from the combustion of fossil fuels in the industry and transportation sectors. Therefore, it has become a major challenge to decouple a steadily increasing world gross product and world population from the production of greenhouse gases.

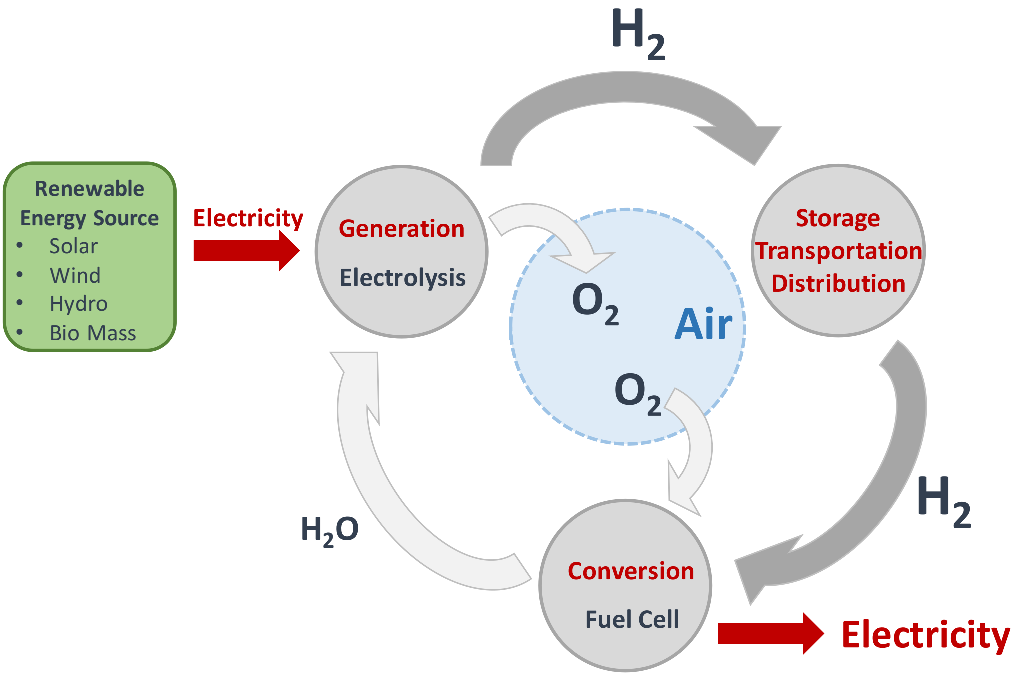

**Figure 1.1** Schematic illustration of the use of Hydrogen for energy conversion and storage. In here, hydrogen is produced by water electrolysis powered by renewable energy sources. Hydrogen is stored and distributed and can be used on demand in a fuel cell to generate electricity.

However, an increasing world population and energy demands of developing nations require the expansion and utilization of clean energy sources. An expanded awareness for sustainability of todays' society combined with alternative and emission-neutral energy resources might be the key in preventing a potentially upcoming environmental crisis. Renewable energies such as wind, solar, hydro and bio mass represent a class of clean energy sources for implementation in the energy grid to provide a sufficient part of the electricity demand. For example, Germany has achieved a pioneering role in the last decade in generating electricity from renewable sources with a contribution of electricity by renewable sources of 39 % in 2017, potentially further increasing in future.[5]

However, renewable energy sources are intermittent with times when the supply does not meet the demand, or when the supply surpasses the demand.[6] Therefore, systems for both energy storage and conversion are needed in order to overcome grit instabilities and ensure reliable energy supply. One $CO_2$ emission-neutral way to use excess power generated by renewable energy sources is the electrolysis of water. The applied electricity enables an efficient splitting of water into its components, oxygen ($O_2$) and hydrogen ($H_2$), see Figure 1.1. In this way, energy generated by renewable resources can be stored chemically in the $H_2$ molecule.
Hydrogen offers the possibility to distribute and transport energy which makes it available and promising for multiple applications. It can be stored stationary (e.g. in metal hydrides, liquified or compressed in tanks)[7] and distributed for the use in industrial applications or the flexible reconversion into water and electricity using a fuel cell device.

Especially for implementation in the transportation sector, low temperature proton exchange membrane fuel cells (PEMFC) offer great potential due to their relative efficient fuel conversion rates, reliability and emission-free character. Several difficulties in sufficient hydrogen storage and transportation and establishing a hydrogen fuel grid as well as technologies for electrolyzers and fuel cells that are comparable to state-of-the-art production/combustion methods are still in the way of establishing a reliable hydrogen community.

## 1.1. Hydrogen Fuel Cell

A fuel cell is a device that is able to efficiently convert chemical energy into electricity and heat. The principle of a hydrogen fuel cell was first observed by W. Grove in 1839, who demonstrated the generation of electricity by two separate Pt electrodes immersed in diluted sulphuric acid in separated hydrogen and oxygen compartments.[8] A single device was called a “gas battery” and a multitude of “gas batteries”, connected in a row, was called a “gas chain”. Grove used the generated electricity to produce hydrogen in an electrolyzer.[9] The first real application of a fuel cell was achieved by the NASA in their space program in 1960 where a fuel cell was used to supply the Gemini and Apollo spacecrafts with electricity and drinking water.

Hydrogen fuel cells are classified by the electrolyte used and by their operating temperature. Proton exchange membrane fuel cells are typically run at 80 °C and use a Nafion® membrane for proton conduction. Alkaline fuel cells (AFC) operate at around 100 °C and due to the lack of proper anion conductive membranes, a liquid electrolyte containing potassium hydroxide is commonly employed. Molten carbonate fuel cells (MCFC) are one example for fuel cells operating at higher temperatures. In here, the electrolyte consists of liquid solution of lithium and sodium carbonates that are soaked in a matrix, allowing operating temperatures up to 1000 °C. In a solid oxide fuel cell (SOFC), running at comparable temperatures to the MCFC, conduction of oxygen anions is enabled by a yttria-stabilized zirconia (YSZ) type membrane.[10]

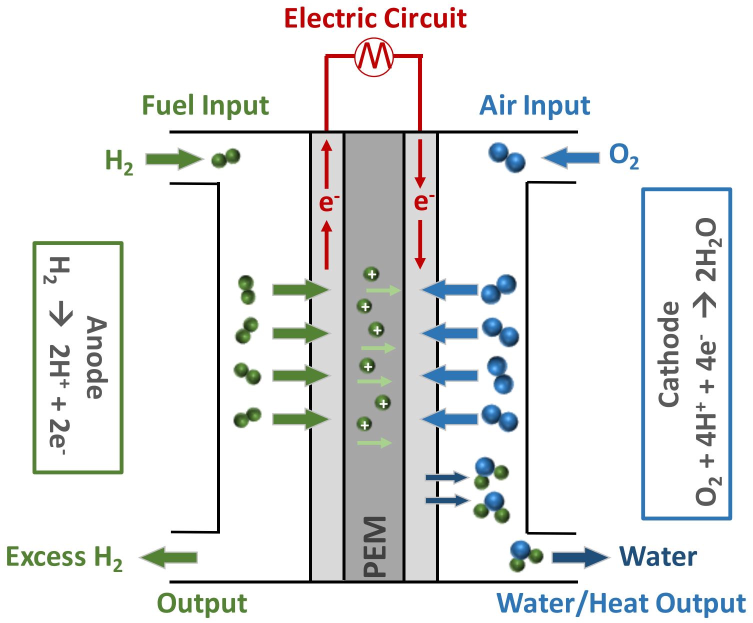

**Figure 1.2** Schematic illustration of the general principle of a proton exchange membrane fuel cell (PEMFC). At the anode the fuel (hydrogen) is oxidized to form protons and electrons. Protons travel through the membrane to the cathode to form water by reacting with oxygen and electrons. The electrons travel through an external electric circuit and can be used as power supply.

The development of PEMFC has increased in the past decades opening its way up to large-scale applications especially in the transportation sector. Cars equipped with hydrogen fuel cells are offered by different manufacturers such as Toyota, Honda or Hyundai.[11] Fuel cell buses for public transportation are already used in several cities around the world [12,13] and recently, a fuel cell train was implemented into the rail network in northern Germany[14].

The general principle of a PEMFC is schematically illustrated in Figure 1.2. A PEMFC comprises of two electrodes that are separated by a proton conducting membrane. At the anode, hydrogen as the fuel is supplied and oxidized to form protons and electrons, see Figure 1.2. The protons can mitigate through the membrane to the cathode side. In a PEMFC, the membrane consists of a polymer, a perfluorosulfonic acid (typically Nafion®) that, when hydrated, is solely conductive for protons and provides the separation for the two electrodes. Hence, the electrons are forced to reach the cathode via an external electric circuit that gives the opportunity to use the electricity by an external device. At the cathode side, oxygen (typically from air) is reduced by reacting with electrons and protons to form water. Catalysts employed at both electrodes usually consist of carbon supported Pt nanoparticles, separated at each side to gas flow fields by gas diffusion backings to provide sufficient gas concentrations at the catalyst surface. Such individual fuel cells, called membrane electrode assemblies (MEAs), can be aligned in rows to generate a stack. Stacks of different sizes and different power ouputs, in which a single cell usually provides around 0.7 V, can be designed with respect to the desired application.[15]

As mentioned before, PEMFC development and commercialization has made great progress recently, still there are several challenges to overcome. Especially in fuel cell application for transportation, storage and distribution of hydrogen becomes an additional issue as a sufficient hydrogen infrastructure is yet not existent. Moreover, costs of fuel cell cars are still not able to compete with cars equipped with state-of-the-art internal combustion engines. The reason for that is the costs of a fuel cell stack for automotive application are strongly dependent on the quantity produced. They were estimated to be 50 $\$/kW_{net}$ (for a 80 $kW_{net}$ PEMFC system) when manufactured at a volume of 100,000 units/yr in 2017. Costs are targeted to decrease to 40 $\$/kW_{net}$ by 2025 for such a manufacturing quantity as claimed by the US Department of Energy.[16] Major contributor to the fuel cell stack costs are not only the noble metal catalysts employed at both electrodes but also other fuel cell components such as the bipolar plates, the ionomer and the gas (re)circulation systems.[16]

When operating a fuel cell, the theoretical available cell voltage ($\Delta E$) for a single cell for the hydrogen/air fuel cell reaction according to

$$H_2 + \frac{1}{2}O_2 \rightarrow H_2O$$

can be calculated by equation (1), with $n$ being the number of transferred electrons per $H_2$ molecule, $F$ Faraday's constant and $\Delta G$ the Gibbs free energy for the above reaction.

$$\Delta E = -\frac{\Delta G}{nF} \tag{1}$$

According to this equation, a single fuel cell gives a theoretical cell voltage (thermodynamic reversible cell potential) of 1.23 V at 1 atm pressure and 25 °C. When a fuel cell is operated at 80 °C, this value reduces to 1.18 V due to the temperature dependency of the Gibbs free energy. However, as mentioned above, single fuel cells nowadays run at around 0.7 V which means that not 100 % of the chemical energy can be converted into electrical energy but partially into heat. Efficiency losses observed in a running fuel cell and their origins will be briefly described in the following paragraphs.

Activation losses are the largest contributor to a decreased efficiency and are originating from sluggish kinetics of the oxygen reduction reaction (ORR) at the cathode. In comparison, the hydrogen oxidation reaction (HOR) at the anode, is much faster and the total activation losses are therefore almost entirely caused by the ORR. In contrast to the fast, two-step oxidation of hydrogen at the anode, the ORR at the cathode involves four elementary reduction steps including four single transfers of an electron and a proton. A possible ORR reaction pathway is proposed as follows:[17,18]

$$O_{2(g)} + 4H^+ + 4e^- + * \rightarrow OOH^* + 3H^+ + 3e^-$$

$$OOH^* + 3H^+ + 3e^- \rightarrow O^* + H_2O_{(l)} + 2H^+ + 2e^-$$

$$O^* + H_2O_{(l)} + 2H^+ + 2e^- \rightarrow OH^* + H_2O_{(l)} + H^+ + e^-$$

$$OH^* + H_2O_{(l)} + H^+ + e^- \rightarrow 2H_2O_{(l)}$$

In this reaction equations, three different surface intermediates ($OOH^*, O^*$ $and$ $OH^*$) are involved and adsorbed with different binding strength on the catalyst surface. The total ORR rate strongly depends on the binding strength of the intermediate involved in the rate limiting step, that is, the step with the highest energy barrier. The goal is to minimize energy barriers for ad- and desorption and, thus, to facilitate each reaction step resulting in improved ORR reaction rates. Therfore, the right choice of catalyst (usually Pt and its alloys[19]), that enables an optimized binding strength to those intermediates, is of tremendous importance.

Another cause for efficiency drops of fuel cells are Ohmic losses resulting from internal resistances of fuel cell components including the membrane, electrodes, bipolar plates and the interconnections. Fuel crossover can additionally cause an increase in overpotential due to fuel that directly crosses from the anode through the membrane without being oxidized. Furthermore, at high reaction rates, thus at high current densities, concentration losses can occur. They result from mass transport limitations at both electrode sites where the concentration of the gases reduces at high reaction rates. At the cathode the increased formation of water at high current densities leading to flooding inhibits the transport of oxygen to the catalyst surface which hampers the overall efficiency.

## 1.2. Degradation Mechanisms of supported, nanoscale Pt ORR Catalysts

As mentioned above, Pt based materials are commonly employed at the PEM cathode as catalysts for the ORR as they enable binding strengths of the intermediates close to the optimum, making them excellent ORR catalysts. While maximizing the ORR activity by engineering the Pt catalysts structure and morphology[18,20-24], the stability behaviour of the catalyst/support couple is of similar importance. In addition, when the catalyst/support ensemble degrades during the lifetime of a fuel cell, severe performance losses are observed, making this one of the biggest drawbacks in fuel cell application and large-scale commercialization. On the way to competing with automotive internal combustion engines, it was reported by the US Department of Energy (DoE) that the system durability still remains the most unresolved issue and hence, has to be improved. On the other hand, system cost, energy efficiency and specific power density are close to meeting the targets.[25]

In order to improve the overall durability, a detailed knowledge on fuel cell related degradation phenomena has to be established. Therefore, the cathode catalyst lifetime behaviour has been intensively studied in PEMFC research due to its major impact on the overall durability of a running fuel cell. With an anticipated ten year lifetime of a fuel cell car (equals 5,000 operation hours or 240,000 km driving distance) as proposed by the DoE[16], it has become an important challenge to investigate and understand the processes that contribute to activity deterioration in PEMFC catalysts. Especially with the aim of continuously lowering Pt loadings, Pt degradation is hardly acceptable as it makes the impact on performance loss even more fierce.

Several different degradation mechanisms, including Pt dissolution, detachment and agglomeration as well as Ostwald ripening and carbon corrosion have been identified and investigated in the past (see Figure 1.3) and will be described point by point in the following. As this work focuses on degradation processes for monometallic Pt nanoparticles and the support components, alloy PtX (X = transition metal) related degradation phenomena will not be discussed.

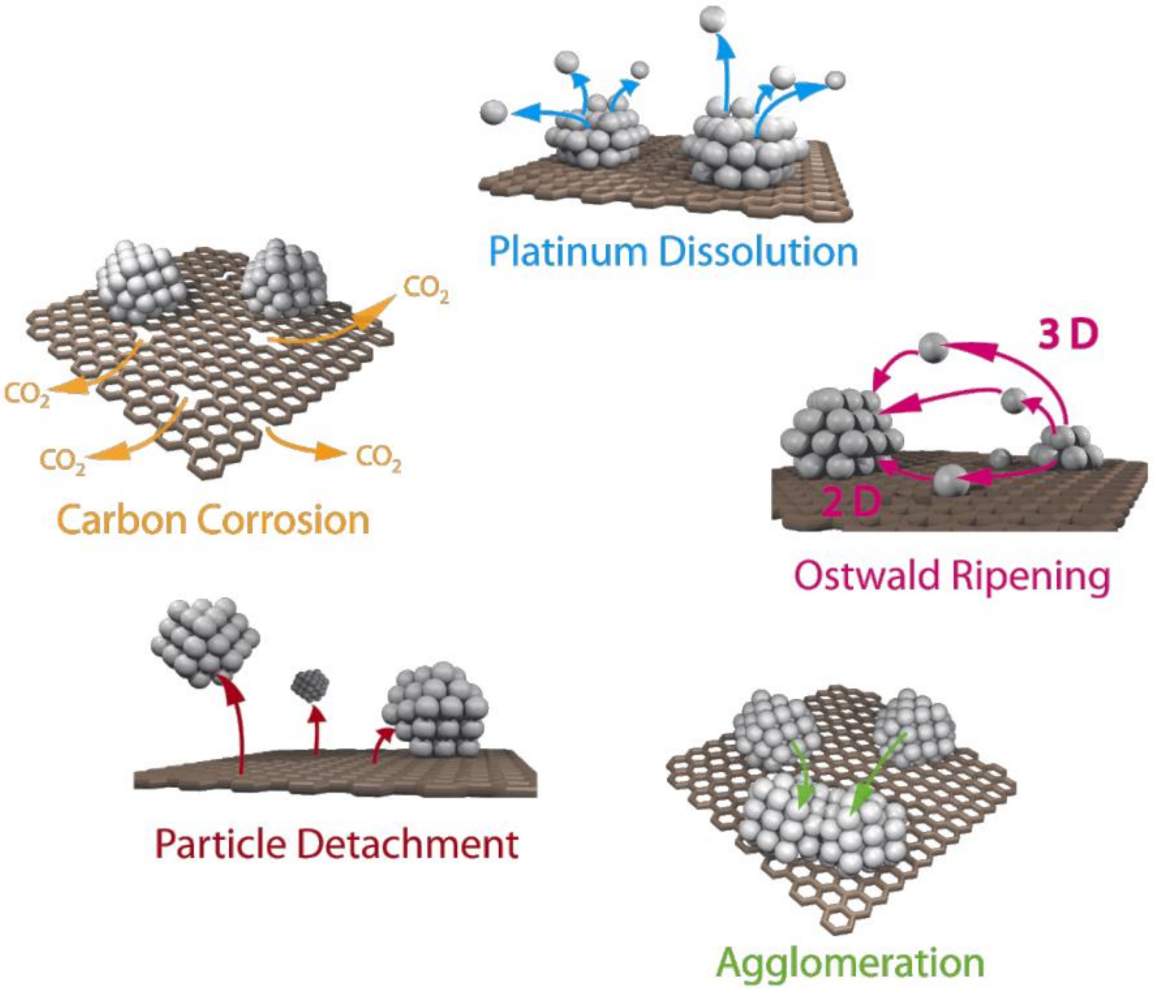

**Figure 1.3** Schematic illustration of proposed degradation mechanisms for Pt nanoparticles supported on carbon including Pt dissolution, Ostwald ripening, agglomeration, detachment and carbon corrosion. Reprinted with permission from Ref. [26] from *Beilstein Journal of Nanotechnology* under the terms of the Creative Commons Attribution License (http://creativecommons.org/licenses/by/2.0).

### *Pt Dissolution and Ostwald Ripening*

Pt dissolution and its role in catalyst degradation has been extensively studied in literature.[27-34] The origin for Pt dissolution arises from the formation of Pt oxide and its thermodynamic (in)stability. The oxidation of Pt is conversely discussed in literature due to the variety in potential Pt oxidation states and Pt-oxide compounds (mostly PtO, $PtO_2$ and $PtO_3$). However, the following reaction equations describe one potential acidic dissolution pathway, that is likely to occur in a fuel cell environment (low pH and potentials close to 1 V).[32] It involves the formation of PtO and its acidic dissolution in the form of $Pt^{2+}$:

$$Pt + H_2O \rightarrow \; PtO + \; 2H^+ + \; 2e^-$$

$$PtO + \; 2H^+ \rightarrow \; Pt^{2+} + \; H_2O$$

Pt dissolution is believed to be more severe for smaller nanoparticles due to their higher surface energy and can therefore dissolve at lower potentials compared to bulk Pt (Gibbs-Thomson effect). Different studies observed a strong dependence of the Pt dissolution rate on the particle size where the critical particle diameter was proposed to be 5 nm (particle size effect).[35-37] Furthermore, it was reported that anodic Pt dissolution can be observed at potentials as low as 0.85 V, but more severe dissolution from oxide reduction was monitored at more positive potentials corresponding to fuel cell start-up/shut-down procedures.[38] As a consequence, the dissolution of Pt from the particles can cause strong performance losses with time. It is considered as a primary degradation mechanism because it can lead to other phenomena such as Ostwald ripening.[39] In this case, the Pt species that were dissolved from smaller Pt particles redeposit on larger particles causing overall increase in particle size and surface area loss (3D Ostwald ripening). Dissolved Pt can furthermore be reduced and deposit in the membrane upon reaction with cross-over hydrogen from the anode.[35,40]

### *Carbon Corrosion*

Another primary degradation mechanism is carbon corrosion originating from oxidation of the carbon support.[26,33,41-45] The carbon corrosion reaction in aqueous acidic environment can be expressed as follows:

$$C + 2H_2O \rightarrow CO_2 + 4H^+ + 4e^-$$

The standard potential ($E_0(C/CO_2)$) for this reaction is 0.207 V.[32] However, due to its slow kinetics, it is not predominant in a fuel cell operating regime below 1 V. But, as during fuel cell start-up/shut-down processes high potentials up to 1.5 V can be reached and as carbon corrosion is believed to be catalyzed by Pt[46,47], it can cause a severe loss of the catalyst's structural intigrety accompanied by performance deterioration. Changes in the hydrophilicity due to the formation of oxygenated surface groups by carbon oxidation and concomitant changes in flooding behaviour and mass transport limitations are other consequences of carbon corrosion.[48]

### *Particle Detachment and Agglomeration*

Carbon corrosion can furthermore trigger other, secondary, degradation processes such as detachment[41,44,49] and agglomeration.[37,50,51] Detachment of whole Pt particles from the support can be caused by a weakened attachment of the particle to the support initiated by carbon corrosion. Thus, even though the particles are still present in the cell, they are not connected to the electrode resulting in both activity and surface area deterioration. Agglomeration or coalescence of catalyst particles due to the migration and collision of single particles to larger particles, which might be facilitated by (local) carbon corrosion weakening particle support interactions, is another cause for activity degradation. It can lead to a loss in overall particle count and a decreased active surface area. Phenomena of agglomeration and coalescence were found to be dependent on the Pt weight loading on the carbon support and on the type of high surface area carbon used.[43]

In order to improve the catalysts overall durability, several synthetic and analytical approaches can be followed. Therefore, the following two chapters (1.3 and 1.4) give a brief literature overview on possibilities to reduce catalyst degradation by engineering of the support. Replacement of the carbon support by a metal oxide or a modified carbon, its properties and influence on the overall structural and electrochemical Pt stability is discussed. Additionally, chapter 1.5 will a give a more detailed overview on Pt oxidation processes from literature and its critical role for the development of stable ORR electrocatalysts.

## 1.3. Metal Oxides as Supports for Pt Nanoparticles

*Reproduced in part from Ref* [52] *(Adv. Energy Mat.,* ***2018****, 8 (4), 1701663) with permission from John Wiley and Sons, Copyright 2018.*

Carbon corrosion, as explained before, can cause severe damage on the catalytic active component accompanied by fuel cell performance and stability losses. One way to completely prevent carbon corrosion, is the use of alternative, carbon-free catalyst supports. Intensive research focused on the replacement of carbon as support in fuel cell catalysts.

Metal oxides have recently gained attention in this field because they offer a variety of features required for a stable electrocatalyst for oxygen reduction.[53,54] Essential properties for cathode catalysts supports are a high surface area, high electrical conductivity, thermal stability, and above all, their corrosion resistance. Therefore, several metal oxides have been investigated: Popov and co-workers showed that Pt on $TiO_2$ has a high stability toward ORR caused by the high corrosion resistance and the strong metal support interaction (SMSI).[55] This SMSI effect was further analyzed by AlonsoVante and co-workers,[56] they were able to show changes in the local electron density of Pt when deposited on titanium oxide-carbon and tungsten oxide-carbon support. By X-ray photoelectron spectroscopy (XPS) analysis they determined an increase in the asymmetry of the Pt 4f peak which the authors attributed to either an alloy formation between Pt and the support or a partial charge transfer from the support to Pt. Furthermore, a molybdenum-doped Ti dioxide was found to be a stable electrocatalyst because of electronic structure changes in the Pt upon synergistic interaction with the support material.[57] A similar phenomenon was observed for $Pt/Ta_{0.3}Ti_{0.7}O_2$ where the electrochemical surface area (ECSA) decreased less compared to Pt/C reference catalyst when exposed to accelerated load cycling test designed to test the electrocatalyst stability.[58,59] The catalyst exhibited good activity when tested in an operating fuel cell and exceptional catalytic stability after 10,000 cycles of a simulated start-up/shut-down stress test. The superior catalyst stability was explained with a lower Pt dissolution rate compared to carbon supported Pt electrocatalyst and the SMSI between Pt nanoparticles and $Ta_{0.3}Ti_{0.7}O_2$.

Another class of stable carbon-free supports was found to be $RuO_2/TiO_2$ and $RuO_2/SiO_2$.[60-63] These materials offer a conductivity and surface area comparable to mesoporous carbon, a promising electrochemical stability against aggressive accelerated test protocols besides improved membrane electrode assembly (MEA) performance. However, incorporation of Pt nanoparticles with a well-defined size into the electrodes to decrease Ohmic and transport losses has to be improved to make it a viable alternative in automotive application. Furthermore, Dou *et al.* reported on tin oxide as another candidate for carbon-free support in PEMFCs.[64] The material retained 27% of its initial ECSA while the Pt/C reference catalyst showed almost no more surface area after 2,000 cycles.[64] In another approach, Tsukatsune *et al.* found that their Pt/$SnO_2$ and Pt/Nb-$SnO_2$ electrocatalysts suffer from low specifc surface area accompanied with low specific activity.[65]

Cognard *et al.* investigated antimony-doped tin oxide supported Pt electrocatalyst as cathode material for PEMFC.[66] The harsh accelerated stress test (AST) conditions of potential jumps between 1.0 and 1.5 V lead to depletion of Sb atoms from the support surface and a decreased conductivity and hence to a loss in catalytic activity. Indium tin oxide (ITO) offers several advantages in regard to the conditions that are present in the environment of fuel cell catalysts at the cathode side such as low pH, high temperatures, and high potentials. Additionally, ITO has the advantage of low electrical resistance. Pt/ITO catalyst systems have been tested as alternative material to conventional Pt nanoparticles dispersed on high surface area carbon. Liu *et al.* showed that a Pt/ITO ORR electrocatalyst offered activity as well as enhanced stability during an AST.[67-69] These Pt nanoparticles were deposited on the ITO via a galvanic displacement of a Cu monolayer from a $K_2PtCl_4$ precursor. While the authors did not provide evidence for a complete displacement or removal of contaminating Cu residues, their data suggested that the enhanced ORR activity is caused by synergistic effects between surface Sn and Pt.[69] A recent XPS study by Wang *et al.* of Pt/ITO as electrocatalyst for PEMFC MEAs revealed strong changes in the indium oxide component after operating conditions.[70] These changes resulted in poor conductivity of the support followed by large activity losses.

## 1.4. Carbon Heteroatom Modification and its Application

*Reprinted in part with permission from Ref*[71] *(Chem. Mat.,* ***2018****, 30 (20), 7287-7295). Copyright (2018) American Chemical Society.*

Instead of employing carbon-free materials as Pt support, one can also change the properties of the high surface area carbons in order to make them more stable in a fuel cell environment. Furthermore, as a result of improving the carbon corrosion resistance, other secondary degradation processes might also be suppressed.

Porous carbon materials are the support material of choice for noble metal nanoparticle catalysts. To make for a good catalyst support, the set of required properties range from high surface area and porosity to sufficient conductivity, corrosion resistance and chemical stability. Different carbons are usually classified by their BET surface area that is in the range of 200-400 $m^2$ $g^{-1}$for Vulcan and CNTs, but can be as high as 1300 $m^2$ $g^{-1}$ for types of Ketjen black, Black Pearls[72] and hollow graphitic/carbon spheres (HGS/HCS)[73,74]. Among the large variety of known porous carbon materials, quite a few carbons are known to meet at least some of the criteria mentioned before and have therefore been studied extensively as supports.

The introduction of new chemical (surface) functionalities offers ample possibilities to tune a carbonaceous material with respect to its electronic, structural, morphological, and hence reactive properties and has emerged as a very popular method in the search for improved catalyst supports.

Nitrogen is one prominent heteroatom used for introducing functional surface groups or for modification of the carbon backbone. In applications for supercapacitors, it was found that functionalization by pyrolysis of organic salts enhances both capacitance and cycle durability of non-porous carbons.[75,76] The efficiency towards electrochemical hydrogen peroxide production was proven to be superior in the nitrogen-doped ordered mesoporous carbon CMK-3 over a wide pH-range.[72] Modified carbon-based materials were furthermore tested as metal-free electrocatalysts towards the oxygen reduction reaction (ORR): nitrogen-doped multi-walled carbon nanotubes (N-MWCNT) showed outstanding activity in alkaline medium.[77,78] Functionalization of Vulcan carbon by coating with zeolitic imidazolate frameworks (ZIF) was reported to enhance both ORR activity and stability.[79] Much work was devoted to analyze and understand the degree and nature of carbon modification/functionalization in various types of carbons ranging from graphene to CNTs and carbon blacks.[80-82] Ammonia treatment of pre-oxidized carbons is one promising way of introducing N-functional groups in relative high concentrations on the carbon surface. While theoretical models have been employed to predict the gasification rate and the creation of an internal porous network[83], other studies were focusing on acid-base properties of N-doped nanocarbons[84,85], the thermal stability[86] and the translation of this method to a wider range of carbon-based materials[87].

When modified carbons are used as support for nanoscale noble metal catalysts, a wide range of application in heterogeneous catalysis such as hydrogenation reactions[88], methanol oxidation[89] and selective oxidation[90] opens up. Along with latest developments in the research field of PEMFC, functionalized carbons are widely employed as electrocatalyst support to stabilize the active component (mostly platinum) from altering under simulated working conditions.[91-96] When hollow carbon-spheres were doped with nitrogen by dopamine treatment and Pt was deposited, an improved Pt distribution was observed which the authors ascribed to interactions between the inserted nitrogen atoms and Pt as binding energy shifts from N 1s and Pt 4f XP spectra were noticed. These interactions were further believed to cause the enhanced ORR long-term stability.[94] Pt supported on N-containing mesoporous carbon obtained from ionic liquids showed higher electrochemical active surface area compared to a commercial Pt/C catalyst with similar particle size.[92] N-doped carbon shells around Pt on CNTs were obtained by a subsequent polymerization of aniline around the Pt precursor impregnated on CNTs, followed by reduction of the Pt precursor. The resulting composite showed enhanced stability against any kind of Pt degradation which was explained by the stabilizing effect of the porous carbon shells around the Pt.[91] Pt on a polyaniline (PANI) based support was tested in an MEA setup and showed first promising results for the application of Pt ORR catalysts on an alternative carbon support.[97] Another beneficial effect of surface modified carbons was recently reported to be a superior distribution of the Nafion ionomer in the MEA.[98] The enhanced fuel cell performance was attributed to interactions between the N-modified carbon surface and the sulfonic groups in the ionomer resulting in decreased local, that is, non Fickian mass transport losses at high current density under hydrogen-air conditions.

## 1.5. Electrochemical Pt Oxidation

As mentioned above, surface processes such as Pt oxidation have key influence on the catalysts stability because the degradation due to Pt dissolution is directly linked to the formation of $PtO_x$-species and the consecutively reductive dissolution. Therefore, knowledge about the origin of these surface processes is of great interest to understand the degradation behavior on a fundamental level.

On Pt single crystal surfaces it was found that Pt oxidation occurs in the form of place exchange of Pt and O atoms on the Pt(111) surface.[99,100] By *in situ* surface X-ray diffraction (XRD) it was shown that with increasing potential the oxide structure consists of a Pt-rich inner and an O-rich outer layer which then transforms to a more homogenous oxide at above 1.1 V. By cycling back to more negative potentials, the authors could proof that up to a critical oxide coverage the process of place exchange is quasi-reversible because place-exchanged atoms are located on top of their original positions. In another study by Feliu *et al.* no changes in the voltammograms were observed by consecutive cycling up to 1.15 V evidencing reversible ordering of Pt(111).[101]

The structural sensitivity of intermediate stages of Pt oxidation was investigated by surface-enhanced Raman spectroscopy on Pt(111) and Pt(100). Therein, it was reported that place-exchange and the formation of an amorphous 3D $\alpha$-$PtO_2$ proceed sequentially on the Pt(111) whereas on Pt(100) both processes proceed simultaneously above 1.1 V.[102] Studies on a monolayer of Pt deposited on a Rh(111) single crystal showed the evolution of a Pt oxide structure by electrochemical oxidation up to high potentials of 1.6 V while at potentials below 1 V chemisorbed oxygen-containing species at the Pt surface were proposed. The onset of Pt oxide formation was found to be dependent on the kinetic stability of chemisorbed species resulting from different surfaces (single crystal vs. nanoparticle). By combined computational and experimental methods, Pt oxide in the form of $Pt_3O_4$ was in best agreement with both methods.[103]

Furthermore, high-energy-resolution X-ray absorption showed that for small Pt nanoparticles different adsorbed species on the Pt surface (hydrogen and O/OH, Pt oxide) can be distinguished in certain potential regions.[104] Onset of Pt oxidation was found at 0.96 V and with that, somewhat lower than on single crystals, which can be explained by a stronger bond of the Pt nanoparticle surface to oxygen. In another study by Adzic *et al.*, a wide potential range up to 2.6 V was investigated by *in situ* X-ray methods.[105] According to the authors, O and OH adsorption at around 0.7 V and place exchange onset at 0.9 V was observed resulting in the formation of an α-$PtO_2$ which was dissolved at high potentials above 1.9 V. Additionally it was found that Pt oxidation only occurs at the outer Pt layers while the inner, bulk part remains metallic. In a work by Imai *et al.* a time-resolved X-ray diffraction and energy dispersive X-ray absorption study on Pt nanoparticles also proposes the formation of an α-$PtO_2$ by analyzing the Pt-O bond length.[106]

A study on the potential dependent structural transformation of Pt on different carbon supports in a potential window from 0.4 to 1.4 V showed that Pt nanoparticle surfaces after aging were oxidized to $Pt^{(2+)}O$ at 1.4 V. Differences were observed for the onset of these oxide formations and the reduction to the metallic state for the different supports from full reversibility to irreversibility.[107]

Pt oxidation was also studied on nanoparticles supported on a metal oxide. For a ceria support it was shown by XPS and TEM that the oxide support has an impact on the formation Pt oxide as a composite of Pt oxide and Ce was formed, but it was reversibly reconverted to metallic Pt.[108] The authors attribute this phenomenon as evidence for strong interaction between $CeO_2$ and Pt. Formation of Pt-O-Ce bonds stabilizes Pt from sintering under oxidative atmosphere. While these studies were conducted at different temperatures and gas atmospheres and not in real electrochemical environments, it still gives a first impression of Pt oxidation/reduction in oxide-supported Pt catalysts.

# 2. Motivation and Goals

The overall objective of this work is to expand our current knowledge and understanding of degradation mechanisms of supported Pt nanoparticle catalysts for PEMFC cathodes. Emphasis is placed on a molecular-level understanding of the ORR activity and cycling stability of Pt catalyst/support couples involving new support materials, in particular oxides and doped carbons, as alternatives to traditional carbon blacks. Understanding is generated through structure-composition-activity-stability relationships established using *in situ* analytics.

The fuel cell cathode environment with its time-variable, quite anodic potentials generates harsh conditions for both the nano-scale catalysts and support components. Detailed knowledge about the exact degradation mechanisms of new support materials is still unknown. This might be due to the fact that, processes such as Pt dissolution, carbon corrosion, particle detachment and coalescence or ripening are oftentimes coupled to each other. Therefore, the application of several different spectroscopic and analytical (*in situ*) methods is the key to gain a comprehensive knowledge. Simulated fuel cell environments and accelerated degradation protocols will help to evaluate the catalysts suitability for fuel cell application on an early stage of the development process.

To contribute to the general goals mentioned above, this work will focus on the following projects:

- In the first part (chapter 4), an indium tin oxide (ITO) supported Pt electrocatalyst is analyzed and evaluated for its suitability as durable fuel cell catalyst. Previous works reported Pt/ITO as a promising catalyst system, but only little work had been done to understand how the entire catalyst/support couple behaves directly under AST conditions with special emphasis on Pt particle growth and agglomeration as well as support degradation. Therefore, Pt/ITO is first intensively characterized by physicochemical methods followed by the application of accelerated stress tests in fuel cell relevant potential windows. Changes in Pt mass-based activity and electrochemicl active surface area upon extended potential cycling are carefully followed. In a next step, several different complementary methods are applied to track structural, compositional and morphological changes in both Pt catalyst and metal oxide support and to link those changes to trends in electrochemical activity and surface area of Pt/ITO. With help of different *in situ* (mostly X-ray based) techniques, new insight on the operating behaviour of this novel class of electrocatalyst is obtained.

- In chapter 5 findings on the impact of carbon support modification by doping with heteroatoms on its physicochemical properties and on the electrochemical Pt stability are presented. A commercial, state-of-the-art high surface area carbon is modified in a simple two step approach involving the acidic oxidation followed by amination at elevated temperatures resulting in a family of heteroatom-doped carbons. The changes in surface area, surface potential and bulk as well as surface composition upon this treatment are reported. A special emphasis is put on the behaviour towards carbon corrosion as it is highlighted to be a major contributor to PEMFC performance deterioration. Furthermore, when used as Pt catalyst support, the influence of the support heteroatom doping on the electrochemical long-term stability is investigated. The application of *in situ* wide and small angle X-ray scattering methods contribute to the understanding about the catalyst's stability. The nature of heteroatom doping in form of nitrogen incorporation in the carbon matrix is analyzed to determine the most abundant surface species and to draw conclusion as to what extent the surface modification influences the stability of the Pt nanoparticles.
- Chapter 6 addresses the electrochemical oxidation of supported Pt nanoparticles in a detailed study applying different *in situ* methods. Three different catalyst supports (indium tin oxide (ITO), mixed ruthenium titanium oxide (RTO) and carbon) are used in order to determine its influence on the Pt oxidation behavior. The catalyst/support systems are first intensively studied regarding their structure and morphology revealing differences in particle shape and electronic structure depending on the different supports and the different Pt synthesis routes. The changes of Pt nanoparticles upon electrochemical oxidation up to 1.5 V are followed by *in situ* X-ray diffraction and absorption. Rietveld refinement and peak fitting of the absorption spectra reveal the potential-dependent structural responses of the Pt catalyst on the different supports. Parameters such as Pt crystallite size, Pt lattice parameter, Pt scale factor as well as the white line area and its components are analyzed as a function of applied oxidizing (and reducing) potentials. Furthermore, *in situ* dissolution experiments show trends in $Pt^{n+}$ dissolution to complement the findings from X-ray investigations and to link changes in crystallite parameters and metallic and oxidized domains to the dissolution rate. With that, support- and morphology-depending properties should help to understand the nature of Pt oxidation at a fundamental level.

# 3. Experimental Part

*Reproduced in part with permission from Ref*[52] *(Adv. Energy Mat.,* ***2018****, 8 (4), 1701663) with permission from John Wiley and Sons, Copyright 2018 and from Ref*[71] *(Chem. Mat.,* ***2018****, 30 (20), 7287-7295), Copyright (2018) American Chemical Society.*

The following sections describe all synthetic procedures including synthesis of the metal oxide supports, the modification of the carbon support and the synthesis and deposition of Pt nanoparticles performed in this work. Afterwards all methods for physicochemical characterization as well as the procedures for electrochemical activity and stability measurements will be described. In the end of this chapter, the experiemental details on the performed *in situ* analytical and X-ray methods will be given including a brief explanation on the theoretical background of the most frequently methods used in this work.

*Detailed information on all chemicals used in this work, can be found in the List of Chemicals on page 137.*

## 3.1. Synthesis Procedures

In this work, two different families of catalyst systems were synthesized and analyzed, Table ***3.1*** gives an overview over the catalysts and in the corresponding chapters they are studied. The first set of catalysts are metal oxide supported Pt nanoparticles that are analyzed in chapter 4 and 6. The second family of materials are Pt nanoparticles, that are supported on modified carbon materials. The results of this study are shown in chapter 5. The synthesis of metal oxide support, Pt nanoparticles and the process of carbon modification will be described in the following.

**Table 3.1** Overview over different materials used in this work with the corresponding chapters in which their characterization is discussed.

| Material | Chapter |
|---|---|
| Pt/ITO | 4, 6 |
| Pt/RTO | 6 |
| Pt/modified Vulcan | 5 |

### 3.1.1. Pt on Indium Tin Oxide

***Indium Tin Oxide***

$In(Cl)_3$ (1.434 g) was dissolved in deionized (DI) water (2.16 mL) and the solution was stirred for 10 min. Then $SnCl_4$ (79.2 µL) was added to the solution under stirring for 10 min followed by addition of ethanol (9 mL). Afterwards propylene epoxide (5.5 mL) was added drop-by-drop to the alcoholic solution at room temperature under continuous stirring for 15 min. When the solution turns milky, stirring was continued for another 10 s and put into an ice bath afterwards for 10 min. The resulting gel was aged for 10 h and then subjected to a series of solvent exchange in acetone for 10 times in 3 days. The acetone-loaded gels were introduced into a supercritical dryer (SFT-100, Supercritical Fluid Technologies, Inc.), and acetone was removed using supercritical $CO_2$ extraction (45 °C and 275.8 bar). The dry gel was further calcined at 820 °C for 150 minutes in air.

***Pt Deposition on ITO***

Platinum nanoparticles were synthesized using a solvothermal synthesis route based on previous work.[109] In detail, $Pt(acac)_2$ (0.6 mmol), 1,2-tetradecanediol (1.2 mmol), oleylamine (300 µL), oleic acid (300 µL) and 100 mg ITO were dispersed in dibenzylether (50 mL). The mixture was stirred under nitrogen atmosphere to remove excess of oxygen. Then, the temperature was raised to 80 °C and held for 5 min to ensure complete dissolution of Pt precursor and the reducing agent. Afterwards, the temperature was raised with the ramping of 1 °C $min^{-1}$ to 165 °C and kept for 1h. The mixture was cooled down to room temperature and ethanol (80 mL) was added, followed by sonication with an ultrasonic horn for 1 h and stirring overnight. The supernatant was removed by centrifugation (7800 rpm, 15 min) and washed with ethanol (40 mL) three times. The received catalyst was freeze dried overnight.

### 3.1.2. Pt on Ruthenium Titanium Oxide

***Ruthenium Titanium Oxide***

In a typical synthesis of Ruthenium Titanium Oxide (RTO)[62,63], $TiO_2$ powder first dispersed in DI water (250 mL) in a sonification bath for 30 min. Afterwards, $RuCl_3 \cdot xH_2O$ was added and the mixture was stirred for another 30 min. The pH then was adjusted to 7 by adding 0.05 M KOH under continuous stirring. The resulting black powder was filtered and washed several times with water, dried at 120 °C in air for 8 h and calcined at 450 °C in air.

***Pt Deposition on RTO***

For the RTO support Pt was deposited via a wet chemical approach as reported elsewhere. [62,63] For a typical synthesis, RTO powder was added to a solution of $H_2PtCl_6 \cdot 6H_2O$ in formic acid and water (600 mL) . The mixture was sonicated for 30 min and then heated to 80°C for 2 h der continuous stirring. Afterwards, the produced was filtered and washed several times with water and dried at 60°C in air.

### 3.1.3. Pt on modified Vulcan

***Carbon Modification***

3 g Vulcan XC 72R (Cabot) were first treated in diluted 1 M HCl (300 mL) for 24 h at room temperature (RT) to remove residual metal traces (referred to as HCl-Vulcan). Afterwards, the carbon was intensively washed with miliQ until the filtrate was neutral and dried overnight at 90°C in air. Oxidation of the carbon was performed by treatment of the HCl-Vulcan (2 g) in concentrated $HNO_3$ (200 mL) at 90°C for 5 h and again washed with miliQ and dried overnight at 90°C in air (referred to as O-Vulcan). For ammonolysis, O-Vulcan (ca. 300 mg) was placed in an oven crucible and the tube furnace was first purged with nitrogen and afterwards heated up (5 $°C\ min^{-1}$) under constant $NH_3$ flow (10 $L\ h^{-1}$) to 400 or 800 °C. The temperature was kept for 2 h and the sample was then naturally cooled down to RT under nitrogen atmosphere. Samples are referred to as N-Vulcan 400°C and N-Vulcan 800°C, respectively.

***Pt Deposition on modified Vulcan***

To deposit the Pt nanoparticles on the different supports, a wet impregnation approach was followed. Therefore, 150 mg of carbon support (Vulcan XC 72r, O-Vulcan, N-Vulcan 400°C or N-Vulcan 800°C) were added to a solution of $H_2PtCl_6 \cdot 6H_2O$ (99.6 mg) in a 1:1 mixture of miliQ and iPrOH. The slurry was mixed using a horn sonifier (Branson, output 6 W) for 15 min in an ice bath and afterwards freeze dried for 2 days. For reduction of the Pt precursor, the powder was treated in hydrogen atmosphere (4 % $H_2$ in Ar): After purging with nitrogen the gas was changed to $H_2$/Ar and the temperature was raised to 200 °C with a ramping of 2 $°C\ min^{-1}$ and held for 2 h and afterwards cooled to room temperature under nitrogen atmosphere.

## 3.2. Physicochemical Characterization

The following sections will give an overview and experimental description of all physicochemical characterization techniques used in this work, starting with essential methods such as XRD, TEM and ICP-OES followed by more advanced spectroscopic and analytical techniques with references to the corresponding result chapters.

Due to the variety of methods used in this work, the following Table 3.2 lists all physicochemial characterization techniques. It gives references to the sub-sections with the experimental descritptions and the corresponding chapters in which the results are presented and discussed.

**Table 3.2** Overview of Methods for physicochemical characterization used in this work with reference to the sections in which they are described. *x* indicates the the application of the method for the corresponding result chapter.

| **Method** | | **Exp. Section** | **Ch. 4 – Pt/ITO** | **Ch. 5 – Pt/N-C** | **Ch. 6 – Pt Ox** |
|---|---|---|---|---|---|
| XRD | | 3.2.1 | *x* | *x* | *x* |
| TEM | | 3.2.2 | *x* | *x* | *x* |
| ICP-OES | | 3.2.3 | *x* | *x* | *x* |
| HAADF STEM | | 3.2.4 | *x* | | |
| Elemental Analysis | | 3.2.5 | | *x* | |
| $N_2$ Pysisorption | | 3.2.6 | | *x* | |
| Zeta Potential | | 3.2.7 | | *x* | |
| HT-DEMS | | 3.2.8 | | *x* | |
| XPS | | 3.2.9 | *x (synchrotron)* | *x (laboratory)* | |
| ***In situ*** | SFC ICP-MS | 3.4.1 | *x* | | *x* |
| | HE-XRD | 3.4.3 | *x* | *x* | *x* |
| | SAXS | 3.4.4 | *x* | *x* | |
| | XAS | 3.4.5 | | | *x* |

### 3.2.1. X-ray Diffraction (XRD)

XRD is a powerful technique to investigate crystalline materials on the bulk scale. It is possible to analyze the sample with respect to its crystalline composition, crystallite size and lattice parameter. The method is based on the elastic scattering of X-rays by atoms that are ordered in lattice planes of a crystal structure.

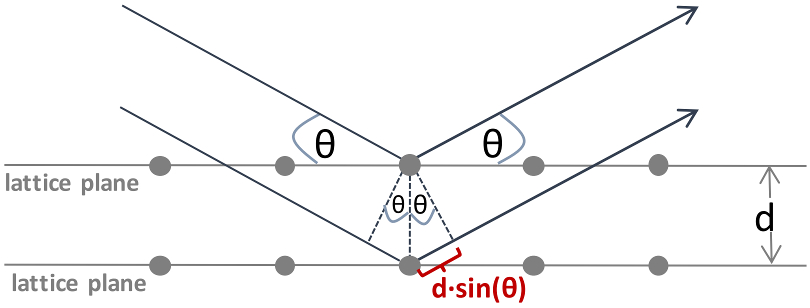

**Figure 3.1** Schematic illustration of the Bragg equation.

Figure 3.1 shows a schematic visualization of the Bragg equation that gives the dependence of the scattering angle $\theta$, the incident X-ray wave $\lambda$ and the distance between two lattice planes $d$, while $n$ is an integer (equation (2)). Constructive interference is obtained if the scattered X-ray waves are in phase ($n = 1,2, \dots$).

$$n\lambda = 2d\ sin\theta \qquad (2)$$

X-ray diffraction patterns were collected on a Bruker D8 Advance diffractometer (Bruker AXS) in Bragg Brentano geometry using Cu $K_\alpha$ radiation (0.154 nm) and a position sensitive device as detector. Profiles were recorded between 20 and 90 ° using a step size of 0.04 ° and 7 s time at each step.

### 3.2.2. Transmission Electron Microscopy (TEM)

TEM images were obtained using a FEI Tecnai $G^2$ 20 S-TWIN equipped with a $LaB_6$ cathode operating with 200 kV acceleration voltage and a resolution limit of 0.24 nm. In order to prepare a sample, a small amount of catalyst powder was dispersed in absolute ethanol using an ultrasonic horn or a sonification bath and afterwards drop casted on a Cu grid (300 mesh with lacey carbon film) and dried in air at 60 °C.

High resolution TEM (HRTEM) was performed using a FEI Titan 80-300 TEM electron microscope with a $C_s$ corrector for the objective lens (CEOS GmbH). The microscope was operated at 300 kV.[110]

### 3.2.3. Inductively Coupled Plasma – Optical Emission Spectroscopy (ICP-OES)

Compositional analysis of the electrocatalysts to obtain the Pt weight loading on the supports was performed using an ICP-OES (Varian 715-ES). 5-10 mg of catalyst powder were digested in a 1:1:3-mixture of concentrated acids $HNO_3/H_2SO_4/HCl$ using a microwave protocol for 20 min at 180 °C and 18 bar. Standards with concentrations 1, 5 and 10 mg/L and Pt emission lines at 203.646, 204.939, 212.863, 214.424, 217.468, 224.552 nm were used for quantitative analysis.

### 3.2.4. High-angle Annular Dark Field (HAADF) Scanning Transmission Electron Microscopy (STEM) and Energy-dispersive X-ray (EDX) Spectroscopy

STEM was performed using a FEI Titan G2 80-200 electron microscope with a $C_s$-probe corrector (CEOS GmbH) and a HAADF detector operated at 200 kV.[111] To achieve Z-Contrast-conditions, a probe semi-angle of 25 mrad and an inner collection semi-angle of the detector of 88 mrad were used. Compositional mappings were received by EDX spectroscopy using four large-solid-angle symmetrical Si drift detectors. Pt L, Sn L and In L peaks were used for the elemental mapping.

*Results from STEM/EDX measurements on Pt/ITO are presented in chapter 4.*

### 3.2.5. Elemental Analysis (EA)

EA for nitrogen, carbon and hydrogen content was performed using a Thermo FlashEA 1112 Organic Elemental Analyzer by dynamic flash combustion at 1020°C.

Bulk oxygen composition analysis by hot gas extraction was performed using a LECO TC-300/EF-300 N/O analyzer. The carbons were thermally decomposed in a Ni/Sn/Pt-melt at ca. 3000 K in Helium atmosphere. For determination of oxygen content, the concentration of $CO_2$ from oxidation of CO was measured using an IR cell.

*Results from elemental analysis on (N-/O-)Vulcan are presented in chapter 5.*

### 3.2.6. Nitrogen Physisorption by BET

For nitrogen physisorption measurements, a defined amount of sample (around 20 mg) was placed in glas tube and first degassed for at least 24 h at 140 °C. Adsorption isotherms were recorded at a Quantachrome Autosorb-1-C at 78 K. The BET surface area was calculated using a NLDFT equilibrium model assuming slit/cylindric pores.

*Results from nitrogen physisorption measurements on (N-/O-)Vulcan are presented in chapter 5.*

### 3.2.7. Zeta Potential (ZP)

Measurement of the nanoparticles ZP is achieved by determining the velocity of particles induced by an electric field. The velocity of particles between two electrodes is proportional to the Zeta potential and can be obtained using a laser. Zeta potential was measured using a Zetasizer Nano Z (Malvern Instruments) equipped with a He/Ne laser (633 nm, 4 mW). For each measurement of the ZP, 5 mg of carbon were dispersed in 80 mL of miliQ and dispersed using a sonification bath.

*Results from Zeta potential measurements on (N-/O-)Vulcan are presented in chapter 5.*

### 3.2.8. High Temperature – Differential Electrochemical Mass Spectroscopy (HT-DEMS)

Gas diffusion electrodes (GDEs) were manufactured via a spray-coating technique to evaluate carbon corrosion of carbon materials via HT-DEMS. For this purpose, inks consisting of the various carbon materials (Vulcan, O-Vulcan, HCl-Vulcan, or N-Vulcan 400°C), a PTFE dispersion and water were used. Firstly, the carbon material was dispersed with water by stirring the mixture for 24 h. Afterwards, the obtained PTFE dispersion was added to the mixture until 5 wt% PTFE (referring to carbon material) was obtained. After sonification of the ink for 45 min, the electrode layer was applied onto gas diffusion layer (GDL) substrate (H23, Freudenberg FCCT) via spray-coating technique with argon as spraying gas. The electrodes were dried for 1 h at 130 °C. Subsequently, the GDEs were weighed and the carbon loading was determined to be 2 $mg_C\ cm^{-2}$ by subtracting the mass of the empty GDLs. The prepared GDEs were round and had a diameter of 2 cm (geometrical area 3.14 $cm^2$).

In the DEMS setup an electrochemical half-cell is combined with a mass spectrometer (MS).[112] Basically, the HT-DEMS setup allows electrochemical investigation of gas diffusion electrodes (GDEs) under gas-phase conditions at elevated temperatures while monitoring products from the electrochemical reactions. The electrochemical cell was mantled by a heating jacket and the temperature was controlled at 140 °C using a therocouple (tolerance of ± 1°C). With the electrochemical cell it is possible to measure under gas flow. During the measurements, $N_2$ gas was supplied with a flow rate of 50 mL min$^{-1}$. Connection between the cell and the MS was achieved using a heated capillary allowing volatile products formed at the working electrode to be transported to the MS. In this way, the products can be analyzed by measuring their specific ion currents after being ionized.[113] During electrochemical tests, the ion current of the MS signal m/z=44 ($CO_2$) was monitored. Preconditioning of GDE samples was achieved by cyclic voltammetry (15 cycles) in $N_2$ atmosphere at a scan rate of 10 mV s$^{-1}$ from 0.06-1.05 V. To evaluate the carbon corrosion, each sample was scanned with a pulse voltammetry technique. The potential ranges used in the study are: 0.06 to 0.1 V, 0.10 to 0.20 V and 0.26 to 1.06 V with 300 s pulse every 0.01, 0.02 and 0.1 V, respectively. The time between pulses was 30 s at a potential of 0.06 V. For evaluation, a mean value of the faradaic and ion current was formed from the data obtained in the last 60 s of each step.

*Results from HT-DEMS measurements on (N-/O-/HCl-)Vulcan are presented in chapter 5.*

### 3.2.9. X-ray Photoelectron Spectroscopy (XPS)

Synchrotron-based X-ray photoelectron spectra were collected at the ISISS beamline of BESSY II facility operated by Helmholtz Zentrum Berlin. For sample preparation of Pt/ITO (chapter 4), the catalyst ink was drop casted onto a 5 mm diameter glassy carbon disc and dried at 60 °C. The catalyst was treated by the LP-AST electrochemical protocol. XPS measurements were conducted at room temperature in ultra-high vacuum (UHV). Pt 4f depth profiling was accessed by using kinetic energy of the photoelectrons of 210, 550 and 1200 eV.

*Results from synchrotron-based XPS measurements on Pt/ITO are presented in chapter 4.*

Laboratory-based XPS measurements were performed in an ultra-high vacuum (UHV) setup at room temperature. Non-monochromatized Al Kα (1486.6 eV) excitation and a hemispherical analyzer (Phoibos 150, SPECS) were used. Catalyst and support powders (chapter 5) were dispersed in a 1:1 mixture of iPrOH and miliQ, horn sonified for 15 min and drop casted on a clean titanium coated silicon wafer and dried afterwards. The binding energy (BE) scale was calibrated by the standard Au4f7/2 and Cu2p3/2 procedure and the spectra were analyzed using CasaXPS software. All spectra have been charge-corrected with respect to the main peak in the C1s spectrum for adventitious carbon that was assigned to have a binding energy of 284.8 eV.[114] To calculate the elemental composition of the modified carbons, theoretical cross sections from

Yeh and Lindau[115] were used. The N 1s region was fitted to identify the types of N species present in the samples. All samples could be fitted with six peaks corresponding to pyridine, pyrrolic, quaternary N, oxidized N, $NO_2^-$ and $NO_3^-$ groups in order of increasing binding energy.

*Results from laboratory-based XPS measurements on (N-/O-)Vulcan and Pt/N-Vulcan are presented in chapter 5.*

## 3.3. Electrochemical Characterization

### 3.3.1. Preparation

***Electrochemical Setup: Rotating Disc Electrode***

A commercial three electrode glas cell setup was applied for the electrochemical measurements performed in this work. The cell consists of a Pt mesh (furled Pt 5x5 $cm^2$) as counter electrode and a mercury/mercury sulfate (MMS) reference electrode ($Hg/Hg_2SO_4$, Ametek, potential +0.722 V vs. reversible hydrogen electrode (RHE), frequently calibrated against $Pt/H_2$ system). A Luggin Capillary connected the reference electrode with the main cell compartment. Diluted 0.1 M $HClO_4$ was used as electrolyte for all electrochemical measurements. A Potentiostat (SP-150 or SP-200, BioLogic Instruments) was used to control the potential of the working electrode and a commercial AFMSRCE rotator (Pine Research) to control rotation.

***Electrode and Ink preparation***

Depending on the different supports used in this work, preparations of the ink for the electrochemical measurements vary slightly from each other and are presented in Table 3.3.

**Table 3.3** Details on Ink preparation and composition depending on the different supports used in this work.

| | **Metal Oxide** | **Modified Carbon** |
|---|---|---|
| Chapter | 4, 6 | 5 |
| Mass of catalyst powder / mg | 6 | 6 |
| miliQ /mL | 1.99 | 3.98 |
| Isopropanol / mL | 0.50 | 1.00 |
| Nafion / µL | 10 | 20 |
| Time horn sonification / min | 30 | 15 |
| Pt loading / $\mu g_{Pt}$ $cm^{-2}$ | 25.0 | 12.5 |

Catalysts inks were prepared according to the table above by mixing the defined mass of catalyst with the volumes of miliQ, isopropanol and Nafion, followed by horn sonification, see Table 3.3. Glassy carbon (GC) electrodes (Pine Research) with diameter of 5 mm were polished in two steps using alumina polishing solution (diameter 1.0 and 0.05 µm, Buehler) and cleaned thoroughly for several times in miliQ, acetone and ethanol. 10 µL of catalyst ink were deposited on the freshly polished, cleaned and dried GC electrode and dried in air at 60 °C for 7 min.

### 3.3.2. Activity and Stability Measurements

Electrochemical activity and stability measurements were conducted in order as presented in the following schematic illustration (Figure 3.2). In short, conditioning by cyclic voltammetry (CV) was performed to clean the Pt surface and obtain a stable CV from which the $H_{upd}$-ECSA was achieved followed by potentiostatic electrochemical impedance spectroscopy (PEIS) for determination of the resistance. Afterwards, the ORR activity was determined by recording an linear sweep voltammogram (LSV) and then the accelerated stress test (AST) was performed followed by a final activity measurement. A schemtaic illustration of such a measurement sequence is presented in Figure 3.2 and detailed information on each step are listed separately below. All shown electrode potentials are referred to the RHE scale.

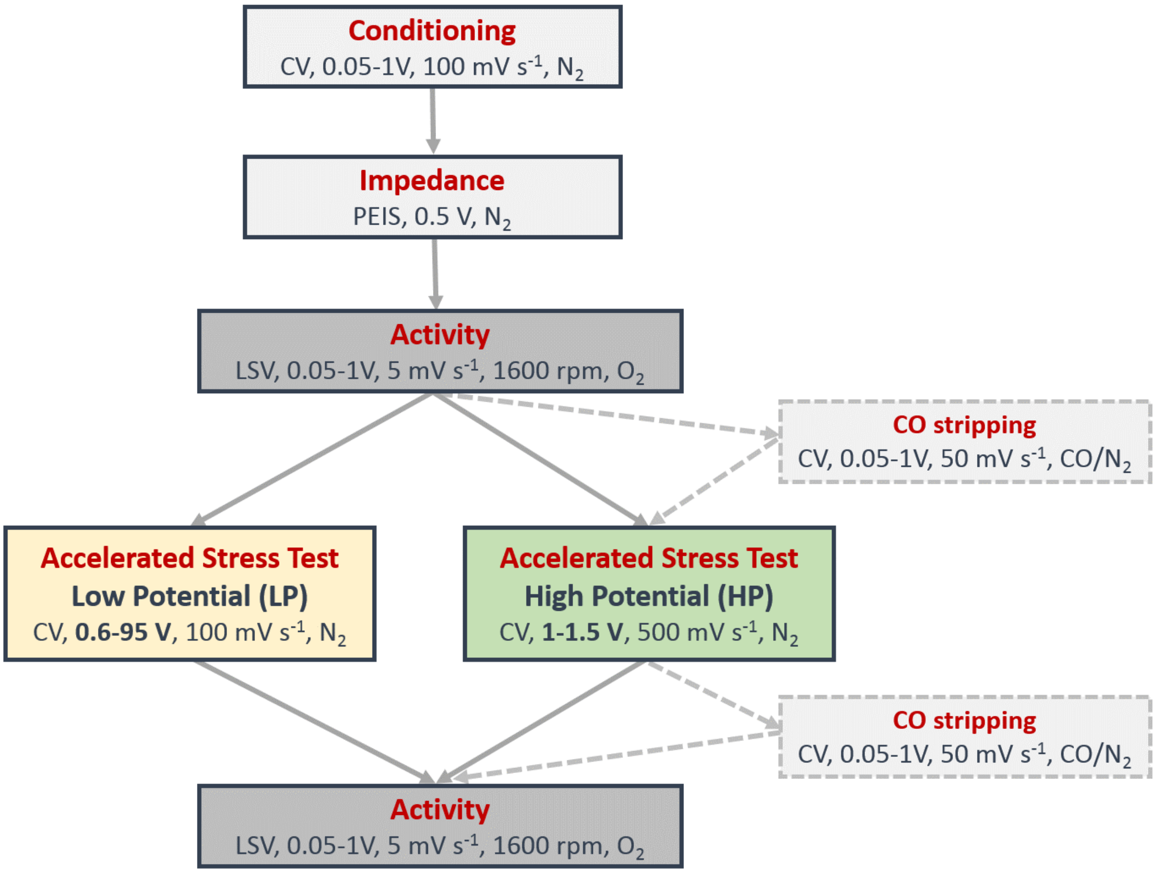
Conditioning
CV, 0.05-1V, 100 mV s$^{-1}$, $N_2$
Impedance
PEIS, 0.5 V, $N_2$
Activity
LSV, 0.05-1V, 5 mV s$^{-1}$, 1600 rpm, $O_2$
CO stripping
CV, 0.05-1V, 50 mV s$^{-1}$, CO/$N_2$
Accelerated Stress Test
Low Potential (LP)
CV, 0.6-95 V, 100 mV s$^{-1}$, $N_2$
Accelerated Stress Test
High Potential (HP)
CV, 1-1.5 V, 500 mV s$^{-1}$, $N_2$
CO stripping
CV, 0.05-1V, 50 mV s$^{-1}$, CO/$N_2$
Activity
LSV, 0.05-1V, 5 mV s$^{-1}$, 1600 rpm, $O_2$

**Figure 3.2** Schematic illustration of the sequence of an electrochemical activity and stability measurement, including conditioning by cyclic voltammetry (CV), impedance measurement by potentiostatic electrochemical impedance spectroscopy (PEIS), activity determination by linear sweep voltammetry (LSV), accelerated stress test (AST) in two different potential windows (low potential (LP) and high potential (HP)) and activity determination after the AST. CO stripping, as applied in chapter 4, was performed directly before and after the AST.

***Conditioning by Cyclic Voltammetry (CV)***

CVs were recorded between 0.05 and 1 V with a scan rate of 100 mV $s^{-1}$ in nitrogen-saturated electrolyte. For Pt on oxide supports (Chapter 3 and 5) 100 cycles were conducted, whereas for carbon-based supports (Chapter 4) 50 cycles were applied. Determination of the electrochemical active surface area (ECSA) based on Hydrogen underpotential deposition ($H_{upd}$) was achieved by integration of both oxidative and reductive currents in the $H_{upd}$ region between 0.05-0.40 V while subtracting capacitive currents in this potential window. Assuming a theoretical value of $Q_H^{theo} = 210\,\mu\mathrm{C\,cm^{-2}}$ for a one electron transfer process for the desorption of hydrogen, the $H_{upd}$-ECSA can be calculated as follows:

$$ECSA = \frac{A_{geo}}{m_{Pt}} = \frac{Q_H}{m_{Pt} \cdot Q_H^{theo}} \quad with \quad Q_H = \frac{1}{v}\int_{E_1}^{E_2} I\,dE \tag{3}$$

In equation (3), $A_{geo}$ is the catalyst's geometric surface area and can be obtained by normalizing the charge $Q_H$ to the theoretical value for the one electron transfer $Q_H^{theo}$ resulting in the $H_{upd}$-ECSA. $Q_H$ describes the charge for Hydrogen adsorption and desorption, that is obtained by integrating the capacitive-corrected currents ($I$) between potentials $E_1 = 0.05V$ and $E_2 = 0.4V$ and dividing this by the scan rate ($v$). The geometrical surface area is then normalized to the Pt mass on the elctrode ($m_{Pt}$) resulting in the $H_{upd}$-ECSA.

***Impedance by Potentiostatic Electrochemical Impedance Spectroscopy (PEIS)***

For correction of the iR-drop, the potentials were iR-corrected by the high frequency resistance $R_{HF}$ determined by potentiostatic electrochemical impedance spectroscopy (PEIS) performed at 0.5 V after the conditioning step in nitrogen-saturated electrolyte.

***Activity by Linear Sweep Voltammetry (LSV)***

LSVs were recorded in oxygen-saturated electrolyte between 0.05 and 1 V in anodic direction with a scan rate of 5 mV $s^{-1}$ and a rotation speed of 1600 rpm. Determination of kinetic currents ($j_k$) was done by applying the following equation (4):

$$\frac{1}{j} = \frac{1}{j_k} + \frac{1}{j_d} \tag{4}$$

Here, $j$ describes the current at 0.9 V whereas $j_d$ was determined by averaging the diffusion limited current between 0.1-0.6 V. Mass based activities ($j_m$) are obtained by normalization to the Pt mass on the electrode ($m_{Pt}$) according to equation (5):

$$j_m = \frac{j_k}{m_{Pt}} \tag{5}$$

Specific activities ($j_{spec}$) can be calculated by normalizing the kinetic current ($j_k$) to the geometrical surface area of the catalyst ($A_{geo}$) obtained from the CV in the following equation (6).

$$j_{spec} = \frac{j_k}{A_{geo}} \tag{6}$$

### *Accelerated Stress Test (AST)*

In order to simulate fuel cell operating conditions to the electrocatalyst, ASTs were performed in two different potential regimes in nitrogen-saturated electrolyte. In the low potential (LP) regime, fuel cell lifetime conditions are simulated, which in RDE setup is achieved by cycling between 0.6-0.95 V with a scan rate of 100 mV $s^{-1}$. Start-up/shut-down conditions are simulated by cycling between 1-1.5 V with a scan rate of 500 mV $s^{-1}$ and are referred to as high potential (HP) AST. Table 3.4 shows an overview of the different ASTs performed for the various catalysts analyzed in this work.

**Table 3.4** Overview of ASTs performed in this with work for Pt/ITO and Pt/(un)modified carbon with respect to the applied cycle numbers.

| | **Pt/ITO** | **Pt/(un)modified carbon** |
|---|---|---|
| Chapter | 4 | 5k |
| Cycle number in LP-AST | 5k | 5k, 10k and 30k |
| Cycle number in HP-AST | 5k | - |

In order to determine the $H_{upd}$-ECSA before and after the AST protocols three CVs between 0.05-1 V with a scan rate of 100 mV $s^{-1}$ were performed and the $H_{upd}$-ECSA was determined as described above.

Parameters for both stability tests were adapted from the US Department of Energy (DoE) fuel cell targets from the year 2016.[116]

### *CO Stripping*

CO stripping was applied to the metal oxide supported catalysts (chapter 4 and 6) in order to determine the CO-ECSA in addition to the $H_{upd}$-ECSA. In a CO stripping experiment, the electrolyte is first saturated with CO to ensure complete CO coverage of the Pt surface. In a next step, excess CO is removed from the electrolyte by saturating it with nitrogen. The CO is stripped from the Pt surface by cycling between 0.05-1 V for 5 cycles with a scan rate of 50 mV $s^{-1}$. CO-ECSA determination was achieved by subtracting the first two consecutive cycles of the stripping protocol and integration of the charge between the two cycles ($Q_{CO}$).[117] The measured $Q_{CO}$ values were normalized with respect to the theoretical value for a two electron transfer $Q_{CO}^{theo} = 420\ \mu\mathrm{C\ cm}^{-2}$ for CO as probe molecule. The CO-ECSA was obtained as described for $H_{upd}$-ECSA above in Equation (3).

### *CVs for Pt Electrooxidation*

For Pt electrooxiadtion as shown in chapter 6, each three CVs starting from 0.05-0.5 V to an increasing upper potential limit of 1.4 V in steps of 0.1 V were measured under nitrogen-saturated atmosphere with a scan rate of 100 mV $s^{-1}$.

## 3.4. *In situ* Characterization

In this work, various *in situ* methods were applied to analyze both catalyst and support components with respect to their changes under accelerated stress test or Pt oxidation conditions. These methods will be described in the following sections, beginning with the *in situ* dissolution measurements followed by the *in situ* X-ray based setup and methods.

### 3.4.1. Scanning Flow Cell Inductively Coupled Plasma Mass Spectroscopy (SFC ICP-MS)

For *in situ* SFC ICP-MS measurements, inks of Pt/RTO, Pt/ITO and Pt/C were prepared with a solution of 25 µL 5 % Nafion and 4.975 mL ultrapure water (18.2 MΩcm, PureLab Plus System, Elga). The ink was sonicated and subsequently 0.3 µL drops were deposited onto the glassy carbon sheet (SIGRADUR® G, HTW) which was polished with 1 µm $Al_2O_3$ suspension and cleaned with ultrapure water before. The spots of catalyst ink had a size of ca. 0.01 $cm^2$ and a final loading of approximately 1.6 $µg_{Pt}$ $cm^{-2}$ for Pt/ITO and Pt/C and 8.33 $µg_{Pt}$ $cm^{-2}$ for Pt/RTO was obtained. *In situ* dissolution measurements were conducted using the previously described SFC ICP-MS setup (NexION 300X, Perkin Elmer).[118,119] Contact area between working electrode and the cell was 035 $cm^2$. A freshly calibrated saturated Ag/AgCl electrode and graphite rod were used as reference and counter electrode, respectively. All shown potentials are reported against RHE. Argon-saturated 0.1 M $HClO_4$ was used as electrolyte. The flow rate of the electrolyte in the SFC was approximately 170 µL $min^{-1}$. 10 µg $L^{-1}$ of Re ($^{187}$Re was monitored) was used as internal standard for Pt and 20 µg $L^{-1}$ of $^{103}$Rh were used as internal standards for In and Sn.

For the Pt, In and Sn dissolution as presented in Chapter 4, dissolution in µg $µg_{Pt}^{-1}$ was determined via integration of the ICP-MS signal data by the flow rate (normalized to Pt mass loading on the working electrode). Ranges for the integration were taken from a constant signal area before and after the analyzed peak.

*Results from SFC ICP-MS measurements on Pt/C and Pt/ITO (Pt, In and Sn dissolution) are presented in chapter 4 and on Pt/C, Pt/ITO and Pt/RTO (Pt dissolution) in chapter 6.*

### 3.4.2. *In situ* Electrochemical Cell and Setup

In order to analyze morphological and structural changes of the electrocatalyst, *in situ* X-ray measurements were performed. Such experiments were conducted at a synchrotron facility where brilliant and high-flux radiation is produced by an electron accelerator as radiation source. The fact that a wide spectrum from soft to hard X-rays can be generated with the opportunity to change the energy relatively easy at such a facility, makes it advantageous compared to lab-based techniques. Figure 3.3 shows a schematic illustration of the setup as applied for the *in situ* experiments performed at a synchrotron in this work.

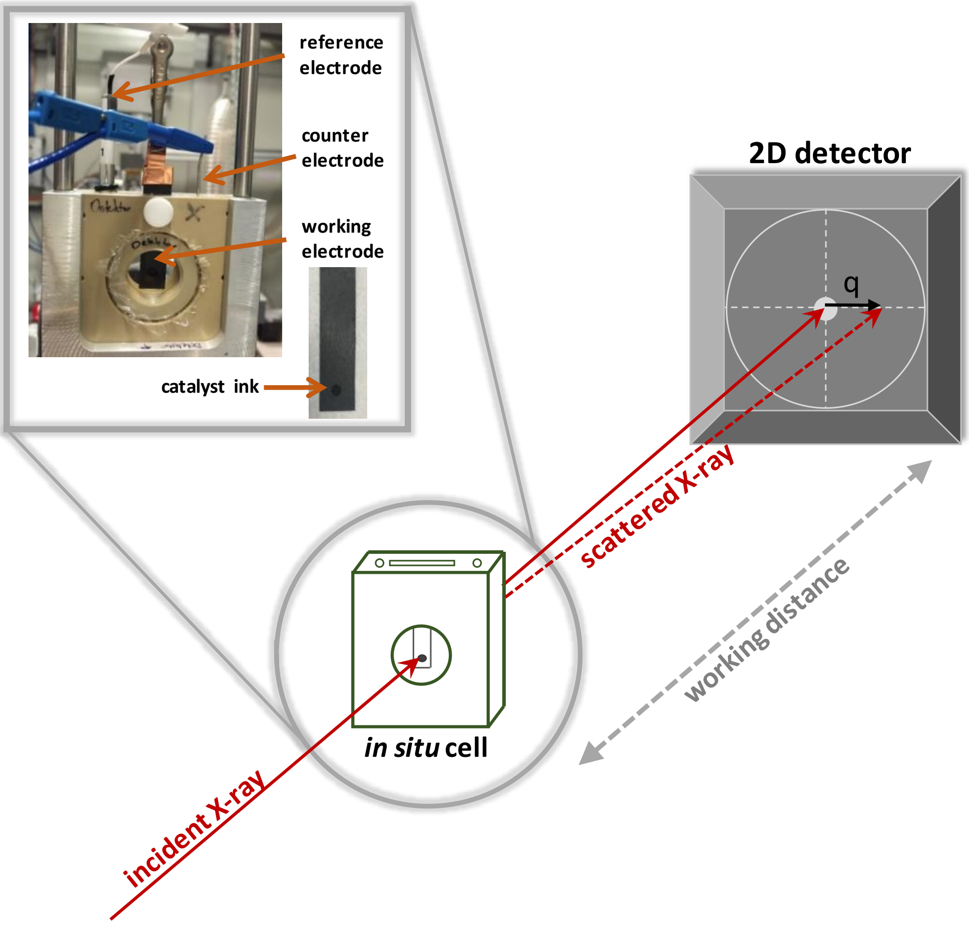

**Figure 3.3** Schematic illustration of the setup and electrochemical *in situ* cell as used at a synchrotron facility, showing the incident and scattered X-rays, the 2D detector and the *in situ* transmission cell. Distance between sample and detector is defined as working distance.

In such a setup, the sample is measured in transmission geometry, in which the incident X-ray beam passes through the sample and is recorded together with the scattered X-rays at a 2D detector. In the *in situ* cell, the electrochemical protocols are applied. Therefore, the catalyst ink (5x10 µL) is drop-casted on a carbon paper sheet, dried and inserted into the electrolyte compartment. A Pt wire acts as counter electrode and a 3M Ag/AgCl reference electrode (freshly calibrated against Pt/$H_2$ electrode) were used. This setup enables electrochemical measurements in a three electrode configuration with a sufficient thickness of electrolyte at the sample and accessibility of the catalyst while minimizing the X-ray attenuation/sacttering by water molecules. Additionally, by fast changes of the working distance between sample and detector, the setup at ID31 allows almost simultaneous measurements of high energy X-ray diffraction (HE-XRD) and (anomalous) small angle X-ray scattering ((A)SAXS).

### 3.4.3. High Energy X-ray Diffraction (HE-XRD)

***Theoretical Background***

X-ray diffraction at sufficiently higher energies than those used in lab-based assemblies is referred to as high energy XRD (HE-XRD). Such measurementsb give rise to a much larger q, and therefore 2θ, range of the diffraction pattern. It can only be performed at synchrotron facilities due to the fact that the energy of the photons can be tuned with respect to the desired properties. In this work, HE-XRD is applied to investigate the crystalline components of the electrocatalyst under simulated fuel cell operating conditions. In this way, crystallite parameters such as crystallite size, lattice constant and scale factor can be followed.

Analysis of the HE-XRD patterns includes not only a proper phase assignment, but also Rietveld refinement. This method developed by Hugo M. Rietveld in the 1960s[120,121] allows to refine several different parameters of the analyzed material, such as crystallite size, weight fraction (of different phases), lattice parameters, atomic positions and occupancies as well as micro strain and scale factor (scattering intensity). Rietveld refinement applies a least square approach and fits an entire profile of a diffraction pattern to a calculated profile. A major advantage of this method is that patterns with several overlapping Bragg peaks can be analyzed.[122] Requirements for successful fitting procedures include high quality experimental data and a large q-range as well as structure model(s) that make sense on a physical and chemical level.

The goal is to minimize the residual function $M$ at $i$ steps of the pattern over all data points $N$ which can be expressed as:

$$M = \sum_{i=1}^{N} w_i \, [I_i(obs) - \, I_i(calc)\,]^2 \tag{7}$$

In equation (7), $I_i(obs)$ describes the intensity measured at point $i$ and $I_i(calc)$ the corresponding calculated intensity. $w_i$ is the weight of the diffraction pattern’s intensity and is given by equation (8):

$$w_i = \; [I_i(obs)\,]^{-1} \tag{8}$$

The calculated intensity $I_i(calc)$ is defined by the following equation (9):

$$I_i(calc) = s \sum_{k=k_1}^{k_2} m_k \, L_k \, |F_k|^2 \, G_{ik} \tag{9}$$

This expression describes the summation over all reflections $k_1$ to $k_2$ for one phase containing the scale factor $s$ that is depending on beam intensity, volume fraction and cell volume. $m_k$ is the multiplicity factor for the $k$th reflection and $L_k$ the Lorentz-polarization factor. $F_k$ represents the structure factor and $G_{ik}$ the so-called peak-shape function. A proper choice for description of this function is often difficult and depends on the nature of the experimental technique (X-ray or neutron diffraction).[122] In case of X-rays, a mixed description of Lorentian and Gaussian components, expressed in a Pseudo-Voigt function $V$, is commonly applied (equation (10))[123-125]:

$$V = \eta L + (1-\eta)G \quad with \quad (0 \leq \eta \leq 1) \tag{10}$$

With the Gaussian component $G$ being the following equation (11):

$$G = I_0 \exp\left(-ln2\left(\frac{2\theta - 2\theta_0}{\omega}\right)^2\right) \tag{11}$$

The Lorentzian contribution $L$ can be described by equation (12):

$$L = I_0 \left(1 + \left(\frac{2\theta - 2\theta_0}{\omega}\right)^2\right)^{-n} \quad with \quad n = 1; 1.5; 2 \tag{12}$$

In these two components, $I_0$ describes the peak intensity, $2\theta_0$ the peak position in measures of $2\theta$ and $\omega$ includes the full width at half maximum (FWHM) in the following correlation (equation (13)):

$$\omega = \frac{FWHM}{2} \tag{13}$$

A correct background estimation is also important in Rietveld refinement. The background can either be determined in regions void of any Bragg reflections[122] or, in another approach, the background of the pattern can be included in the refinement model as a polynomial function.[126]

### *Experimental Description*

In the presented work, the HE-XRD measurements were performed at beamline ID31 at the European synchrotron radiation facility (ESRF) in Grenoble, France. Here, relatively high energies (68-78 keV) were used resulting in transmission values for the sample including the substrate and the electrolyte layer that are approaching one and therefore enabling high quality data. A large area detector (Pilatus3X CdTe 2M, Dectris) was used to record the diffraction images. The working distance between the sample and the detector was calibrated using a $CeO_2$ standard (NIST SRM 674b). The diffraction patterns were corrected by the background. Rietveld refinement was performed using the TOPAS® software package (Bruker).

*Results from HE-XRD and Rietfeld refinement of Pt and ITO are presented in chapter 4 and of Pt on different carbon supports in chapter 5.*

HE-XRD pattern of Pt/ITO, Pt/RTO and Pt/C (chapter 6) were integrated and the intensity plots fitted using TOPAS®. Therein, the unit cell parameter was fitted and the occupancy of the tetrahedral sites with O atoms refined. The size- and microstrain-induced broadening of the Pt diffraction peaks were fitted. The size-induced broadening was fitted using the anisotropy approach developed by Ectors *et al.*[127,128] In the case of the HE-XRD pattern of Pt nanoparticles on ITO, spherical nanoparticles were considered with all three main axes of the ellipsoids identical ($R_x=R_y=R_z$). In the case of the Pt nanoparticles on RTO and on carbon, the size-induced broadening was fitted with three independently-fitted principal axes of the ellipsoids ($R_x \neq R_y \neq R_z$). The polydispersity of the nanoparticles representing the particle size distribution was taken into account, too. The crystal properties of each catalyst were individually fitted in each investigated state but a joint fit approach was applied to determine zero offset and sample displacement.

*Results from fitting of the HE-XRD patterns of Pt on ITO, RTO and carbon are presented in chapter 6.*

### 3.4.4. Small Angle X-ray Scattering (SAXS)

#### *Theoretical Background*

Small angle X-ray scattering is an useful technique to investigate materials on the nanoscale.[129-131] In this work, SAXS is applied to analyze the morphological stability of Pt with respect to the size of the Pt nanoparticles during electrochemical degradation protocols in a simulated fuel cell environment.

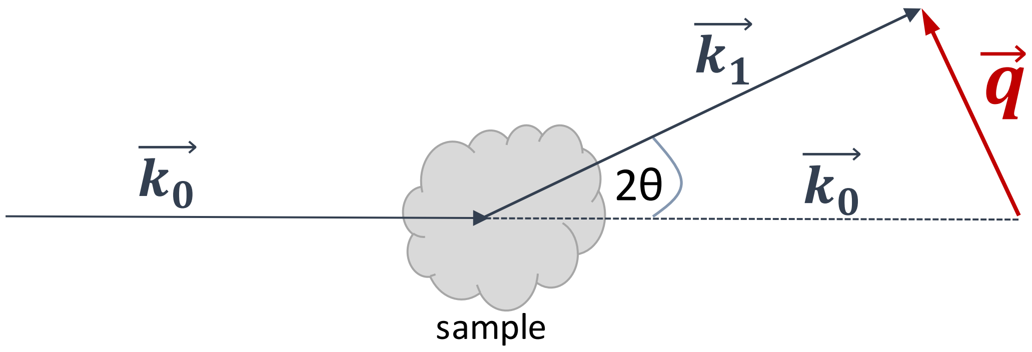

**Figure 3.4** Schematic illustration of the elastic scattering as the basis of SAXS.

The information obtained from SAXS analysis are based on elastic scattering of X-rays at the electron clouds of atoms and interference of the resulting scattered waves.[132,133] The scattered intensity is a function of the scattering vector $\vec{q}$, that is, in contrast to the scattering angle 2θ, independent on the used wavelength (Figure 3.4). The scattering vector can be described by the incoming wave vector $\overrightarrow{k_0}$ and the scattered one $\overrightarrow{k_1}$ as follows in equation (14):

$$\vec{q} = \overrightarrow{k_1} - \overrightarrow{k_0} \quad with \quad |\vec{k}| = \frac{2\pi}{\lambda} \tag{14}$$

The magnitude of the scattering vector can therefore be expressed according to equation (15):

$$|\vec{q}| = q = \frac{4\pi}{\lambda}\sin(\theta) \tag{15}$$

When incoming X-ray waves are scattered at the electron cloud of an atom, an outgoing X-ray wave with the amplitude $A_1(q)$ can be written as (equation (16)):

$$A_1(q) = A_0 b_e \int_V n(r)e^{-iqr}dr \tag{16}$$

In here, $n(r)$ describes the electron density distribution within one given atom and $r$ the position of the electron from the atomic center. $A_0$ represents the amplitude of the incoming wave and $b_e$ the scattering length of a single electron. To obtain the amplitude of the scattered wave, integration is performed over the volume of the atom.

When the amplitude is normalized to units of $A_0 b_e$, the atomic scattering factor $f(q)$ is obtained as follows in equation (17):

$$f(q) = \int_V n(r)e^{-iqr}dr \tag{17}$$

Under the assumption, that a sample contains an ensemble of various atomic species $i$ with the density distribution of the atomic centers $n_i$, the scattering length density distribution $\rho(r)$ can be expressed in equation (18) as the sum of the various atomic species and the density distribution of the centers:

$$\rho(r) = \sum f_i n_i(r) \tag{18}$$

The scattered intensity $I(q)$, that describes the q-dependent pattern of the scattered X-rays, can be written as (equation (19)):

$$I(q) = |A_1(q)|^2 = \left|\int_V \rho(r)e^{-iqr}dr\right|^2 \tag{19}$$

When incoming X-rays are scattered at diluted and spherical particles (e.g. supported Pt nanoparticles), it is assumed that the position of the individual particles are independent from each other. Therefore, the scattered intensity $I_{sphere}\,(q)$ of such a system with particles of the radius $R$ and the scattering length density distribution $\rho$ can be expressed as follows in equation (20):

$$I_{sphere}\,(q) = \rho^2 \left(\frac{4}{3}\pi R^3\right)^2 \left[\frac{3(sinqR - qRcosqR)}{(qR)^3}\right]^2 \tag{20}$$

The last term in this equation represents the squared particle form factor $P(q, R)$ of a spherical particle. In case all particle radii are of the same dimensions, hence the particle system is monodisperse, periodic variations in $I_{sphere}\,(q)$ are observed that smear out with increasing polydispersity.

Anomalous SAXS is a method to measure element-specific scattering curves and can therefore be applied to analyze bi- or trimetallic particles systems or, as used in this work, to isolate the Pt-scattering from scattering of the support (particle) components. This variation to the conventional SAXS method relies on the energy dependence of the atomic scattering factor, exemplified in the following equation (21) for the atomic scattering factor of Pt[132,134,135]:

$$f_{Pt}(E) = f_{Pt}^0 + f_{Pt}' + if_{Pt}'' \tag{21}$$

In this equation, $f_{Pt}^0$ represents the energy independent scattering factor, $f_{Pt}'$ the anomalous, energy dependent scattering factor and $if_{Pt}''$ the imaginary part of the form factor. Therefore, the scattering curves are recorded at an energy before the Pt absorption edge ($E_1$) and close to the edge ($E_2$), while the scattering factor of the support components stays constant. The difference of the two scattering intensities ($I(E_1) - I(E_2)$) can then lead to the isolated Pt-scattering pattern.

### *Experimental Description*

For the (A)SAXS experiments at ID31 at the ESRF a PerkinElmer DEXELA 2923 detector was used and the working distance was calibrated using an Ag Behenate reference sample. In case anomalous SAXS was performed, scattering patterns were recorded before (77 keV) and close to the Pt K-edge (77.8 keV). Alignment for the energy of the beamline was achieved using the Pt K-edge absorption spectrum. The scattering curves were corrected by the background and normalized with respect to the transmission of the sample. Fitting of the (A)SAXS curves was performed using the Sasfit software package.

*Results from ASAXS measurements on Pt/ITO are presented in chapter 4 and from SAXS measurements on Pt/(N-/O-)Vulcan in chapter 5.*

### 3.4.5. X-ray Absorption Spectroscopy (XAS)

*In situ* XAS experiments were carried out at the mySpot beamline of the BESSY II synchrotron radiation facility operated by the Helmholtz-Zentrum Berlin (HZB). A Si(111) double crystal monochromator was used and measurements were performed at the Pt L-edge. Alignment of the X-ray energy for each spectrum was achieved by shifting the first derivate of the simultaneously-measured X-ray absorption spectrum of the Pt reference (Pt foil) to 11654 eV. Here, instead of 2D detector as used for the HE-XRD and SAXS experiments, a scintillation counter was used as detector to monitor the fluorescence yield. The detector was covered with Al foil in order to reduce background radiation.

For the *in situ* electrochemical measurements the transmission cell was used as shown in Figure 3.3, but tilted by 45 ° with respect to the incoming beam while the fluorescence detector was placed perpendicular to the incoming beam in vicinity of the sample.

*Results from XAS measurements on Pt/C, Pt/ITO and Pt/RTO are presented in chapter 6.*

# 4. Unravelling Degradation Pathways of Oxide-Supported Pt Fuel Cell Nanocatalysts under *In Situ* Operating Conditions

Knowledge of degradation pathways of catalyst/support ensembles aids the development of rational strategies to improve their stability. Here, this is exemplifed using indium tin oxide (ITO)-supported Platinum nanoparticles as electrocatalysts at fuel cell (FC) cathodes under degradation protocols to mimic operating conditions in two potential regimes. The evolution of crystal structure, composition, crystallite and particle size is tracked by *in situ* X-ray techniques (small and wide angle scattering), metal dissolution by *in situ* scanning flow cell coupled with mass spectrometry (SFC ICP-MS) and Pt surface morphology by advanced electron microscopy. In a regular FC operation regime, Pt poisoning rather than Pt particle growth, agglomeration, dissolution or detachment was found to be the likely origin of the observed degradation and ORR activity losses. In the start-up regime degradation is actually suppressed and only minor losses in catalytic activity are observed. The presented data thus highlight the excellent nanoparticle stabilization and corrosion resistance of the ITO support, yet point to a degradation pathway involving Pt surface modifcations by deposition of sub-monolayers of support metal ions. The identifed degradation pathway of the Pt/oxide catalyst/support couple contributes to our understanding of cathode electrocatalysts for polymer electrolyte fuel cells (PEFC).

*Chapter 4 and section Appendix A1 were reproduced from Ref* [52] *(Adv. Energy Mat.,* ***2018****, 8 (4), 1701663) with permission from John Wiley and Sons, Copyright 2018.*

Henrike Schmies, Arno Bergmann, Jakub Drnec, Guanxiong Wang, Detre Teschner, Stefanie Kühl, Daniel J.S. Sandbeck, Serhiy Cherevko, Martin Gocyla, Meital Shviro, Marc Heggen, Vijay Ramani, Rafal E. Dunin-Borkowski, Karl J.J. Mayrhofer, Peter Strasser, *"Unravelling Degradation Pathways of Oxide-Supported Pt Fuel Cell Nanocatalysts under In Situ Operating Conditions",* Adv. Energy Mater. **2018**, 8 (4), 1701663; doi: 10.1002/aenm.201701663

H.S. performed the experiments and analyzed the data, A.B. helped designing the experiments and analyzed the synchrotron data; J.D. and A.B. helped performing and the synchrotron experiments; G.W. and V.R. synthesized the support; D.T. performed XPS measurements and analysis; S.K. recorded TEM images; D.J.S.S., S.C. and K.J.J.M. produced and analyzed the SFC ICP-MS data; M.G., M.S., M.H. and R.E.D.-B. performed and analyzed the STEM EDX mappings; H.S., A.B. and P.S. wrote the manuscript; all authors contributed to the discussion.

## 4.1.Introduction

In this study, we report new molecular insight in the degradation mechanisms of Pt/ITO electrocatalysts for oxygen reduction at fuel cell cathodes. What sets this study apart from previous ones is the use of a number of different *in situ* electrochemical X-ray and scanning flow cell-inductively coupled plasma (ICP) techniques to track the change in the molecular structure and composition of the catalysts during ORR catalysis. *In situ* high energy X-ray diffraction (HE-XRD) and anomalous small angle X-ray scattering (ASAXS) were applied to follow the structure and morphology of the Pt and ITO particles. In addition, scanning flow cell tests coupled to inductively coupled plasma mass spectroscopy (SFC ICP-MS), X-ray photoelectron spectroscopy (XPS), high angle annular dark field scanning transmission electron microscopy (HAADF-STEM) combined with energy-dispersive X-ray (EDX) spectroscopy yielded a deeper understanding of the evolution of morphology and surface composition after the ASTs. Together, our experimental study unravels critical parameters determining structural, morphological, compositional, and, thus, electrochemical stability of Pt on ITO.

## 4.2. Physicochemical Characterization

Platinum nanoparticles supported on indium tin oxide have been synthesized using a solvothermal route using oleylamine and oleic acid as surfactants and dibenzylether as the solvent. The support material was introduced in the reaction mixture from the beginning to enable Pt nanoparticle growth directly on the support. Slow heatin g rates of 1 ℃ min$^{-1}$ were applied to obtain monodisperse Pt nanoparticles. Figure 4.1 shows the XRD pattern of Pt on ITO as well as the pure ITO.

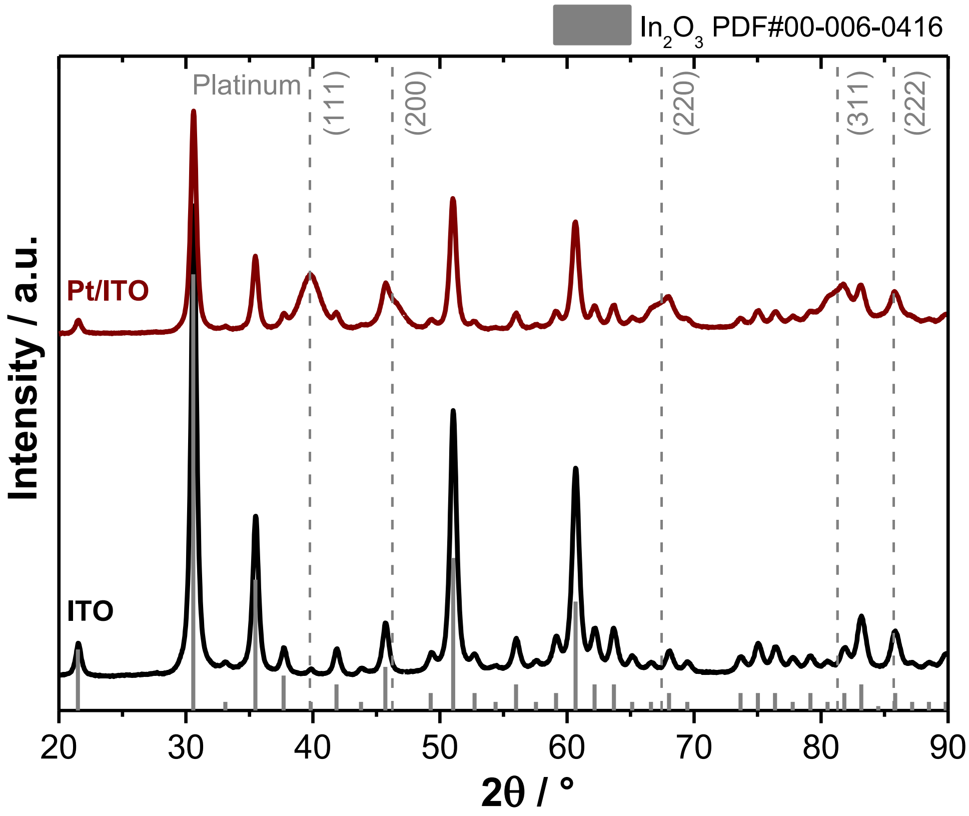

**Figure 4.1** X-ray diffraction patterns of the bare ITO support material (black, bottom) and Pt/ITO catalyst (dark red, top) obtained using Cu K$\alpha$ radiation. Solid lines denote pure $In_2O_3$ reference powder diffraction pattern (PDF#00-006-0416). Vertical dashed lines denote reference patterns of fcc Pt (PDF#00-004-0802).

All reflexes in the ITO pattern can be clearly assigned to an $In_2O_3$ phase (PDF#00-006-0416). No additional Sn oxide phase was present indicating complete incorporation of Sn into the $In_2O_3$ lattice thus, forming $In_{2-x}Sn_xO_3$ crystallites. The Pt/ITO pattern shows broad Pt reflections for pure face-centered cubic (fcc) Pt. To analyze Pt particle size and Pt particle distribution on the support, transmission electron microscopy (TEM) was applied.

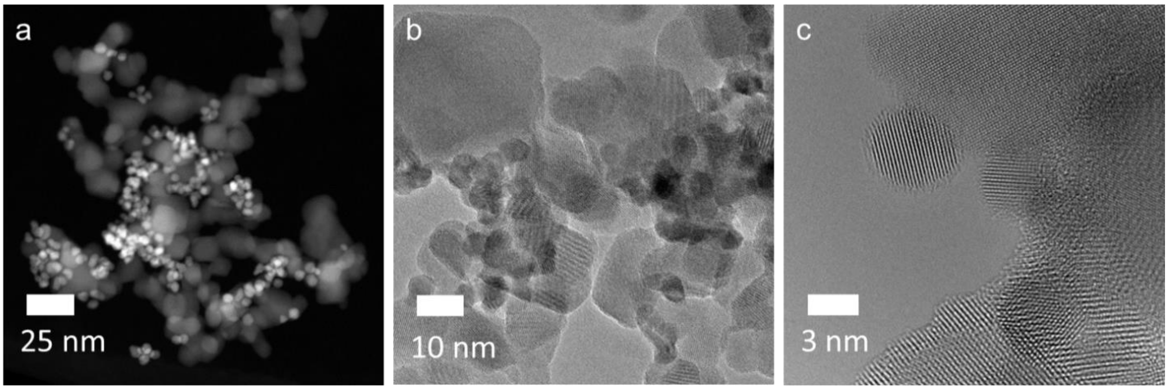

**Figure 4.2** Morphology of Pt/ITO in the initial state: (a) showing overview HAADF-STEM image, (b) TEM and (c) HR-TEM images.

Figure 4.2a,b and Figure 4.3a,b shows quite homogeneously distributed Pt nanoparticles on the ITO support with an average size of 5.3 ± 0.7 nm (Figure 4.3c). Furthermore, the support consists of mostly well faceted nanocrystals with a size >10 nm. These crystals are randomly oriented and clearly distinguishable from the small Pt nanoparticles.

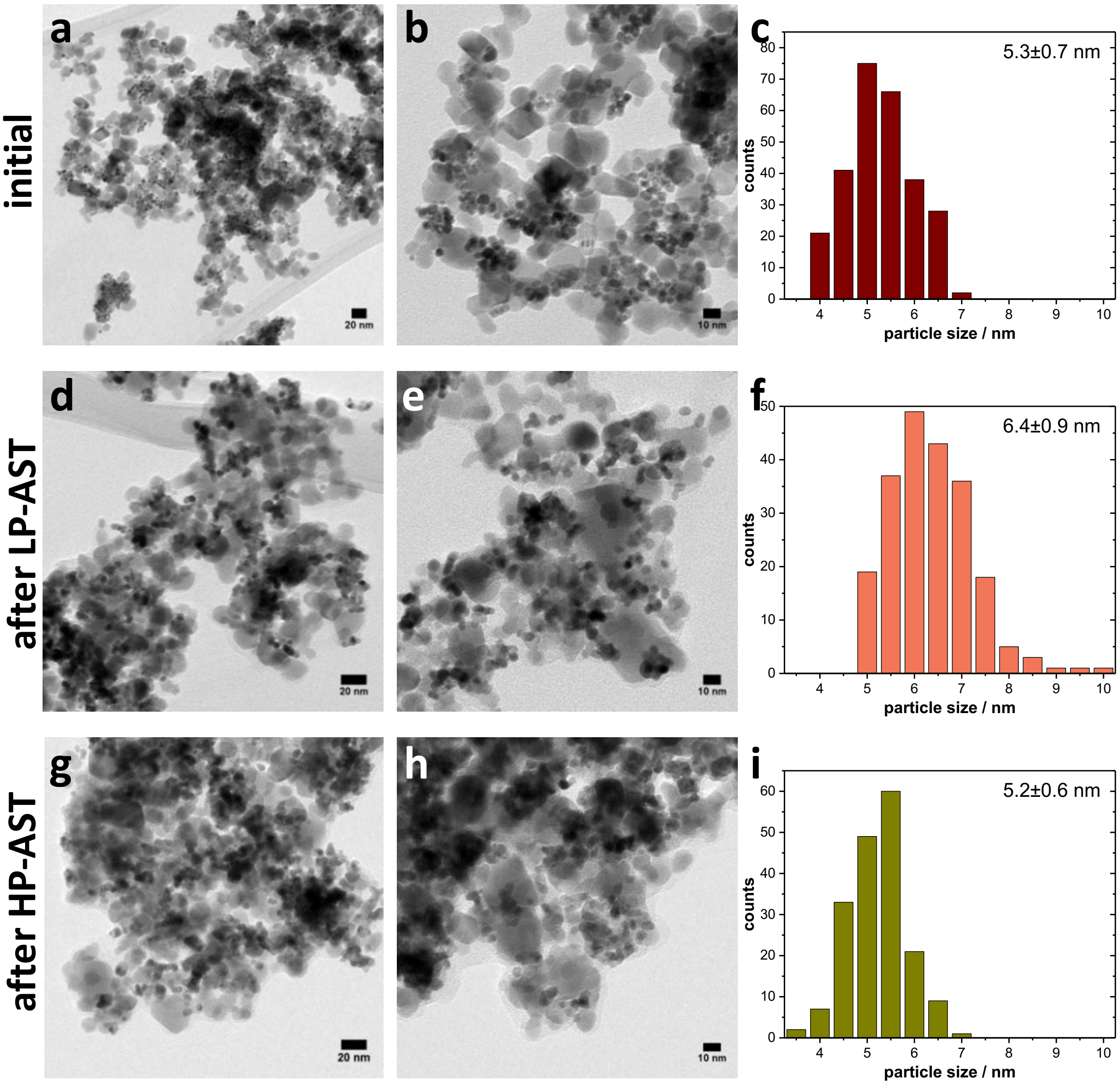

**Figure 4.3** (a,b) TEM images of the as prepared Pt nanoparticles on the ITO support, after electrochemical cycling for 5k times in d,e) lower potential region and in (g,h) the higher potential region, as well as the corresponding histograms showing (c,f,i) the particle size distribution. Histograms were obtained by measuring the diameter of at least 200 particles with errors obtained from standard deviation of mean particle diameter.

The composition of the Pt/ITO as determined by inductively coupled plasma optical emission spectroscopy (ICP-OES) revealed a weight loading of 22.0 wt% Pt on ITO for the initial state (Figure 4.3a,b). This sample was used for low potential-AST (LP-AST) experiments. For all high potential (HP)-AST experiments the sample had a weight loading of 29.9 wt% Pt on ITO. Figure A1 (Appendix A1) shows TEM images and the corresponding histogram of the Pt particle size in the initial state. It can be clearly seen that Pt particle size and distribution as well as the shape and size of the support crystallites was almost identical compared to the sample with lower loading that was used for LP-AST.

## 4.3. Electrochemical Characterization

Figure 4.4a depicts the cyclic voltammograms (CVs) of the Pt/ITO catalyst in the initial state and after 5k CV in the lower potential region from 0.6–0.95 V versus reversible hydrogen electrode (RHE) (denoted as LP-AST). The ASTs were preceded and followed by CVs in the activation regime (0.05–1.00 V).

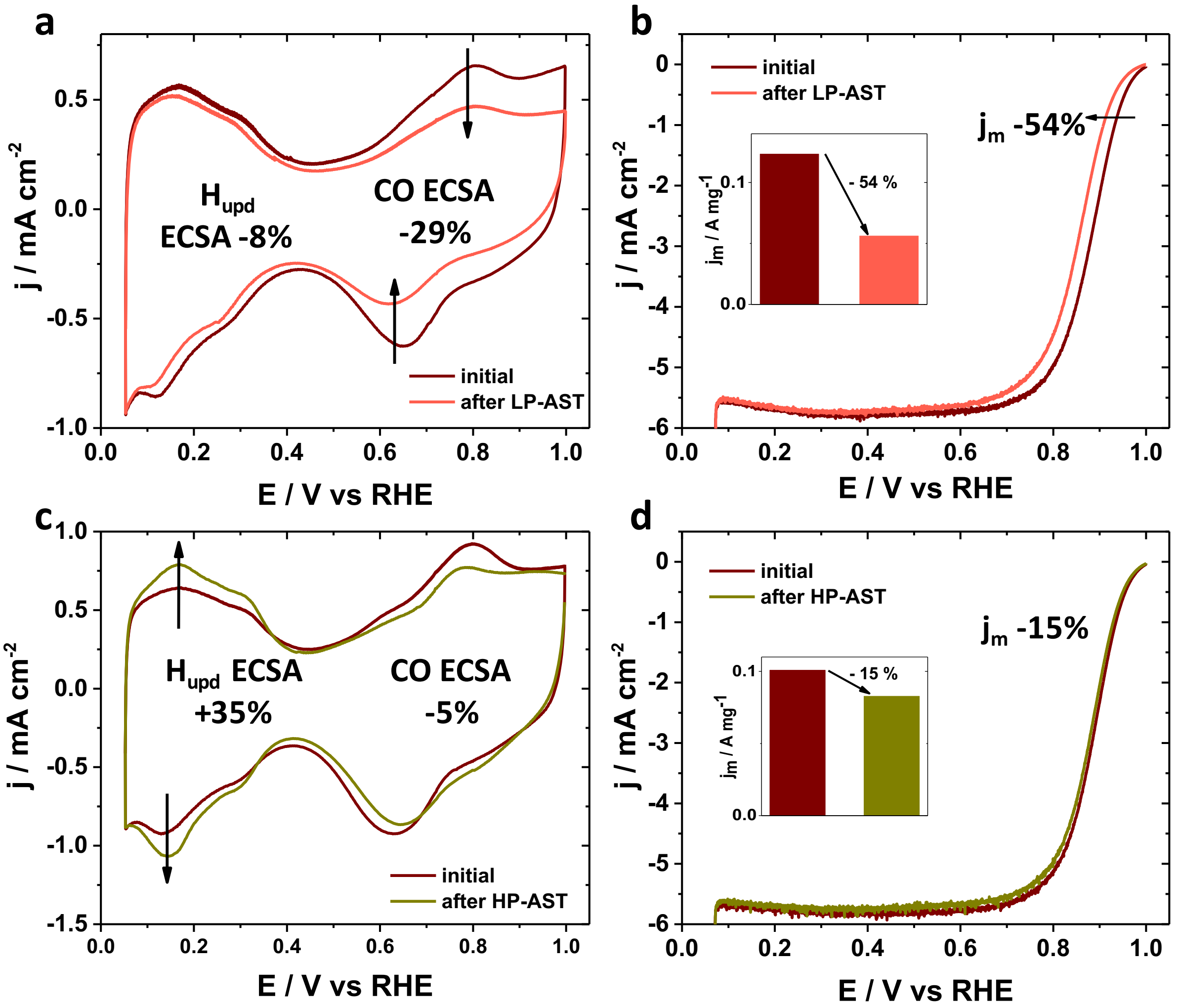

**Figure 4.4** Cyclic voltammograms of Pt/ITO catalyst before and after potential cycling in (a) lower and (c) higher potential region. CVs were recorded in nitrogen saturated electrolyte from 0.05–1 V with a scan rate of 100 mV s$^{-1}$. b,d) LSVs of the particular states with the bar plots in the inlets representing the mass activity (j$_m$) evaluated at 0.9 V. LSVs were recorded in oxygen-saturated electrolyte from 0.05–1 V with a scan rate of 5 mV s$^{-1}$ and 1600 rpm. All electrode potentials have been corrected for iR drop.

It can be clearly seen that the CVs changed after the AST as the current in the Pt-O/-OH region (0.6-0.8 V) drastically decreased. This suggests a lower number of oxidizable Pt sites on the nanoparticles after LP-AST. By contrast, the charge transferred in the Hupd region (0.05-0.4 V) decreased by only 8% as shown in Figure 4.5 representing a minor loss in the hydrogen-based ECSA ($H_{upd}$-ECSA). The corresponding linear sweep voltammograms (LSV) in Figure 4.4b revealed a loss of the platinum mass-based activity ($j_m$) by 54% after LP-AST as evaluated at 0.9 V. To quantify the number of oxidizable Pt sites and to investigate their relation to the loss in mass activity, CO stripping experiments were performed at selected stages of the electrochemical stability test (Figure A3a).

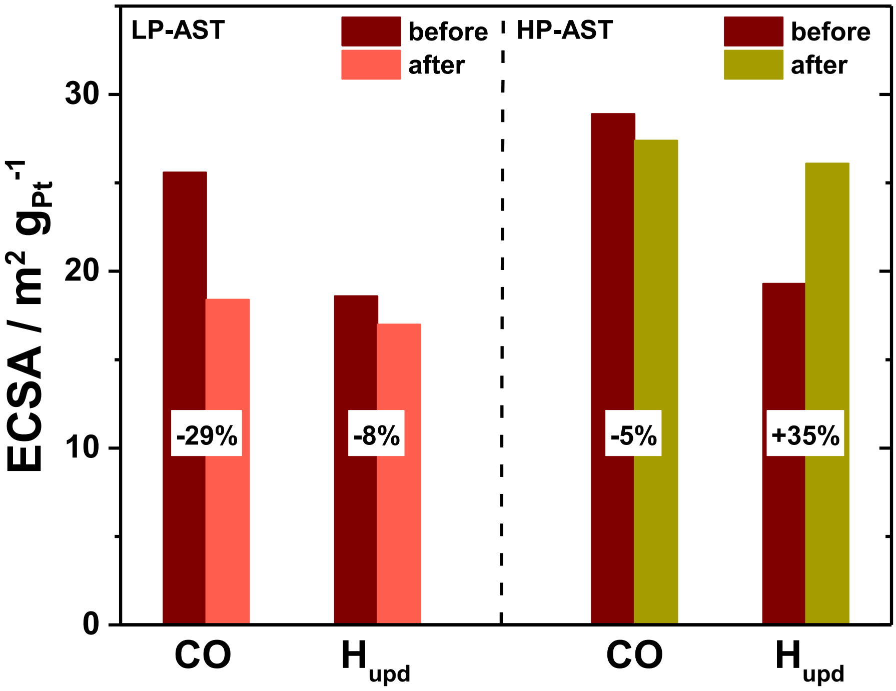

**Figure 4.5** Comparison of ECSAs based on the integration in the $H_{upd}$ and the CO oxidation potential range. CO-ECSAs were determined by integrating the CO oxidation peak area from the first cycle of the CO stripping experiment after subtraction of the second cycle representing the bare CO-free Pt surface. $H_{upd}$-ECSA was determined by subtracting the first from the second cycle of the CO stripping experiment.

Figure 4.5 shows a comparison of ECSAs determined in the $H_{upd}$ and CO oxidation region of the CO stripping experiment. Note that the absolute values of CO-ECSAs as presented in Figure 4.5 are larger compared to the $H_{upd}$ based values due to a stronger adsorption of CO on Pt as it is well known from literature for Pt-based systems.[117,136-139] However, it can be seen that the CO-ECSA decreased in the course of the LP-AST (-29%) measurement, whereas the $H_{upd}$-ECSA was rather stable (-8%). This also becomes clear as the ratio (CO/$H_{upd}$) of both ECSAs decreased as seen by Table A1. After the stability test in the higher potential range from 1.0-1.5 V (denoted as HP-AST) the cyclic voltammogram exhibited higher currents in the $H_{upd}$ region compared to the initial state representing an increase of the $H_{upd}$-ECSA by 35% (Figure 4.4c). In contrast to the LP-AST, mass-based activity of Pt/ITO decreased by only 15%

(Figure 4.4d) and the CO-ECSA by only 5% during the HP-AST (Figure 4.5). Thus, the catalytic activity of the Pt/ITO is signifcantly more stable in the HP-AST than in the LP-AST. However, in both cases the catalytic activity followed rather the CO-ECSA than the $H_{upd}$-ECSA.

To compare the Pt/ITO electrocatalyst to a commercial carbon supported material, a 20 wt% Pt/C reference catalyst was applied to the same ASTs. Figure A2a,b shows CVs and LSVs before and after the LP-AST. Pt/C exhibited higher stability in the lower potential regime than Pt/ITO with a loss in mass activity of only 14% (see also Table A2). In contrast to that, the carbon supported catalyst showed a decrease of 38% in ORR mass activity after the HP-AST and an increase in $H_{upd}$-ECSA of 9% (Figure A2c,d) suggesting a lower electrochemical stability than Pt/ITO in this potential regime. To explain the changes in electrochemical surface area and catalytic activity toward the ORR, the evolution of the Pt particle size on ITO after the ASTs was analyzed by TEM (Figure 4.3d-i). The size of the Pt nanoparticles increased only slightly by around 1 nm from 5.3 ± 0.7 to 6.4 ± 0.9 nm after LP-AST (Figure 4.3d-e) which could explain the small decrease observed in $H_{upd}$-ECSA. Additionally, the edges of ITO nanocrystals appeared rather rounded compared to the faceted ITO crystallites of the initial state and the Pt particles seem to be more agglomerated. After HP-AST (Figure 4.3g-i), the Pt nanoparticles did not grow as they exhibited an average diameter of 5.2 ± 0.6 nm. Therefore, the observed increase in $H_{upd}$-ECSA cannot be explained by the stable particle size distribution. In contrast to LP-AST, the nanocrystals of the ITO support did not only change in shape after HP-AST but also did not appear to be well separated anymore indicating coalescence to larger particles.

## 4.4. XPS and STEM/EDX Results

To get deeper insight into the changes of the Pt surface, XPS was performed on the Pt/ITO before and after the LP-AST and Figure 4.6 shows the Pt 4f as well as the In and Sn 3d spectra of Pt/ITO. From the Pt 4f depth profile it can be seen that Pt in both samples is mostly metallic with a binding energy of around 71.1 eV (Figure 4.6a,b).

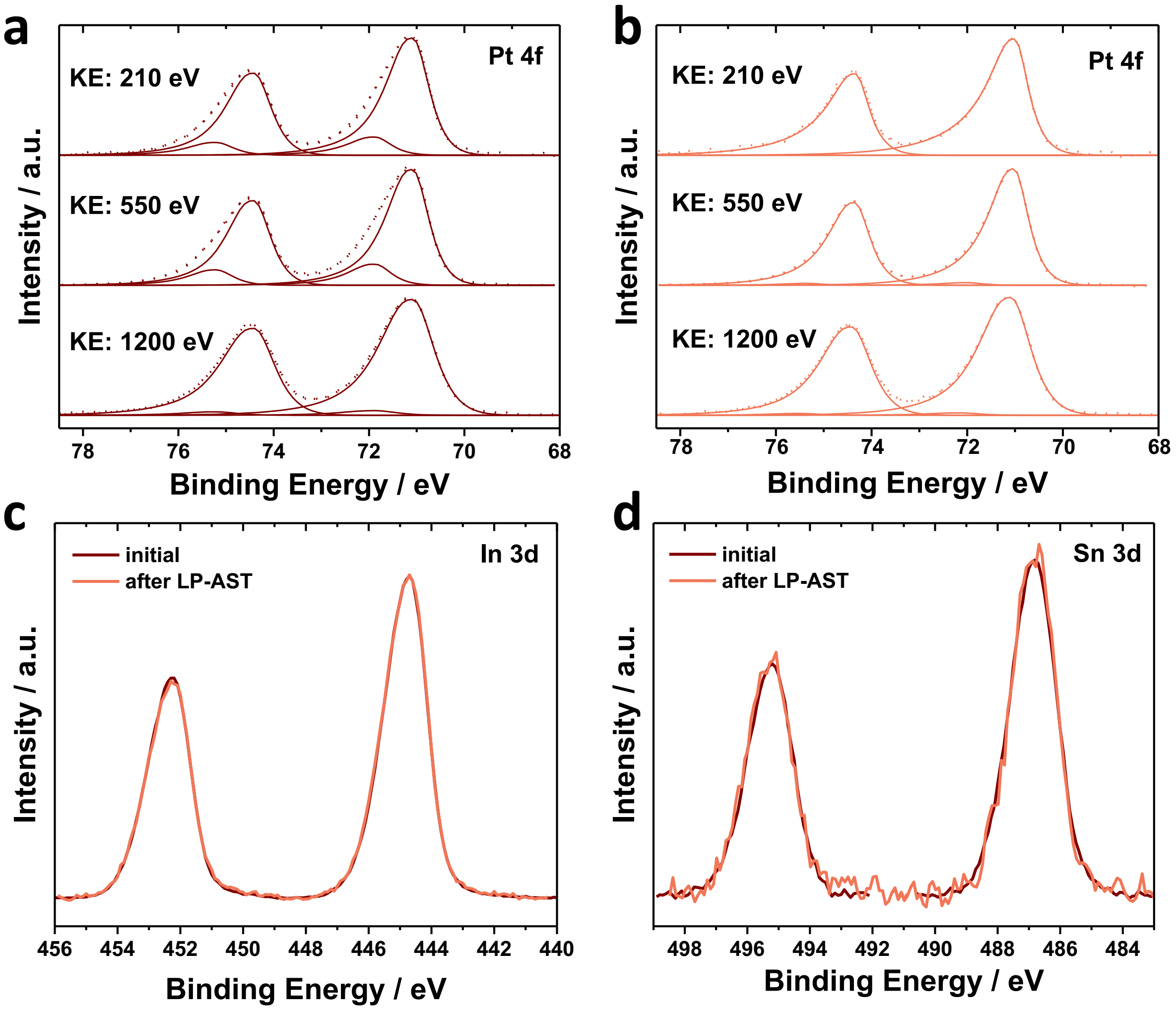

**Figure 4.6** X-ray photoelectron spectroscopy measurements. (a) and (b) are showing the Pt 4f depth profiling accessed by the kinetic energy of the photoelectrons of 210, 550 and 1200 eV at the initial (a) and the state after LP-AST (b) Dotted lines represent measured data and solid lines the fits and component peaks. (c) and (d) are showing the 3d core levels for In and Sn, respectively, each at the initial and the cycled state.

The initial state exhibited also a small fraction of $PtO_x$ species (contribution at around 72 eV) which was significantly weaker at deeper probing depth of the photoelectrons and absent after the LP-AST. This finding is in agreement with the high resolution TEM (HR-TEM) micrographs in Figure 4.2c where a sub-nanometer amorphous shell around the metallic Pt nanoparticles is visible in the as-prepared state. This shell can be explained with a thin layer of Pt oxide around the nanoparticles that disappeared upon electrochemical cycling. The ITO was assessed by In and Sn 3d core levels (see Figure 4.6c,d) and no difference was identified between the two analyzed states.

Table 4.1 shows the quantitative results from the XP spectra as obtained at two different positions of the sample. On the one hand the Pt/(In + Sn) ratio increased slightly indicating support leaching and furthermore, the In/Sn ratio changed toward lower Sn concentration.

**Table 4.1** Near-surface composition of Pt/ITO before and after LP-AST in the lower potential regime as obtained from XPS measurements. The molar ratios Pt, In, and Sn were determined from the peak areas of the Pt 4f as well as In and Sn 3d spectra recorded with a kinetic energy of the photoelectrons of 550 eV. The number in brackets denotes the composition at a second beam position of each sample.

| | **Pt/(In+Sn)** | **Sn/In** |
|---|---|---|
| initial | 0.2 (0.21) | 0.17 (0.17) |
| after LP-AST | 0.25 (0.27) | 0.14 (0.13) |

To analyze the Pt surface and the elemental distribution in the catalyst in more detail, HAADF-STEM images and EDX maps were acquired. In Figure 4.7a,b the STEM-EDX mappings of a Pt nanoparticle deposited on ITO particles are shown before and after the LP-AST.

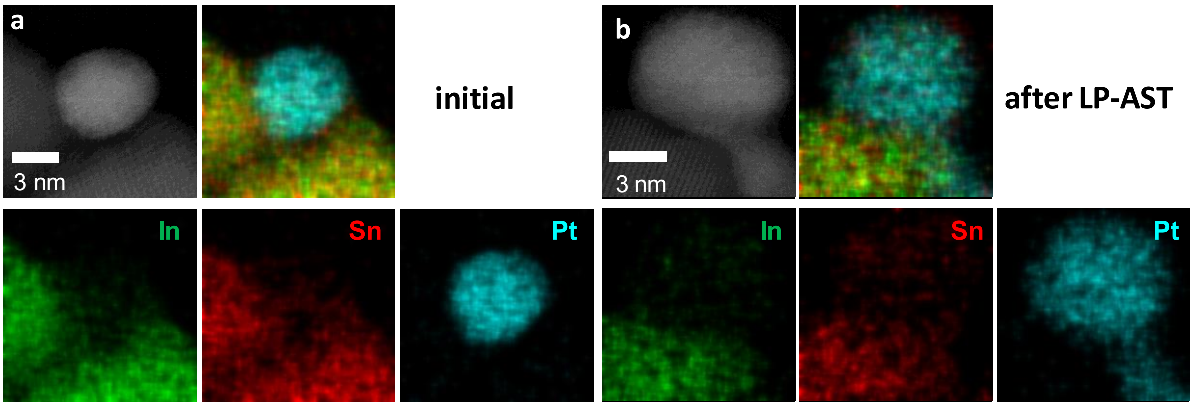

**Figure 4.7** HAADF-STEM images and EDX mapping of (a) Pt/ITO initial and (b) after LP-AST. Platinum is depicted in light blue, indium in green, and tin in red.

Pt can be clearly distinguished from the support and no clear difference between the two states in terms of Pt particle size and elemental distribution is observed. In addition, In and Sn were homogenously distributed in the ITO support and did not change drastically after potential cycling.

## 4.5. *In Situ* HE X-ray Investigation

We performed *in situ* high energy XRD and ASAXS to track and analyze the structural and morphological evolution of Pt particles as well as of $In_{2-x}Sn_xO_3$ crystallites during the AST and, thus, to gain deeper understanding about their degradation pathways. Figure 4.8a shows the evolution of the *in situ* X-ray diffraction patterns during the LP-AST including the initial state.

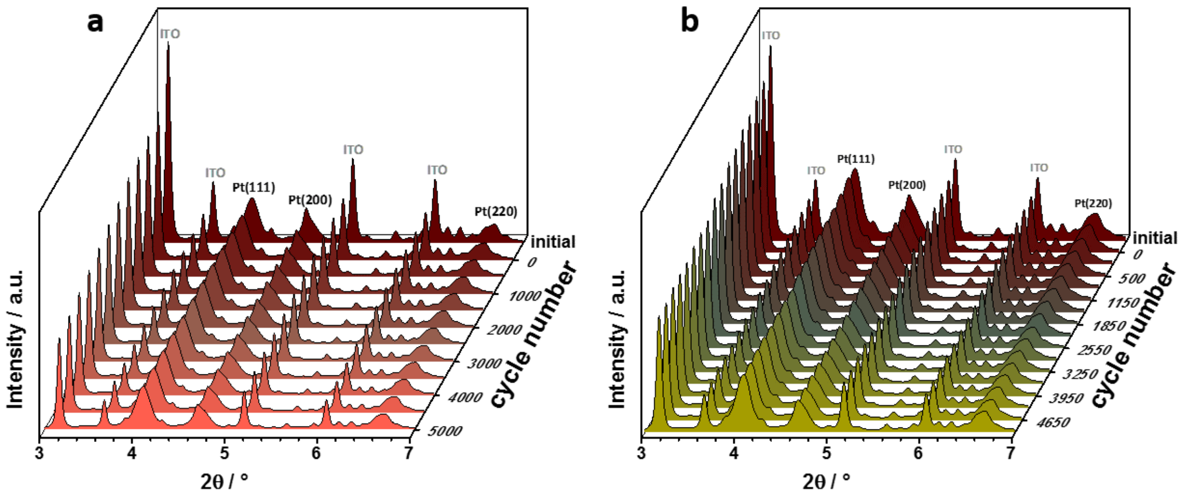

**Figure 4.8** *In situ* HE XRD measurements depicted as the evolution of diffraction patterns from the initial state to the end of the electrochemical cycling for the LP-AST (a) and the HP-AST (b).

It can be clearly seen that the Pt reflexes did not decrease in intensity whereas the intensity of the $In_{2-x}Sn_xO_3$ reflexes decreased drastically and thus, Pt/$In_{2-x}Sn_xO_3$ ratio increased. The results from Rietveld refinement of the HE-XRD patterns are shown in Figure 4.9a,b. It can be seen that the crystalline fraction of $In_{2-x}Sn_xO_3$ decreased from 79% to 61% during the LP-AST.

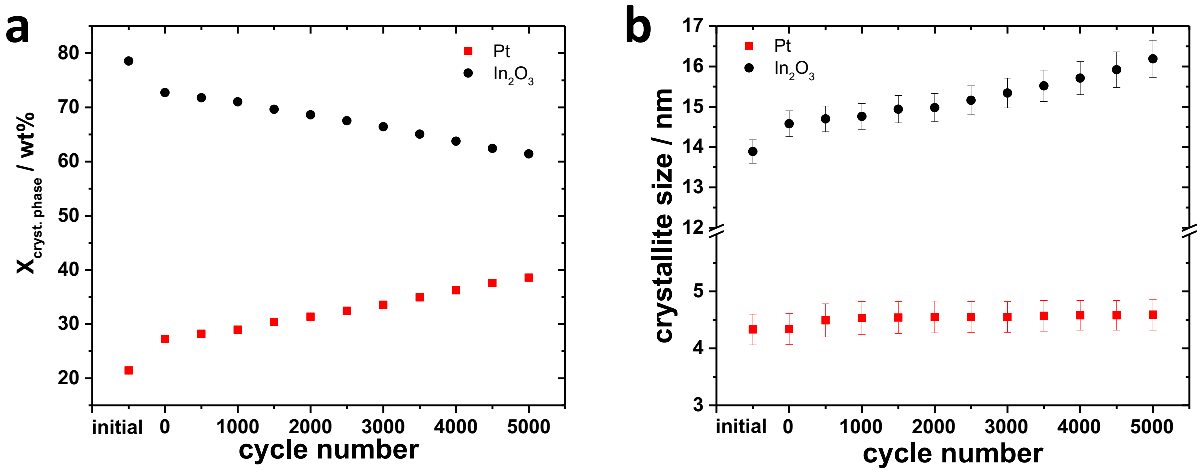

**Figure 4.9** Results from *in situ* HE-XRD for LP-AST. Weight fractions of (a) crystalline phases and (b) their crystallite size as determined by Rietveld refinement.

The scale factor of the two crystalline phases (Figure 4.10a) confirms the constant absolute amount of Pt and the loss of $In_{2-x}Sn_xO_3$ during LP-AST. Simultaneously, the Pt coherence length grew only slightly from the initial value of 4.33 ± 0.27 nm to 4.59 ± 0.27 nm, whereas the $In_{2-x}Sn_xO_3$ coherence length strongly increased from 13.89 ± 0.29 nm to 16.19 ± 0.46 nm.

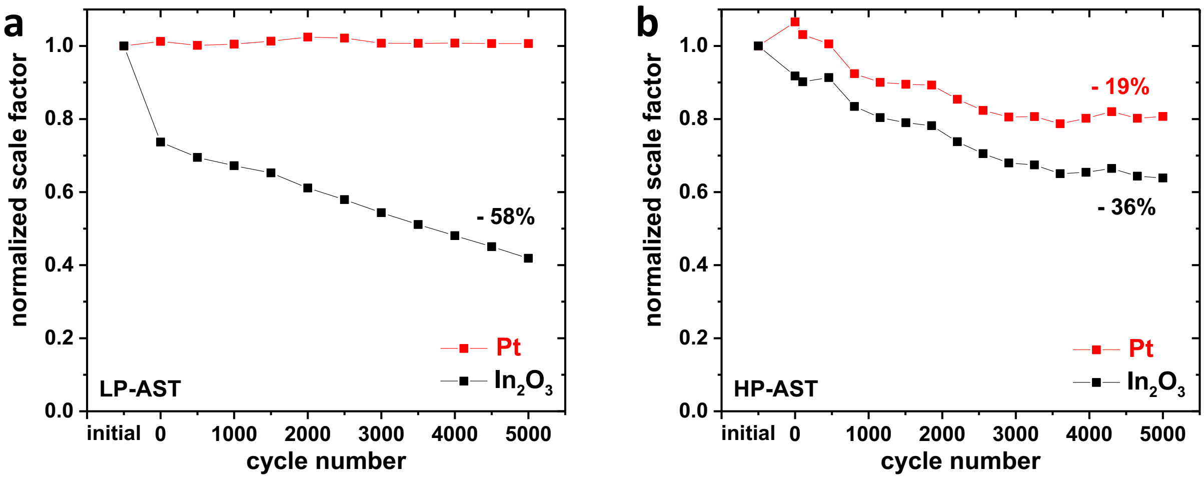

**Figure 4.10** Evolution of normalized scale factors for Pt and $In_2O_3$ from fits of HE-XRD patterns over the cycle number for (a) LP-AST and (b) HP-AST.

To gain a deeper insight in the evolution of the Pt nanoparticles, Pt-specific scattering curves were obtained from ASAXS measurements around the Pt K-edge. Figure 4.11a shows the background-corrected scattering curves with a clear feature visible above 0.1 Å$^{-1}$ resulting from Pt nanoparticles. By fitting these scattering curves and assuming a Gaussian distribution of spheres the particle size distribution (PSD) can be obtained (Figure 4.11b).

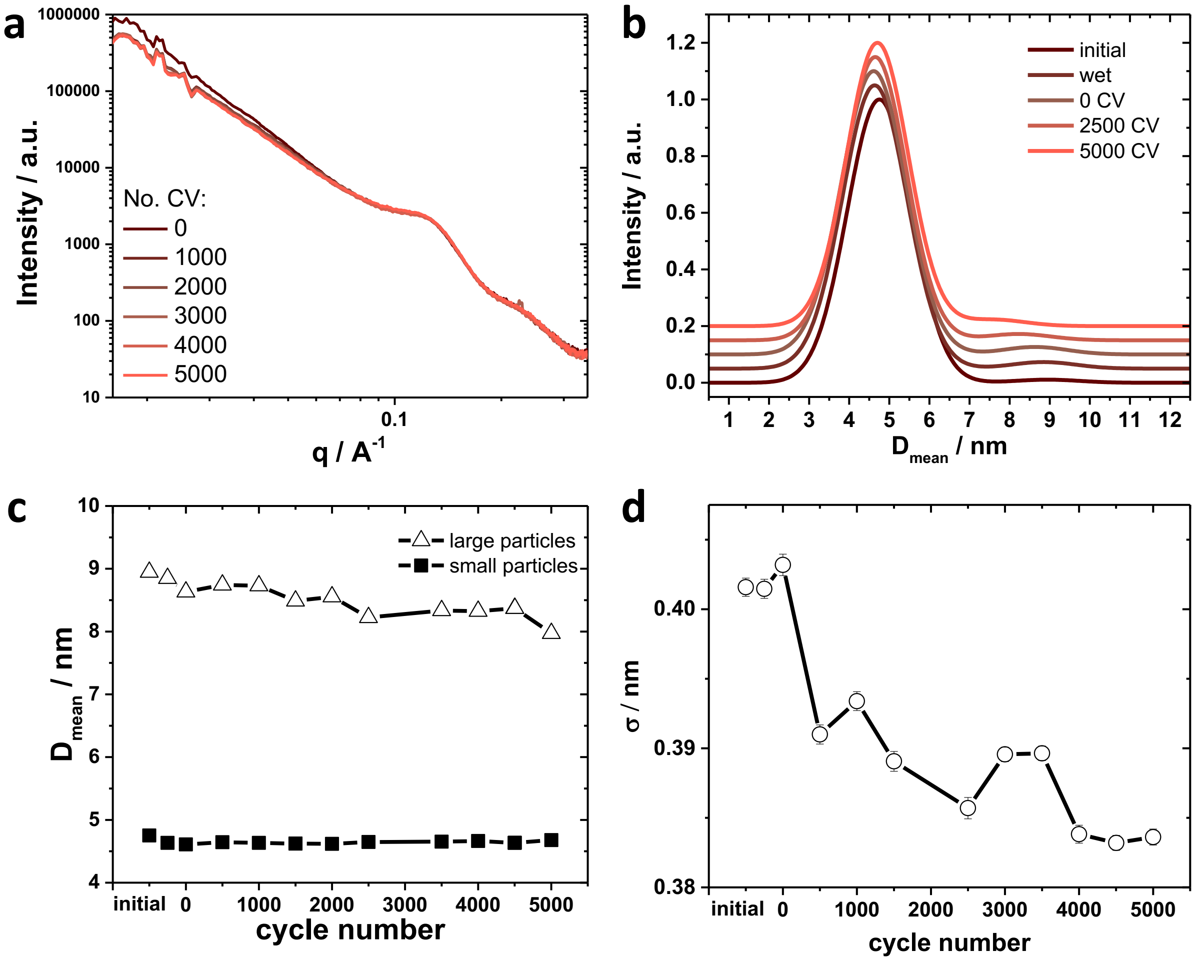

**Figure 4.11** *In situ* ASAXS measurements for LP-AST: background subtracted, Pt element specific scattering curves for selected cycle numbers (a), particle size distribution (PSD) as a function of rel. intensity over the mean particle diameter for selected cycle numbers (b), mean Pt particle diameter (c) and the evolution of monodispersity as a function of σ over the cycle number (d).

We identified a bimodal PSD with a high fraction (≈99%) of Pt particles with a size of around 4.5 nm and a small fraction (≈1%) of larger particles with a diameter of 9 nm (Figure 4.11c). This finding shows that only a very slight fraction of the Pt particles was agglomerated. The size of Pt nanoparticles stayed almost constant during the LP-AST but the agglomerated Pt particles shrink by ≈1 nm. Additionally, we noticed a slight decrease in size of the Pt particles between the as-prepared state and the start of the stability test. Furthermore, we identified that the polydispersity σ of the Pt nanoparticles decreased slightly from 0.40 to 0.38 (Figure 4.11d).

Thus, the results achieved by ASAXS measurements support the findings from Rietveld analysis and show the excellent morphological and structural stability of the Pt nanoparticles, which contrasts the evolution of the ITO support. Furthermore, we state that no significant loss in the absolute intensity of the Pt scattering/reflections (as seen by the scale factor) was obtained although the ITO support dissolved or became amorphous indicating a negligible loss of Pt nanoparticles.

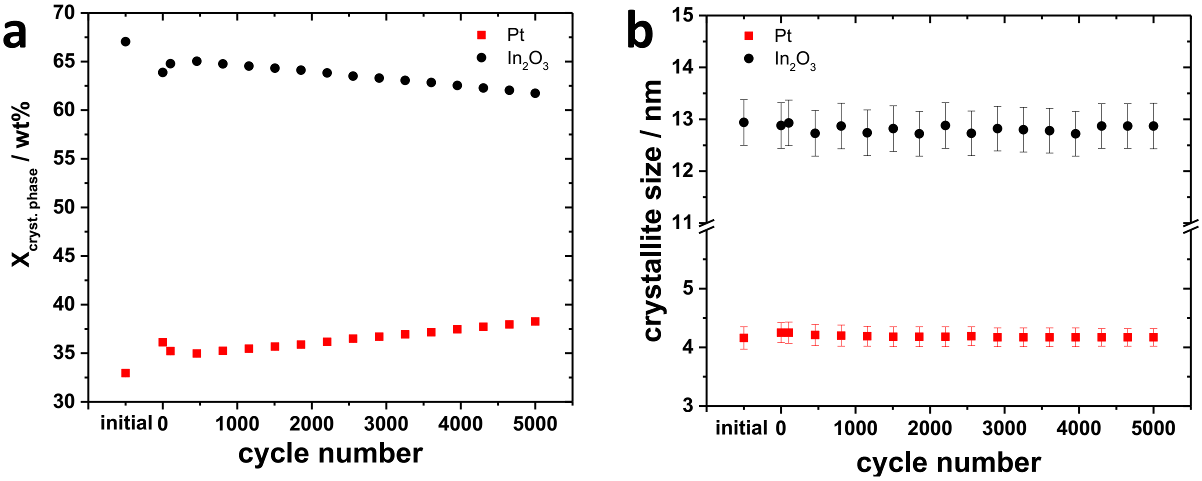

**Figure 4.12** Results from *in situ* HE-XRD measurements for HP-AST. Weight fractions of (a) crystalline phases and (b) their crystallite size as determined by Rietveld refinement.

Figure 4.8b shows the evolution of diffraction patterns during HP-AST. It can be clearly seen that the intensities of the ITO reflexes decreased less strongly than during the LP-AST. The evolution of fraction of the crystalline phases as determined by Rietveld refinement is shown in Figure 4.12a. It can be seen that the fraction of $In_{2-x}Sn_xO_3$ decreased by around 5% from 67% to 62%, whereas the Pt fraction simultaneously increased by the same extent. From the initial dry state to the state directly before the stability test an initial drop of the $In_{2-x}Sn_xO_3$ fraction of 3% was observed which can be explained with a partial dissolution (or amorphization) of the $In_{2-x}Sn_xO_3$ during the CVs in the activation regime. During the first 500 CVs of the HP-AST the $In_{2-x}Sn_xO_3$ fraction increased again. The scale factor of the two crystalline phases (Figure 4.10b) confirms the loss of absolute amount of Pt and of $In_{2-x}Sn_xO_3$ during HP-AST. Throughout the whole HP-AST, the coherence lengths of both Pt and $In_{2-x}Sn_xO_3$ remained constant with a size of 4.25 ± 0.19 nm and 12.94 ± 0.44 nm, respectively (Figure 4.12b).

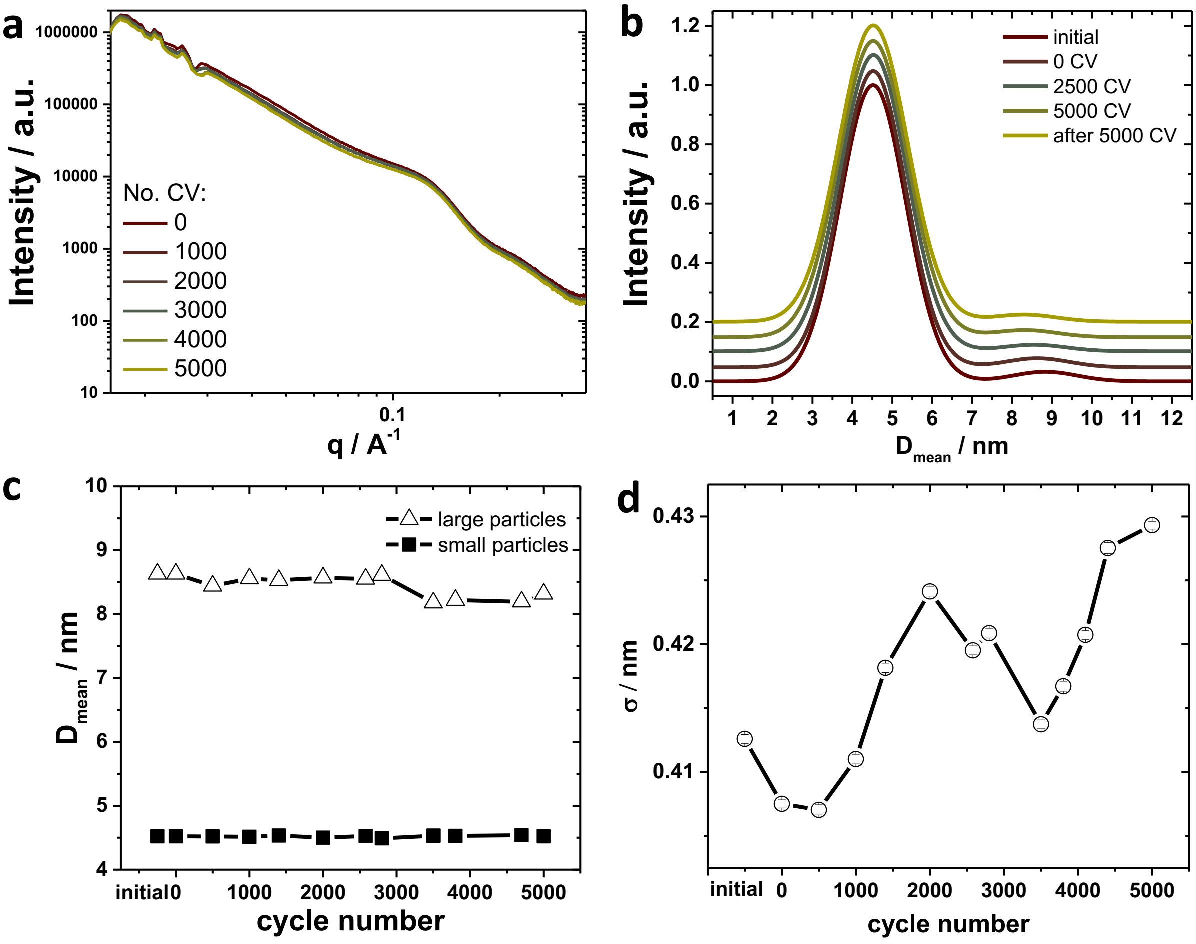

**Figure 4.13** *In situ* ASAXS measurements for HP-AST: background subtracted, Pt element specific scattering curves for selected cycle numbers (a), particle size distribution (PSD) as a function of rel. intensity over the mean particle diameter for selected cycle numbers (b), mean Pt particle diameter (c) and the evolution of monodispersity as a function of σ over the cycle number (d).

Complementary to these *in situ* HE-XRD measurements, the results from ASAXS experiments for the HP-AST are shown in Figure 4.13. They show the stability of the Pt nanoparticles during the HP-AST as the mean particle size of both smaller and larger particle (agglomerates) remained constant (Figure 4.13c) and the polydispersity σ increased slightly from 0.41 to 0.43 (Figure 4.13d).

Generally, we state that perfect agreement between particle, crystallite size, and structural coherence length determination by TEM, (A)SAXS, and HE-XRD demands very high degree of homogeneity in shape, size, and crystallinity, which was not given in this study.[140]

## 4.6. *In Situ* Pt, In and Sn Dissolution by SFC ICP-MS

To differentiate between amorphization and dissolution/detachment of the ITO support and to track the dissolution of Pt, In, and Sn, experiments with an *in situ* SFC coupled to an ICP-MS were performed. The LP- and HP-ASTs were applied to the Pt/ITO and to the Pt/C reference catalyst. Figure 4.14 shows the results from *in situ* SCF ICP-MS experiments for the two different potential regimes.

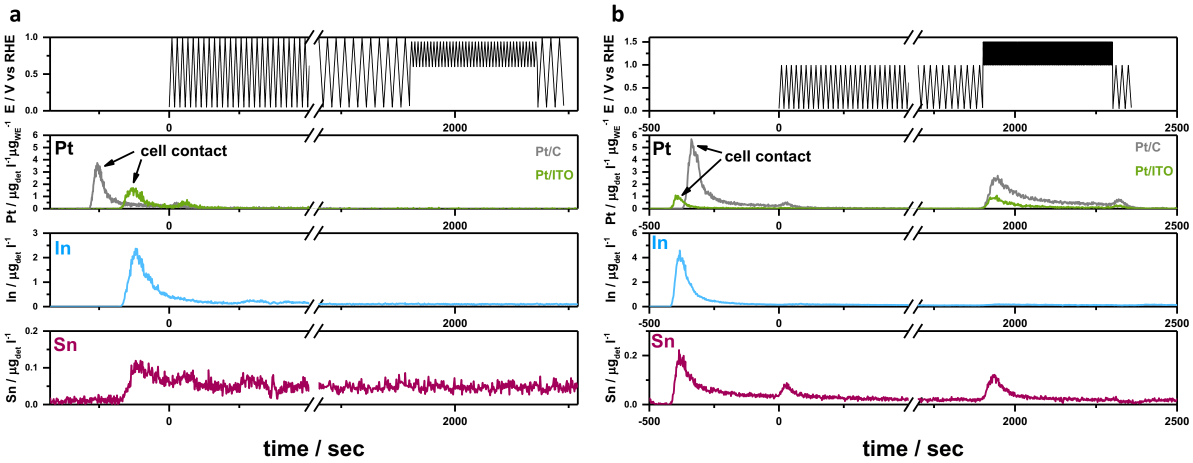

**Figure 4.14** *In situ* scanning flow cell ICP-MS measurements. Depicted are the Sn, In and Pt dissolution rates and the applied electrochemical protocols from the bottom to the top for (a) LP-AST and (b) HP-AST. The respective dissolution rates in detected (det) metal in µg per volume electrolyte (µg$_{det}$ L$^{-1}$) are plotted against the time. A Pt/C reference sample was measured and therefore, the Pt dissolution rate was also normalized to the Pt mass loading on the working electrode (WE) (µg$_{det}$ L$^{-1}$ µg$_{WE}$$^{-1}$). The electrochemical protocol was conducted as follows: Beginning with 100 CVs (activation regime) from 0.05-1 V, followed by potential cycling in the LP regime (0.6-0.95 V, 40 CVs, 100 mV s$^{-1}$) or in the HP regime (1.0-1.5 V, 200 CVs, 500 mV s$^{-1}$) and followed by another 3 cycles from 0.05-1 V, all CVs were recorded with a scan rate of 100mV/s. The first contacts between catalyst and electrolyte (cell contact) are denoted with arrows. Breaks at the time axis of (a) and (b) have been implemented between 500 and 1700 s. Graphs with complete time axis can be found in Figure A5 and Figure A6.

It can be seen that a large dissolution peak arises for all three metals when the first contact between the electrode and the acidic electrolyte under open circuit potential (OCP) conditions was established (denoted as cell contact). During potential cycling in the activation regime Pt dissolution was observed in case of the ITO and C support. The Pt dissolution was up to 0.5 µg$_{det}$ L$^{-1}$ µg$_{WE}$$^{-1}$ but limited to the first potential cycles (see Figure 4.14a) and no major difference between Pt/ITO and Pt/C was observed. Furthermore, no Pt dissolution was observed during potential cycling in the activation and the LP regime.

During potential cycling in the activation and in the LP regime a low but constant dissolution of In and Sn was observed (0.05 and 0.1 µg$_{det}$ L$^{-1}$, respectively). Thus, the ITO dissolved continuously over the whole course of the applied electrochemical protocol without any specific potential dependence. In case of the HP regime (Figure 4.14b) a relatively broad Pt dissolution peak can be observed for both carbon and oxide supports, but again, Pt dissolution was significantly more pronounced for Pt/C than for Pt/ITO. We determined the amount of Pt dissolution during the first cycles in the HP regime to be $1 \cdot 10^{-3}$ $\mu g_{det}$ $\mu g_{WE}^{-1}$ for Pt/C and $3 \cdot 10^{-4}$ $\mu g_{det}$ $\mu g_{WE}^{-1}$ for Pt/ITO (see Figure 4.15). Note that Pt dissolution becomes more pronounced during the activation potential cycles after the potential cycling in the HP regime compared to that in the LP regime. A likely explanation is the reductive dissolution of the electrochemically formed $PtO_x$ species.[38,141] Pt-specific dissolution behavior with a small oxidative dissolution peak and a big and sharp peak in the reductive scan of the AST were superimposed by a broad and decreasing dissolution signal due to the relatively high scanrate of 500 mV $s^{-1}$ in the HP-AST.

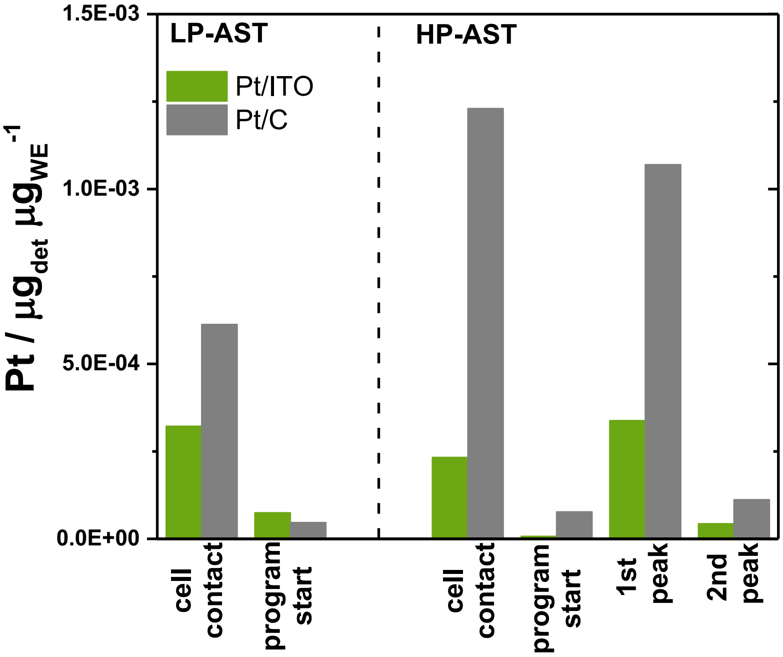

**Figure 4.15** Results from *in situ* SFC ICP-MS of the integration of the peaks arising from Pt dissolution over time of the measurement (in $\mu g_{det}$) detected by the ICP-MS per mass loading Pt on the working electrode (in $\mu g_{WE}$) for LP- and HP-AST.

In addition to the dissolution peaks of In and Sn upon first cell contact, a small Sn dissolution peak was observed at the beginning of the activation regime which remained comparable in intensity to Sn dissolution during the LP-AST. Slight In, and a more pronounced Sn dissolution was also detected during the first cycles in the HP regime and, thus, the observed Pt loss was likely caused by Pt nanoparticle detachment due to support dissolution. Data evidence that Sn is more prone to dissolve during the HP-AST. Generally, we state that only 0.04% (0.10%) of Pt and 1.89% (2.47%) of the ITO support was dissolved over the whole course of the applied though shorter electrochemical protocol for the LP (HP) regime. For comparison, in case of the Pt/C reference 0.09% (0.29%) of the total Pt mass was dissolved (see also Table A3).

## 4.7. Discussion

Associated with the need of developing new and stable electrocatalysts for PEMFCs, an *in situ* stability study of ITO- supported Pt nanoparticles has been conducted. We were able to successfully deposit Pt nanoparticles with a uniform size on the crystalline support. The catalyst was tested for electrochemical stability under simulated fuel cell conditions by applying two different ASTs representing conventional operating (0.6-0.95 V) and start-up/shut-down (1.0-1.5 V) conditions. By employing a wide range of *in situ* (X-ray) techniques as well as advanced spectroscopy and electron microscopy, we aimed to determine fundamental descriptors for electrochemical catalyst and support stability as well as the most prominent degradation pathway.

***Electrochemical versus Structural Stability***

The investigation of electrocatalytic stability in acidic media applying two different protocols has revealed that Pt/ITO shows higher electrochemical stability in the HP-AST than in the LP-AST. In particular, ORR activity and CO-ECSA decreased strongly during the LP-AST, while $H_{upd}$-ECSA stays rather stable, suggesting that the CO-ECSA is a better descriptor for the ORR active site density. These findings show that the Pt surface after LP-AST remains accessible for H adsorbates represented by a stable $H_{upd}$-ECSA but not for O/OH adsorbates which are essential for the oxygen reduction reaction. TEM analysis shows almost no growth of Pt nanoparticles and a slightly higher degree of Pt agglomeration. This slightly higher degree of agglomeration of the Pt particles can explain the small decrease of the accessible surface area as measured via $H_{upd}$ but the CO-ECSA decreased to a higher extent. *In situ* X-ray investigations again proved that Pt particle and crystallite size was stable over the LP-AST and *in situ* SFC ICP-MS showed negligible Pt dissolution. The morphological and structural stability of the Pt nanoparticles contrasts the strong loss in catalytic activity. Thus, the major changes in ITO indicate a strong influence of the morphological stability of ITO on the catalytic activity of Pt. *In situ* X-ray investigations revealed that the fraction of crystalline ITO strongly decreased and the crystallite size increased. Hence, the ITO is partially dissolved/detached or loses crystallinity during LP-AST. From *in situ* SFC ICP-MS measurements a small but continuous dissolution of In and Sn was observed, but the observed loss from HE-XRD in ITO weight fraction is much higher suggesting partial amorphization of ITO. Dissolved In/Sn ions are prone to be (electro) chemically and isostructurally redeposited on the ITO crystallites which can explain the determined growth via Ostwald ripening.[39] Alternatively, the loss of smaller crystallites could lead to a larger mean crystallite size.

We have to note that the loss of crystalline ITO is not directly linked to a loss of Pt nanoparticles. Rietveld refinement shows that the absolute amount of Pt remained stable during the LP-AST, whereas the absolute amount of crystalline ITO strongly decreased (as measured by the scale factor extracted from fits of the HE-XRD pattern, see Figure 4.10a). These findings suggest that ITO gets preferentially dissolved where locally no Pt is present and that the Pt nanoparticles might be stabilizers of ITO. By acting as electron scavenger the Pt inhibits the electrochemical reduction of the surface In/Sn ions and thus, reduces their dissolution into the electrolyte. This function is similar to the role of an appropriate cocatalyst on photoanodes acting as hole scavengers leading to enhanced photoelectrocatalytic stability.[142] Thus, we can conclude that while Pt is almost unaffected by the conditions present during LP-AST, the strong changes of the ITO influence the stability of the electrocatalytic activity of the Pt nanoparticles.

The AST in the HP regime from 1.0-1.5 V revealed a significantly better stability of the catalytic activity. TEM analysis and *in situ* X-ray results showed that ITO nanocrystals and Pt nanoparticles did not grow and the composition remained stable compared to the LP-AST. This agrees with a rather stable CO-ECSA and hence with a stable mass-based activity, which again shows the dependency of these two descriptors. By contrast, the Pt surface area became larger as it exhibited a higher $H_{upd}$-ECSA. This can be explained by an electrochemical roughening of the Pt surface as elevated Pt dissolution was observed rom *in situ* SCF ICP-MS during the HP-AST. Furthermore, the dissolved Pt ions could be redeposited on the cathode as sub-nanometer clusters or single atom sites which we did not detect by electron microscopy and HE-XRD. But these domains would contribute to the increase in the $H_{upd}$-ECSA and would lower the dissolution rate with respect to the loss of crystalline Pt nanoparticles. The Pt dissolution during HP-AST was accompanied by small In and more pronounced Sn dissolution affecting the shape of the ITO crystallites as observed in TEM images. However, these changes influenced the structure and morphology of the ITO less strongly than during the LP-AST and without a tremendous impact on the catalytic performance. Additionally, the loss of crystalline $In_{2-x}Sn_xO_3$ from *in situ* HE-XRD could rather be assigned to support leaching than to amorphization as concluded for LP-AST.

The comparison of the electrochemical results revealed a higher stability for the Pt/C reference in the LP-AST when compared to the Pt/ITO catalyst. Dissolution of Pt in Pt/C during the LP-AST was very low and comparable to that of Pt/ITO, indicating similar morphological Pt stability in Pt/C and Pt/ITO. After HP-AST the reference material revealed a lower stability with a relatively big loss in catalytic activity. From *in situ* ICP-MS it can be seen that during cycling in the range of 1.0-1.5 V Pt dissolution was much more pronounced in Pt/C than in Pt/ITO. This can be explained with a stronger electronic interaction between the metal particles and the oxide support impeding nanoparticle detachment or dissolution but could also be caused by the differences in particle size and, thus, electrochemical surface area. In that respect, initial Pt dissolution peaks at cell contact due to $PtO_x$ reduction at OCP conditions were again smaller for ITO supported Pt. ITO might decrease $PtO_x$ formation resulting in lower peak intensity compared to the Pt/C reference.

***Catalyst/Support Degradation Pathways***

From the above described electrochemical and structural behavior of Pt/ITO under operating conditions we conclude that the support stability has a tremendous impact on the stability of the catalytically active sites. We are able to exclude well-known catalyst degradation phenomena caused by Pt particle growth, agglomeration, and dissolution/detachment and propose a pathway based on strong influence of support degradation on the availability of Pt active sites. In detail, we found an overall excellent structural and morphological stability of Pt but we determined altering of the ITO support as a likely actuator for Pt (surface) poisoning and resulting performance loss in the ASTs, especially in the LP-AST.

For the LP-AST, XPS data indicate support loss in the form of Sn leaching and continuous but small support dissolution was also found by *in situ* ICP-MS. The dissolved metal ions could be electrochemically redeposited not only preferentially on the ITO surface but also on the Pt surface during the relative reductive conditions of cycling between 0.6 and 0.95 V. The increasing Pt/(In+Sn) ratio from XPS after LP-AST is dominated by the preferential dissolution (or detachment) of the support but does not exclude Pt surface modification.

Consequently, we aim to uncover the origin for this poisoning effect in the form of proposed degradation pathways. Possible mechanisms for Pt surface poisoning could be (a) support metal incorporation into Pt nanoparticles leading to alloy formation, (b) formation of an amorphous metal (oxyhydr)oxide layer, or (c) redeposition of In and/or Sn ions on the Pt surface. Metal diffusion into Pt leading to alloy formation preferentially due to Sn alloying into the Pt lattice could also lower catalytic activity. In that respect, no other phase was observed during potential cycling in the HE-XRD. Nevertheless, the evolution of Pt lattice constant based on Rietveld refinement during the LP-AST was tracked, because Partial PtSn alloy formation should increase the lattice constant ($PtSn_3$, PDF#00-035-1360). Figure A7a shows the lattice constant as a function of the cycle number in the LP-AST. Here, it can be seen that the lattice constant decreases from beginning to end of cycling. Furthermore, the formation of a near-surface alloy leading to a PtSn shell is unlikely because this would lead to a decrease of the Pt coherence length. Thus, PtSn alloy formation is unlikely and can therefore be excluded for the major Pt poisoning contributors.

Another interpretation of the combination of electrochemical and *in situ* results can be the partial transformation of ITO to an amorphous In/$SnO_x(OH)_y$. This (oxyhydr)oxide formation could then lead to a (partial) encapsulation in the form of a thin (mono)layer around Pt. This theory would go in line with relatively strong loss of crystalline $In_{2-x}Sn_xO_3$ fraction from HE-XRD and only little In and Sn dissolution from ICP-MS. Such a layer would be permeable for protons but not for larger molecules like CO or OH and could thus, explain the different trends in $H_{upd}$- and CO-ECSA. This phenomenon, also known as “decoration effect,” originates from SMSI and is well known in literature for different metals (Rh, Pt, Pd, Ni, Co) supported on metal oxides ($TiO_2$, $Fe_3O_4$, $WO_x$).[143-152] In these studies, the encapsulation has been induced by thermal/chemical reduction of the oxide support as well as electrochemical reduction at low potentials in the case of Pt/$WO_x$. In our case, the LP-AST in acidic electrolyte implies reductive reaction conditions for the oxide support. Furthermore, in photocatalysis this effect is intentionally induced to suppress ORR in hydrogen evolution catalysts by growing a proton- and hydrogen-permeable $Cr_2O_3$ shell around an Rh catalyst. This shell is impermeable for $O_2$ molecules inhibiting undesired ORR.[153] We identified a marginal growth of Pt particles by less than 1 nm in TEM micrographs after LP-AST (Figure 4.3), while the coherence length/domain size (as obtained by HE-XRD) and particle size (as obtained by ASAXS) remained constant. This finding would go in line with the formation of sub-nanometer (oxyhydr)oxide layer around Pt but can also be within the error of particle size estimation from TEM due to higher degree of agglomeration. However, we could not prove the formation of this layer by STEM images and EDX spectroscopy even though a sub-monolayer coverage or adsorption might be hard to detect. Also XP spectroscopy does not give the sensitivity to differentiate between the chemically unchanged isostructurally grown $In_{2-x}Sn_xO_3$ crystallites and sub-monolayer coverage of the support metal ions on the surface of the Pt nanoparticles. However, we expect the ad-atoms to differ chemically from the Sn/In ions in the $In_{2-x}Sn_xO_3$.

It is known from literature that In and/or Sn metal adsorbates present as sub-monolayer on Pt single crystal surfaces can strongly affect the CO oxidation behavior.[154] Therein, adsorbed Sn on various Pt surfaces lead to a growth of the oxidation peak at 0.53 V. In case of the Pt (111) surface Sn coverage blocks the more anodic CO oxidation peak at 0.65 V, whereas it does not affect the CO electrooxidation on Pt (100) and (110) surfaces. CO electrooxidation on the

Pt/ITO catalyst also shows a preferential poisoning of the high potential oxidation peak after the LP-AST (Figure A3), and thus, our electrochemical data are in agreement with the surface poisoning of the Pt nanoparticles with metal (Sn) ions. We note that the anodic shift of the CO oxidation potential might be caused by the In adsorbates in addition to Sn. In another approach, Pt supported on Nb- and Sb-doped $SnO_2$ was used as catalyst for single cell stability tests and it was found that Sn was dissolved at reducing potentials resulting in Pt poisoning by Sn redeposition.[155] Nakada *et al.* studied $SnO_2$ supported Pt electrocatalyst and they found decreased Pt oxidation/reduction currents due to stronger interactions of Sn with Pt after electrochemical cycling.[156] Additionally, under potential deposited (UPD) Sn on Pt was found to change the Pt oxidation behavior when cycling in $HClO_4$.[157]

In case of the HP-AST the dominant degradation mechanism is Pt dissolution from $PtO_x$ species by reaching potentials as high as 1.5 V. Interestingly, ITO support dissolved as well in this potential regime leading to support modification, but did not affect the electrochemical performance drastically. We explain that with the slight but continuous dissolution of surface Pt atoms under oxidative conditions, which continuously pours away potentially adsorbed In/Sn atoms. This process prevents significant poisoning with In/Sn atoms and, thus, leads to a rather stable mass-based catalytic activity. Furthermore, cathodic potentials as low as 0.6 V as in LP-AST might be required to form metal (oxyhydr)oxides or Sn UPD layer on the Pt surface.

For the HP-AST regime we clearly established a superior structural stability of Pt nanoparticles on ITO versus C supports. Some earlier work put forward strong electronic interactions between metal particles and the oxide support impeding nanoparticle detachment.[59,158] Recent DFT calculations showed that the electronic influence of oxide support is limited to a few atom layers of Pt.[159] The Pt nanoparticles in this work are significantly larger and, thus, electronic interactions may remain masked from spectroscopic identification although they are indeed anchored more strongly to oxide supports.

Combining all these results, we propose that the activity loss during the LP-AST is caused by a kind of Pt surface modification due to In and, more likely, Sn accumulation. During HP-AST this degradation pathway is blocked because slight anodic dissolution of Pt keeps the active sites accessible.

## 4.8. Conclusion

We have explored the stability and degradation of Pt nanoparticles supported on ITO during the electrocatalytic reduction of molecular oxygen as well as during two distinct degradation regimes corresponding to normal fuel cell operation and a start-up/shut-down operation, respectively. The Pt/ITO electrocatalyst consisted of monodisperse, well-distributed Pt particles with a size of around 5 nm and was investigated using a number of different *in situ* techniques (i) to gain fundamental insight in the degradation mechanisms, (ii) to unravel fundamental descriptors of structural and morphological stability, and (iii) to determine stability limitations of this material system. Our combination of X-ray and electron microscopic techniques has advanced our understanding of the fundamental processes associated with the degradation behavior of Pt/ITO electrocatalysts.

Under catalytic ORR operation conditions (LP-AST) we have demonstrated that Pt nanoparticles remain morphologically stable and degradation pathways due to Pt instability can be excluded, whereas the ITO support suffers from cathodic corrosion coaffecting the catalytic stability and mechanical/chemical attachment of the Pt nanoparticles. ITO crystallites partially dissolve, become amorphous, and grow via an Ostwald ripening mechanism. Therefore, we have strong indications that the significantly declined catalytic ORR activity after LP-AST is attributed to partial In/Sn redeposition and concomitant surface decoration of active Pt particle. Such oxidic Pt surface adlayers change the Pt redox chemistry and lower the density of specific O-adsorption sites. An encapsulation of the Pt nanoparticles with an (oxyhydr)oxide layer could equally account for this behavior, yet was not fully supported by the available data. By contrast, during start-up/shut-down cycles (HP-AST), the catalyst/support couple showed excellent stability, thanks to the improved structural and morphological durability of the oxide support compared to the commercial Pt/C couple. We found evidence for slight continuous anodic Pt dissolution which aided in suppressing Pt surface poisoning and thus stabilizing the available active site density.

Overall, this study has unraveled the major degradation pathways of ITO-supported Pt nanoparticle fuel cell catalysts over wide cathode potential ranges; our findings advance our understanding of the fundamental aspects of support stability. They are also of practical value for the development of improved fuel cell devices, as they offer design criteria and performance limitations of oxide-based PEMFC cathode catalysts.

# 5. The Impact of Carbon Support Functionalization on the Electrochemical Stability of Pt Fuel Cell Catalysts

Nitrogen-enriched porous carbons have been discussed as supports for Pt nanoparticle catalysts deployed at cathode layers of proton exchange membrane fuel cells (PEMFC). Here, we present an analysis of the chemical process of carbon surface modification using ammonolysis of pre-oxidized carbon blacks, and correlate their chemical structure with their catalytic activity and stability using *in situ* analytical techniques. Upon ammonolysis, the support materials were characterized with respect to their elemental compositional, the physical surface area and the surface zeta potential (ZP). The nature of the introduced N-functionalities was assessed by X-ray photoelectron spectroscopy (XPS). At lower ammonolysis temperatures, pyrrolic-N were invariably the most abundant surface species while at elevated treatment temperatures pyridinic-N prevailed. The corrosion stability under electrochemical conditions was assessed by *in situ* high temperature - differential electrochemical mass spectroscopy (HT-DEMS) in a single gas diffusion layer (GDL) electrode; this test revealed exceptional improvements in corrosion resistance for a specific type of nitrogen modification. Finally, Pt nanoparticles were deposited on the modified supports. *In situ* X-ray scattering techniques (XRD and SAXS) revealed the time evolution of the active Pt phase during accelerated electrochemical stress tests (AST) in electrode potential ranges where the catalytic oxygen reduction reaction (ORR) proceeds. Data suggest that abundance of pyrrolic nitrogen moieties lower carbon corrosion and lead to superior catalyst stability compared to state-of-the-art Pt catalysts. Our study suggests with specific materials science strategies how chemically tailored carbon supports improve the performance of electrode layers in PEMFC devices.

*Chapter 5 and section Appendix A2 were reprinted with permission from Ref*[71] *(Chem. Mat.,* ***2018****, 30 (20), 7287-7295). Copyright (2018) American Chemical Society.*

Henrike Schmies, Elisabeth Hornberger, Björn Anke, Tilman Jurzinsky, Hong Nhan Nong, Fabio Dionigi, Stefanie Kühl, Jakub Drnec, Martin Lerch, Carsten Cremers, Peter Strasser, *"The Impact of Carbon Support Functionalization on the Electrochemical Stability of Pt Fuel Cell Catalysts*", *Chemistry of Materials* **2018**, 30 (20), 7287-7295; doi: 10.1021/acs.chemmater.8b03612

H.S. performed the experiments and analyzed the data, E.H. helped designing the experiments and discussing the data; B.A. and M.L. performed the ammonolysis; T.J. and C.C. conducted the HT-DEMS measurements and analysis; H.N.N. performed and analyzed the XPS measurements; F.D. and J.D. assisted in the synchrotron experiments and data evaluation; S.K. recorded TEM images; H.S. and P.S. wrote the manuscript; all authors assisted in discussing and writing the manuscript.

## 5.1.Introduction

In this work, we studied a family of nitrogen-doped carbons, prepared by ammonolysis, looked at a range of their physicochemical properties and used the carbons as high surface area support materials for catalytically active Pt nanoparticles. N-modified carbon-supported Pt particles, with a high ration of pyrrolic nitrogen moieties, revealed exceptional catalytic performance stabilities during accelerated stress tests. To learn about the origin and the mechanism of this chemical stabilization, we utilized a range of *in situ* X-ray and mass spectrometric techniques. These methods enabled us to pinpoint the underlying chemistry of the stabilization and to exclude competing mechanisms. We close with a specific synthetic recommendation for more corrosion stable fuel cell catalysts.

## 5.2. Compositional and Surface Characterization

The controlled modification of Vulcan XC72R powders was achieved by treatment in liquid HCl, followed by subsequent oxidation in concentrated nitric acid (referrred to here as ”O-Vulcan”), and then followed by ammonolysis in pure ammonia at two different temperatures resulting in powder materials referred to as ”N-Vulcan 400°C” and ”N-Vulcan 800°C” (see Figure 5.1).

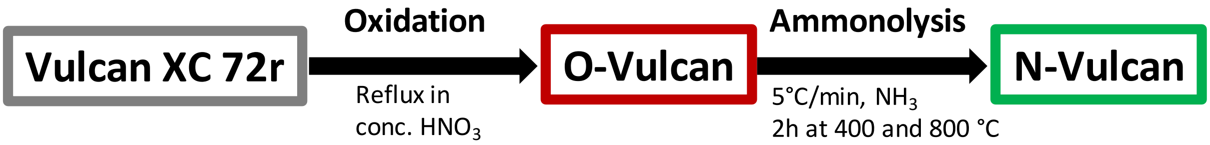

**Figure 5.1** Schematic illustration of the carbon modification procedure including oxidation step in concentrated nitric acid resulting in O-Vulcan, and ammonolysis in pure $NH_3$ at 400 and 800°C resulting in N-Vulcan.

In order to analyze the degree of carbon modification, surface area and bulk compositional analyses of the unmodified Vulcan, the oxidized Vulcan and the aminated Vulcans were performed (Figure 5.2 and Table A4, Appendix A2). Elemental analysis revealed that highest N content is achieved for N-Vulcan 400°C with 2.5 atomic (at)%, while for N-Vulcan 800°C it was 1.5 at%, see Figure 5.2a. The oxidized Vulcan contained a small fraction of nitrogen, presumably due to residues from the nitric acid treatment. The oxygen content was analyzed by hot gas extraction and was highest for O-Vulcan with 12.6 at%, while a fraction of 3.0 and 0.9 at% is detected for N-Vulcan 400°C and N-Vulcan 800°C, respectively. This suggests that the carbon modification through oxidation and ammonolysis involves the reduction of the oxygenated surface groups to nitrogenated ones. Furthermore, it can be stated that this modification approach leads to relative high concentrations of heteroatoms in the carbon but is presumably dependent on the experimental conditions and the type of carbon used. Earlier works applying comparable oxidation/amination routes resulted in slightly lower fractions of heteroatoms.[84-86,98]

After the oxidation step, the BET surface area decreased from 300 $m^2 g^{-1}$ for Vulcan to 138 $m^2 g^{-1}$ for O-Vulcan (Figure 5.2b) which we ascribe to blocking of carbon pores. The value stayed similar for N-Vulcan 400°C but increased to 252 $m^2 g^{-1}$ for N-Vulcan 800°C. The increase of surface area with higher ammonolysis temperature could be attributed to ammonia etching and clearance of previously blocked pores by the loss of oxygenated species (phenolic-/ether-/carboxylic-groups[84]).

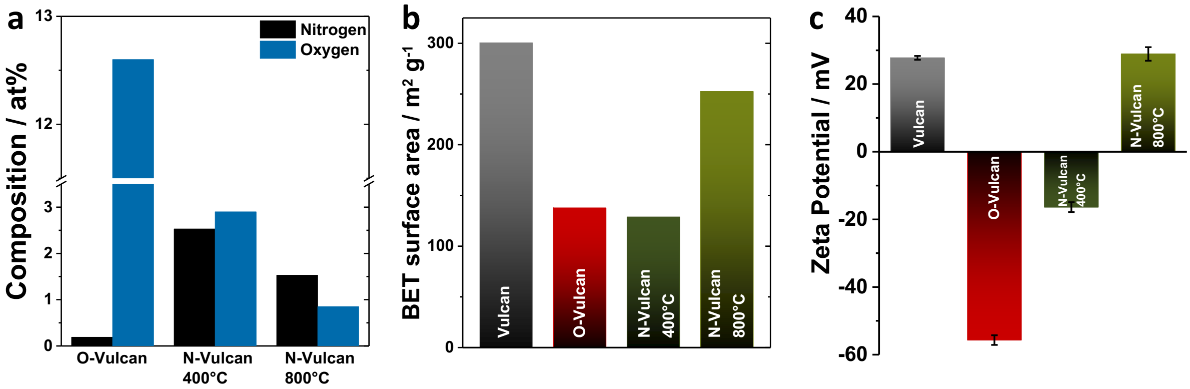

**Figure 5.2** Surface and compositional analysis of the carbon materials: content of nitrogen (from elemental analysis) and oxygen (from hot gas extraction) for the modified carbons (a), physical BET surface area (b) and zeta potential (c) for modified carbons in comparison to the unmodified Vulcan.

Furthermore, the influence of carbon modification onto the electric surface zeta potential was investigated. The zeta potential was positive (28 mV) for unmodified Vulcan and decreased to a very negative value for O-Vulcan (-56 mV) and increased again after ammonolysis until it reached 29 mV for N-Vulcan 800°C (Figure 5.2c). Herein, a negative surface potential can be related to the presence of partially negatively charged O-groups on the surface, whereas the reduction of the oxygenated surface groups into N-containing functionalities reflects a positive surface potential. Accordingly, the observed variations in zeta potential confirm a successful surface modification instead of bulk heteroatom incorporation. However, we do not expect any drastic changes in conductivity upon carbon modification as shown in an earlier work by Arrigo *et al.* on aminated CNFs.[85]

## 5.3. Analysis on Carbon Surface Functionalization by XPS

To gain a deeper understanding of the chemical nature of the carbon functionalization, XPS analysis of the aminated carbon support materials was performed. Four major N-functionalities at distinct binding energies (BE) were identified by peak fitting and deconvolution (Figure 5.3a and Table 5.1).

**Table 5.1** Assignment of binding energy (BE) for different N-functionalities from individual deconvolution of the N 1s XP spectra.

| N-Species | BE / eV |
|---|---|
| Graphitic | 402.8-402.9 |
| Quaternary | 401.2-401.4 |
| Pyrrolic | 400.0-400.3 |
| Pyridinic | 398.3-398.7 |

Graphitic N-functionalities were assigned to core level peaks around 402.8-402.9 eV, while quaternary N functionalities, such as nitrogen atoms that substitute in-plane C atoms and carry a partially positive charge or else substitute edge C atoms in six-membered rings and are protonated, were assigned to a BE of 401.2-401.4 eV (see chemical structures in Figure 5.3b). Peaks at 400.0-400.3 eV were lumped and assigned to surface species containing all possible kinds of N-H bond motifs in five-membered rings, most prominently in pyrrolic N, where the N contributes with two p-electrons to the $\pi$-system, but can also be ascribed to imides or lactams. Pyridinic N, in which the N atom contributes with one p-electron to the $\pi$-system of a six membered ring, are ascribed to peaks in the BE region of 398.3-398.7 eV, see also Table 5.1.[84-86,95] Figure 5.3a displays the N 1s spectra of the stepwise modified carbon materials, including the individual peak deconvolutions for different types of N-moieties.

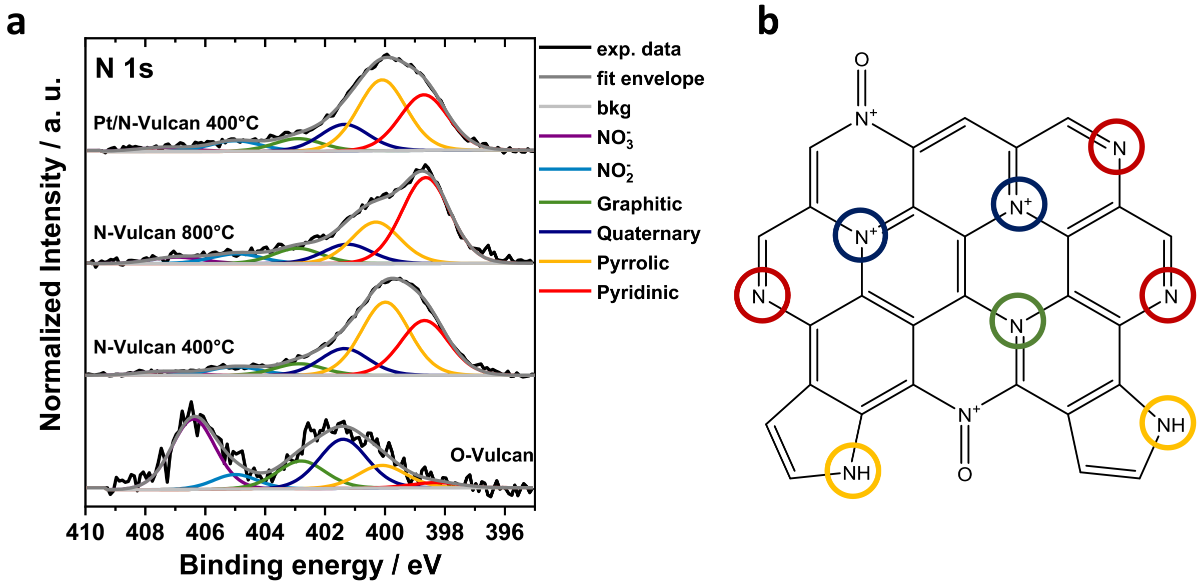

**Figure 5.3** (a) XPS N 1s spectra and individual peak deconvolution for modified carbons and Pt/N-Vulcan 400°C and (b) schematic illustrastion of different N-functionalities (green: graphitic N, blue: quaternary N, yellow: pyrrolic N and red: pyridinic N) in graphene-like plane.

N-Vulcan 400°C shows the highest fraction of pyrrolic-type functionalities with around 40 %, while for N-Vulcan 800°C pyridinic-type N-groups were most abundant species with 47 % (Figure 5.4). The fraction of quaternary N decreased slightly with increased amination temperature from ca. 15 % to 11 %, while the amount of graphitic N increased slightly from 6 % to 9 %. The total amount of surface nitrogen was highest for the N-Vulcan 400°C with around 3.9 at% and decreases to 2.3 at% for the samples aminated at 800°C. This could be explained by a temperature-dependent stability of N functionalities as well as by a lower local ammonia partial pressure in the synthesis reactor, due to the dynamic nitrogen, hydrogen, and ammonia equlibrium. Thus, pyridinic N was most stable at higher ammonolysis temperatures in agreement with earlier ammonolysis studies[84-86] and is genereally assumed to originate from the decomposition of pyrrolic N by the release of HCN.[86]

A small amount of surface N was also found in O-Vulcan (0.7 at%) that is mostly ascribed to residual nitrite/nitrate groups ($NO_2^-$/$NO_3^-$) from inclomplete removal of nitric acid. Additionally, N-moieties at lower BE around 400-402 eV are present in O-Vulcan. The occurrence of these N-functionalities in oxidized carbons is often observed in literature[160-162] yet their origin is somewhat unclear. However, it is mostly believed to be formed by the reduction of the nitric groups through the X-ray beam during the XPS measurement.[85] The nitrite/nitrate residues are not removed upon amination as they are also seen in the deconvolution for the N-Vulcans but only contribute to the total N amount in a small extent.

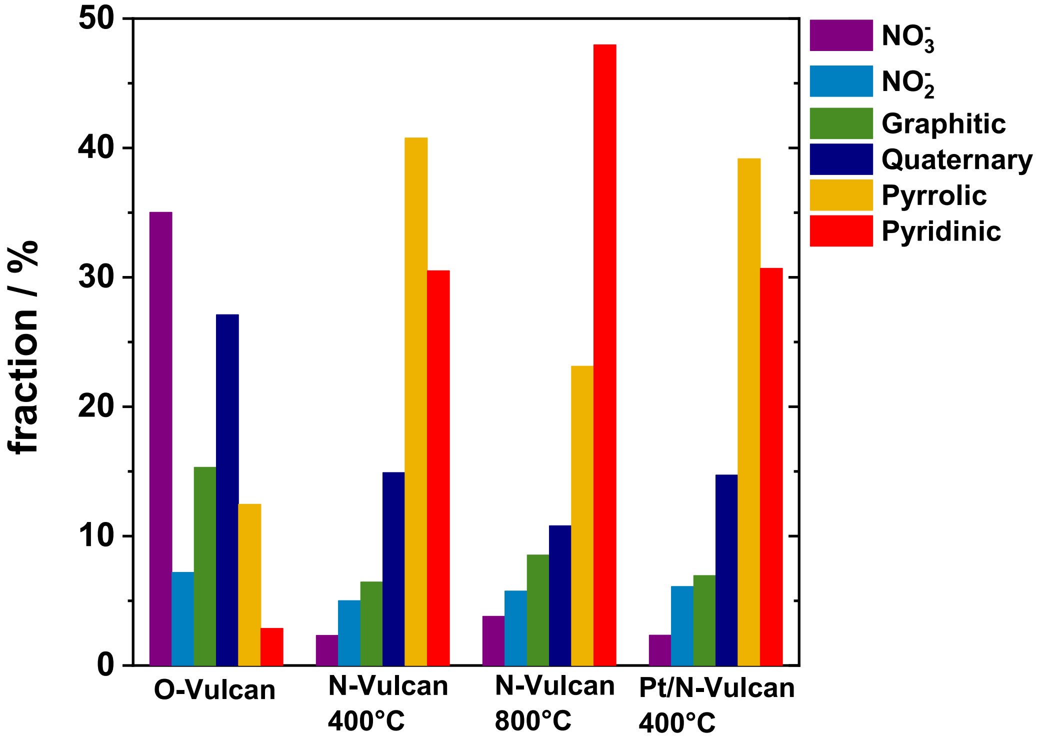

**Figure 5.4** Fractions of the different N-moieties from deconvolution of the N 1s spectra in the modified carbons and in Pt/N-Vulcan 400°C.

Deconvolution of the C 1s spectra (Figure A8) reveals a high majority of C-C/C-H species for both unmodified and modified carbons. The amount of O-containing C-species changes due to the different amounts of O found in the carbon surface (Table A4). Highest O-content on the surface as determined by XPS is found for O-Vulcan with around 13 at%, which decreases with increasing ammonolysis temperature to ca. 7 at% for N-Vulcan 800°C as similarly observed from elemental analysis. Generally, a higher total fraction of N and O found by XPS analysis points to the high degree of surface instead of bulk carbon modification.

## 5.4. Corrosion Behaviour by HT-DEMS

The carbon corrosion was quantitatively investigated by HT-DEMS performed at 140°C for the unmodified and the N-modified carbon supports (Figure 5.5). The electrochemical current (j) normalized to the initial mass of carbon, as depicted in Figure 5.5a, showed a similar trajectory for unmodified and modified carbons up to 0.9 V. Past this potential, however, the unmodified Vulcan displayed a sharp increase in corrosion current accompanied with a comparable strong increase in mass ion current with m/z=44 for $CO_2$ indicating carbon corrosion (Figure 5.5b).

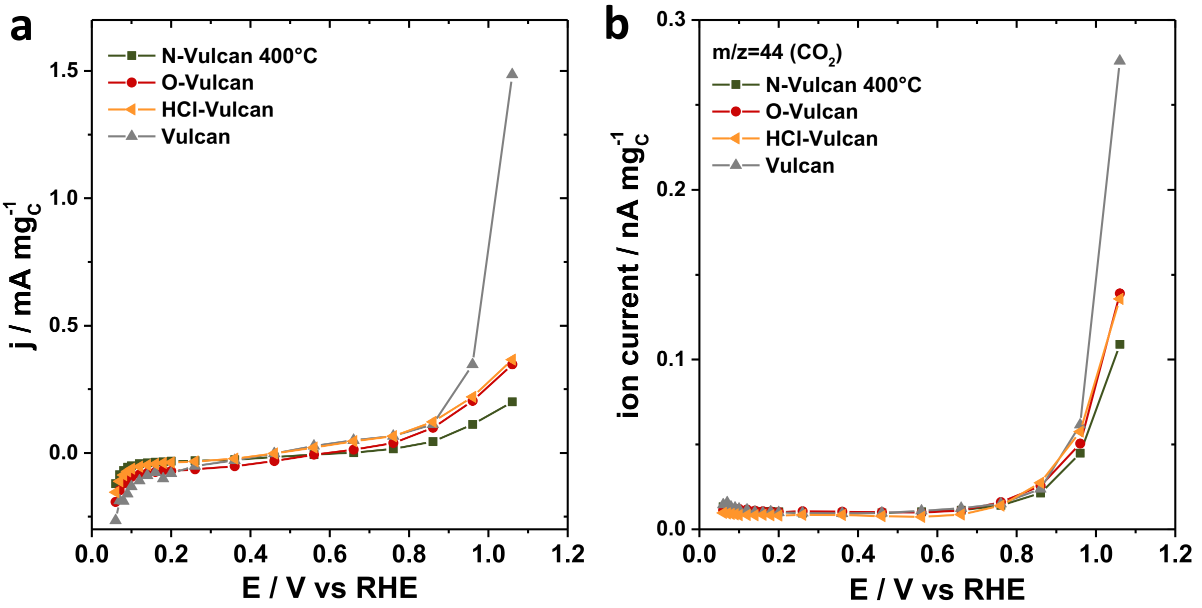

**Figure 5.5** High Temperature-DEMS measurements from 0.06-1.05 V at 140 °C for modified carbons and the Vulcan reference carbon with respect to the resulting current j normalized to mass loading of carbon (a) and the ion current for $CO_2$ (m/z = 44) from the MS normalized to mass loading of carbon (b). HCl-Vulcan represents a HCl-treated Vulcan (1M HCl, RT, 24h) in order to remove metal traces from the unmodified Vulcan.

The lowest currents and tendency towards carbon corrosion were observed for N-Vulcan 400°C, for which also no NO-species (m/z=30) could be detected. This suggests that the high degree of surface functionalization is beneficial for a superior carbon stability. O-Vulcan shows slightly higher currents and corrosion rates than the aminated carbon, but still features a much higher stability than the unmodified carbon. When Vulcan carbon was pretreated with diluted hydrochloric acid (HCl-Vulcan), it showed comparable currents and corrosion to O-Vulcan. This indicates that residual metal traces in the unmodified Vulcan, which are removed upon HCl-treatment, might catalyze carbon corrosion. On the other hand, it confirms that the presence of relatively high concentrations of O for O-Vulcan (as seen from elemental analysis and XPS) on the surface does not necessarily favor carbon corrosion and, most importantly, that the N-functionalization prevents the carbon from corrosion.

## 5.5. Pt Deposition and ORR Stability

In a next step, Pt was deposited on the unmodified and modified carbon supports. Therefore, a wet impregnation/reduction approach was applied resulting in a Pt mass loading of around 20 weight (wt)% for all samples (see Table A5). The reduction of the Pt precursor was performed thermally in a tube furnace at 200 °C leading to crystalline particles with X-ray diffraction patterns that could be clearly attributed to fcc Pt (Figure 5.6). All samples consist of very small Pt particles and larger agglomerates, as seen from the TEM images (Figure 5.7a and Figure A9). Here, the degree of agglomeration is linked to the BET surface area, as for the Pt/Vulcan with the highest BET surface area the Pt nanoparticles seem to be distributed most homogeneously.

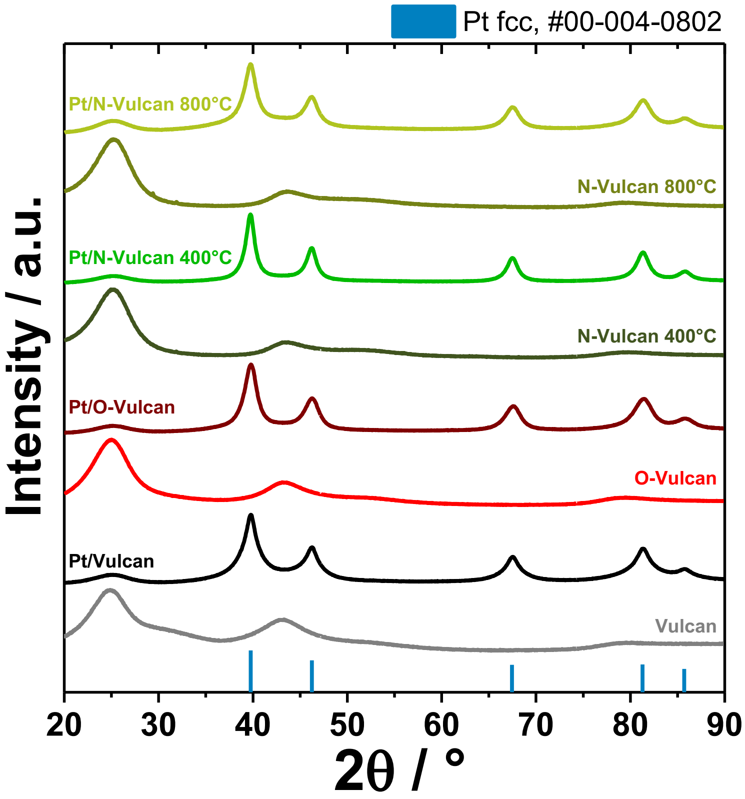

**Figure 5.6** X-ray powder diffraction patterns of the modified and unmodified carbon supports and the respective Pt electrocatalysts. Vertical blue lines represent the reference pattern for fcc Pt (PDF#00-004-0802).

The samples were tested as powder electrocatalysts for the oxygen reduction reaction (ORR) during prolonged cycling tests in order to evaluate their long-term performance stability. To this end, accelerated stress tests (AST) were performed including 5k, 10k and 30k cycles between 0.6-0.95 V. The resulting mass activity values at 0.9 V ($j_{mass}$), the electrochemical active surface area (ECSA) and specific activity ($j_{spec}$) values are all shown in Figure 5.8. All samples showed comparable mass activities of around 0.2 A $mg_{Pt}^{-1}$, while the values for the

ECSA range between 50-70 $m^2\ g_{Pt}^{-1}$. Here, the highest ECSA is observed for the unmodified Pt/Vulcan, while the lowest for the oxidized Pt/O-Vulcan. We note that there is a direct correlation between the hydrogen underpotential deposition ($H_{upd}$) -derived catalytically active Pt surface area (ECSA) and the nitrogen sorption-derived BET surface area of the carbon support. The larger BET surface area of the unmodified carbon (cf. Figure 5.2b) favors a higher particle dispersion and is thus conducive for a larger value of the ECSA. The ratio between the Pt mass normalized catalytic ORR activity and the ECSA value is the specific ORR activity and represent the reactivity of the catalyst normalized to the real surface area of the Pt nanoparticles. The initial specific activity of Pt/N-Vulcan 400°C (Figure 5.7b) was consistently the largest with a high level of statistical confidence. This indicates a higher intrinsic catalytic ORR activity of these Pt particles, likely a compounded consequence of a slightly larger mean diameter of the Pt particles and possibly interactions between Pt particles and the modified N-C support.

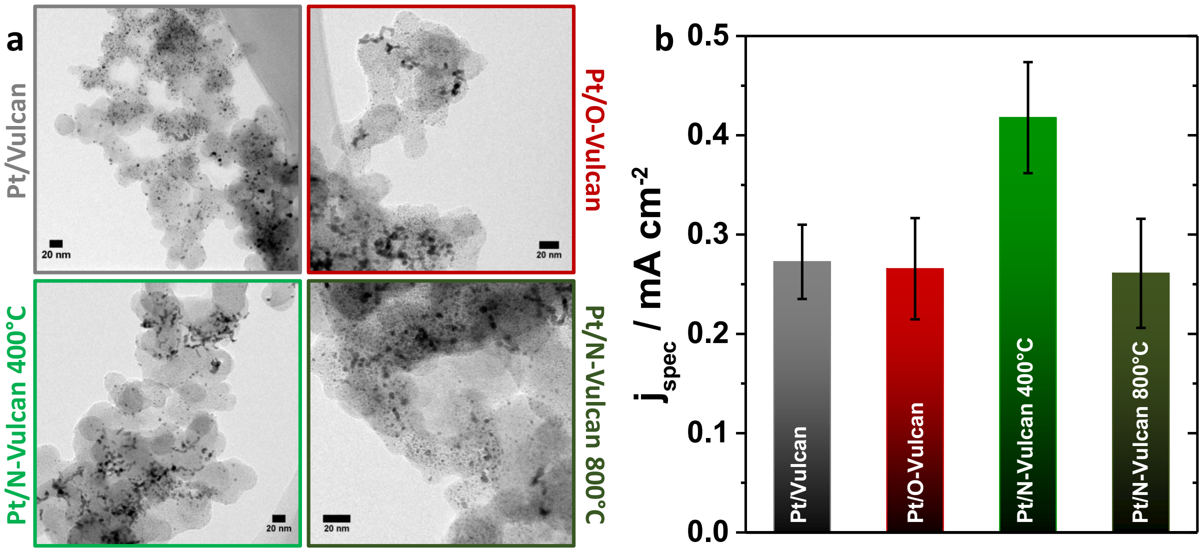

**Figure 5.7** TEM images (a) and ORR specific activity ($j_{spec}$) for the four catalysts (b) for Pt/Vulcan, Pt/O-Vulcan, Pt/N-Vulcan 400°C and Pt/N-Vulcan 800°C. See Figure A9 in the Appedix section A2 for more TEM overview images.

When tested for durability using an AST, Pt/N-Vulcan 400°C catalysts showed a remarkable stability with an exceptionally small loss of only around 10% in $j_{mass}$, whereas Pt/Vulcan lost more than 30% of its mass activity after 30k cycles under identical conditions (see Figure 5.8a,g). Both Pt/O-Vulcan and Pt/N-Vulcan 800°C showed lower stability, in particular ca. 40% losses in $j_{mass}$. While a large number of ORR stability studies of carbon-supported Pt catalysts in comparable potential windows were reported in literature to date[34,43,92,163-170], there is only one study that actually reported stability data up to 30k cycles and that study reported losses in mass activity of 60%.[170] Hence, to the best of our knowledge, the cycling stability presented here for Pt/N-Vulcan 400°C is very high on a Pt mass activity basis of a supported Pt/C catalyst in a fuel cell relevant potential range.

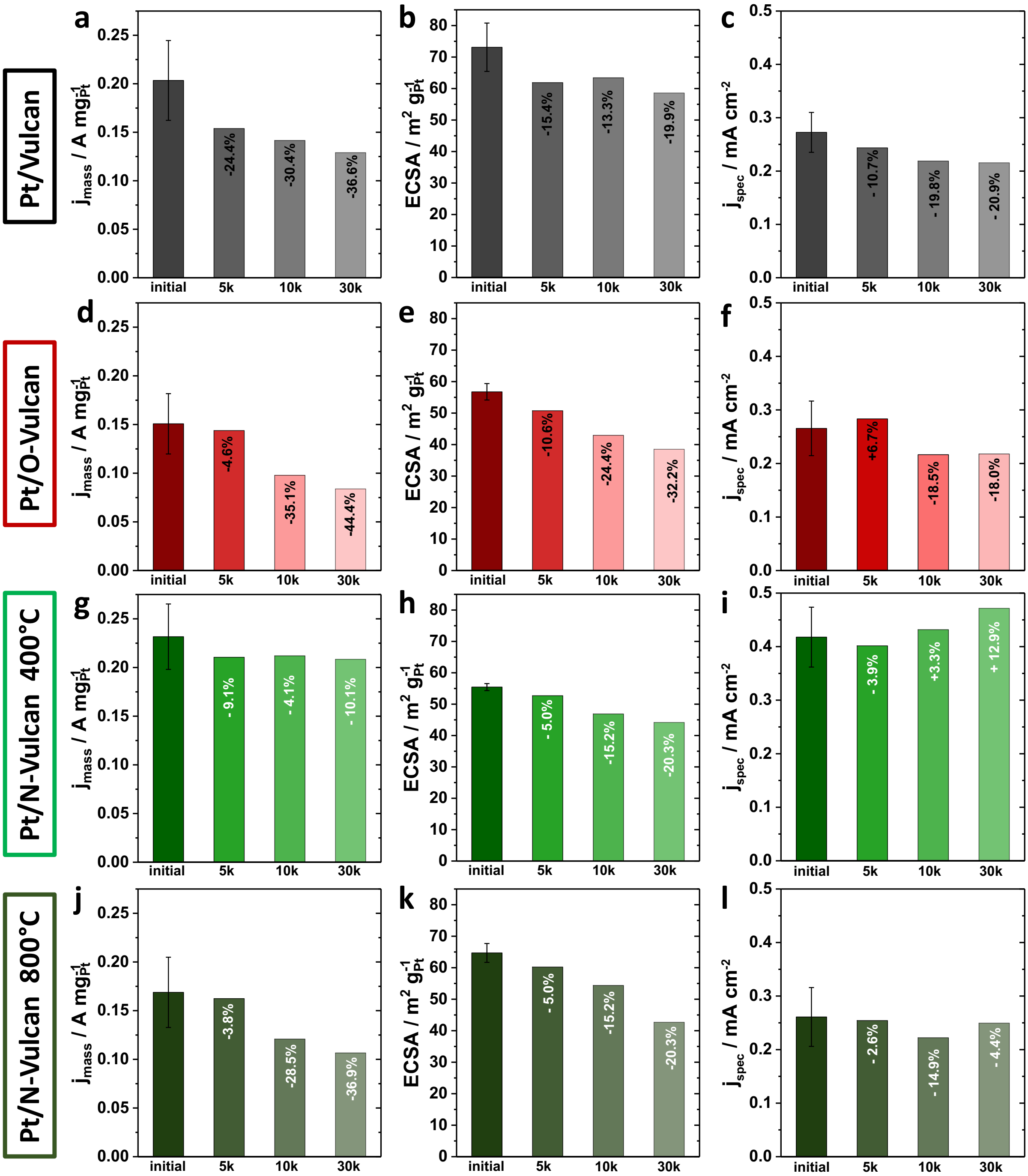

**Figure 5.8** Results from AST for 5k, 10k and 30k cycles from 0.6-0.95 V in Nitrogen-saturated 0.1 M $HClO_4$ for Pt/Vulcan, Pt/O-Vulcan, Pt/N-Vulcan 400°C and Pt/N-Vulcan 800°C as a function of mass activity at 0.9 V $j_{mass}$(a,d,g,j), ECSA (b,e,h,k) and specific activity $j_{spec}$ (c,f,i,l).

Considering the time changes of the real active electrochemical surface area (ECSA), comparable drops of 20-30% for all four catalysts were observed (see Figure 5.8b,e,h,k). As a result of this, trends in the specific, Pt surface area-normalized activity followed those of the Pt mass-based ORR activities: Those of Pt/Vulcan and Pt/O-Vulcan decreased by around 20%, that of Pt/N-Vulcan 800°C decreased by 4%, while that of Pt/N-Vulcan 400°C actually showed an increase of around 13% (Figure 5.8c,f,i,l). So we can conclude that support modifications have a significant influence on the long-term electrochemical stability of the catalyst/support couples, but do not directly cause an improvement of initial catalytic ORR activity. Amination at an intermediate temperature resulted in the optimal overall electrochemical performance stability.

In order to track the morphological and structural stability of the catalytically active Pt nanoparticles in more detail, *in situ* high energy X-ray diffraction (HE-XRD) and small angle X-ray scattering (SAXS) experiments during stability cycling were conducted. The diffraction patterns for all four samples at selected stages of the stability test are presented in Figure A10. Direct comparison between Pt/Vulcan and Pt/N-Vulcan 400°C is shwon in Figure 5.9.

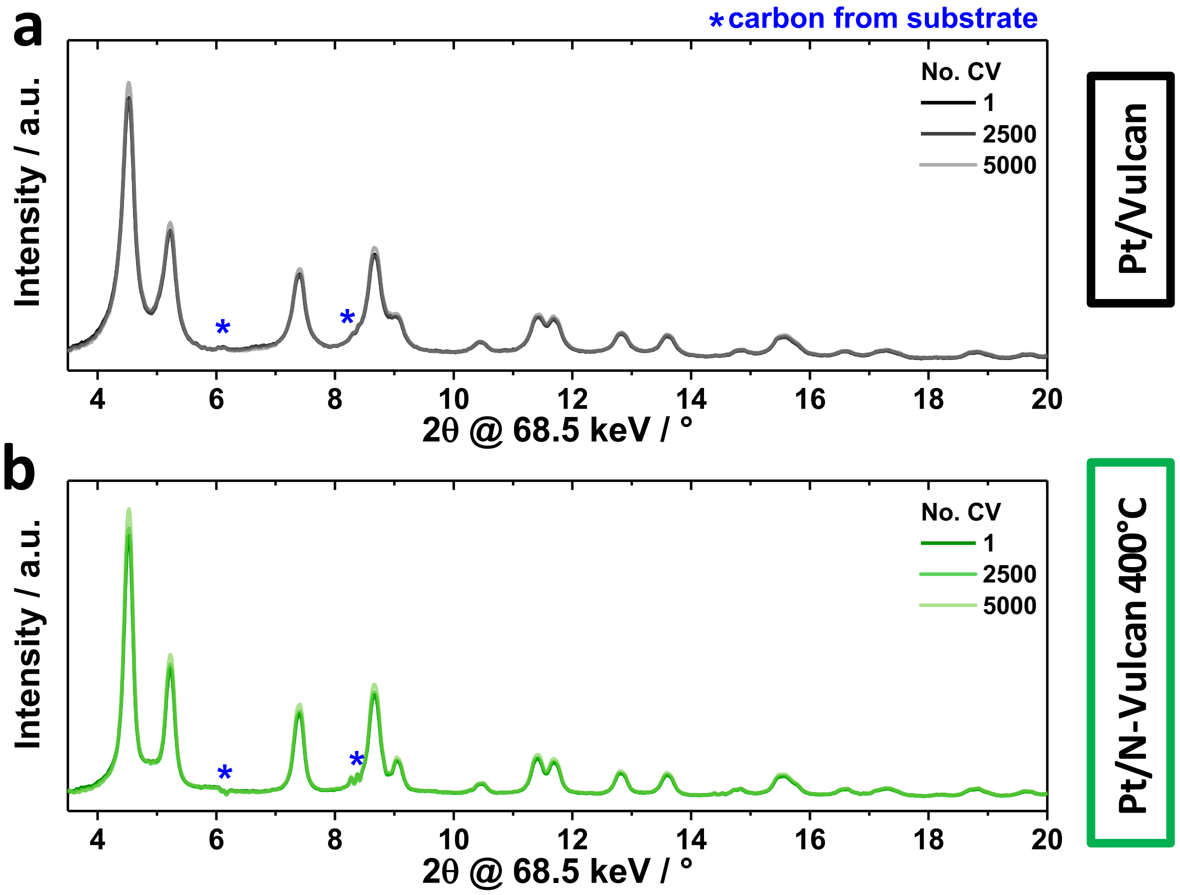

**Figure 5.9** *In situ* high energy X-ray diffraction patterns over 5k cycle of the AST for Pt/Vulcan (a), and Pt/N-Vulcan 400°C (b). A full set of *in situ* HE-XRD patterns for all samples can be found in the Appendix section A2, Figure A10.

During the stability test, the diffraction patterns did not significantly change, which is reflected in a large stable crystallite size obtained from Rietveld refinement (see Figure A11). The crystallite sizes for the different catalysts ranged from 3.7 nm for Pt/Vulcan to 4.8 nm for

Pt/N-Vulcan 400°C and showed negligible alterations or trends during the stress test. The direct comparison between the *in situ* Pt crystallite size trajectories of the 400°C-aminated Vulcan and the unmodified Vulcan support is presented in Figure 5.10. Interestingly, both the electrochemically stable catalyst (Pt/N-Vulcan 400°C) and the electrochemically unstable catalyst (Pt/Vulcan) showed little to no changes in crystallite size. This excludes particle growth by Ostwald ripening as a major source of the observed ECSA and Pt mass activity losses. To account for the comparable ECSA loss of all catalysts, we hypothesize that well-ordered crystallites aggregate on their supports or get buried into the support bulk during the AST.

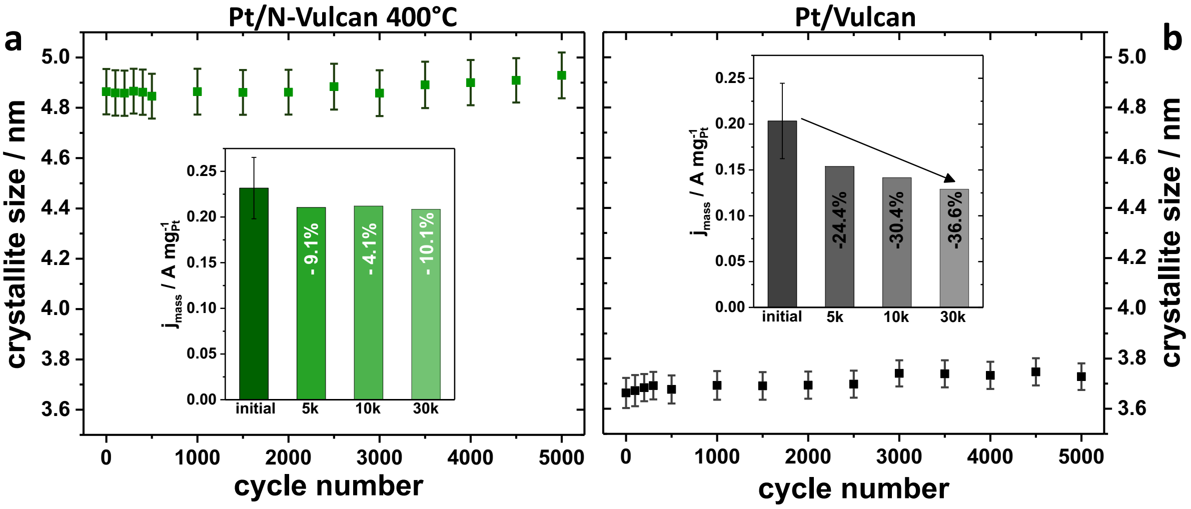

**Figure 5.10** Crystallite sizes obtained from Rietveld Refinement of the *in situ* HE-XRD patterns over 5k cycles of the AST for Pt/N-Vulcan 400°C (a) and Pt/Vulcan (b). Inlets in both graphs showing the mass activity up to 30k cycles between 0.6-0.95 V of the AST in nitrogen-saturated 0.1 M $HClO_4$. A full set evolution of crystallite size for all samples can be found in the Appendix section A2, Figure A11.

Similar observations can be made from the *in situ* SAXS results. Here, no major changes were observed in the scattering profiles for all four samples (Figure 5.11 and Figure A12), coupled to negligible changes in the mean particle diameter, as derived from the individual scattering curves (Figure 5.11 and Figure A13). The initial particle sizes ranged from 2.8 nm for Pt/Vulcan to 3.6 nm for Pt/O-Vulcan and Pt/N-Vulcan 400°C. Only minor changes were observed during the AST, for Pt/Vulcan and O-Vulcan the mean particle size decreased by around 0.2 nm, while a small increase by less than 0.2 nm after 5k cycles was observed for Pt/N-Vulcan 400°C, see Figure 5.11d. We note that the observed variations were close to the experiemental error. Due to the inhomogeneity in Pt particle distribution and size in all four samples, crystallite sizes from Rietveld refinement and particle sizes from SAXS are not in good agreement to each other. This is mainly due to the fact that SAXS fitting requires assumptions with respect to the particle size distribution owing to the relative “feature-less” scattering curves for all four samples (Figure A12).

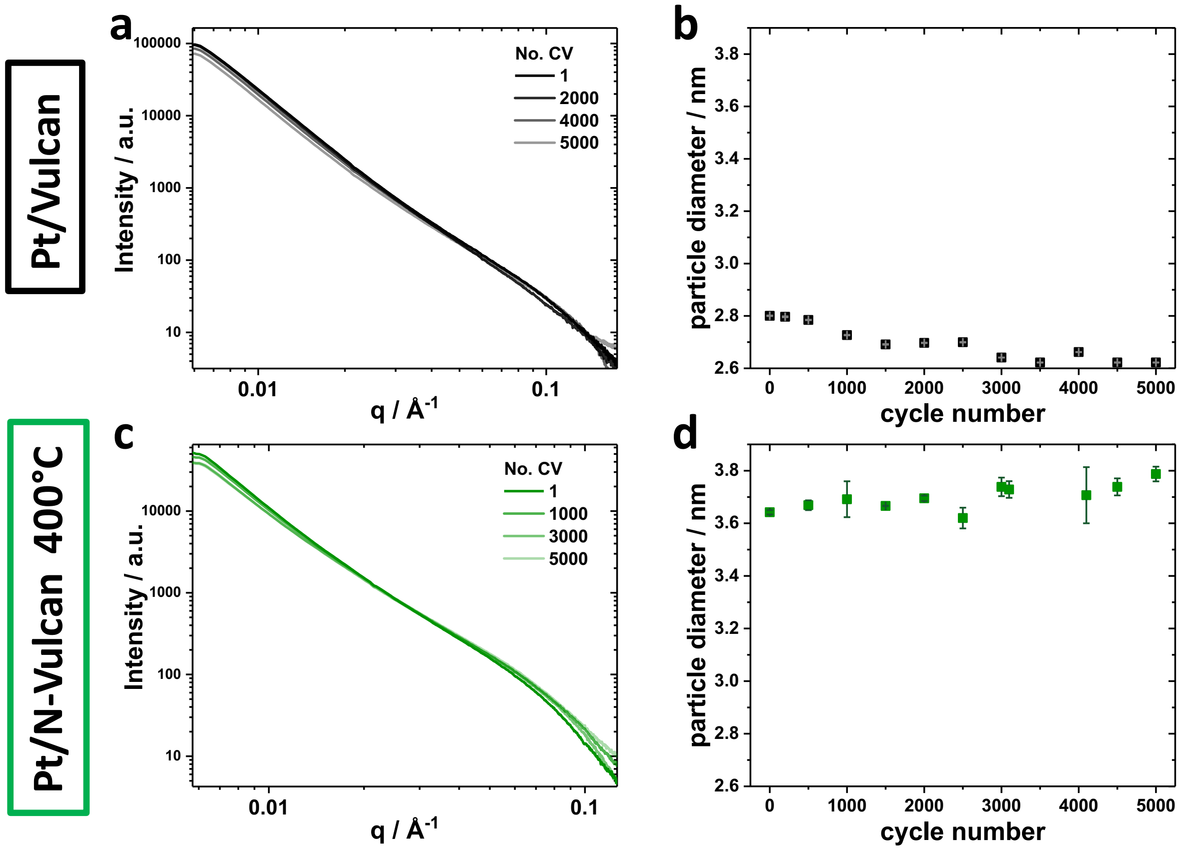

**Figure 5.11** *In situ* small angle X-ray scattering curves and mean particle diameter from SAXS fitting over 5k cycle of the AST for Pt/Vulcan (a,b) and Pt/N-Vulcan 400°C (c,d). A full set of *in situ* SAXS curves and evolution of mean particle diameters for all samples can be found in the Appendix section A2, Figure A12 and Figure A13.

The fact that there was no significant variation in the morphological stability of the Pt nanoparticles among the catalysts suggests that the carbon supports were solely responsible for the pronounced differences in long-term cycling stability (insets in Figure 5.10). While Pt/N-Vulcan 400°C showed superior stability, Pt/Vulcan and Pt/O-Vulcan but also Pt/N-Vulcan 800°C degrade with activity losses up to 44 % (Figure 5.8).

To discuss the implications of our observations in terms of prevailing degradation mechanisms we note that Pt/C catalyst degradation during potential cycling has been known to proceed via a number of different pathways. Pt dissolution is most likely linked to Pt oxidation but starts above 1.0 V[29,32,38,99,104] and can therefore be excluded as a major contributor to the present activity and ECSA losses. Agglomeration, detachment and Ostwald ripening[39] are more likely to cause degradation in the fuel cell lifetime regime below 1 V.[26,32,51] In particular, agglomoration of crystallites could account for the observed ECSA losses for all samples. However, it would not account for the stark differences in the retention of the Pt mass activity, with Pt/N-Vulcan 400°C displaying 90% retention. Therefore, other processes must contribute to this exceptional catalyst stability.

From HT-DEMS experiments, we found that the nitrogen functionalized N-Vulcan 400°C showed the lowest carbon corrosion rates due to the highest chemical stability of the nitrogen-doped carbon lattice. Considering that carbon corrosion is linked to particle migration, diffusion, and detachment it appears only reasonable that the Pt/N-Vulcan 400°C showed the highest electrochemical cycling stability. Furthermore, the catalyzing effect of the Pt nanoparticles on the tendency towards carbon corrosion might be less pronounced in Pt/N-Vulcan 400°C as a similar phenomenon was observed by Wang *et al.*.[47]

In our XPS analysis, pyrrolic N functionalities were most prevalent on the surface of the stable N-Vulcan 400°C catalyst, and their abundance did not change noticeably upon Pt deposition (Figure 5.3a and Figure 5.4). Thus, the presence of surface pyrrolic N groups appears to have a statistically significant stabilizing effect on the chemical structure of the carbon support and, ultimately, on the electrochemical activity of supported Pt nanoparticles.

## 5.6. Conclusion and Summary

In this study, we prepared a family of nitrogen-functionalized carbon blacks and used them as supports for Pt nanoparticles and employed these catalyst/support couples as powder electrocatalysts for the catalytic electroreduction of molecular oxygen (ORR). Followed by oxidation of the carbon surface, ammonia treatment at elevated temperatures lead to the incorporation of atomic nitrogen into the chemical structure of the carbons. This was accompanied by a concomitant reduction in the oxygen amount and concomitant increase in the surface zeta potential. At modest ammonolysis temperatures of 400 °C, pyrrolic N moieties were the most abundant surface N species. The resistance of the pyrrolic N-modified carbons to carbon corrosion and $CO_2$ formation was greatly improved in comparison to all other carbon supports. Finally, in simulated fuel cell stability tests, platinized versions of the corrosion stable carbons, such as Pt/N-Vulcan 400°C, again showed superior performance stabilities during prolonged potential cycling, with only minor ORR activity losses of 10% compared to over 30% of reference catalysts. In contrast, pyridinic N moieties did not offer any beneficial stability effects. Cross checks of the time evolution of the Pt particle size, using *in situ* techniques during cycling, confirmed that differences in the stability of the active Pt particles can be excluded as the origin for the observed stability difference among the catalysts. The stability benefits are a direct consequences of the chemical behavior of the modified supports.

We conclude that the controlled introduction of chemical pyrrolic nitrogen into Vulcan carbons, generated at intermediate ammonolysis temperatures, should be a pathway to fuel cell catalysts with superior stability.

# 6. On the Anisotropy of Pt Nanoparticles on Carbon- and Oxide-Support and Their Structural Response to Electrochemical Oxidation

Identifying the structural response of nanoparticle-support ensembles to the reaction conditions are essential to determine their structure in the catalytically-active state as well as to unravel possible degradation pathways. In this work, we investigate the (electronic) structure of carbon- and oxide-supported Pt nanoparticles by *in situ* X-ray diffraction, absorption spectroscopy as well as the Pt dissolution rate by *in situ* mass spectrometry during electrochemical oxidation. We prepared ellipsoidal Pt nanoparticles by impregnation of carbon and titanium-based oxide support as well as spherical Pt nanoparticles which incorporate interstitial oxygen atoms on an indium-based oxide support by surfactant-assisted synthesis route. During electrochemical oxidation we show that the oxide-supported Pt nanoparticles resist surface oxide formation and Pt dissolution both phenomena independent of their morphology. The lattice of smaller Pt nanoparticles exhibits a size-induced lattice contraction in the as-prepared state but it expands reversibly during electrochemical oxidation. This expansion is suppressed for the O-containing Pt nanoparticles with bulk-like relaxed lattice. We could correlate the formation of d-band vacancies in the metallic Pt with the Pt lattice expansion whereas the formation of $PtO_x$ is accompanied by a loss in structural coherence length. The $PtO_x$ formation is strongest for platelet-like nanoparticles and we explain this with a higher fraction of exposed Pt(100) facets. Of all investigated nanoparticle-support ensembles, the structural response of $RuO_2/TiO_2$-supported Pt nanoparticles are most promising with respect to their morphological and structural integrity under electrochemical reaction conditions.

This chapter was prepared in collaboration with Arno Bergmann, Elisabeth Hornberger, Jakub Drnec, Guanxiong Wang, Stefanie Kühl, Daniel J.S. Sandbeck, Serhiy Cherevko, Vijay Ramani, Karl J.J. Mayrhofer and Peter Strasser

H.S. and A.B. performed the experiments and analyzed the data, E.H. and J.D. assited in the synchrotron experiments and data evaluation; G.W. and V.R. synthesized the support;  S.K. recorded TEM images; D.J.S.S., S.C. and K.J.J.M. produced and analyzed the SFC ICP-MS data; H.S., A.B. and P.S. wrote the manuscript; all authors assisted in discussing and writing the manuscript.

## 6.1. Introduction

In this work, we studied the structural response of Pt nanoparticles on different supports to the electrochemical oxidation using different *in situ* X-ray techniques. We tracked the Pt dissolution rate as well as their voltammetric profiles and monitored the crystallite properties and the electronic structure during oxidation. Therefore, we aim to understand the differences in electrochemical oxidation of Pt nanoparticles on different supports aiding the development of improved durability in Pt fuel cell cathode materials.

## 6.2. Structure and Morphology

In order to investigate the differences in electrochemical oxidation of Pt nanoparticles on various kinds of support, a commercial carbon supported Pt electrocatalyst was compared to two oxide-supported materials; an Indium Tin Oxide (ITO) and $RuO_2$-$TiO_2$ (RTO). Compositional analysis by ICP-OES revealed a Pt weight loading of 46.1 wt% for Pt/RTO, of 29.9 wt% for Pt/ITO and of 20 wt% for Pt/C (Table A6 in the Appendix section A3). Figure 6.1 shows the diffractograms and morphology by TEM of the three catalysts in the as-prepared state.

The diffractograms for Pt/RTO, Pt/ITO and Pt/C in Figure 6.1a show broad reflexes corresponding to fcc Pt phase. In the case of the ITO support, only one other phase additional to fcc Pt is present that can be clearly assigned to $In_2O_3$ (see also Figure A14 for more detailed information on XRD), meaning that Sn was incorporated into the Indiumoxide-lattice. In the case of the RTO support, three additional crystalline support phases can be identified: an anatase $TiO_2$ as well as a rutile-type $TiO_2$ and $RuO_2$ as depicted in Figure A14b. Rietveld refinement of the HE-XRD pattern in Figure A15 showed that the morphology of the nanoparticles depends on the different Pt synthesis routes.

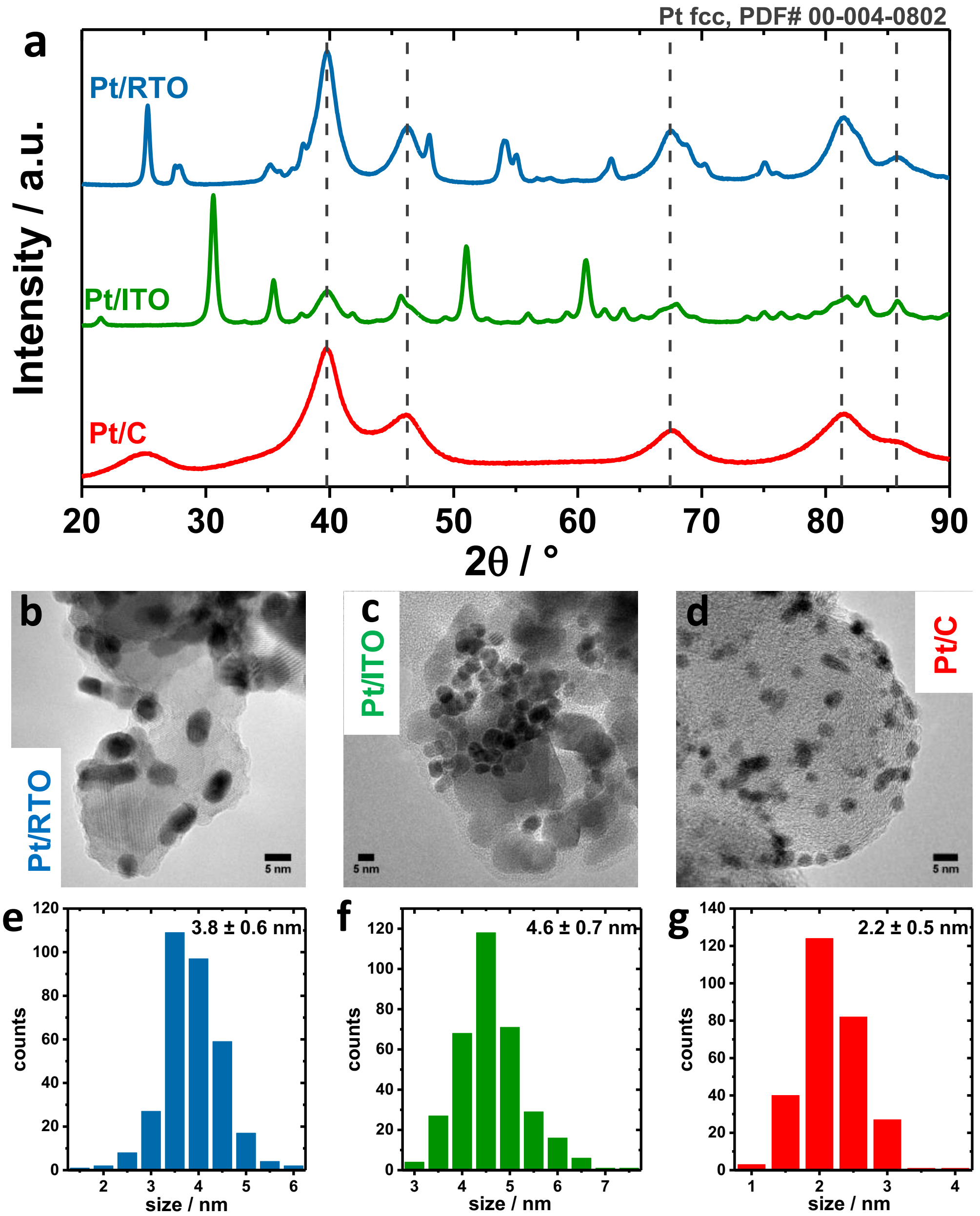

**Figure 6.1** Structure and morphology of Pt nanoparticles supported on RTO (blue), ITO (green) and carbon (red) as determined by powder X-ray diffraction pattern (a) and transmission electron microscopy images (b,c,d). The Pt particle sizes as depicted in the histograms in (e,f,g) were determined from analyzing > 200 Pt particles along their shortest principal axes.

Impregnation of support as applied for RTO and C support leads to more ellipsoidal and platelet-like nanoparticles, respectively, as shown by the crystallite diameters D that we extracted from the principal axes of the ellipsoids. For Pt/C, $D_x$ and $D_y$ are ~2.4 nm and $D_z$ is ~1.8 nm whereas for Pt/RTO $D_x$, $D_y$, and $D_z$ are ~3.3 nm, 4.5 nm and 2.4 nm, respectively (see also Table A7). The surfactant-assisted route yields in spherical Pt nanoparticles with a structural coherence length of ~4.0 nm on the ITO. The morphology of the catalysts is depicted in Figure 6.1b-d in TEM images. For all three supports, the Pt nanoparticles are homogenously distributed on the supports (see also Figure A16 for overview images).

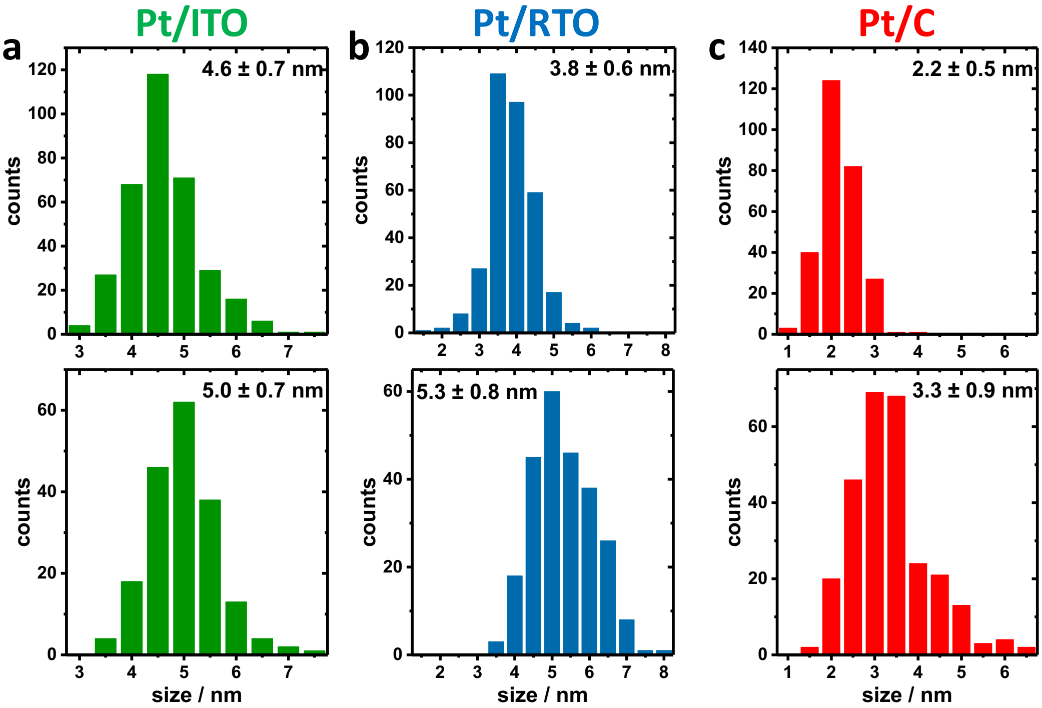

**Figure 6.2** Histograms of mean particle diameter for Pt supported on (a) ITO (green), (b) RTO (blue) and (c) carbon (red) support. Top row shows the average particle diameter measured along their shortest particle axis and bottom row along their longest particle axes.

By analyzing the Pt particle size along the shortest particle axes, ITO-supported nanoparticles exhibit the largest average size with 4.6±0.7 nm, RTO-supported nanoparticles 3.8±0.6 nm and carbon-supported nanoparticles the smallest size with 2.2±0.5 nm. To further quantify the anisotropy of the Pt nanoparticles, the TEM particle sizes were also determined along the longest particle axis. For Pt/RTO and Pt/C particle sizes estimated in this way are around 1.5 and 1.1 nm larger, proofing anisotropic ellipsoidal shape of these nanoparticles (see also Figure 6.2). In the case of Pt/ITO, the Rietveld refinement estimated spherical nanoparticles and the TEM nanoparticles size determined along the shortest and longest particle axes are 4.6±0.7 nm and 5.0±0.7 nm, respectively, and thus, in good agreement to each other. The anisotropy of the Pt nanoparticles suggested by Rietveld refinement was additionally investigated in a tilting study in TEM. Figure 6.3 shows a series of TEM micrographs for Pt/RTO and Pt/C recorded under tilting angles between 0 and 30°. The tilting of the sample plane with respect to the incident electron beam changes the apparent shape of individual Pt nanoparticles showing their ellipsoidal shape.

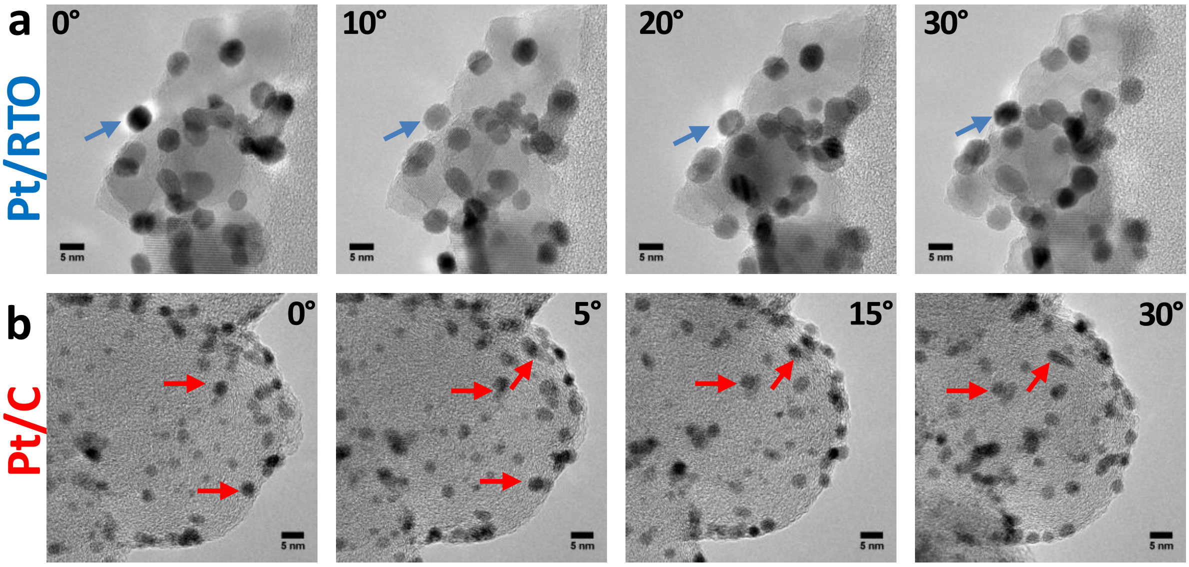

**Figure 6.3** Morphology of Pt nanoparticles on (a) RTO (blue) and (b) carbon (red) support in a TEM tilting study from 0-30°.

In addition to the morphology, we identified a correlation between structural coherence length and the crystal lattice of the Pt nanoparticles. The Pt lattice parameter $a_{Pt}$ as determined by Rietveld refinement (Table A8) decreases from the Pt/ITO with $a_{Pt}$=3.930 Å to Pt/RTO with $a_{Pt}$=3.920 Å to Pt/C with $a_{Pt}$=3.914 Å. The contraction of the Pt lattice is induced by decreasing structural coherence length.[171,172] We note that the lattice parameter of the nanoparticles can also be influenced by various adsorbates. Additionally, the most expanded Pt lattice exhibits interstitial oxygen on the tetrahedral sites ($O_{Td}$) in Pt lattice as Rietveld refinement revealed an occupancy of 0.15±0.02. In contrast, the occupancy of $O_{Td}$ for the Pt nanoparticles on RTO and C was zero within the fit error (see also Table A8). Furthermore, any kind of metal incorporation in the Pt nanoparticles from the oxide supports was not verifiable via Rietveld refinement.

Thus, we conclude that the impregnation route of RTO and C support lead to smaller ellipsoidal and platelet-like Pt nanoparticles exhibiting a contracted crystal lattice due to the smaller domain coherent size, whereas surfactant-assisted synthesis route leads to spherical Pt nanoparticles with a bulk-like Pt lattice wherein interstitial O are present on the tetrahedral sites.

## 6.3. Electrochemical Characterization

To identify differences in the electrochemical behavior towards Pt oxidation of the three catalysts, a series of cyclic voltammograms (CV) in 0.1 M $HClO_4$ were conducted. Figure 6.4a-c shows CVs from 0.05 V with a stepwise increasing upper potential limit from 0.5-1.4 V after an initial activation step for each catalyst of 100 CVs between 0.05 and 1.0 V. The typical Pt-$H_{upd}$ and Pt-O/OH features are clearly visible for all three materials between 0.05 and 0.4 V as well as above 0.6 V, respectively.

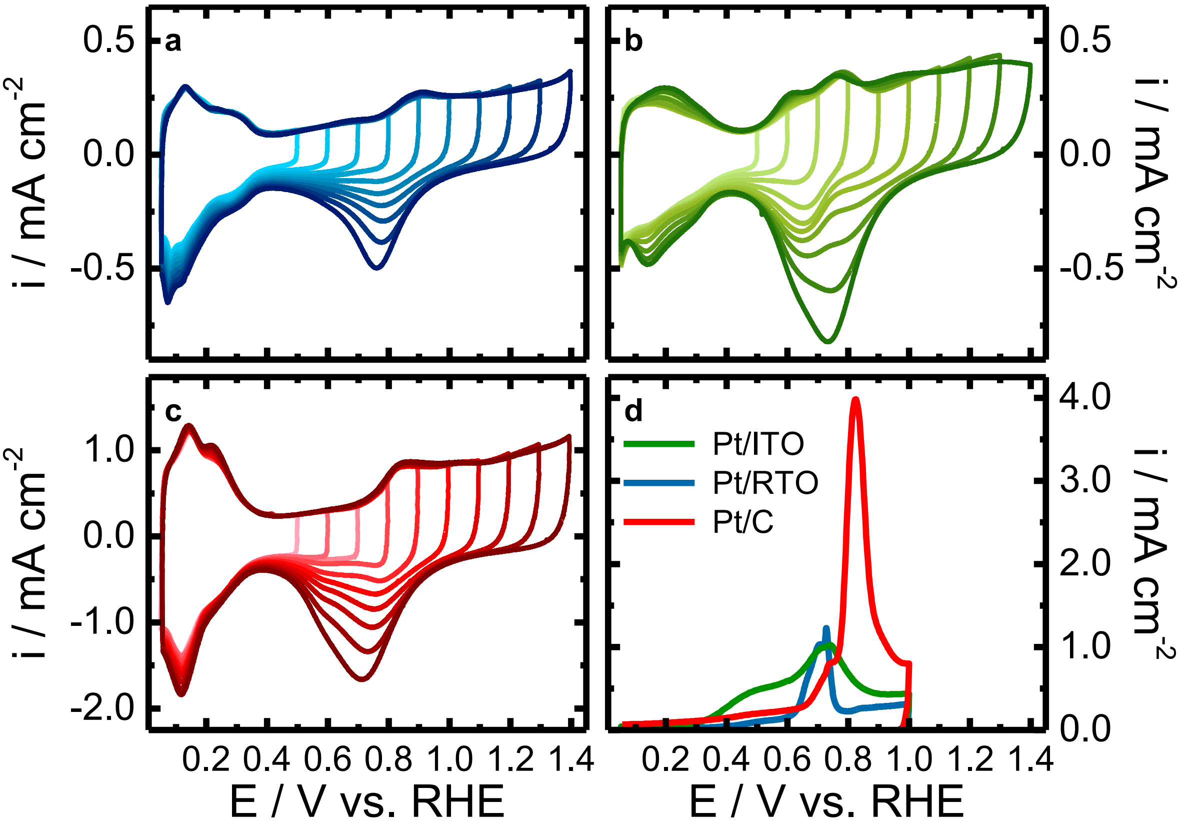

**Figure 6.4** Electrochemical characterization of Pt nanoparticles on RTO (blue), ITO (green) and carbon (red) support by the evolution of cyclic voltammogram with increasing upper potential limit in $N_2$-saturated 0.1 M $HClO_4$ from 0.5-1.4 V (a-c) and from CO stripping experiments (d).

By increasing the upper potential limit, the oxidative currents in the H-desorption region between 0.05-0.4 V stay rather stable compared to the H-adsorption region of the reductive scan. The H-desorption region of Pt/ITO shows the strongest growth with increasing upper potential limit. Additionally, Pt-Oxidation peak(s) arising from around 0.6 V are stable, while the corresponding reduction peak(s) steadily increase. These findings indicate an increasing degree of Pt surface oxidation/reduction with higher upper potential limit. The larger currents in the $H_{upd}$ region can be explained with an increasing roughening of the nanoparticle surface and with prolonged reduction of the Pt oxides under these dynamic conditions of the cyclic voltammograms.

Furthermore, the position of the Pt-O/OH reduction peak differs between the materials and shifts cathodically with the increasing potential limit for Pt/C, anodically for Pt/ITO and stays more or less constant for Pt/RTO. The reduction peak of Pt/C is convoluted by two individual reduction features and this binary character is less pronounced for Pt/RTO. The shape of the reduction peak does not strongly vary with increasing upper potential limit. The Pt-O/OH reduction peak of Pt/ITO consists of a single reduction at low upper potential limit but a binary shape developed with increasing upper potential limit similar to the reductive behavior determined for Pt on the other two supports. These support-dependent variations in peak positions indicate that not only the degree of Pt surface oxidation changes but also the surface of the Pt nanoparticles itself, especially on the ITO, where the CVs alter with increasing potential. Correlations could be drawn to a study by Chattot *et al.* where structural defects originating from microstrain resulted in different CO oxidation profiles and peak positions.[173]

To further characterize the Pt surface on the different supports, the electrochemical active surface area was determined from the $H_{upd}$-region and from CO stripping experiments. Figure 6.4d shows the CO oxidation profiles and the carbon-support catalyst shows largest oxidation peak corresponding to a high CO-ECSA of 67.5 $m^2\ g_{Pt}^{-1}$. For Pt/ITO the CO-stripping profile is rather broad and the overall current is lower resulting in an CO-ECSA of 25.6 $m^2\ g_{Pt}^{-1}$. CO electrooxidation on Pt/RTO caused a small and narrower peak at lower potentials compared to Pt/C and Pt/RTO exhibits with 16.7 $m^2\ g_{Pt}^{-1}$ the lowest CO-ECSA (see Table A9).

## 6.4. *In Situ* Electrochemical Pt Oxidation

### *In situ High Energy X-ray Diffraction*

To identify the structural response of the Pt nanoparticles on the different supports to electrochemical oxidation, *in situ* high-energy diffraction (HE-XRD) patterns were recorded during step-wise oxidation between 0.6-1.4 V and a reverse scan to 1.0 V to check the reversibility (see Figure 6.5). Again, all three catalysts were first electrochemically-activated by 100 CVs as described before.

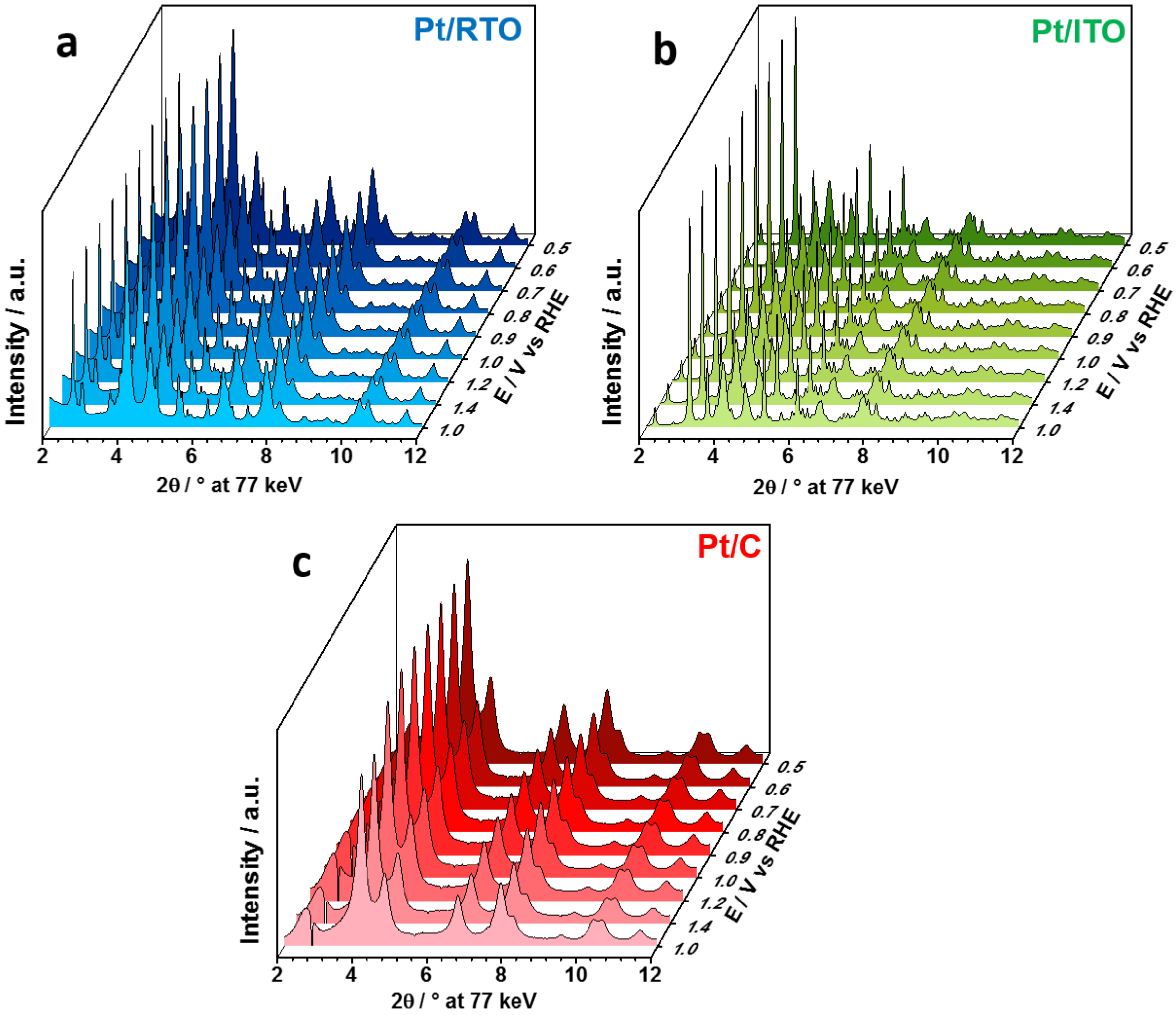

**Figure 6.5** *In situ* high-energy X-ray diffraction patterns of Pt nanoparticles supported on ITO (green, a), RTO (blue, b) and carbon (red, c) on stepwise electrochemical oxidation of Pt (potential hold for 10 min each).

Rietveld refinement of the HE-XRD patterns in Figure 6.5 allowed us to follow several structural parameters of the crystalline Pt nanoparticles. Figure 6.6 shows the changes of Pt lattice parameter $\Delta a_{Pt}$ as well as the Pt scale factor $k_{Pt}$ which is directly correlated to the volume of the crystalline Pt domains. The Pt lattice parameter $a_{Pt}$ as shown in Figure 6.6a increases almost linearly and reversibly with electrode potential above 0.9-1.0 V for the carbon- and

RTO-supported Pt as a response to the electrochemical Pt oxidation; The Pt lattice expands to a similar degree for Pt/RTO and Pt/C with $\Delta a_{Pt} \cong 0.3$ pm at 1.4 V. The lattice of the ITO-supported Pt nanoparticles expands significantly less strongly with $\Delta a_{Pt} \cong 0.07$ pm at 1.4 V.

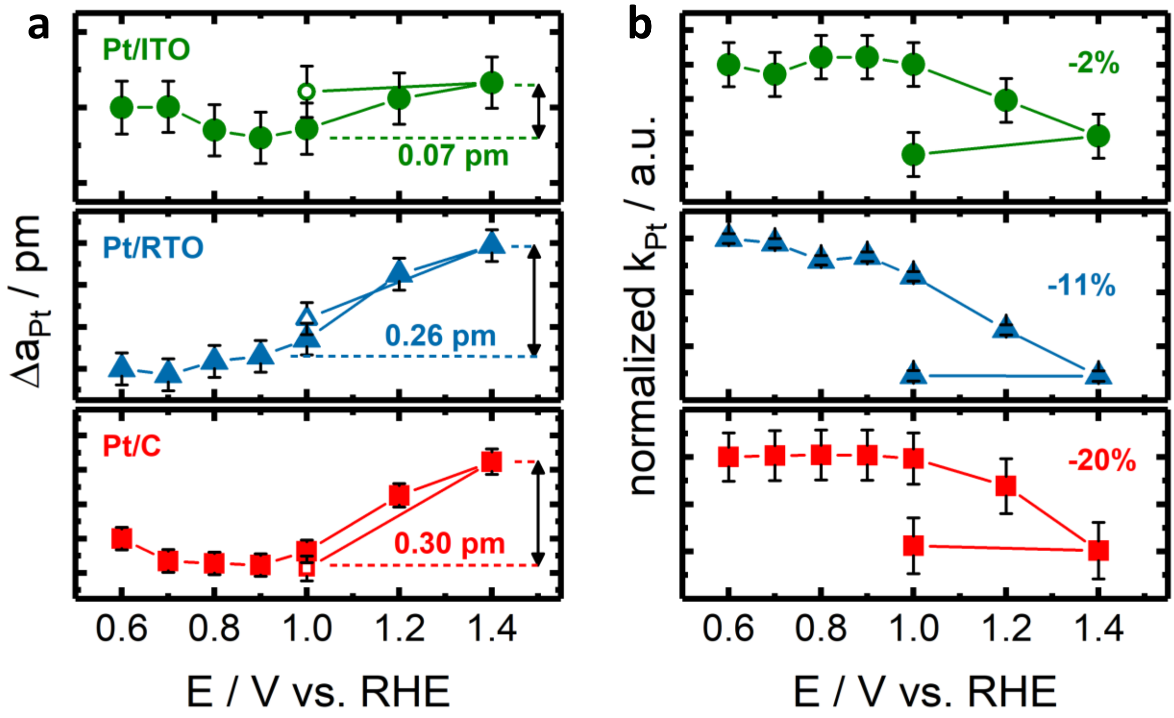

**Figure 6.6** Structural response of crystalline Pt nanoparticles supported on ITO (green circles), RTO (blue triangles) and carbon (red squares) on stepwise electrochemical oxidation (potential hold for 10 min each; reducing step to 1.0 V represented by open symbols) with respect to the change of Pt lattice parameter (a), normalized change of the Pt scale factor (b) as determined by Rietveld refinement of *in situ* high-energy X-ray diffraction pattern. The solid lines are shown to guide the eyes of the reader.

The scale factor $k_{Pt}$ as extracted from Rietveld refinement is directly correlated to the absolute Pt metal diffraction intensity and can thus be treated as a measure of absolute amount of metallic Pt probed by the X-ray beam. Figure 6.6b shows the evolution of the normalized change in Pt scale factor which decreased irreversibly above 1.0 V for all three catalysts. The normalized changes follow the initial TEM particle size as the largest and ITO-supported nanoparticles showed the least decrease in metallic Pt volume whereas the carbon-supported particles the highest decrease.

In addition, we also tracked the evolution of the coherence length of the metallic Pt domains. Despite the considerable fit error for the coherence length of the oxide-supported Pt particles, we identified an irreversible decrease of the coherence length of the carbon-supported Pt particles above 1.0 V as shown in Figure 6.7.

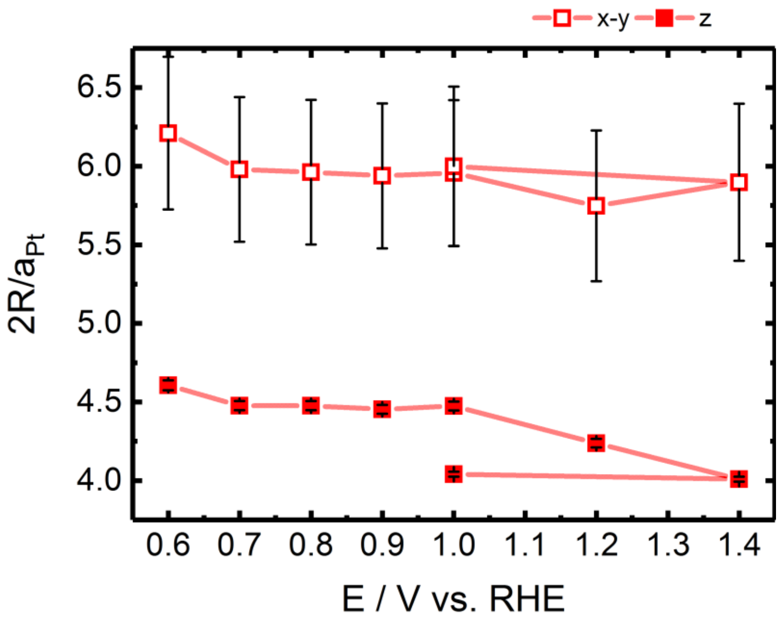

**Figure 6.7** Evolution of the number of unit cells ($2R/a_{Pt}$) of the metallic Pt domains for Pt/C along the x,y and z-axes. The solid lines are shown to guide the eyes of the reader.

Along the shortest axis of the platelet-like Pt particles (z-axis), the mean coherence length decreased irreversibly by half a unit cell ($2R/a_{Pt}$) which corresponds to a structural change of the first layer of Pt atoms on the (100) surface. The mean coherence length, perpendicular to the shortest axis (x- and y-axis), shows no significant changes beyond the error of the fit with a mean length of six unit cells, see Figure 6.7. This finding indicates an anisotropic structural response of the Pt particles to the electrochemical oxidation. Furthermore, for all three catalysts, no variation with electrode potential for the occupancy with interstitial O on the tetrahedral sites was identified.

Thus, the oxidizing electrochemical conditions induce a structural response of the metallic Pt domains of the nanoparticles with respect to their Pt lattice and to the volume of the metallic Pt domains. The structural transformation of the Pt nanoparticles starts at ~0.9-1.0 V and is irreversible between 1.0 and 1.4 V as primarily shown by the evolution of the scale factor of the metallic Pt domains. The decrease in the metallic Pt volume follows the initial Pt coherent domain size independent of the type of support material. This change in Pt coherent domain size is induced by the formation of a structurally-different $PtO_x$ (shell).

In addition, the electrochemically-oxidizing conditions cause a reversible lattice expansion of the metallic bulk of Pt nanoparticles on the different supports. This phenomenon contrasts the correlation between Pt coherent domain size and lattice parameter because the formation of an oxide shell on the smaller metallic Pt core should let the Pt lattice contract due to a particle size effect.

### *In situ X-ray Absorption Spectroscopy*

In a next step, we recorded *in situ* X-ray absorption spectra on the Pt $L_3$-edge at selected electrode potentials to study the influence of the electrode potential and electrochemical oxidation on the (electronic) structure of the Pt nanoparticles and obtain complementary information. Figure 6.8 shows the normalized Pt $L_3$-edge absorption spectra for Pt on the three supports in potentials steps between 0.6 and 1.4 V.

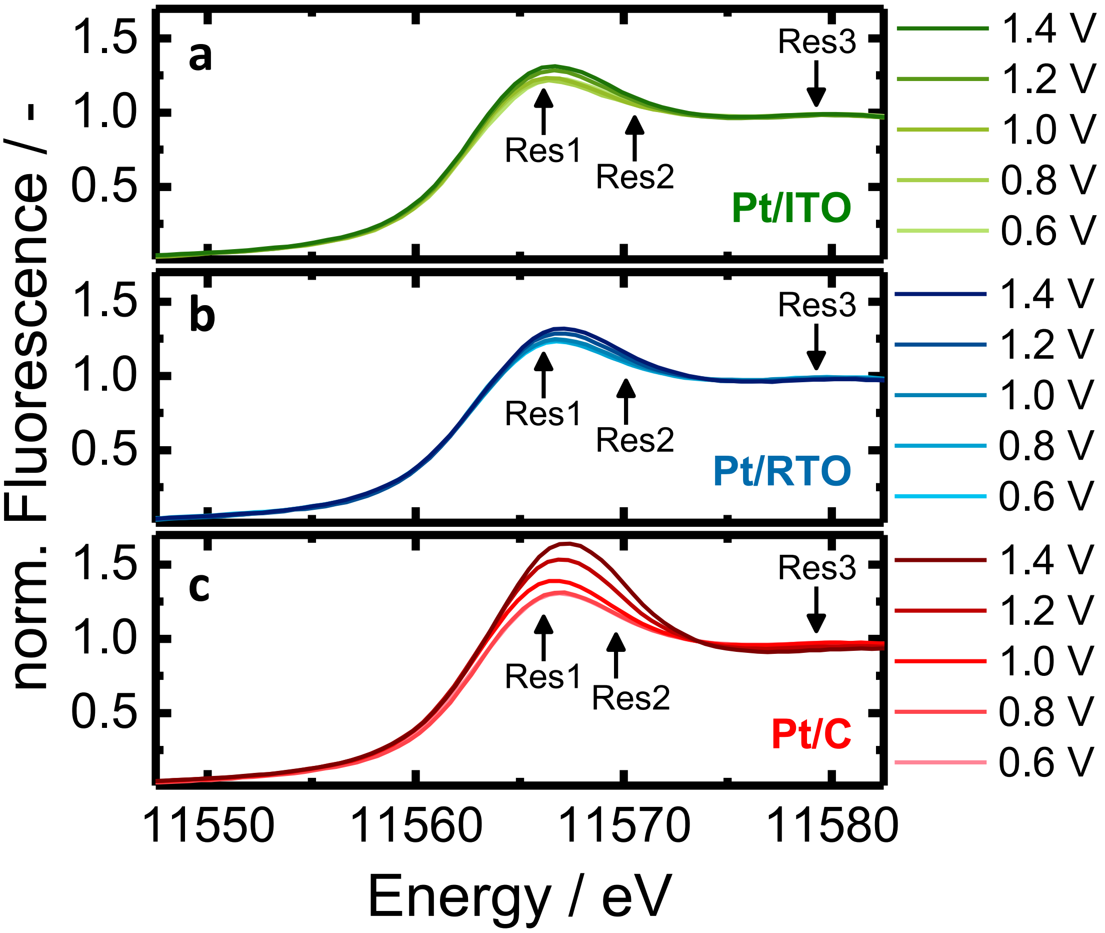

**Figure 6.8** Normalized *in situ* Pt $L_3$–edge X-ray near-edge absorption spectra for Pt nanoparticles supported on ITO (green, a), RTO (blue, b) and carbon (red, c) for potentials from 0.6 - 1.4 V of electrochemical oxidation of Pt. The positions of the Pt $L_3$ resonances applied in the fit procedure are denoted.

The so-called white line (WL) between ~11564 and 11572 eV originates from $2p_{3/2}$ to 5d orbital transitions and thus, its spectral weight is proportional to the total density of unoccupied 5d states (d-band vacancies) in the Pt atoms. A higher WL area therefore indicates a higher density of d-band vacancies associated with oxidized Pt. Figure 6.9a shows the integrated WL area for Pt particle supported on ITO, RTO, and carbon. The WL area of all three catalysts increases almost linearly with an onset potential between 0.8 and 1.0 V indicating electrochemical oxidation of Pt and formation of additional d-band vacancies. The absolute change was found to be strongest for the carbon-supported Pt particles and similarly strong for the oxide-supported Pt particles (see Figure 6.9a) and qualitatively follows the initial Pt particle size.

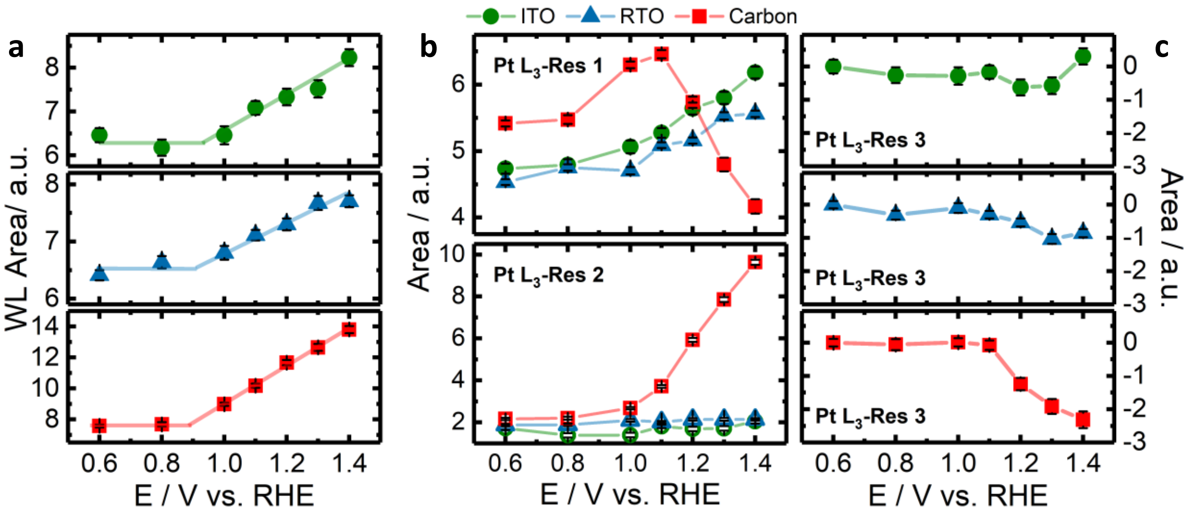

**Figure 6.9** Structural response of Pt nanoparticles supported on ITO (green circles), RTO (blue triangles), and carbon (red squares) on stepwise electrochemical oxidation (potential hold for 10 min each) with respect to the white line area (a) the integrated areas as the resonances 1 (Pt $L_3$-Res 1) at ~11566 eV and Pt $L_3$-Res 2 at ~11570 eV (b) and Pt $L_3$-Res 3 at ~11580 eV (c) as determined by peak fitting of *in situ* Pt $L_3$–edge X-ray near-edge absorption spectra. The solid lines are shown to guide the eye of the reader.

Following Merte *et al.*[174] the Pt $L_3$ XANES spectra are convoluted by at least two spectroscopic features, the WL of the metallic Pt at ~11566 eV (Res1) and of a $Pt^{n+}$ at ~11570 eV (Res2), see also Figure 6.8. We tracked the spectral weight of these features with electrode potential by fitting the corresponding XANES spectra to follow the increase of the d-band vacancies in the metallic Pt and the formation of a $Pt^{n+}$ (Figure 6.9b). Below 0.9 V the (electronic) structure of the metallic Pt does not strongly vary for all three catalysts because the spectral weight of Res1 does not change. For Pt/C and Pt/RTO even the degree of $Pt^{n+}$ remained constant as seen in the spectral weight of Res2. Above ~0.9 V more d-band vacancies in the metallic Pt domains are generated for all three catalysts as the spectral weight of Res1 increases. For the oxide-supported Pt nanoparticles the spectral weight of Res1 increases linearly up to 1.4 V whereas in the case of the carbon-supported Pt nanoparticles it grows only up to 1.1 V. Following the spectral weight of Res2 in the XANES spectra, we identified that a significant fraction of the carbon-supported Pt nanoparticles form $Pt^{n+}$ species increases above 0.9 V. This $Pt^{n+}$ formation is strongly suppressed for the oxide-supported Pt nanoparticles as the spectral weight of Res2 remains almost constant. In contrast to carbon-supported Pt particles, no significant change in the slope of Res1 can be seen. Thus, we conclude that there is a substantial difference in the oxidation of the carbon- and oxide-supported Pt particles. A significant decrease in the volume of the metallic domains and in the coherence length of the carbon supported Pt particles above 1.1 V is observed accompanied by the formation of $Pt^{n+}$ species and thus, a $PtO_x$.

This restructuring can also be followed in the spectral weight of the first local maximum above the WL at ~11580 eV (Res3), see Figure 6.8. We tracked this feature (see Figure 6.9c) in addition to WL features typical for metallic Pt and the $Pt^{n+}$ because it is typically well-pronounced in the case of large Pt metallic domains such as Pt foils.[172] Therefore, we assign the Res3 feature to be a fingerprint of the metallic domains independent of the corresponding d-band vacancies. We found that the spectral weight of Res3 is constant up to 1.1 V and decreases at higher potentials for all three catalysts. The decrease is limited and significantly stronger in the case of the carbon-supported Pt particles than for the oxide-supported particles thus, being correlated to the initial Pt particle size. Together with the increasing spectral weight of oxide-typical Res2, we conclude that the carbon-supported metallic Pt particle restructure above 1.1 V leading to a strong but limited fraction of $PtO_x$ (shell). In contrast, the metallic domains of the oxide-supported Pt particles restructure significantly less and negligible spectroscopic contribution of features typical for $PtO_x$ can be seen showing a suppressed structural response to the electrochemical oxidation.

We identified that the Pt lattice parameter and the spectral weight of the Pt $L_3$ Res1 feature exhibit a similar potential dependence and both are linked changes in the atomic and electronic structure of the metallic Pt, respectively. In the case of the carbon-supported Pt particles the d-band vacancy formation in the metallic Pt is superimposed by the restructuring to a $PtO_x$ leading to a decreasing spectral weight above 1.1 V. However, we expect that more d-band vacancies are formed in the remaining metallic Pt. Two processes can lead to an expansion of the Pt lattice. On the one hand, the coverage of the Pt surface with O atoms as well as the place-exchange mechanism occurring above 1.17 V on the Pt(111) can expel the surface atomic layers.[100,175] The bulk of the Pt nanoparticles response to these process with an expansion of the lattice. On the other hand, the formation of d-band vacancies in the metallic Pt decreases the electron density and thus, weakens the metallic Pt-Pt bond leading to a longer Pt-Pt distance. The identified reversibility of the lattice expansion between 1.0 and 1.4 V supports rather a structural response to the electrode potential and the d-band vacancies initiated by a Pt-O formation at ~0.9 V. A purely oxide-induced structural response is unlikely because the oxygen coverage and the place-exchange process are not kinetically-limited leading to a potential-dependent increase. Furthermore, we expect the $PtO_x$ shell (or an intermediate stage preceding the electrochemical reduction) yet to be present on the metallic Pt core (Figure 6.4) because the $PtO_x$ get primarily reduced below 1.0 V.

The quantitative differences in the response to the electrochemical oxidation seen in the changes of the Pt $L_3$ features, e.g. slope of Res1, are caused by the different particle size leading to the differences in the ECSA. The qualitative differences, however, can be partially explained with the different morphology of the Pt nanoparticles. The rather platelet-like Pt nanoparticles on the carbon support potentially exhibit a higher projected area of (100) facets to the electrolyte than the rather spherical and ellipsoidal Pt particles on the oxide supports. Pt(100) facets are known to oxidize differently than the (111) facets on which the place-exchange and the formation of an amorphous 3D $\alpha$-$PtO_2$ proceeds sequentially at 1.1 V and above 1.3 V, respectively. On Pt(100) both processes occur simultaneously above 1.1 V.[102] In our case the platelet-like Pt particles exhibit a strong structural response to the electrochemical oxidation above 1.1 V as seen in the coherence length and as the oxide-typical WL feature grows. These changes are indicative for the formation of an amorphous 3D $\alpha$-$PtO_2$ on the Pt particles. The rather spherical/ellipsoidal Pt nanoparticles on the oxide support, which are thus characterized by rather convex surfaces, exhibit more Pt sites similar to the Pt(111) or high-index surfaces. We found that these particles response to the electrochemical oxidation (mainly in the metal typical WL feature but also in the Pt lattice) but form negligible fraction of $PtO_x$ up to 1.4 V and thus, formation of an amorphous 3D $\alpha$-$PtO_2$ on the Pt particles is strongly suppressed.

Interestingly, the contracted lattice of the ITO-supported Pt particles between 0.8 and 1.0 V is accompanied with a reduced spectral weight of Res2. Thus, a lower fraction of oxidized (or electron-deficient) Pt is accompanied by a contraction of the Pt lattice. This can be explained with the higher electron density in the Pt d-band strengthening the metallic Pt-Pt bond.

### *In situ Pt dissolution by SFC ICP-MS*

The potential-dependent dissolution of Pt on the different supports was followed by *in situ* SFC ICP-MS measurements in order to evaluate the stability towards Pt dissolution in comparison to the above described responses of Pt towards electrochemical oxidation. Therefore, CVs between 0.05 and 1.5 V after electrochemical activation of 100 CVs were conducted and the resulting Pt dissolution profiles recorded, see Figure 6.10.

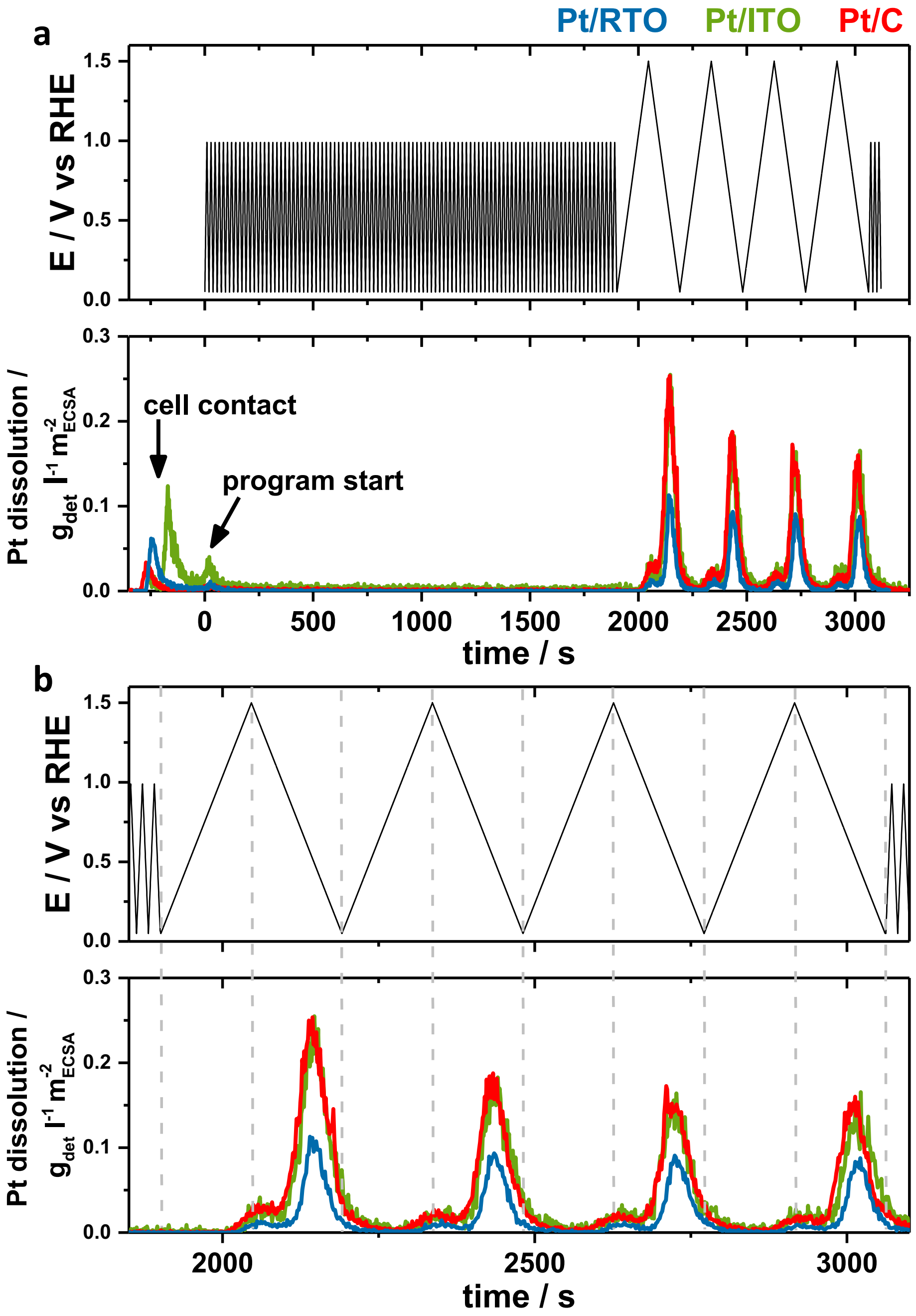

**Figure 6.10** Pt dissolution profiles from *in situ* SFC ICP-MS measurement in $g_{det}$ Pt per volume electrolyte in l and electrochemical surface area (ECSA) in $m^2_{ECSA}$. (a) shows the whole electrochemical measurement (100 CVs of activation with a scanrate 100 mV $s^{-1}$ and 4 CVs of Pt Oxidation from 0.05-1.5 V with a scanrate 10 mV $s^{-1}$) and the corresponding dissolution profiles for Pt on carbon (red), ITO (green) and RTO (blue) support and (b) the four oxidation cycles from 0.05-1.5 V.

Dissolution peaks arise for all three materials for the first contact of the sample with the electrolyte (denoted as cell contact) and at start of the electrochemical protocol (denoted as program start), see Figure 6.10a. No Pt dissolution was observed during potential cycling in the activation regime, but strong dissolution peaks arise during electrochemical oxidation up to 1.5 V and reduction to 0.05 V, Figure 6.10b.

Figure 6.11 shows the ECSA-normalized Pt dissolution of the initial anodic potential sweep to 1.5 V mimicking the electrochemical oxidation tracked by the *in situ* X-ray experiments. The anodic Pt dissolution has an onset potential at 1.1-1.2 V and continuously increases up to 1.5 V. The $H_{upd}$-ECSA-normalized Pt dissolution is strongest for the Pt/C, lowest for Pt/RTO and Pt/ITO shows intermediate Pt dissolution rate with the highest background dissolution rate even below 1.1 V.

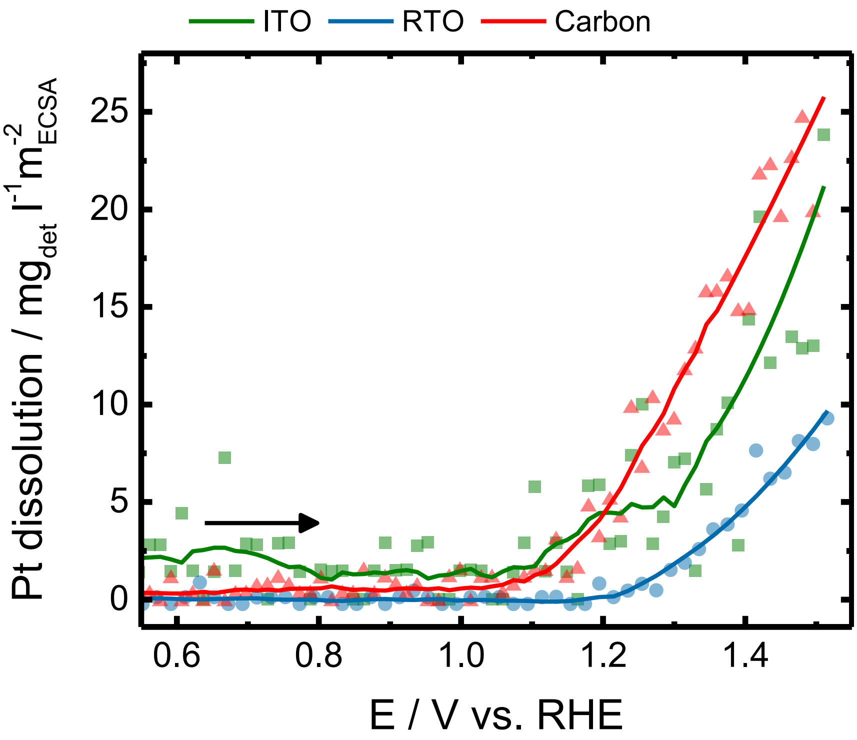

**Figure 6.11** Evolution of ECSA-normalized Pt dissolution rate for Pt nanoparticles supported on ITO (green), RTO (blue), and carbon (red) during the initial anodic potential sweep from 0.05-1.5 V with a scanrate of 10 mV $s^{-1}$ as determined by SFC ICP-MS measurements.

The onset of Pt dissolution corresponds to the decrease in the Pt scale factor as well as in the loss of spectral weight for Res1 and Res3. Therefore, the $Pt^{n+}$ rate might be caused by dissolution of $Pt^{n+}$ species during place-exchange between surface-O and Pt and $PtO_x$ formation. Thus, a fraction of the electrochemically formed $Pt^{n+}$ species is dissolved into the electrolyte. On the other hand, a constant anodic dissolution of $Pt^{n+}$ could limit the growth of an oxide shell around the nanoparticle or lead to the formation of a “stable” $PtO_x$ on the surface.

Additionally, one has to consider the difference between the dynamic *in situ* SFC ICP-MS measurements and the quasi-stationary *in situ* X-ray experiments. Noteworthy, strong Pt dissolution peaks arise in the reductive scan below 1.0 V with similar dissolution rate for Pt on C and ITO and lowest dissolution for Pt/RTO, see Figure 6.12.

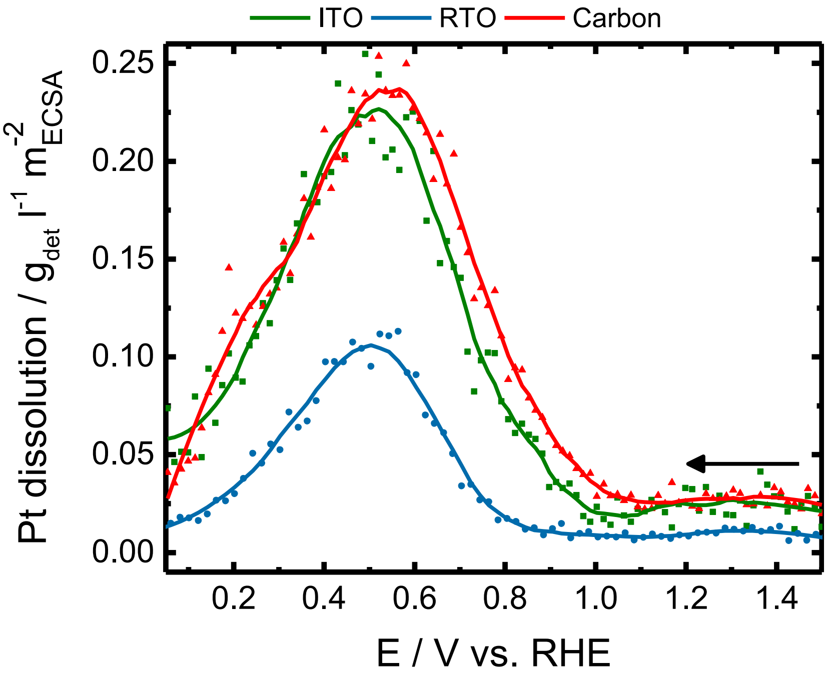

**Figure 6.12** Evolution of ECSA-normalized Pt dissolution rate of electrochemically-oxidized Pt nanoparticles supported on ITO (green), RTO (blue), and carbon (red) as determined by SFC ICP-MS measurements during the cathodic potential sweep from 1.5-0.05 V with a scanrate of 10 mV $s^{-1}$ after initial anodic potential sweep up to 1.5 V.

Compared to anodic Pt dissolution, electrochemical reduction of the formed $PtO_x$ causes a Pt dissolution which is one order of magnitude higher and thus, representing an important degradation pathway of Pt-based electrocatalysts (Figure 6.12). The onset of the cathodic Pt dissolution rate is below 1.0 V and might exhibit a binary profile especially for the Pt/C. It is known that the $PtO_2$ phase is reduced at lower electrode potentials than a lower $PtO_x$.[176,177] These differences furthermore suggest that $PtO_2$ formation is suppressed for the oxide-supported nanoparticles but more distinct for the carbon-supported.

## 6.5. Conclusion

In this study, we investigated the response of Pt nanoparticles on different supports towards electrochemical oxidation in order to establish a more comprehensive understanding of stability determining properties of fuel cell catalysts.

We found that the applied synthesis route determines the morphology of the Pt nanoparticles. A surfactant assisted synthesis as used for the ITO support yields ~4 nm spherical nanoparticles with interstitial O on tetrahedral (Td) sites of the Pt lattice and a bulk-like Pt lattice constant. Impregnation of the support on the other hand leads to ellipsoidal/platelet-like nanoparticles in smaller sizes without interstitial O on the tetrahedral sites and a size-induced contraction of the Pt lattice. The anisotropic shape of Pt on carbon (more platelet-like) and on RTO (more ellipsoidal) was confirmed from TEM micrographs.

Our *in situ* HE-XRD investigations revealed that the Pt lattice parameter of the nanoparticles on carbon and RTO increases reversibly and linearly with potential above 1.0 V while only small changes are observed for Pt/ITO. This could be due to place-exchange and/or buckling of surface Pt atoms during the oxidation. From *in situ* X-ray absorption spectroscopy we show that the Pt $L_3$ WL intensity increases with potential above 1.0 V and peak fitting reveals that the formation of $Pt^{n+}$ species is much more pronounced for Pt/C but follows to a certain extent the ECSA and particle size. Furthermore, *in situ* dissolution experiments show anodic Pt dissolution that follows the trend as observed from the *in situ* X-ray investigations.

Overall, it can be stated that Pt on RTO shows the lowest tendency towards $Pt^{n+}$ formation and Pt dissolution that could point towards a higher total electrochemical stability of an RTO-supported Pt electrocatalyst.

Overall, it can be stated that Pt on RTO shows the lowest tendency towards $Pt^{n+}$ formation and Pt dissolution that could point towards a higher total electrochemical stability of an RTO-supported Pt electrocatalyst.

# 7. Summary and Outlook

This work addressed degradation-related phenomena in supported Pt fuel cell catalysts with an emphasis on the use of novel catalyst support materials. In light of the need for developing more stable PEMFC cathode catalysts for an accelerated commercialization of fuel cells in the transportation sector, it is highly important to improve the overall catalyst durability. This can only be achieved by gaining a detailed knowledge on the catalyst and support properties under (simulated) working conditions in order to design new and advanced electrocatalysts.

Therefore, a number of different supports were employed to disperse the catalytically active Pt nanoparticles. A wide range of various analytical methods was applied to investigate the catalysts and their components on a fundamental level and to draw structure-stability correlations. The overall goal was to contribute to the understanding of PEMFC catalyst degradation phenomena. This was engaged by using two different (mixed) metal oxides (ITO and RTO) as Pt support and investigating the long term stability exemplified by accelerated stress tests as well as stability determining properties exemplified by the behavior towards Pt oxidation. Furthermore, a state-of-the-art carbon support was modified by introducing heteroatoms and its influenece on the structural and morphological stability of the Pt nanoparticles was analyzed.

## 7.1. *In Situ* Stability Study of Pt Supported on Indium Tin Oxide

In the first part of this thesis (chapter 4), indium tin oxide was employed as Pt catalyst support in order to investigate its potential as carbon replacement in cathode catalysts. It was shown that small Pt nanoparticles were successfully deposited on the oxide support resulting in a narrow size distribution. Electrochemical degradation protocols in two potential regimes were applied to mimic fuel cell operating conditions. In a regular fuel cell operation range (LP-AST), a discrepancy between the stability of catalytic Pt mass activity and active surface area probed by hydrogen underpotential deposition pointed towards a surface-induced Pt poisoning effect responsible for overall stability losses. During simulated start/stop procedures, the Pt/ITO catalyst proved superior stability when compared to a commercial Pt/C reference.

By applying *in situ* wide and small angle X-ray scattering, it could be shown that Pt nanoparticles remained morphologically fully stable under operating conditions whereas the support suffered from the reducing conditions, as the ITO crystallites partially dissolve and grow via Ostwald ripening. With the help of *in situ* dissolution measurements by SFC ICP-MS and STEM EDX mappings combined with the findings from XP spectroscopy, the loss in catalytic activity could be linked to Pt surface modification by most likely redeposited In/Sn ions from the support. This modification led to a poisoning effect accompanied with a reduced availability of specific O-adsorption sites on the Pt nanoparticles, Figure 7.1 schematically illustrates these degradation mechanisms schematically.

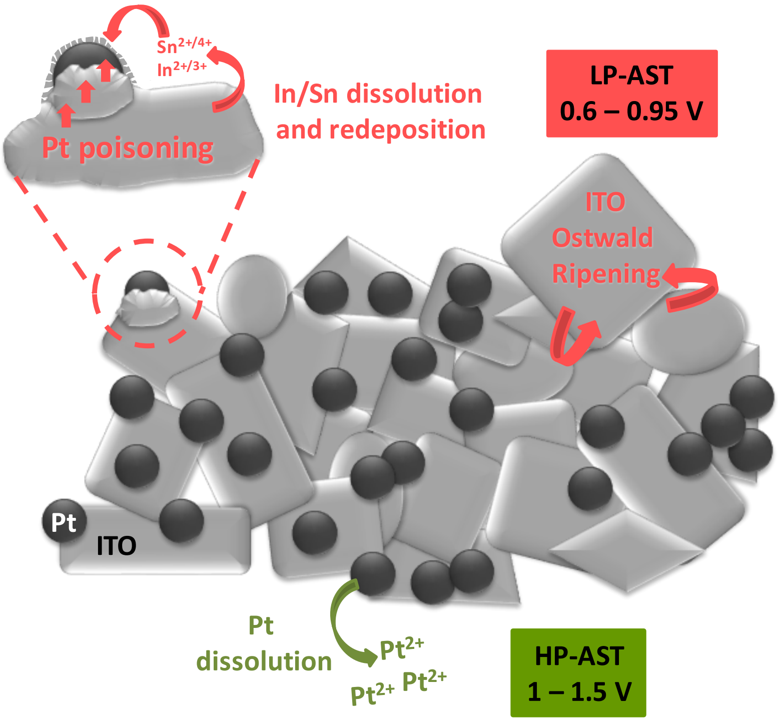

**Figure 7.1** Schematic illustration of degradation phenomena as found to occur in Pt/ITO electrocatalyst during two different simulated degradation protocols: low potential AST and high potential AST (denoted as LP-AST and HP-AST). Reproduced from Ref [52] (Adv. Energy Mat., **2018**, 8 (4), 1701663) with permission from John Wiley and Sons, Copyright 2018.

During demanding high potential cycling (HP-AST), in contrast, the catalytic stability of oxide-supported Pt nanoparticles was greatly enhanced compared to the reference carbon-supported catalyst. This was due to a higher stability of the ITO support, as no ITO particle growth was observed by *in situ* HE-XRD. Pt nanoparticles again showed a superior morphological stability proven by TEM and ASAXS measurements. The small but continuous anodic Pt dissolution during the HP-AST was proposed to prevent Pt surface poisoning and thus, contributing to regaining ORR activity and stability.

By the application of complementary analytical techniques in a detailed study, several principle degradation mechanisms could be excluded. This aided in identifying the cause for activity deterioration as well as stabilization for Pt/ITO. Therefore, this study contributed to the essential knowledge about fuel cell relevant degradation phenomena in novel oxide-supported Pt cathode catalysts.

## 7.2. Carbon Heteroatom Modification in Pt/C ORR Catalysts

In chapter 5, a study on the carbon support modification by heteroatom doping and its influence on the long-term ORR stability of the Pt electrocatalyst was presented. Therefore, a family of modified carbons from a two-step functionalization approach including acidic oxidation followed by ammonolysis at elevated temperatures was investigated and used as Pt support. Elemental analysis showed the introduction of O (up to 12.6 %) and N (up to 2.5 %) into the carbon matrix yielding in O- and N-enriched carbons. Changes in the BET surface area and the surface zeta potential upon oxidation and ammonolysis proved the successful modification of the carbon surface. XP spectroscopy revealed differences in relative amounts of N-moieties on the carbon surface depending the ammonolysis temperature; at 400 °C pyrrolic-N were found to be the most abundant surface species while at 800 °C pyridinic-N were present in highest fractions.

Differences in carbon corrosion behavior upon functionalization were analyzed by high temperature DEMS in which the carbon aminated at 400 °C showed strongly improved corrosion resistance with low $CO_2$ production rates compared to the unmodified references and the oxidized carbon. Furthermore, when used as Pt catalyst support, the influence of the support heteroatom doping on the electrochemical long-term stability was investigated. By applying ASTs up to 30k cycles to simulate fuel cell operating conditions to a row of Pt electrocatalysts on the modified and reference supports, differences in catalytic stability were observed.

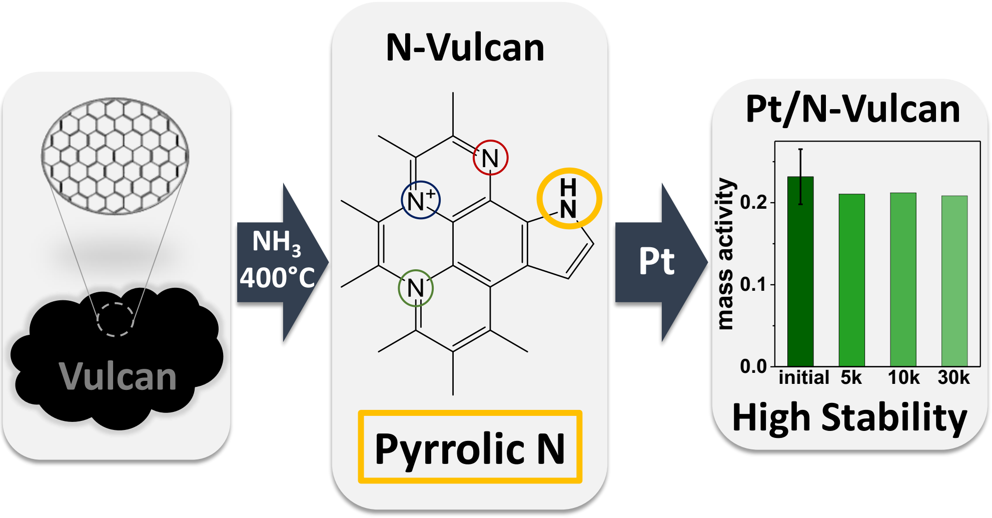

**Figure 7.2** Schematic illustration of the process of support functionalization by ammonolysis at 400°C and introduction of surface abundant pyrrolic-N. In the second step, Pt deposition on modified support and the improved ORR long-term stability is illustrated. Reprinted with permission from Ref [71] (Chem. Mat., **2018**, doi: 10.1021/acs.chemmater.8b03612). Copyright (2018) American Chemical Society.

Interestingly, it was found that the excellent stability of Pt/N-Vulcan 400°C was accompanied with the highest specific ORR activity within the row of these catalysts, see also Figure 7.2. The application of *in situ* wide and small angle X-ray scattering aided in excluding certain degradation mechanisms. Over the first 5k cycles of the ASTs a stable particle and crystallite sizes for all samples was observed, indicating that changes influencing the electrochemical Pt stability appear in later stages of the AST. Correlating ORR performances and catalyst properties, it was proposed that the outstanding stability and specific activity of Pt/N-Vulcan 400°C was originating from a beneficial effect of the pyrrolic-N surface species together with an enhanced corrosion resistance.

This study provided new valuable insights into the effect of carbon heteroatom modification and the origin of the improved long-term ORR stability. Furthermore, it highlights the great potential of a synthetic pathway for corrosion stabilized Pt supports in the field of PEM fuel cells.

## 7.3. Electrochemical Oxidation of Pt on different Supports

The third study of this work (chapter 6) addressed the topic of electrochemical oxidation of Pt as exemplified by using different supports and following the structural responses by *in situ* X-ray methods and morphological changes due to Pt dissolution by *in situ* ICP-MS. Besides a commercial carbon-supported Pt catalyst, two oxide-supported materials were used; an indium-based (ITO) oxide and a mixed ruthenium-titaniumoxide (RTO) support. It could be shown that the Pt nanoparticles exhibited different particle shapes depending on the applied synthesis route, where impregnation led to more ellipsoidal Pt particles and surfactant-assisted synthesis resulted in spherical particles.

Spherical particles were found on ITO support both by TEM analysis as well as by Rietveld refinement. Additionally, it was shown that a small fraction of interstitial oxygen was incorporated in the Pt lattice accompanied with an expansion of the Pt lattice. On RTO and carbon support, the Pt particles exhibited a smaller size and showed ellipsoidal shape without O incorporated in the Pt lattice.

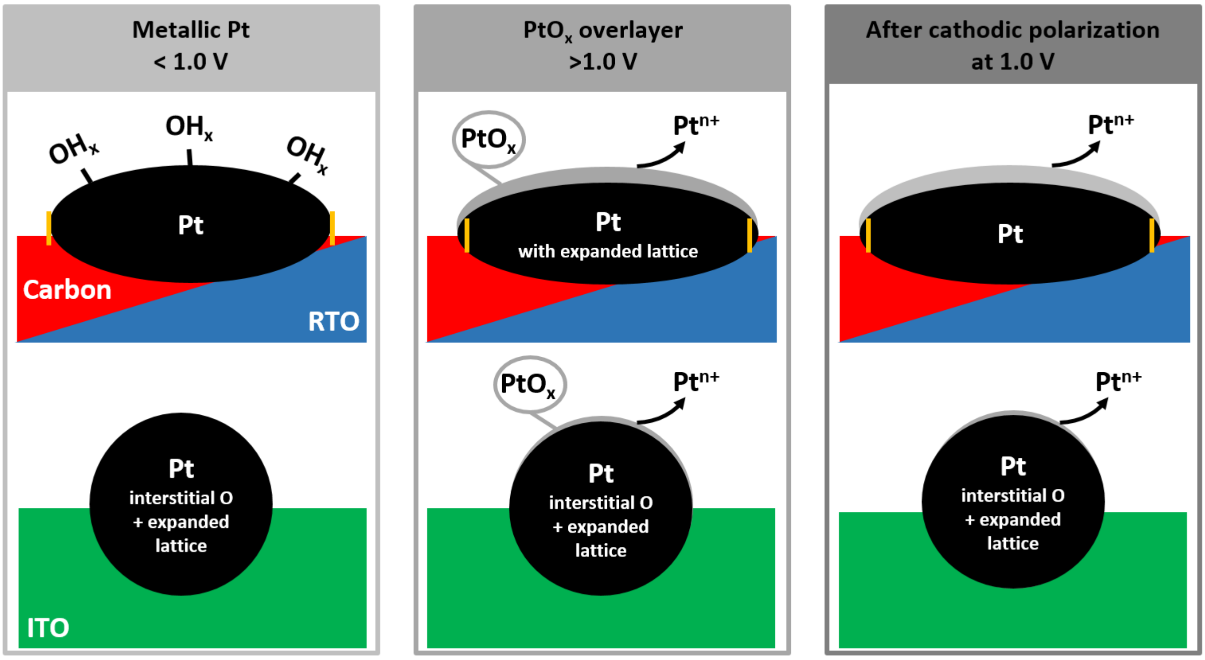

**Figure 7.3** Schematic illustration of potential-dependent responses of Pt nanoparticles on carbon, RTO and ITO support on electrochemical oxidation with respect to lattice expansion, formation of PtO$_x$ and Pt$^{n+}$ dissolution.

During electrochemical oxidation it could be proven by *in situ* HE-XRD measurements that structural responses of the metallic Pt domains with respect to their Pt lattice, to the volume and amount of the metallic Pt domain were induced. The smaller ellipsoidal particles showed initial size-induced lattice contraction and a reversible lattice expansion upon oxidation to 1.4 V while this was suppressed in the ITO-supported catalyst with already expanded lattice (see Figure 7.3). Fitting of the WL-area of the *in situ* X-ray absorption spectra revealed that the formation of PtO$_x$ species is favored in the carbon-supported nanoparticles due to an increased tendency towards the formation of Pt$^{n+}$. For Pt/ITO, a higher electron density in the d-band strengthening the metallic Pt-Pt bonds resulted in a lower fraction of oxidized Pt. However, *in situ* Pt dissolution measurements by SFC ICP-MS showed the highest dissolution rates for the carbon supported Pt particles and lowest for Pt/RTO pointing towards a higher electrochemical stability of the RTO-supported Pt nanoparticles.

The novel insights gained in this work can be of high importance for the determination of catalytic active states in ORR catalysts as well as for the design of new and stable ORR electrocatalyst. Besides the implementation of simulated degradation protocols as summarized in the previous sections, the discovery of indications for possible degradation pathways as exemplified by electrochemical Pt oxidation is another promising way for pioneering improved catalysts materials.

## 7.4. Outlook

With the overall goal towards an increased awareness for sustainability within the society, the implementation of hydrogen fuel cells in the transportation sector can contribute to a green energy future. However, the knowledge about a wide range of already known Pt-based catalysts, that might be considered as fuel cell cathode materials has to be extended with respect to its availability, activity and durability.

The stability of the electrocatalyst remains a major drawback in fuel cell commercialization. Therefore, new materials have to be developed based on the knowledge of detailed evaluations of former generations of catalysts. Thus, the insights gained in the presented studies on Pt/ITO, Pt/RTO and Pt/N-Vulcan contributing to the overall understanding of cathode catalysts can lead to the development of improved catalysts.

It was found that the support stability plays a key role in the overall catalyst durability. Hence, as ITO seems to be suffering from the reducing conditions in ORR catalysis, it might be more suitable as support for oxygen evolution reaction (OER) catalysts demanding stability at more anodic potentials. Nevertheless, metal oxide supports represent a promising class of catalysts supports, and, for example, doping of indium-oxide with other metals, could be a way to stabilize the oxide and prevent Pt poisoning under cathodic working conditions. In this context, *in situ* methods using X-ray radiation are promising tools to investigate more stable metal oxide supported Pt catalysts. On the other hand, the superior stability of N-modified Vulcan offers great possibilities for the use as support for highly active Pt-alloy ORR catalysts such as PtNi or PtCo nanoparticles. The fast and facile two-step modification approach enables the production of carbon supports with high fractions of stabilizing N-functionalities and the use of such N-Vulcans as catalyst support for other electrochemical reactions.

Upscaling of established catalyst systems consisting of alternative supports with improved stability and implementation in MEA setups would represent the ultimate goal. Catalyst evaluation under MEA conditions would verify the “real” suitability of stabilizing catalysts supports for an overall improved MEA durability.

# 8. References

1 Jackson, R. B.;Le Quere, C.;Andrew, R. M.;Canadell, J. G.;Peters, G. P.;Roy, J.;Wu, L., Warning signs for stabilizing global CO2 emissions. *Environ Res Lett* **2017,** *12* (11).

2 Le Quéré, C.;Andrew, R. M.;Friedlingstein, P.;Sitch, S.;Pongratz, J.;Manning, A. C.;Korsbakken, J. I.;Peters, G. P.;Canadell, J. G.;Jackson, R. B.;Boden, T. A.;Tans, P. P.;Andrews, O. D.;Arora, V. K.;Bakker, D. C. E.;Barbero, L.;Becker, M.;Betts, R. A.;Bopp, L.;Chevallier, F.;Chini, L. P.;Ciais, P.;Cosca, C. E.;Cross, J.;Currie, K.;Gasser, T.;Harris, I.;Hauck, J.;Haverd, V.;Houghton, R. A.;Hunt, C. W.;Hurtt, G.;Ilyina, T.;Jain, A. K.;Kato, E.;Kautz, M.;Keeling, R. F.;Klein Goldewijk, K.;Körtzinger, A.;Landschützer, P.;Lefèvre, N.;Lenton, A.;Lienert, S.;Lima, I.;Lombardozzi, D.;Metzl, N.;Millero, F.;Monteiro, P. M. S.;Munro, D. R.;Nabel, J. E. M. S.;Nakaoka, S.-i.;Nojiri, Y.;Padin, X. A.;Peregon, A.;Pfeil, B.;Pierrot, D.;Poulter, B.;Rehder, G.;Reimer, J.;Rödenbeck, C.;Schwinger, J.;Séférian, R.;Skjelvan, I.;Stocker, B. D.;Tian, H.;Tilbrook, B.;Tubiello, F. N.;van der Laan-Luijkx, I. T.;van der Werf, G. R.;van Heuven, S.;Viovy, N.;Vuichard, N.;Walker, A. P.;Watson, A. J.;Wiltshire, A. J.;Zaehle, S.;Zhu, D., Global Carbon Budget 2017. *Earth System Science Data* **2018,** *10* (1), 405-448.

3 https://www.esrl.noaa.gov/gmd/ccgg/trends/ (accessed 30.07.2018).

4 Peters, G. P.;Le Quere, C.;Andrew, R. M.;Canadell, J. G.;Friedlingstein, P.;Ilyina, T.;Jackson, R. B.;Joos, F.;Korsbakken, J. I.;McKinley, G. A.;Sitch, S.;Tans, P., Towards real-time verification of CO2 emissions. *Nat Clim Change* **2017,** *7* (12), 848-850.

5 https://www.energy-charts.de/energy_pie.htm?year=2017 (accessed 01.08.2018).

6 https://www.energy-charts.de/ren_share_de.htm?source=ren-share&period=monthly&year=all (accessed 24.09.2018).

7 Pellow, M. A.;Emmott, C. J. M.;Barnhart, C. J.;Benson, S. M., Hydrogen or batteries for grid storage? A net energy analysis. *Energy & Environmental Science* **2015,** *8* (7), 1938-1952.

8 Grove, W. R., XXIV. On voltaic series and the combination of gases by platinum. *The London, Edinburgh, and Dublin Philosophical Magazine and Journal of Science* **1839,** *14* (86-87), 127-130.

9 Grove, W. R., On a Gaseous Voltaic Battery. *Philos. Mag.* **2012,** *92* (31), 3753-3756.

10 Larminie, J.;Dicks, A., *Fuel Cell Systems Explained*. John Wiley & Sons Ltd: West Sussex, 2003.

11 https://www.fueleconomy.gov/feg/fcv_sbs.shtml (accessed 09.08.2018).

12 https://www.nrel.gov/docs/fy11osti/49342-1.pdf (accessed 18.09.2018).

13 http://ec.europa.eu/regional_policy/en/projects/germany/hydrogen-fuel-cells-drive-clean-quiet-buses-in-cologne-and-amsterdam (accessed 18.09.2018).

14 https://www.alstom.com/press-releases-news/2018/9/world-premiere-alstoms-hydrogen-trains-enter-passenger-service-lower (accessed 17.09.2018).

15 Strasser, P., Fuel Cells. In *Chemical Energy Storage*, R. Schloegl, Ed. De Gruyter: 2012; pp 163-184.

16 https://www.hydrogen.energy.gov/pdfs/17007_fuel_cell_system_cost_2017.pdf (accessed 01.08.2018).

17 Stephens, I. E. L.;Bondarenko, A. S.;Gronbjerg, U.;Rossmeisl, J.;Chorkendorff, I., Understanding the electrocatalysis of oxygen reduction on platinum and its alloys. *Energy & Environmental Science* **2012,** *5* (5), 6744-6762.

18 Rossmeisl, J.;Karlberg, G. S.;Jaramillo, T.;Norskov, J. K., Steady state oxygen reduction and cyclic voltammetry. *Faraday Discussions* **2008,** *140*, 337-346.

19 Stamenkovic, V.;Mun, B. S.;Mayrhofer, K. J. J.;Ross, P. N.;Markovic, N. M.;Rossmeisl, J.;Greeley, J.;Nørskov, J. K., Changing the Activity of Electrocatalysts for Oxygen Reduction by Tuning the Surface Electronic Structure. *Angew. Chem.* **2006,** *118* (18), 2963-2967.

20 Stamenkovic, V. R.;Fowler, B.;Mun, B. S.;Wang, G.;Ross, P. N.;Lucas, C. A.;Markovic, N. M., Improved Oxygen Reduction Activity on Pt3Ni(111) via Increased Surface Site Availability. *Science* **2007**.

21 Stamenkovic, V. R.;Mun, B. S.;Arenz, M.;Mayrhofer, K. J. J.;Lucas, C. A.;Wang, G. F.;Ross, P. N.;Markovic, N. M., Trends in electrocatalysis on extended and nanoscale Pt-bimetallic alloy surfaces. *Nat. Mater.* **2007,** *6* (3), 241-247.

22 Gan, L.;Heggen, M.;Rudi, S.;Strasser, P., Core-Shell Compositional Fine Structures of Dealloyed PtxNi1-x Nanoparticles and Their Impact on Oxygen Reduction Catalysis. *Nano Lett.* **2012,** *12* (10), 5423-5430.

23 Gan, L.;Cui, C. H.;Rudi, S.;Strasser, P., Core-Shell and Nanoporous Particle Architectures and Their Effect on the Activity and Stability of Pt ORR Electrocatalysts. *Top. Catal.* **2014,** *57* (1-4), 236-244.

24 Bligaard, T.;Norskov, J. K., Ligand effects in heterogeneous catalysis and electrochemistry. *Electrochimica Acta* **2007,** *52* (18), 5512-5516.

25 https://www.energy.gov/sites/prod/files/2017/11/f46/FCTT_Roadmap_Nov_2017_FINAL.pdf (accessed 02.08.2018).

26 Meier, J. C.;Galeano, C.;Katsounaros, I.;Witte, J.;Bongard, H. J.;Topalov, A. A.;Baldizzone, C.;Mezzavilla, S.;Schuth, F.;Mayrhofer, K. J. J., Design criteria for stable Pt/C fuel cell catalysts. *Beilstein J. Nanotechnol.* **2014,** *5*, 44-67.

27 Keeley, G. P.;Cherevko, S.;Mayrhofer, K. J. J., The Stability Challenge on the Pathway to Low and Ultra-Low Platinum Loading for Oxygen Reduction in Fuel Cells. *ChemElectroChem* **2016,** *3* (1), 51-54.

28 Rice, C. A.;Urchaga, P.;Pistono, A. O.;McFerrin, B. W.;McComb, B. T.;Hu, J., Platinum Dissolution in Fuel Cell Electrodes: Enhanced Degradation from Surface Area Assessment in Automotive Accelerated Stress Tests. *Journal of The Electrochemical Society* **2015,** *162* (10), F1175-F1180.

29 Topalov, A. A.;Katsounaros, I.;Auinger, M.;Cherevko, S.;Meier, J. C.;Klemm, S. O.;Mayrhofer, K. J., Dissolution of platinum: limits for the deployment of electrochemical energy conversion? *Angew. Chem., Int. Ed. Engl.* **2012,** *51* (50), 12613-12615.

30 Xing, L. Y.;Hossain, M.;Tian, M.;Beauchemin, D.;Adjemian, K.;Jerkiewicz, G., Platinum Electro-dissolution in Acidic Media upon Potential Cycling. *Electrocatalysis* **2014,** *5* (1), 96-112.

31 Matsumoto, M.;Miyazaki, T.;Imai, H., Oxygen-Enhanced Dissolution of Platinum in Acidic Electrochemical Environments. *J Phys Chem C* **2011,** *115* (22), 11163-11169.

32 Cherevko, S.;Kulyk, N.;Mayrhofer, K. J. J., Durability of platinum-based fuel cell electrocatalysts: Dissolution of bulk and nanoscale platinum. *Nano Energy* **2016,** *29*, 275-298.

33 Borup, R.;Meyers, J.;Pivovar, B.;Kim, Y. S.;Mukundan, R.;Garland, N.;Myers, D.;Wilson, M.;Garzon, F.;Wood, D.;Zelenay, P.;More, K.;Stroh, K.;Zawodzinski, T.;Boncella, J.;McGrath, J. E.;Inaba, M.;Miyatake, K.;Hori, M.;Ota, K.;Ogumi, Z.;Miyata, S.;Nishikata, A.;Siroma, Z.;Uchimoto, Y.;Yasuda, K.;Kimijima, K.-i.;Iwashita, N., Scientific Aspects of Polymer Electrolyte Fuel Cell Durability and Degradation. *Chem. Rev.* **2007,** *107* (10), 3904-3951.

34 Pizzutilo, E.;Geiger, S.;Grote, J. P.;Mingers, A.;Mayrhofer, K. J. J.;Arenz, M.;Cherevko, S., On the Need of Improved Accelerated Degradation Protocols (ADPs): Examination of Platinum Dissolution and Carbon Corrosion in Half-Cell Tests. *J. Electrochem. Soc.* **2016,** *163* (14), F1510-F1514.

35 Holby, E. F.;Sheng, W.;Shao-Horn, Y.;Morgan, D., Pt nanoparticle stability in PEM fuel cells: influence of particle size distribution and crossover hydrogen. *Energy & Environmental Science* **2009,** *2* (8), 865.

36 Darling, R. M.;Meyers, J. P., Kinetic model of platinum dissolution in PEMFCs. *Journal of the Electrochemical Society* **2003,** *150* (11), A1523-A1527.

37 Yano, H.;Watanabe, M.;Iiyama, A.;Uchida, H., Particle-size effect of Pt cathode catalysts on durability in fuel cells. *Nano Energy* **2016**.

38 Cherevko, S.;Keeley, G. P.;Geiger, S.;Zeradjanin, A. R.;Hodnik, N.;Kulyk, N.;Mayrhofer, K. J. J., Dissolution of Platinum in the Operational Range of Fuel Cells. *Chemelectrochem* **2015,** *2* (10), 1471-1478.

39 Ostwald, W., Studien über die Bildung und Umwandlung fester Körper. *Z. Phys. Chem.* **1897,** *22*, 289-330.

40 Shao-Horn, Y.;Ferreira, P. J.;O’, G. J. l.;Morgan, D.;Gasteiger, H.;Makharia, R., Coarsening of Pt Nanoparticles in Proton Exchange Membrane Fuel Cells. *ECS Transactions* **2006,** *1* (8), 185-195.

41 Speder, J.;Zana, A.;Spanos, I.;Kirkensgaard, J. J. K.;Mortensen, K.;Hanzlik, M.;Arenz, M., Comparative degradation study of carbon supported proton exchange membrane fuel cell electrocatalysts – The influence of the platinum to carbon ratio on the degradation rate. *J. Power Sources* **2014,** *261*, 14-22.

42 Riese, A.;Banham, D.;Ye, S.;Sun, X., Accelerated Stress Testing by Rotating Disk Electrode for Carbon Corrosion in Fuel Cell Catalyst Supports. *Journal of the Electrochemical Society* **2015,** *162* (7), F783-F788.

43 Castanheira, L.;Dubau, L.;Mermoux, M.;Berthome, G.;Caque, N.;Rossinot, E.;Chatenet, M.;Maillard, F., Carbon Corrosion in Proton-Exchange Membrane Fuel Cells: From Model Experiments to Real-Life Operation in Membrane Electrode Assemblies. *ACS Cat.* **2014,** *4* (7), 2258-2267.

44 Shao-Horn, Y.;Sheng, W. C.;Chen, S.;Ferreira, P. J.;Holby, E. F.;Morgan, D., Instability of supported platinum nanoparticles in low-temperature fuel cells. *Top. Cat.* **2007,** *46* (3-4), 285-305.

45 Antolini, E., Carbon supports for low-temperature fuel cell catalysts. *Applied Catalysis B: Environmental* **2009,** *88* (1-2), 1-24.

46 Willsau, J.;Heitbaum, J., The Influence of Pt-Activation on the Corrosion of Carbon in Gas-Diffusion Electrodes - a Dems Study. *Journal of Electroanalytical Chemistry* **1984,** *161* (1), 93-101.

47 Wang, X.;Li, W.;Chen, Z.;Waje, M.;Yan, Y., Durability investigation of carbon nanotube as catalyst support for proton exchange membrane fuel cell. *J. Power Sources* **2006,** *158* (1), 154-159.

48 Schulenburg, H.;Schwanitz, B.;Linse, N.;Scherer, G. G.;Wokaun, A.;Krbanjevic, J.;Grothausmann, R.;Manke, I., 3D Imaging of Catalyst Support Corrosion in Polymer Electrolyte Fuel Cells. *The Journal of Physical Chemistry C* **2011,** *115* (29), 14236-14243.

49 Mayrhofer, K. J. J.;Meier, J. C.;Ashton, S. J.;Wiberg, G. K. H.;Kraus, F.;Hanzlik, M.;Arenz, M., Fuel cell catalyst degradation on the nanoscale. *Electrochemistry Communications* **2008,** *10* (8), 1144-1147.

50 Hasche, F.;Oezaslan, M.;Strasser, P., Activity, stability and degradation of multi walled carbon nanotube (MWCNT) supported Pt fuel cell electrocatalysts. *Physical Chemistry Chemical Physics* **2010,** *12* (46), 15251-15258.

51 Shao-Horn, Y.;Sheng, W. C.;Chen, S.;Ferreira, P. J.;Holby, E. F.;Morgan, D., Instability of supported platinum nanoparticles in low-temperature fuel cells. *Top Catal* **2007,** *46* (3-4), 285-305.

52 Schmies, H.;Bergmann, A.;Drnec, J.;Wang, G.;Teschner, D.;Kühl, S.;Sandbeck, D. J. S.;Cherevko, S.;Gocyla, M.;Shviro, M.;Heggen, M.;Ramani, V.;Dunin-Borkowski, R. E.;Mayrhofer, K. J. J.;Strasser, P., Unravelling Degradation Pathways of Oxide-Supported Pt Fuel Cell Nanocatalysts under In Situ Operating Conditions. *Adv. Energy Mater.* **2018,** *8* (4), 1701663.

53 Shao, Y.;Liu, J.;Wang, Y.;Lin, Y., Novel catalyst support materials for PEMfuelcells: current status and future prospects. *J. Mater. Chem.* **2009,** *19* (1), 46-59.

54 Zheng, N. F.;Stucky, G. D., A general synthetic strategy for oxide-supported metal nanoparticle catalysts. *Journal of the American Chemical Society* **2006,** *128* (44), 14278-14280.

55 Huang, S.-Y.;Ganesan, P.;Park, S.;Popov, B. N., Development of Titanium Dioxide-supported Platinum catalyst with ultrahigh stability for PEMFC applications. *JACS* **2009**.

56 Lewera, A.;Timperman, L.;Roguska, A.;Alonso-Vante, N., Metal–Support Interactions between Nanosized Pt and Metal Oxides (WO3and TiO2) Studied Using X-ray Photoelectron Spectroscopy. *The Journal of Physical Chemistry C* **2011,** *115* (41), 20153-20159.

57 Ho, V. T.;Pan, C. J.;Rick, J.;Su, W. N.;Hwang, B. J., Nanostructured Ti(0.7)Mo(0.3)O2 support enhances electron transfer to Pt: high-performance catalyst for oxygen reduction reaction. *J Am Chem Soc* **2011,** *133* (30), 11716-11724.

58 Kumar, A.;Ramani, V., Ta0.3Ti0.7O2 Electrocatalyst Supports Exhibit Exceptional Electrochemical Stability. *Journal of the Electrochemical Society* **2013,** *160* (11), F1207-F1215.

59 Kumar, A.;Ramani, V., Strong Metal–Support Interactions Enhance the Activity and Durability of Platinum Supported on Tantalum-Modified Titanium Dioxide Electrocatalysts. *ACS Catalysis* **2014,** *4* (5), 1516-1525.

60 Kumar, A.;Ramani, V. K., RuO2–SiO2 mixed oxides as corrosion-resistant catalyst supports for polymer electrolyte fuel cells. *Applied Catalysis B: Environmental* **2013,** *138-139*, 43-50.

61 Lo, C.-P.;Ramani, V., SiO2–RuO2: A Stable Electrocatalyst Support. *ACS Applied Materials & Interfaces* **2012,** *4* (11), 6109-6116.

62 Lo, C.-P.;Wang, G.;Kumar, A.;Ramani, V., TiO2–RuO2 electrocatalyst supports exhibit exceptional electrochemical stability. *Applied Catalysis B: Environmental* **2013,** *140-141*, 133-140.

63 Parrondo, J.;Han, T.;Niangar, E.;Wang, C.;Dale, N.;Adjemian, K.;Ramani, V., Platinum supported on titanium-ruthenium oxide is a remarkably stable electrocatayst for hydrogen fuel cell vehicles. *Proc Natl Acad Sci U S A* **2014,** *111* (1), 45-50.

64 Dou, M. L.;Hou, M.;Liang, D.;Lu, W. T.;Shao, Z. G.;Yi, B. L., SnO2 nanocluster supported Pt catalyst with high stability for proton exchange membrane fuel cells. *Electrochimica Acta* **2013,** *92*, 468-473.

65 Tsukatsune, T.;Takabatake, Y.;Noda, Z.;Daio, T.;Zaitsu, A.;Lyth, S. M.;Hayashi, A.;Sasaki, K., Platinum-Decorated Tin Oxide and Niobium-Doped Tin Oxide PEFC Electrocatalysts: Oxygen Reduction Reaction Activity. *Journal of the Electrochemical Society* **2014,** *161* (12), F1208-F1213.

66 Cognard, G.;Ozouf, G.;Beauger, C.;Berthomé, G.;Riassetto, D.;Dubau, L.;Chattot, R.;Chatenet, M.;Maillard, F., Benefits and limitations of Pt nanoparticles supported on highly porous antimony-doped tin dioxide aerogel as alternative cathode material for proton-exchange membrane fuel cells. *Applied Catalysis B: Environmental* **2017,** *201*, 381-390.

67 Liu, Y.;Mustain, W. E., High stability, high activity Pt/ITO oxygen reduction electrocatalysts. *J Am Chem Soc* **2013,** *135* (2), 530-533.

68 Zhao, S.;Wangstrom, A. E.;Liu, Y.;Rigdon, W. A.;Mustain, W. E., Stability and Activity of Pt/ITO Electrocatalyst for Oxygen Reduction Reaction in Alkaline Media. *Electrochim. Acta* **2015,** *157*, 175-182.

69 Liu, Y.;Mustain, W. E., Stability limitations for Pt/Sn-In2O3 and Pt/In-SnO2 in acidic electrochemical systems. *Electrochimica Acta* **2014,** *115*, 116-125.

70 Wang, G.;Bhattacharyya, K.;Parrondo, J.;Ramani, V., X-ray photoelectron spectroscopy study of the degradation of Pt/ITO electrocatalyst in an operating polymer electrolyte fuel cell. *Chemical Engineering Science* **2016,** *154*, 81-89.

71 Schmies, H.;Hornberger, E.;Anke, B.;Jurzinsky, T.;Nong, H. N.;Dionigi, F.;Kühl, S.;Drnec, J.;Lerch, M.;Cremers, C.;Strasser, P., The Impact of Carbon Support Functionalization on the Electrochemical Stability of Pt Fuel Cell Catalysts. *Chemistry of Materials* **2018**.

72 Sun, Y. Y.;Sinev, I.;Ju, W.;Bergmann, A.;Dresp, S.;Kuhl, S.;Spori, C.;Schmies, H.;Wang, H.;Bernsmeier, D.;Paul, B.;Schmack, R.;Kraehnert, R.;Cuenya, B. R.;Strasser, P., Efficient Electrochemical Hydrogen Peroxide Production from Molecular Oxygen on Nitrogen-Doped Mesoporous Carbon Catalysts. *ACS Catalysis* **2018,** *8* (4), 2844-2856.

73 Mezzavilla, S.;Baldizzone, C.;Mayrhofer, K. J.;Schuth, F., General Method for the Synthesis of Hollow Mesoporous Carbon Spheres with Tunable Textural Properties. *ACS Appl Mater Interfaces* **2015,** *7* (23), 12914-12922.

74 Galeano, C.;Meier, J. C.;Soorholtz, M.;Bongard, H.;Baldizzone, C.;Mayrhofer, K. J. J.;Schüth, F., Nitrogen-Doped Hollow Carbon Spheres as a Support for Platinum-Based Electrocatalysts. *ACS Catalysis* **2014,** *4* (11), 3856-3868.

75 Xu, B.;Zheng, D.;Jia, M.;Cao, G.;Yang, Y., Nitrogen-doped porous carbon simply prepared by pyrolyzing a nitrogen-containing organic salt for supercapacitors. *Electrochim. Acta* **2013,** *98*, 176-182.

76 Hulicova-Jurcakova, D.;Kodama, M.;Shiraishi, S.;Hatori, H.;Zhu, Z. H.;Lu, G. Q., Nitrogen-Enriched Nonporous Carbon Electrodes with Extraordinary Supercapacitance. *Adv. Funct. Mater.* **2009,** *19* (11), 1800-1809.

77 Vikkisk, M.;Kruusenberg, I.;Joost, U.;Shulga, E.;Tammeveski, K., Electrocatalysis of oxygen reduction on nitrogen-containing multi-walled carbon nanotube modified glassy carbon electrodes. *Electrochim. Acta* **2013,** *87*, 709-716.

78 Zhao, A.;Masa, J.;Muhler, M.;Schuhmann, W.;Xia, W., N-doped carbon synthesized from N-containing polymers as metal-free catalysts for the oxygen reduction under alkaline conditions. *Electrochim. Acta* **2013,** *98*, 139-145.

79 Ni, B.;Ouyang, C.;Xu, X. B.;Zhuang, J.;Wang, X., Modifying Commercial Carbon with Trace Amounts of ZIF to Prepare Derivatives with Superior ORR Activities. *Adv. Mater.* **2017,** *29* (27), 1701354.

80 Toupin, M.;Belanger, D., Spontaneous functionalization of carbon black by reaction with 4-nitrophenyldiazonium cations. *Langmuir* **2008,** *24* (5), 1910-1917.

81 Lakhi, K. S.;Park, D. H.;Al-Bahily, K.;Cha, W.;Viswanathan, B.;Choy, J. H.;Vinu, A., Mesoporous carbon nitrides: synthesis, functionalization, and applications *Chem. Soc. Rev.* **2017,** *46* (2), 560-560.

82 Punetha, V. D.;Rana, S.;Yoo, H. J.;Chaurasia, A.;McLeskey, J. T.;Ramasamy, M. S.;Sahoo, N. G.;Cho, J. W., Functionalization of carbon nanomaterials for advanced polymer nanocomposites: A comparison study between CNT and graphene. *Prog. Polym. Sci.* **2017,** *67*, 1-47.

83 Jaouen, F.;Dodelet, J. P., Non-noble electrocatalysts for O-2 reduction: How does heat treatment affect their activity and structure? Part I. Model for carbon black gasification by NH3: Parametric calibration and electrochemical validation. *J. Phys. Chem. C* **2007,** *111* (16), 5963-5970.

84 Ortega, K. F.;Arrigo, R.;Frank, B.;Schlogl, R.;Trunschke, A., Acid-Base Properties of N-Doped Carbon Nanotubes: A Combined Temperature-Programmed Desorption, X-ray Photoelectron Spectroscopy, and 2-Propanol Reaction Investigation. *Chem. Mat.* **2016,** *28* (19), 6826-6839.

85 Arrigo, R.;Havecker, M.;Wrabetz, S.;Blume, R.;Lerch, M.;McGregor, J.;Parrott, E. P. J.;Zeitler, J. A.;Gladden, L. F.;Knop-Gericke, A.;Schlogl, R.;Su, D. S., Tuning the Acid/Base Properties of Nanocarbons by Functionalization via Amination. *J. Am. Chem. Soc.* **2010,** *132* (28), 9616-9630.

86 Arrigo, R.;Havecker, M.;Schlogl, R.;Su, D. S., Dynamic surface rearrangement and thermal stability of nitrogen functional groups on carbon nanotubes. *Chem. Commun.* **2008,** (40), 4891-4893.

87 Li, X. L.;Wang, H. L.;Robinson, J. T.;Sanchez, H.;Diankov, G.;Dai, H. J., Simultaneous Nitrogen Doping and Reduction of Graphene Oxide. *J. Am. Chem. Soc* **2009,** *131* (43), 15939-15944.

88 Lepró, X.;Terrés, E.;Vega-Cantú, Y.;Rodríguez-Macías, F. J.;Muramatsu, H.;Kim, Y. A.;Hayahsi, T.;Endo, M.;Torres R, M.;Terrones, M., Efficient anchorage of Pt clusters on N-doped carbon nanotubes and their catalytic activity. *Chem. Phys. Lett.* **2008,** *463* (1-3), 124-129.

89 Du, H. Y.;Wang, C. H.;Hsu, H. C.;Chang, S. T.;Chen, U. S.;Yen, S. C.;Chen, L. C.;Shih, H. C.;Chen, K. H., Controlled platinum nanoparticles uniformly dispersed on nitrogen-doped carbon nanotubes for methanol oxidation. *Diamond Relat. Mater.* **2008,** *17* (4-5), 535-541.

90 Chen, S.;Qi, P.;Chen, J.;Yuan, Y., Platinum nanoparticles supported on N-doped carbon nanotubes for the selective oxidation of glycerol to glyceric acid in a base-free aqueous solution. *RSC Adv.* **2015,** *5* (40), 31566-31574.

91 Guo, L.;Jiang, W.-J.;Zhang, Y.;Hu, J.-S.;Wei, Z.-D.;Wan, L.-J., Embedding Pt Nanocrystals in N-Doped Porous Carbon/Carbon Nanotubes toward Highly Stable Electrocatalysts for the Oxygen Reduction Reaction. *ACS Cat.* **2015,** *5* (5), 2903-2909.

92 Hasché, F.;Fellinger, T.-P.;Oezaslan, M.;Paraknowitsch, J. P.;Antonietti, M.;Strasser, P., Mesoporous Nitrogen Doped Carbon Supported Platinum PEM Fuel Cell Electrocatalyst Made From Ionic Liquids. *ChemCatChem* **2012,** *4* (4), 479-483.

93 Tuaev, X.;Paraknowitsch, J. P.;Illgen, R.;Thomas, A.;Strasser, P., Nitrogen-doped coatings on carbon nanotubes and their stabilizing effect on Pt nanoparticles. *Phys. Chem. Chem. Phys.* **2012,** *14* (18), 6444-6447.

94 Shi, Q. R.;Zhu, C. Z.;Engelhard, M. H.;Du, D.;Lin, Y. H., Highly uniform distribution of Pt nanoparticles on N-doped hollow carbon spheres with enhanced durability for oxygen reduction reaction. *RSC Adv.* **2017,** *7* (11), 6303-6308.

95 Arrigo, R.;Schuster, M. E.;Xie, Z. L.;Yi, Y. M.;Wowsnick, G.;Sun, L. L.;Hermann, K. E.;Friedrich, M.;Kast, P.;Havecker, M.;Knop-Gericke, A.;Schlogl, R., Nature of the N-Pd Interaction in Nitrogen-Doped Carbon Nanotube Catalysts. *ACS Cat.* **2015,** *5* (5), 2740-2753.

96 Shanmugam, S.;Sanetuntikul, J.;Momma, T.;Osaka, T., Enhanced Oxygen Reduction Activities of Pt Supported on Nitrogen-Doped Carbon Nanocapsules. *Electrochim. Acta* **2014,** *137*, 41-48.

97 Peter, B.;Melke, J.;Muench, F.;Ensinger, W.;Roth, C., Stable platinum nanostructures on nitrogen-doped carbon obtained by high-temperature synthesis for use in PEMFC. *J. Appl. Electrochem.* **2014,** *44* (5), 573-580.

98 Orfanidi, A.;Madkikar, P.;El-Sayed, H. A.;Harzer, G. S.;Kratky, T.;Gasteiger, H. A., The Key to High Performance Low Pt Loaded Electrodes. *J. Electrochem. Soc.* **2017,** *164* (4), F418-F426.

99 Ruge, M.;Drnec, J.;Rahn, B.;Reikowski, F.;Harrington, D. A.;Carla, F.;Felici, R.;Stettner, J.;Magnussen, O. M., Electrochemical Oxidation of Smooth and Nanoscale Rough Pt(111): An In Situ Surface X-ray Scattering Study. *J. Electrochem. Soc.* **2017,** *164* (9), H608-H614.

100 Drnec, J.;Ruge, M.;Reikowski, F.;Rahn, B.;Carlà, F.;Felici, R.;Stettner, J.;Magnussen, O. M.;Harrington, D. A., Initial stages of Pt(111) electrooxidation: dynamic and structural studies by surface X-ray diffraction. *Electrochimica Acta* **2017,** *224*, 220-227.

101 Gomez-Marin, A. M.;Feliu, J. M., Oxide growth dynamics at Pt(111) in absence of specific adsorption: A mechanistic study. *Electrochimica Acta* **2013,** *104*, 367-377.

102 Huang, Y.-F.;Kooyman, P. J.;Koper, M. T. M., Intermediate stages of electrochemical oxidation of single-crystalline platinum revealed by in situ Raman spectroscopy. *Nat Commun* **2016,** *7*, 12440.

103 Friebel, D.;Miller, D. J.;O'Grady, C. P.;Anniyev, T.;Bargar, J.;Bergmann, U.;Ogasawara, H.;Wikfeldt, K. T.;Pettersson, L. G.;Nilsson, A., In situ X-ray probing reveals fingerprints of surface platinum oxide. *Phys Chem Chem Phys* **2011,** *13* (1), 262-266.

104 Merte, L. R.;Behafarid, F.;Miller, D. J.;Friebel, D.;Cho, S.;Mbuga, F.;Sokaras, D.;Alonso-Mori, R.;Weng, T.-C.;Nordlund, D.;Nilsson, A.;Roldan Cuenya, B., Electrochemical Oxidation of Size-Selected Pt Nanoparticles Studied Using in Situ High-Energy-Resolution X-ray Absorption Spectroscopy. *ACS Catal.* **2012,** *2* (11), 2371-2376.

105 Sasaki, K.;Marinkovic, N.;Isaacs, H. S.;Adzic, R. R., Synchrotron-Based In Situ Characterization of Carbon-Supported Platinum and Platinum Mono layer Electrocatalysts. *ACS Catalysis* **2016,** *6* (1), 69-76.

106 Imai, H.;Izumi, K.;Matsumoto, M.;Kubo, Y.;Kato, K.;Imai, Y., In Situ and Real-Time Monitoring of Oxide Growth in a Few Monolayers at Surfaces of Platinum Nanoparticles in Aqueous Media. *Journal of the American Chemical Society* **2009,** *131* (17), 6293-6300.

107 Nagasawa, K.;Takao, S.;Higashi, K.;Nagamatsu, S.;Samjeske, G.;Imaizumi, Y.;Sekizawa, O.;Yamamoto, T.;Uruga, T.;Iwasawa, Y., Performance and durability of Pt/C cathode catalysts with different kinds of carbons for polymer electrolyte fuel cells characterized by electrochemical and in situ XAFS techniques. *Phys Chem Chem Phys* **2014,** *16* (21), 10075-10087.

108 Hatanaka, M.;Takahashi, N.;Takahashi, N.;Tanabe, T.;Nagai, Y.;Suda, A.;Shinjoh, H., Reversible changes in the Pt oxidation state and nanostructure on a ceria-based supported Pt. *Journal of Catalysis* **2009,** *266* (2), 182-190.

109 Rudi, S.;Gan, L.;Cui, C. H.;Gliech, M.;Strasser, P., Electrochemical Dealloying of Bimetallic ORR Nanoparticle Catalysts at Constant Electrode Potentials. *Journal of the Electrochemical Society* **2015,** *162* (4), F403-F409.

110 Thust, A.;Barthel, J.;Tillmann, K., FEI Titan 80-300 TEM. *Journal of large-scale research facilities JLSRF* **2016,** *2*.

111 Kovács, A.;Schierholz, R.;Tillmann, K., FEI Titan G2 80-200 CREWLEY. *Journal of large-scale research facilities JLSRF* **2016,** *2*.

112 Niether, C.;Rau, M. S.;Cremers, C.;Jones, D. J.;Pinkwart, K.;Tübke, J., Development of a novel experimental DEMS set-up for electrocatalyst characterization under working conditions of high temperature polymer electrolyte fuel cells. *Journal of Electroanalytical Chemistry* **2015,** *747*, 97-103.

113 Baltruschat, H., Differential electrochemical mass spectrometry. *J. Am. Soc. Mass Spectrom.* **2004,** *15* (12), 1693-1706.

114 Biesinger, M. C.;Payne, B. P.;Grosvenor, A. P.;Lau, L. W. M.;Gerson, A. R.;Smart, R. S., Resolving surface chemical states in XPS analysis of first row transition metals, oxides and hydroxides: Cr, Mn, Fe, Co and Ni. *Appl. Surf. Sci.* **2011,** *257* (7), 2717-2730.

115 Yeh, J. J.;Lindau, I., Atomic Subshell Photoionization Cross-Sections and Asymmetry Parameters - 1 Less-Than-or-Equal-to Z Less-Than-or-Equal-to 103. *At. Data Nucl. Data Tables* **1985,** *32* (1), 1-155.

116 https://www.energy.gov/sites/prod/files/2016/06/f32/fcto_myrdd_fuel_cells.pdf (accessed 17.07.2018).

117 Rudi, S.;Cui, C.;Gan, L.;Strasser, P., Comparative Study of the Electrocatalytically Active Surface Areas (ECSAs) of Pt Alloy Nanoparticles Evaluated by Hupd and CO-stripping voltammetry. *Electrocatalysis* **2014,** *5* (4), 408-418.

118 Cherevko, S.;Zeradjanin, A. R.;Topalov, A. A.;Keeley, G. P.;Mayrhofer, K. J. J., Effect of Temperature on Gold Dissolution in Acidic Media. *Journal of the Electrochemical Society* **2014,** *161* (9), H501-H507.

119 Schuppert, A. K.;Topalov, A. A.;Katsounaros, I.;Klemm, S. O.;Mayrhofer, K. J. J., A Scanning Flow Cell System for Fully Automated Screening of Electrocatalyst Materials. *Journal of the Electrochemical Society* **2012,** *159* (11), F670-F675.

120 Rietveld, H. M., A Profile Refinement Method for Nuclear and Magnetic Structures. *Journal of Applied Crystallography* **1969,** *2*, 65.

121 Rietveld, H. M., Line profiles of neutron powder-diffraction peaks for structure refinement. *Acta Crystallography* **1967,** *22*, 151.

122 Albinati, A.;Willis, B. T. M., The Rietveld method. *International Tables for Crystallography Vol. C* **2006**, 710-712.

123 Ahtee, M.;Unonius, L.;Nurmela, M.;Suortti, P., A Voigtian as Profile Shape Function in Rietveld Refinement. *Journal of Applied Crystallography* **1984,** *17* (Oct), 352-357.

124 Young, R. A.;Wiles, D. B., Profile Shape Functions in Rietveld Refinements. *Journal of Applied Crystallography* **1982,** *15* (Aug), 430-438.

125 Young, R. A.;Wiles, D. B., Profile Shape Functions in Rietveld Refinement. *Journal of Applied Crystallography* **1982,** *15*, 430-438.

126 Will, G., *Powder Diffraction: The Rietveld Method and the Two Stage Method to Determine and Refine Crystal Structures from Powder Diffraction Data*. Springer Science & Business Media: 2006.

127 Ectors, D.;Goetz-Neunhoeffer, F.;Neubauer, J., Domain size anisotropy in the double-Voigt approach: an extended model. *J Appl Crystallogr* **2015,** *48*, 1998-2001.

128 Ectors, D.;Goetz-Neunhoeffer, F.;Neubauer, J., A generalized geometric approach to anisotropic peak broadening due to domain morphology. *J Appl Crystallogr* **2015,** *48*, 189-194.

129 Li, T.;Senesi, A. J.;Lee, B., Small Angle X-ray Scattering for Nanoparticle Research. *Chem Rev* **2016**.

130 Brumberger, H.;Hagrman, D.;Goodisman, J.;Finkelstein, K. D., In situanomalous small-angle X-ray scattering from metal particles in supported-metal catalysts. II. Results. *Journal of Applied Crystallography* **2005,** *38* (2), 324-332.

131 Schnablegger, H.;Singh, Y., The SAXS Guide - Getting acquainted with the principles. Anton Paar GmbH: 2011.

132 Tuaev, X.;Strasser, P., Small angle X-ray scattering (SAXS) techniques for polymer electrolyte membrane fuel cell characterization. In *Polymer Electrolyte Membrane and Direct Methanol Fuel Cell Technology - In Situ Characterization Techniques for Low Temperature*

*Fuel Cells*, Christoph Hartnig & Christina Roth, Eds. Woodhead Publishing Limited: 2012; Vol. 2, pp 87-119.

133 Guinier, A.;Fournet, G.;Walker, C. B.;Yudowitch, K. L., *Small-Angle Scattering of X-Rays* Wiley: New York, 1955.

134 Brumberger, H.;Hagrman, D.;Goodisman, J.;Finkelstein, K. D., In situanomalous small-angle X-ray scattering from metal particles in supported-metal catalysts. I. Theory. *Journal of Applied Crystallography* **2005,** *38* (1), 147-151.

135 Haubold, H. G.;Vad, T.;Waldofner, N.;Bonnemann, H., From Pt molecules to nanoparticles: in-situ (anomalous) small-angle X-ray scattering studies. *Journal of Applied Crystallography* **2003,** *36* (1), 617-620.

136 Cuesta, A.;Couto, A.;Rincón, A.;Pérez, M. C.;López-Cudero, A.;Gutiérrez, C., Potential dependence of the saturation CO coverage of Pt electrodes: The origin of the pre-peak in CO-stripping voltammograms. Part 3: Pt(poly). *Journal of Electroanalytical Chemistry* **2006,** *586* (2), 184-195.

137 López-Cudero, A.;Cuesta, Á.;Gutiérrez, C., Potential dependence of the saturation CO coverage of Pt electrodes: The origin of the pre-peak in CO-stripping voltammograms. Part 2: Pt(100). *Journal of Electroanalytical Chemistry* **2006,** *586* (2), 204-216.

138 Maillard, F.;Eikerling, M.;Cherstiouk, O. V.;Schreier, S.;Savinova, E.;Stimming, U., Size effects on reactivity of Pt nanoparticles in CO monolayer oxidation: The role of surface mobility. *Faraday Discussions* **2004,** *125*, 357-377.

139 van der Vliet, D. F.;Wang, C.;Li, D. G.;Paulikas, A. P.;Greeley, J.;Rankin, R. B.;Strmcnik, D.;Tripkovic, D.;Markovic, N. M.;Stamenkovic, V. R., Unique Electrochemical Adsorption Properties of Pt-Skin Surfaces. *Angew Chem Int Edit* **2012,** *51* (13), 3139-3142.

140 Borchert, H.;Shevehenko, E. V.;Robert, A.;Mekis, I.;Kornowski, A.;Grubel, G.;Weller, H., Determination of nanocrystal sizes: A comparison of TEM, SAXS, and XRD studies of highly monodisperse COPt3 particles. *Langmuir* **2005,** *21* (5), 1931-1936.

141 Cherevko, S.;Zeradjanin, A. R.;Keeley, G. P.;Mayrhofer, K. J. J., A Comparative Study on Gold and Platinum Dissolution in Acidic and Alkaline Media. *Journal of the Electrochemical Society* **2014,** *161* (12), H822-H830.

142 Wang, L.;Dionigi, F.;Nguyen, N. T.;Kirchgeorg, R.;Gliech, M.;Grigorescu, S.;Strasser, P.;Schmuki, P., Tantalum Nitride Nanorod Arrays: Introducing Ni–Fe Layered Double Hydroxides as a Cocatalyst Strongly Stabilizing Photoanodes in Water Splitting. *Chemistry of Materials* **2015,** *27* (7), 2360-2366.

143 Diebold, U., The surface science of titanium dioxide. *Surface Science Reports* **2003,** *48* (5-8), 53-229.

144 Fu, Q.;Wagner, T., Interaction of nanostructured metal overlayers with oxide surfaces. *Surface Science Reports* **2007,** *62* (11), 431-498.

145 Fu, Q.;Wagner, T.;Olliges, S.;Carstanjen, H. D., Metal-oxide interfacial reactions: Encapsulation of Pd on TiO2 (110). *J Phys Chem B* **2005,** *109* (2), 944-951.

146 O'Shea, V. A.;Galvan, M. C.;Prats, A. E.;Campos-Martin, J. M.;Fierro, J. L., Direct evidence of the SMSI decoration effect: the case of Co/TiO2 catalyst. *Chem Commun (Camb)* **2011,** *47* (25), 7131-7133.

147 Yoshida, M.;Takanabe, K.;Maeda, K.;Ishikawa, A.;Kubota, J.;Sakata, Y.;Ikezawa, Y.;Domen, K., Role and Function of Noble-Metal/Cr-Layer Core/Shell Structure Cocatalysts for Photocatalytic Overall Water Splitting Studied by Model Electrodes. *J Phys Chem C* **2009,** *113* (23), 10151-10157.

148 Bonanni, S.;Aït-Mansour, K.;Brune, H.;Harbich, W., Overcoming the Strong Metal−Support Interaction State: CO Oxidation on TiO2(110)-Supported Pt Nanoclusters. *ACS Catalysis* **2011,** *1* (4), 385-389.

149 Willinger, M. G.;Zhang, W.;Bondarchuk, O.;Shaikhutdinov, S.;Freund, H. J.;Schlogl, R., A Case of Strong Metal-Support Interactions: Combining Advanced Microscopy and Model Systems to Elucidate the Atomic Structure of Interfaces. *Angew Chem Int Edit* **2014,** *53* (23), 5998-6001.

150 Shi, X. Y.;Zhang, W.;Zhang, C.;Zheng, W. T.;Chen, H.;Qi, J. G., Real-space observation of strong metal-support interaction: state-of-the-art and what's the next. *J Microsc-Oxford* **2016,** *262* (3), 203-215.

151 Spoeri, C.;Kwan, J. T.;Bonakdarpour, A.;Wilkinson, D.;Strasser, P., The Stability Challenges of Oxygen Evolving Electrocatalysts: Towards a Common Fundamental Understanding and Mitigation of Catalyst Degradation. *Angew Chem Int Ed Engl* **2016**.

152 Micoud, F.;Maillard, F.;Bonnefont, A.;Job, N.;Chatenet, M., The role of the support in CO(ads) monolayer electrooxidation on Pt nanoparticles: Pt/WO(x)vs. Pt/C. *Phys Chem Chem Phys* **2010,** *12* (5), 1182-1193.

153 Dionigi, F.;Vesborg, P. C. K.;Pedersen, T.;Hansen, O.;Dahl, S.;Xiong, A.;Maeda, K.;Domen, K.;Chorkendorff, I., Suppression of the water splitting back reaction on GaN:ZnO photocatalysts loaded with core/shell cocatalysts, investigated using a μ-reactor. *Journal of Catalysis* **2012,** *292*, 26-31.

154 Rizo, R.;Lázaro, M. J.;Pastor, E.;Koper, M. T. M., Ethanol Oxidation on Sn-modified Pt Single-Crystal Electrodes: New Mechanistic Insights from On-line Electrochemical Mass Spectrometry. *ChemElectroChem* **2016**.

155 Kakinuma, K.;Chino, Y.;Senoo, Y.;Uchida, M.;Kamino, T.;Uchida, H.;Deki, S.;Watanabe, M., Characterization of Pt catalysts on Nb-doped and Sb-doped SnO2–δ support materials with aggregated structure by rotating disk electrode and fuel cell measurements. *Electrochimica Acta* **2013,** *110*, 316-324.

156 Nakada, M.;Ishihara, A.;Mitsushima, S.;Kamiya, N.;Ota, K., Effect of tin oxides on oxide formation and reduction of platinum particles. *Electrochem Solid St* **2007,** *10* (1), F1-F4.

157 Santos, M. C.;Bulhoes, L. O. S., The underpotential deposition of Sn on Pt in acid media. Cyclic voltarnmetric and electrochemical quartz crystal microbalance studies. *Electrochimica Acta* **2003,** *48* (18), 2607-2614.

158 Oh, H.-S.;Nong, H. N.;Reier, T.;Bergmann, A.;Gliech, M.;Ferreira de Araújo, J.;Willinger, E.;Schlögl, R.;Teschner, D.;Strasser, P., Electrochemical Catalyst–Support Effects and Their Stabilizing Role for IrOxNanoparticle Catalysts during the Oxygen Evolution Reaction. *Journal of the American Chemical Society* **2016,** *138* (38), 12552-12563.

159 Vayssilov, G. N.;Lykhach, Y.;Migani, A.;Staudt, T.;Petrova, G. P.;Tsud, N.;Skala, T.;Bruix, A.;Illas, F.;Prince, K. C.;Matolin, V.;Neyman, K. M.;Libuda, J., Support nanostructure boosts oxygen transfer to catalytically active platinum nanoparticles. *Nat. Mater.* **2011,** *10* (4), 310-315.

160 Pietrzak, R.;Wachowska, H., The influence of oxidation with HNO3 on the surface composition of high-sulphur coals: XPS study. *Fuel Process. Technol.* **2006,** *87* (11), 1021-1029.

161 Batich, C. D.;Donald, D. S., X-ray photoelectron spectroscopy of nitroso compounds: relative ionicity of the closed and open forms. *J. Am. Chem. Soc.* **1984,** *106* (10), 2758-2761.

162 Yang, C.-M.;Kim, D. Y.;Lee, Y. H., Formation of Densely Packed Single-Walled Carbon Nanotube Assembly. *Chem. Mater.* **2005,** *17*, 6422-6429.

163 Beermann, V.;Gocyla, M.;Kuhl, S.;Padgett, E.;Schmies, H.;Goerlin, M.;Erini, N.;Shviro, M.;Heggen, M.;Dunin-Borkowski, R. E.;Muller, D. A.;Strasser, P., Tuning the Electrocatalytic Oxygen Reduction Reaction Activity and Stability of Shape-Controlled Pt-Ni Nanoparticles by Thermal Annealing - Elucidating the Surface Atomic Structural and Compositional Changes. *J. Am. Chem. Soc.* **2017,** *139* (46), 16536-16547.

164 Aran-Ais, R. M.;Dionigi, F.;Merzdorf, T.;Gocyla, M.;Heggen, M.;Dunin-Borkowski, R. E.;Gliech, M.;Solla-Gullon, J.;Herrero, E.;Feliu, J. M.;Strasser, P., Elemental Anisotropic Growth and Atomic-Scale Structure of Shape-Controlled Octahedral Pt-Ni-Co Alloy Nanocatalysts. *Nano Lett.* **2015,** *15* (11), 7473-7480.

165 Tuaev, X.;Rudi, S.;Strasser, P., The impact of the morphology of the carbon support on the activity and stability of nanoparticle fuel cell catalysts. *Catal Sci Technol* **2016,** *6* (23), 8276-8288.

166 Asset, T.;Job, N.;Busby, Y.;Crisci, A.;Martin, V.;Stergiopoulos, V.;Bonnaud, C.;Serov, A.;Atanassov, P.;Chattot, R.;Dubau, L.;Maillard, F., Porous Hollow PtNi/C Electrocatalysts:

Carbon Support Considerations To Meet Performance and Stability Requirements. *ACS Cat.* **2018,** *8* (2), 893-903.

167 Hasche, F.;Oezaslan, M.;Strasser, P., Activity, stability and degradation of multi walled carbon nanotube (MWCNT) supported Pt fuel cell electrocatalysts. *Phys. Chem. Chem. Phys.* **2010,** *12* (46), 15251-15258.

168 Antolini, E., Graphene as a new carbon support for low-temperature fuel cell catalysts. *Appl. Catal., B* **2012,** *123-124*, 52-68.

169 Li, D.;Wang, C.;Strmcnik, D. S.;Tripkovic, D. V.;Sun, X.;Kang, Y.;Chi, M.;Snyder, J. D.;van der Vliet, D.;Tsai, Y.;Stamenkovic, V. R.;Sun, S.;Markovic, N. M., Functional links between Pt single crystal morphology and nanoparticles with different size and shape: the oxygen reduction reaction case. *Energy Environ. Sci.* **2014,** *7* (12), 4061-4069.

170 Beermann, V.;Gocyla, M.;Willinger, E.;Rudi, S.;Heggen, M.;Dunin-Borkowski, R. E.;Willinger, M.-G.;Strasser, P., Rh-Doped Pt–Ni Octahedral Nanoparticles: Understanding the Correlation between Elemental Distribution, Oxygen Reduction Reaction, and Shape Stability. *Nano Lett.* **2016,** *16* (3), 1719-1725.

171 Diehm, P. M.;Agoston, P.;Albe, K., Size-dependent lattice expansion in nanoparticles: reality or anomaly? *ChemPhysChem* **2012,** *13* (10), 2443-2454.

172 Lei, Y.;Jelic, J.;Nitsche, L. C.;Meyer, R.;Miller, J., Effect of Particle Size and Adsorbates on the L3, L2 and L1 X-ray Absorption Near Edge Structure of Supported Pt Nanoparticles. *Top. Catal.* **2011,** *54* (5-7), 334-348.

173 Dubau, L.;Nelayah, J.;Moldovan, S.;Ersen, O.;Bordet, P.;Drnec, J.;Asset, T.;Chattot, R.;Maillard, F., Defects do Catalysis: CO Monolayer Oxidation and Oxygen Reduction Reaction on Hollow PtNi/C Nanoparticles. *Acs Catalysis* **2016,** *6* (7), 4673-4684.

174 Merte, L. R.;Behafarid, F.;Miller, D. J.;Friebel, D.;Cho, S.;Mbuga, F.;Sokaras, D.;Alonso-Mori, R.;Weng, T.-C.;Nordlund, D.;Nilsson, A.;Roldan Cuenya, B., Electrochemical Oxidation of Size-Selected Pt Nanoparticles Studied Using in Situ High-Energy-Resolution X-ray Absorption Spectroscopy. *ACS Catalysis* **2012,** *2* (11), 2371-2376.

175 Ruge, M.;Drnec, J.;Rahn, B.;Reikowski, F.;Harrington, D. A.;Carla, F.;Felici, R.;Stettner, J.;Magnussen, O. M., Electrochemical Oxidation of Smooth and Nanoscale Rough Pt(111): An In Situ Surface X-ray Scattering Study. *Journal of the Electrochemical Society* **2017,** *164* (9), H608-H614.

176 Angerste.H;Conway, B. E.;Sharp, W. B. A., Real Condition of Electrochemically Oxidized Platinum Surfaces .1. Resolution of Component Processes. *J Electroanal Chem* **1973,** *43* (1), 9-36.

177 Conway, B. E., Electrochemical Oxide Film Formation at Noble-Metals as a Surface-Chemical Process. *Prog Surf Sci* **1995,** *49* (4), 331-452.

# Appendix

## A1 Supporting Information to Chapter 4[52]

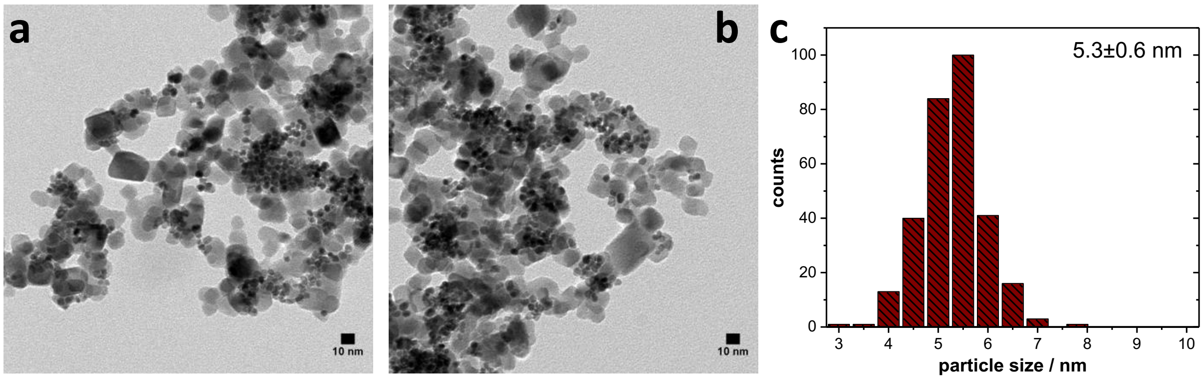

**Figure A1** TEM images of as prepared Pt nanoparticles on the ITO support which was used for the HP-AST experiments with a weight loading of 29.9 wt% (a,b) and the corresponding histogram showing particle size distribution (c). Histograms were obtained by measuring the diameter of at least 200 particles with errors obtained from standard deviation of mean particle diameter.

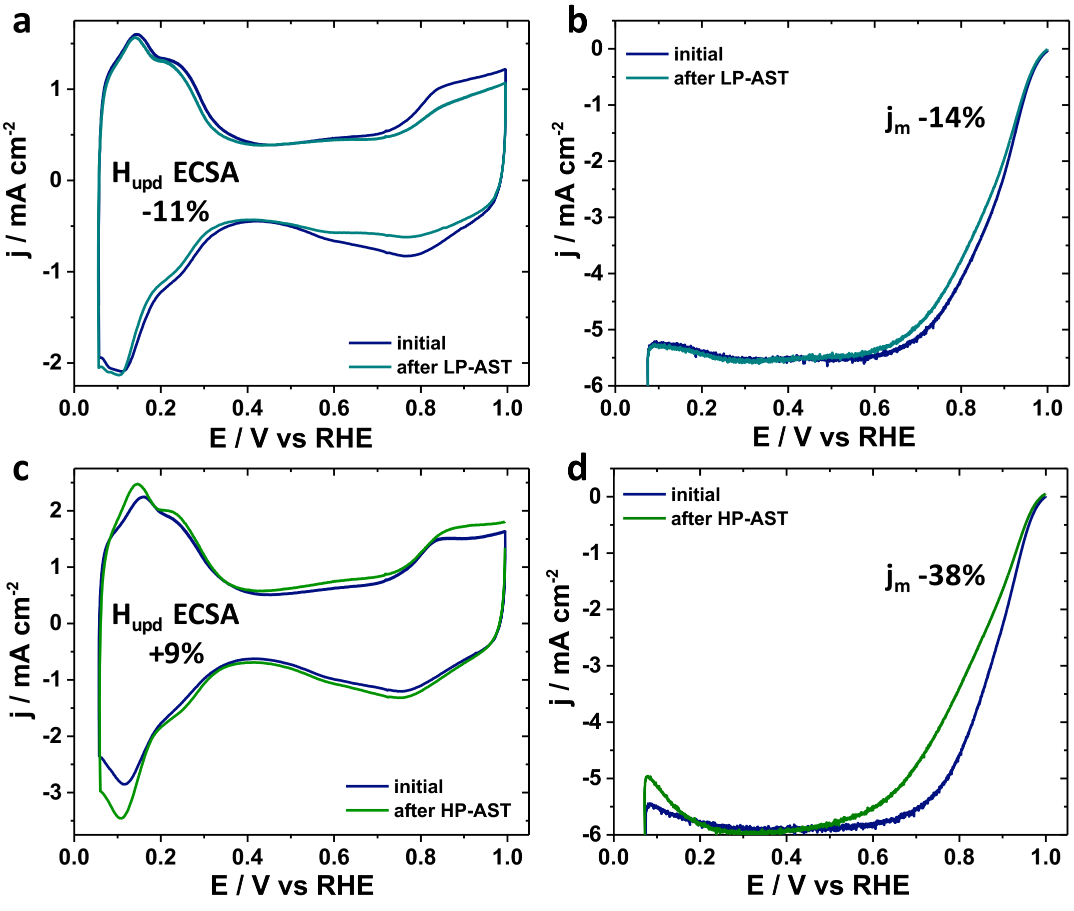

**Figure A2** Cyclic voltammograms of Pt/C reference catalyst (weight loading 20 wt% Pt on carbon) before and after potential cycling in lower (a) and higher (c) potential region. CVs were recorded in nitrogen saturated electrolyte from 0.05-1 V with a scan rate of 100 mV s$^{-1}$. Figure b and d are showing LSVs of the particular states LSVs were recorded in oxygen saturated electrolyte from 0.05-1 V with a scan rate of 5 mV·s$^{-1}$and 1600 rpm. All electrode potentials have been corrected for iR drop.

**Table A1** Comparison of ECSAs based on the integration in the $H_{upd}$ and the CO oxidation potential range. CO-ECSAs were determined by integrating the CO oxidation peak area from the first cycle of the CO stripping experiment after subtraction of the second cycle representing the bare CO-free surface. $H_{upd}$-ECSAs were determined by subtracting the first from the second cycle of the CO stripping experiment.

| **ECSA / $m^2\ g_{Pt}^{-1}$** | **LP-AST** | | **HP-AST** | |
|---|---|---|---|---|
| | **before** | **after** | **before** | **after** |
| CO | 25.6 | 18.4 | 28.9 | 27.4 |
| $H_{upd}$ | 18.6 | 17.0 | 19.3 | 26.1 |
| CO/$H_{upd}$ | 1.38 | 1.04 | 1.50 | 1.05 |

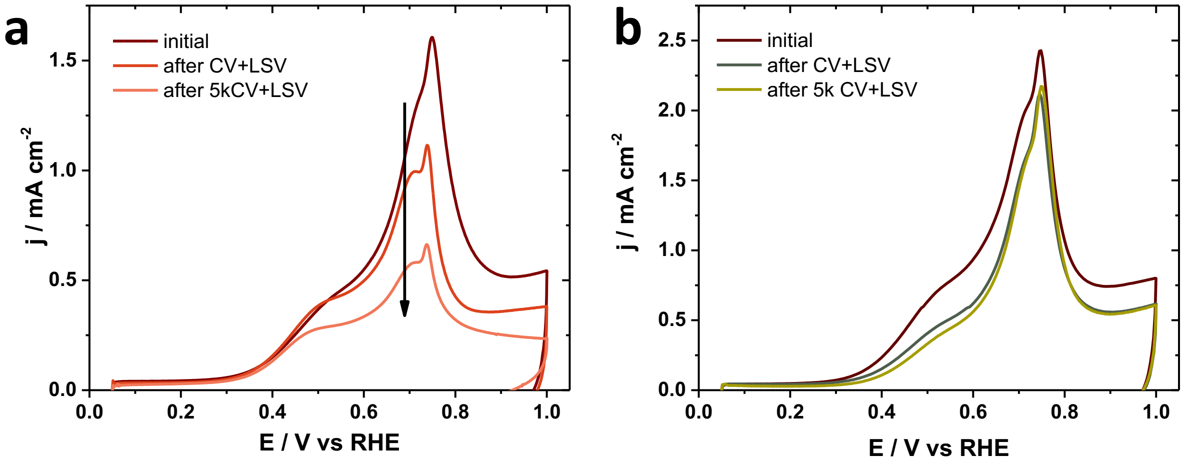

**Figure A3** Electrochemical CO stripping experiments for Pt/ITO electrocatalyst. For the two different stability tests in low (a) and high (b) potential regime three different points in the characterization protocol were chosen for CO stripping: initial, after CV+LSV and after 5k CV+LSV.

**Table A2** Comparison of $j_m$ and ECSA before and after LP- and HP-AST for Pt/C reference catalyst. $j_m$ was determined at 0.9 V. ECSAs were determined by integrating the H-desorption and adsorption area between 0.05-0.4 V and subtracting the capacitive current.

| | **LP-AST** | | **HP-AST** | |
|---|---|---|---|---|
| | **initial** | **after** | **initial** | **after** |
| $j_m$ / A $mg_{Pt}^{-1}$ | 0.18 | 0.15 | 0.16 | 0.10 |
| ECSA / $m^2\ g_{Pt}^{-1}$ | 61.1 | 54.0 | 61.4 | 67.0 |

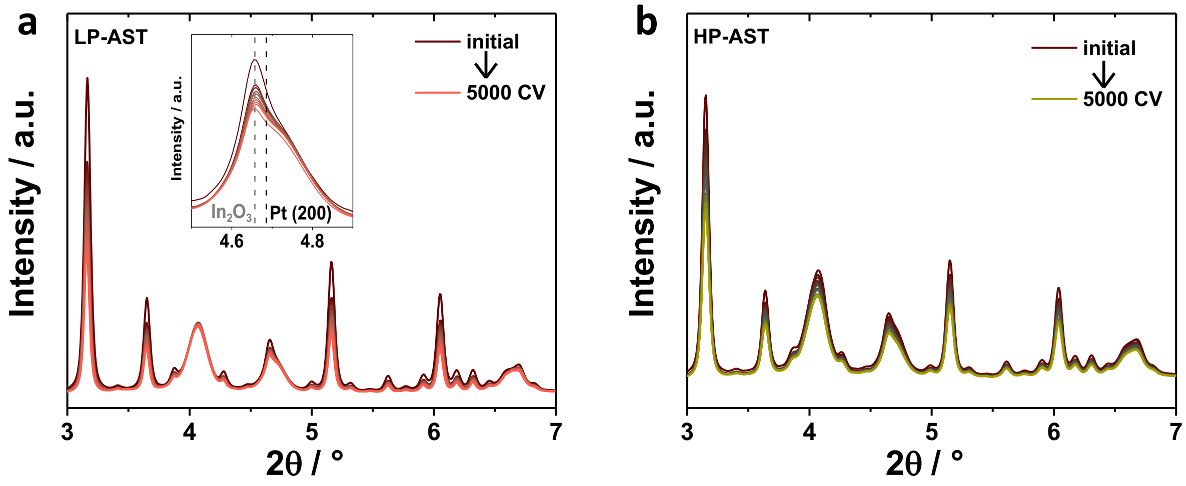

**Figure A4** *In situ* HE XRD measurements depicted as the evolution of diffraction patterns from the initial state to the end of the electrochemical cycling for the LP-AST (a) and the HP-AST (b). The inlet in (a) is showing the Pt (200) diffraction peak superimposed by an $In_2O_3$ peak (denoted with dashed vertical lines).

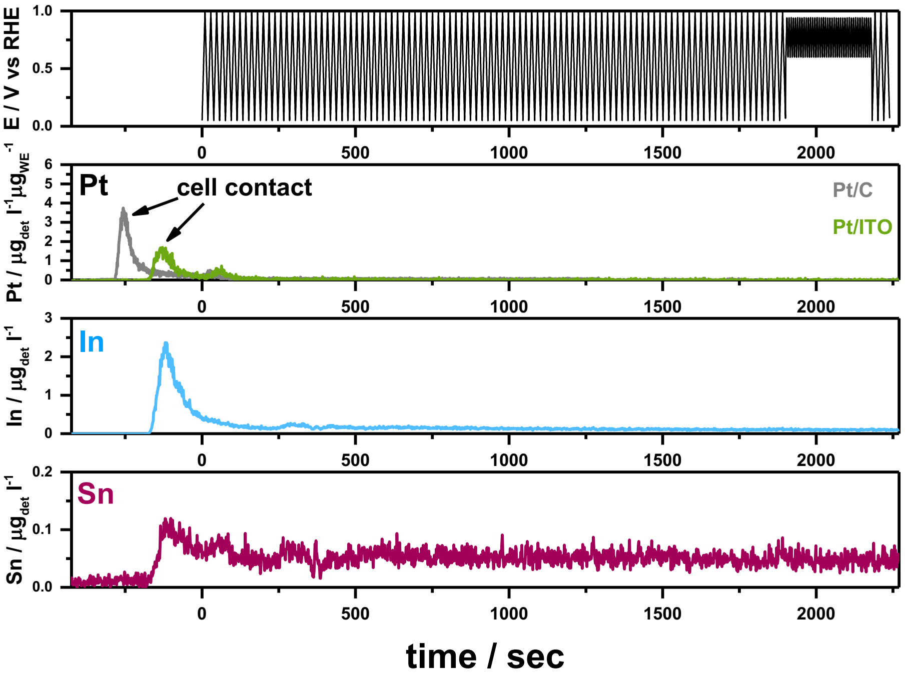

**Figure A5** *In situ* scanning flow cell ICP-MS measurements. Depicted are the Sn, In and Pt dissolution rates and the applied electrochemical protocols from the bottom to the top for LP-AST. The respective dissolution rates in detected metal per volume electrolyte ($\mu g_{det}\ l^{-1}$) are plotted against the time. A Pt/C reference sample was measured and therefore, the Pt dissolution rate was also normalized to the Pt mass loading on the working electrode (WE) ($\mu g_{det}\ l^{-1} \mu g_{WE}^{-1}$). The electrochemical protocol was conducted as follows: Beginning with 100 CVs (activation regime) from 0.05-1 V, followed by potential cycling in the LP regime (0.6-0.95 V, 40 CVs, 100 mV·s$^{-1}$) and followed by another 3 cycles from 0.05-1 V, all CVs were recorded with a scan rate of 100mV s$^{-1}$. The first contacts between catalyst and electrolyte (cell contact) are denoted with arrows.

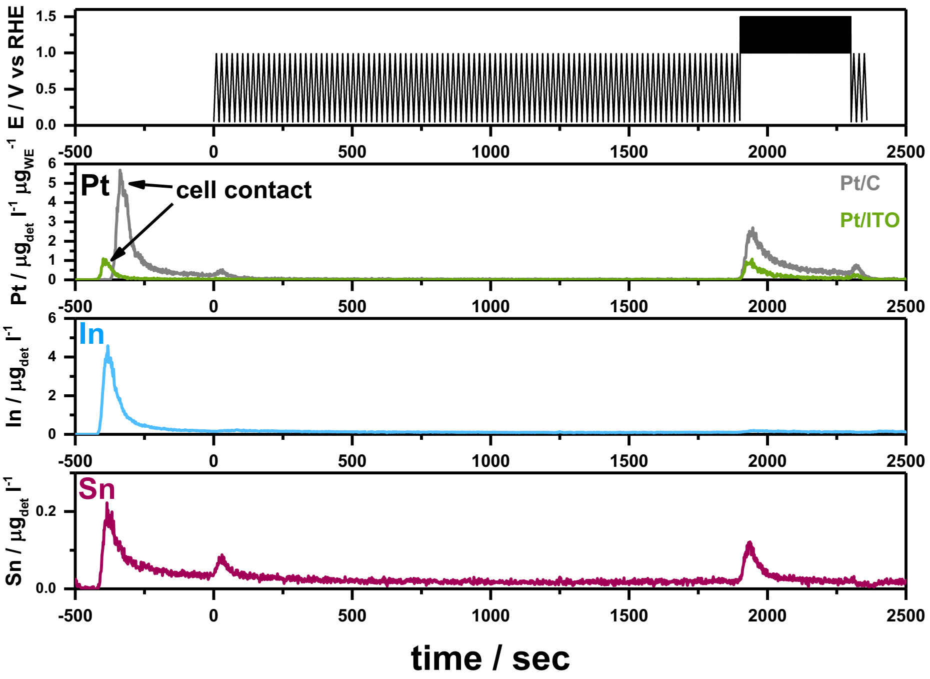

**Figure A6** *In situ* scanning flow cell ICP-MS measurements. Depicted are the Sn, In and Pt dissolution rates and the applied electrochemical protocols from the bottom to the top for HP-AST. The respective dissolution rates in detected metal per volume electrolyte (µg$_{det}$ l$^{-1}$) are plotted against the time. A Pt/C reference sample was measured and therefore, the Pt dissolution rate was also normalized to the Pt mass loading on the working electrode (WE) (µg$_{det}$ l$^{-1}$µg$_{WE}$$^{-1}$). The electrochemical protocol was conducted as follows: Beginning with 100 CVs (activation regime) from 0.05-1 V, followed by potential cycling in the HP regime (1.0-1.5 V, 200 CVs, 500 mV·s$^{-1}$) and followed by another 3 cycles from 0.05-1 V, all CVs were recorded with a scan rate of 100mV s$^{-1}$. The first contacts between catalyst and electrolyte (cell contact) are denoted with arrows.

**Table A3** Results from in situ SFC ICP-MS of the integration over time of the measurement of the peaks arising from Pt dissolution in Pt/ITO and Pt/C reference and In and Sn from ITO support. Pt dissolution in µg is normalized to Pt mass loading on the working electrode in µg$_{Pt}$ and In and Sn dissolution in µg is normalized to In+Sn mass loading on the working electrode in µg$_{(In+Sn)}$.Potential dissolution peaks are arising from cell contact, program start and distinct dissolution peaks during the electrochemical cycling (1st and 2nd peak).Additionally, dissolution values are listed each without (wo/) and with (w/) contribution of metal dissolution at cell contact.

| | **LP-AST** | | | | **HP-AST** | | | |
|---|---|---|---|---|---|---|---|---|
| **Dissolved Metal** | **Pt in Pt/ITO** | **Pt in Pt/C** | **In** | **Sn** | **Pt in Pt/ITO** | **Pt in Pt/C** | **In** | **Sn** |
| Unit | µg· µg$_{Pt}$ | | µg· µg$_{(In+Sn)}$ | | µg· µg$_{Pt}$ | | µg· µg$_{(In+Sn)}$ | |
| Cell Contact | 3.22E-4 | 6.13E-4 | 5.55E-3 | 3.52E-4 | 2.33E-4 | 1.23E-3 | 1.04E-2 | 1.19E-3 |
| Program Start | 7.47E-5 | 4.66E-5 | - | - | 7.22E-6 | 7.74E-5 | - | 2.80E-4 |
| 1st Peak | - | - | - | - | 3.38E-4 | 1.07E-3 | - | 3.00E-4 |
| 2nd Peak | - | - | - | - | 4.32E-5 | 1.12E-4 | - | - |
| Total wo/ Contact | 5.96E-5 | 3.36E-4 | 9.61E-3 | 3.41E-3 | 7.37E-4 | 1.68E-3 | 9.12E-3 | 3.96E-3 |
| Total w/ Contact | 3.80E-4 | 9.49E-4 | 1.51E-2 | 3.77E-3 | 9.69E-4 | 2.91E-3 | 1.95E-2 | 5.15E-3 |
| Total wo/ Contact % | 0.01 | 0.03 | 0.96 | 0.34 | 0.07 | 0.17 | 0.91 | 0.40 |
| Total w/ Contact % | 0.04 | 0.09 | 1.51 | 0.38 | 0.10 | 0.29 | 1.95 | 0.52 |

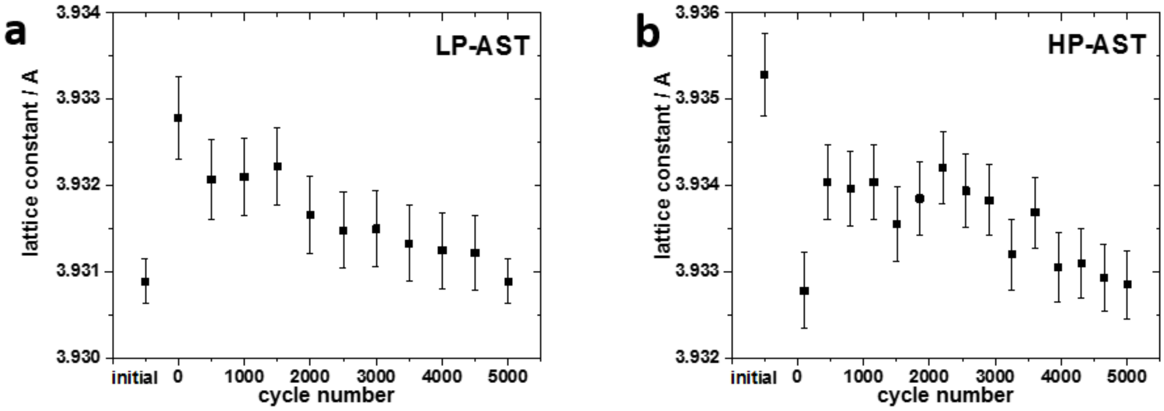

**Figure A7** Evolution of Pt lattice constant as extracted from Rietveld Refinement from *in situ* HE-XRD measurements over the cycle number for (a) LP-AST and (b) HP-AST.

# A2 Supporting Information to Chapter 5[71]

**Table A4** Elemental bulk and surface composition in at% of unmodified Vulcan, O-Vulcan and N-Vulcan 400°C and 800°C from elemental analysis, hot gas extraction and XPS.

| [at%] | **N**<br>bulk from elemental analysis | **C**<br>bulk from elemental analysis | **H**<br>bulk from elemental analysis | **N**<br>bulk from hot gas extraction | **O**<br>bulk from hot gas extraction | **N**<br>surface from XPS | **O**<br>surface from XPS | **C**<br>surface from XPS | **Ti**<br>(substrate) surface from XPS |
|---|---|---|---|---|---|---|---|---|---|
| **Vulcan** | 0.00 | 98.10 | 0.00 | - | - | 0 | 5.84 | 92.16 | 2.00 |
| **O-Vulcan** | 0.19 | 85.58 | 0.38 | 0.268 | 12.6 | 0.73 | 12.61 | 86.15 | 0.51 |
| **N-Vulcan 400°C** | 2.53 | 93.26 | 0.13 | 2.5 | 2.9 | 3.86 | 9.35 | 83.35 | 3.44 |
| **N-Vulcan 800°C** | 1.53 | 95.08 | 0.02 | 1.8 | 0.85 | 2.26 | 7.3 | 87.38 | 3.07 |

**Table A5** Pt weight loading (wt%) from ICP-OES for Pt/Vulcan, Pt/O-Vulcan, Pt/N-Vulcan 400°C and Pt/N-Vulcan 800°C.

| **Pt loading** | **[wt%]** |
|---|---|
| Pt/Vulcan | 20.1 |
| Pt/O-Vulcan | 23.1 |
| Pt/N-Vulcan 400°C | 19.8 |
| Pt/N-Vulcan 800°C | 20.9 |

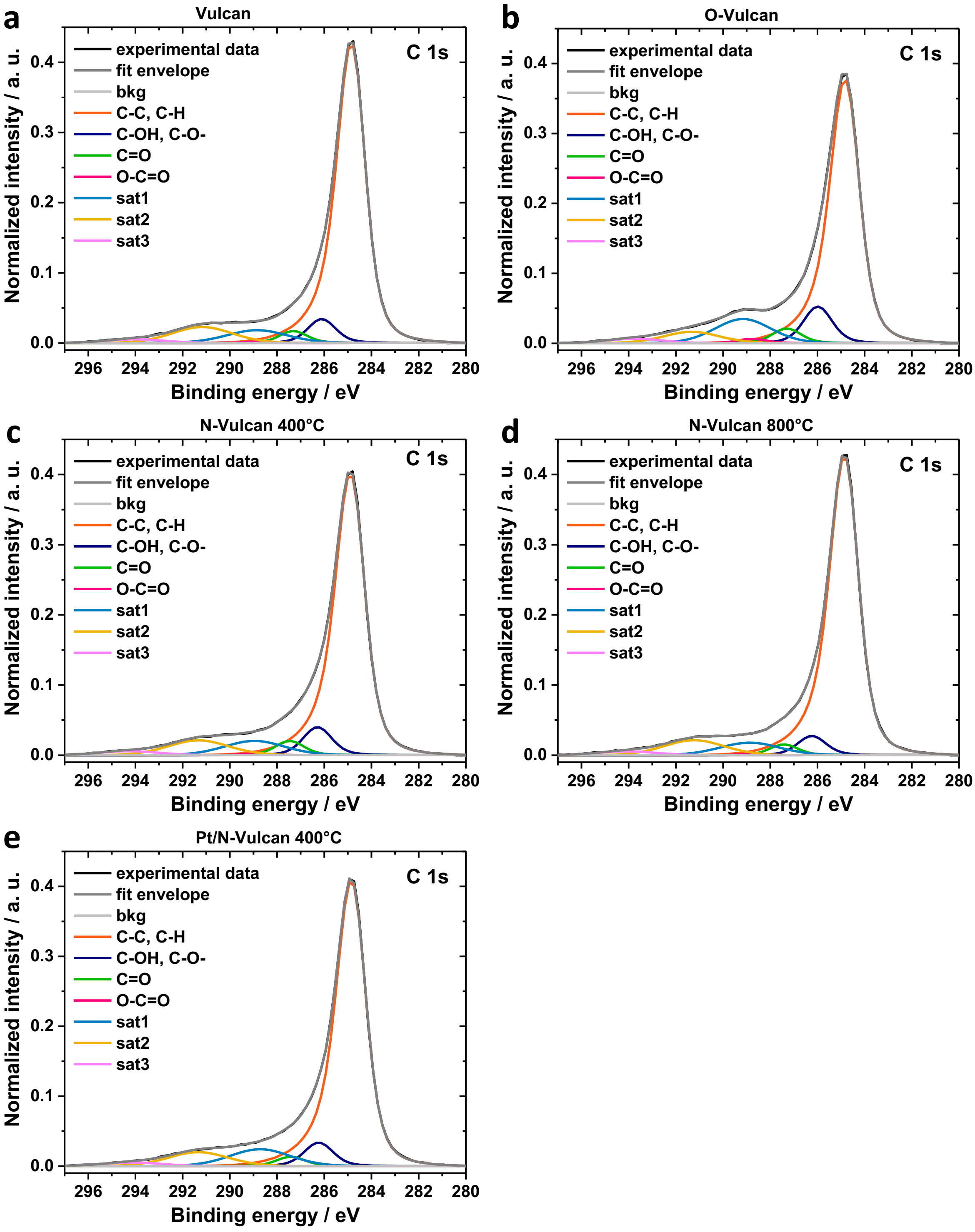

**Figure A8** XPS C 1s spectra and individual peak deconvolution for unmodified Vulcan (a), O-Vulcan (b), N-Vulcan 400° (c), N-Vulcan 800°C (d) and for Pt/N-Vulcan 400°C (e).

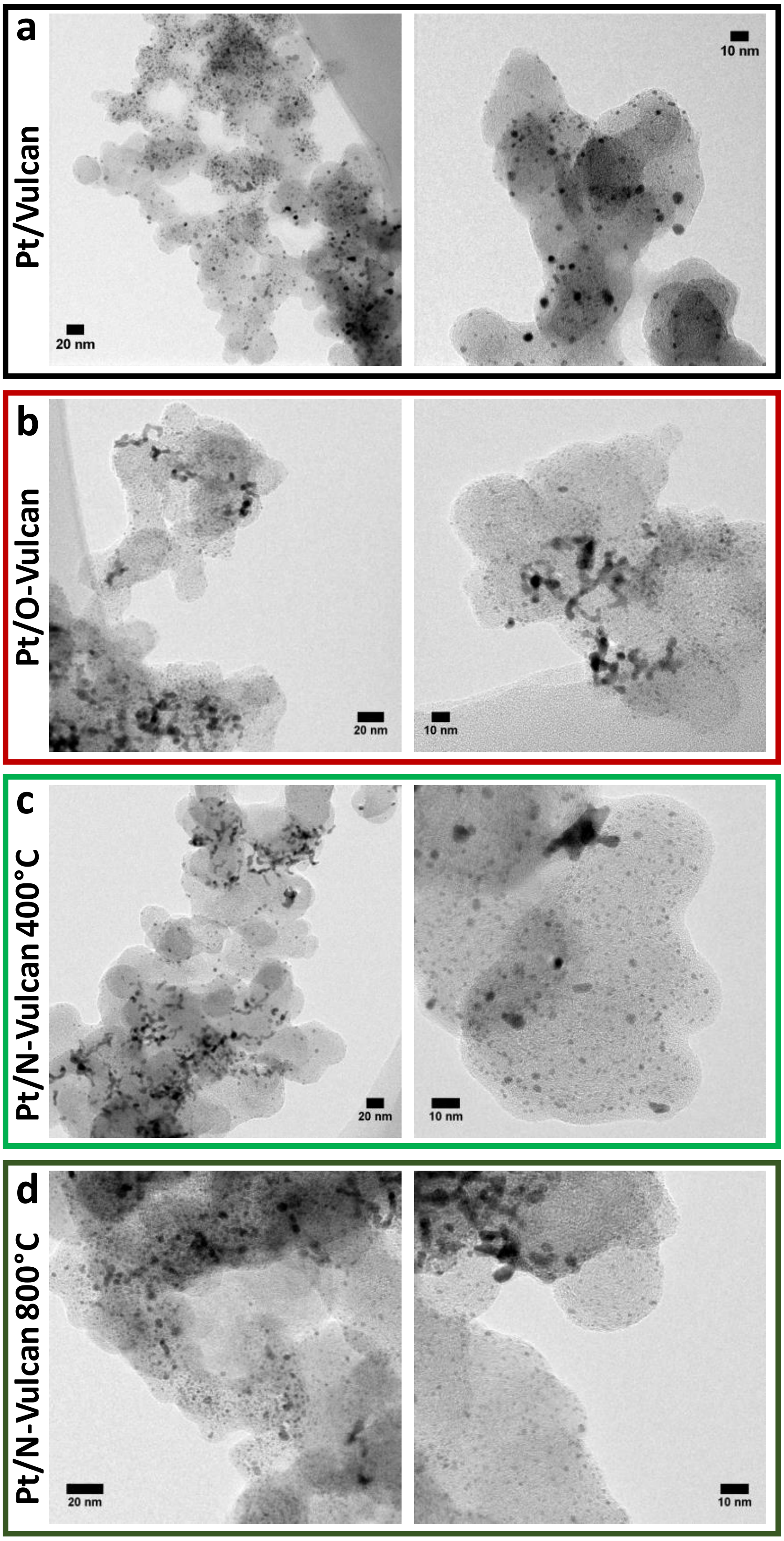
a
Pt/Vulcan
20 nm
10 nm
b
Pt/O-Vulcan
20 nm
10 nm
c
Pt/N-Vulcan 400°C
20 nm
10 nm
d
Pt/N-Vulcan 800°C
20 nm
10 nm

**Figure A9** TEM images for Pt on unmodified Vulcan (a), O-Vulcan (b), N-Vulcan 400°C (c), and N-Vulcan 800°C (d).

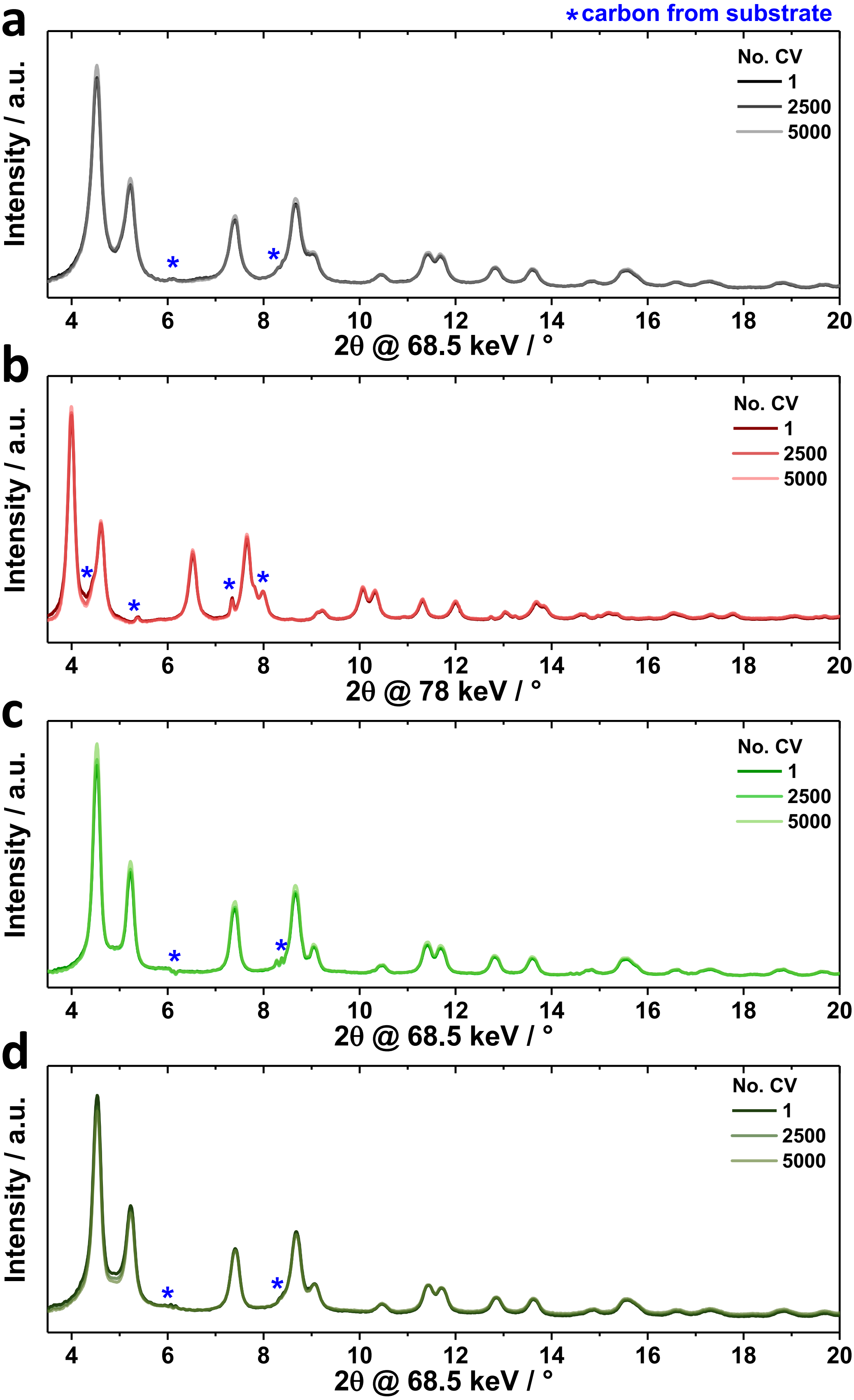

**Figure A10** *In situ* high energy X-ray diffraction patterns over 5k cycle of the AST for Pt/Vulcan (a), Pt/O-Vulcan (b), Pt/N-Vulcan 400°C (c) and Pt/N-Vulcan 800°C (d).

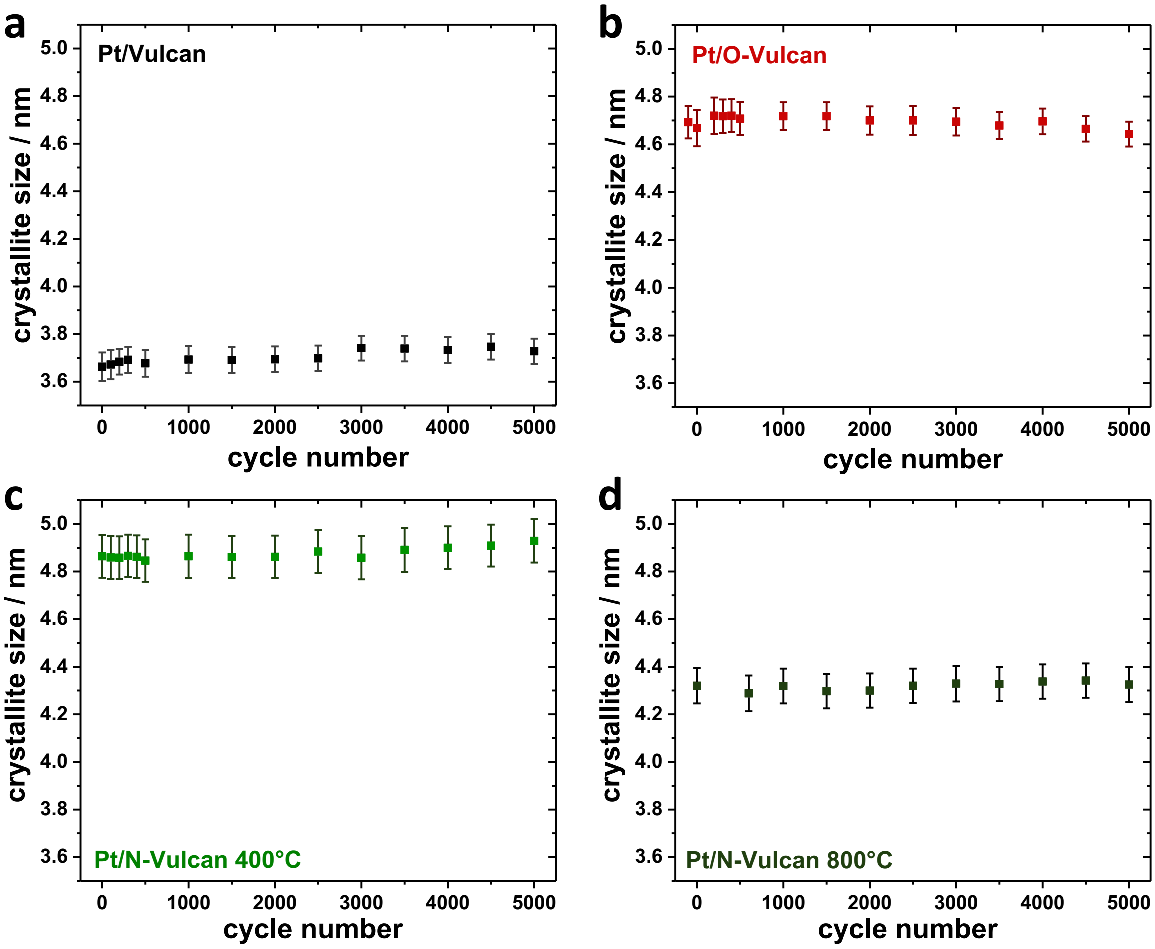

**Figure A11** Crystallite size from Rietveld refinement of the *in situ* high energy X-ray diffraction patterns over 5k cycle of the AST for Pt/Vulcan (a), Pt/O-Vulcan (b), Pt/N-Vulcan 400°C (c) and Pt/N-Vulcan 800°C (d).

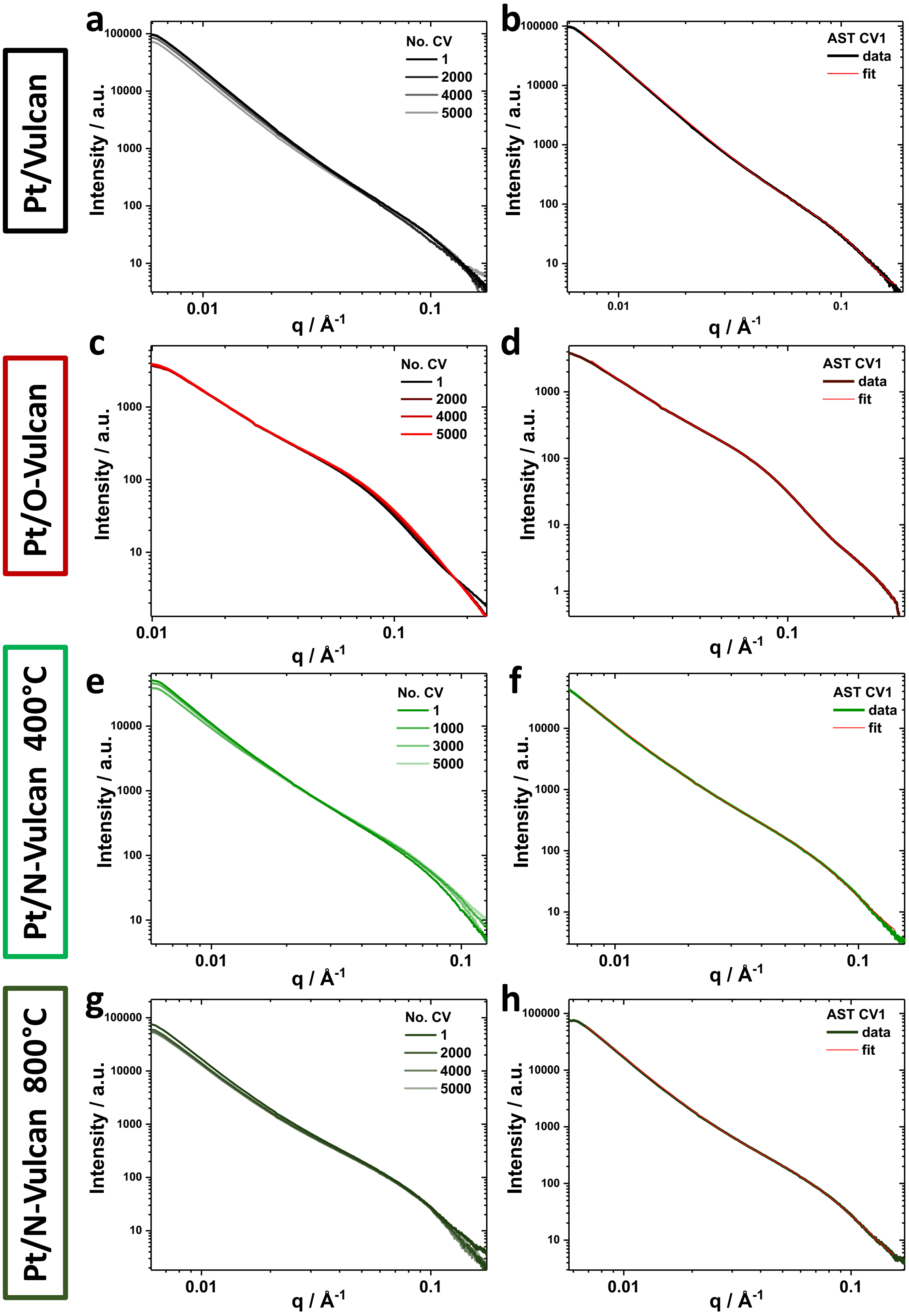

**Figure A12** *In situ* small angle X-ray scattering curves over 5k cycle of the AST for Pt/Vulcan, Pt/O-Vulcan, Pt/N-Vulcan 400°C and Pt/N-Vulcan 800°C (a,c,e,g) and scattering curves at start of the AST including the individual fit curves (b,d,f,h).

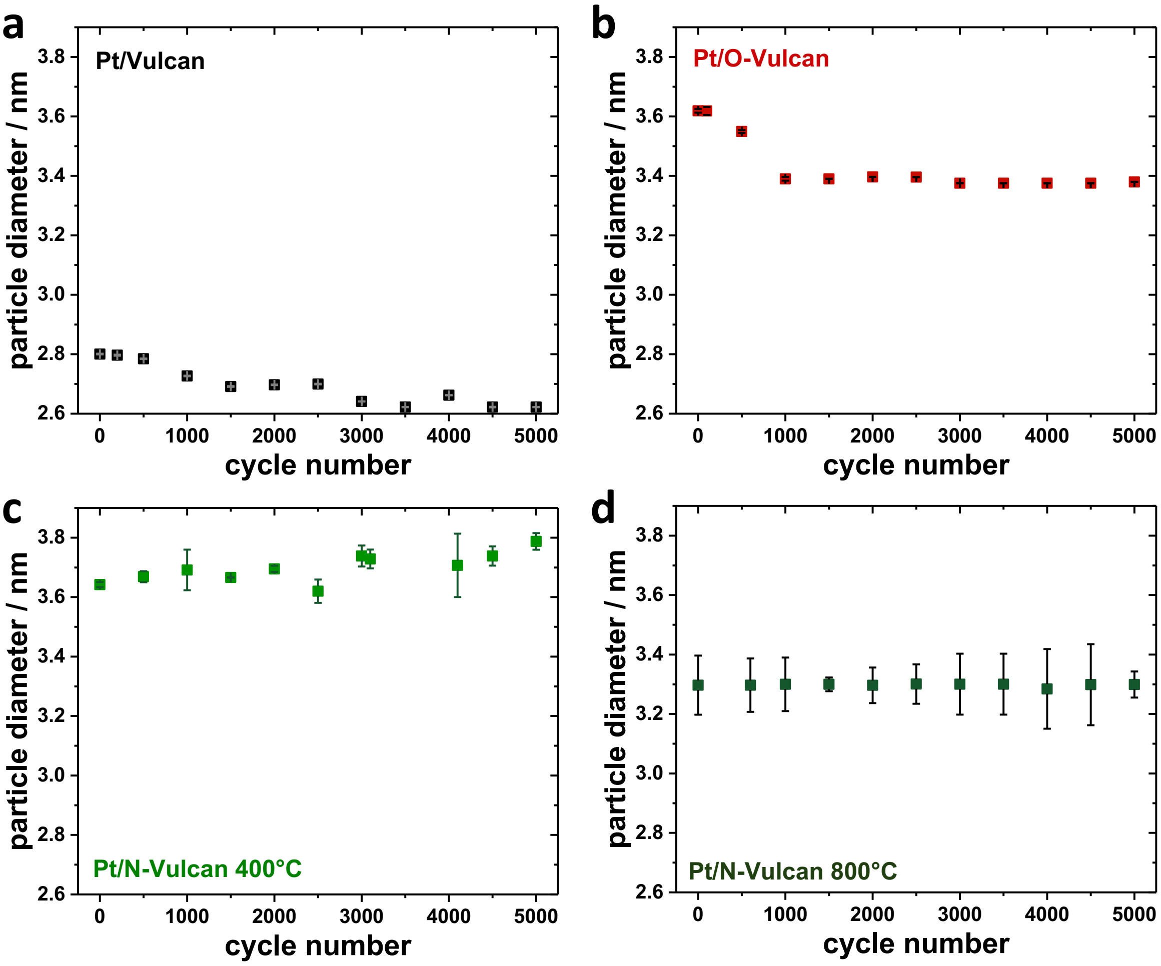

**Figure A13** Mean particle diameter from fit of the *in situ* small angle X-ray scattering curves over 5k cycle of the AST for Pt/Vulcan (a), Pt/O-Vulcan (b), Pt/N-Vulcan 400°C (c) and Pt/N-Vulcan 800°C (d).

# A3 Supporting Information to Chapter 6

**Table A6** Pt weight loading (wt%) for Pt on ITO, RTO and C as determined by ICP-OES analysis.

| **Pt loading** | **[wt%]** |
|---|---|
| Pt/C | 20.0 |
| Pt/ITO | 29.9 |
| Pt/RTO | 46.1 |

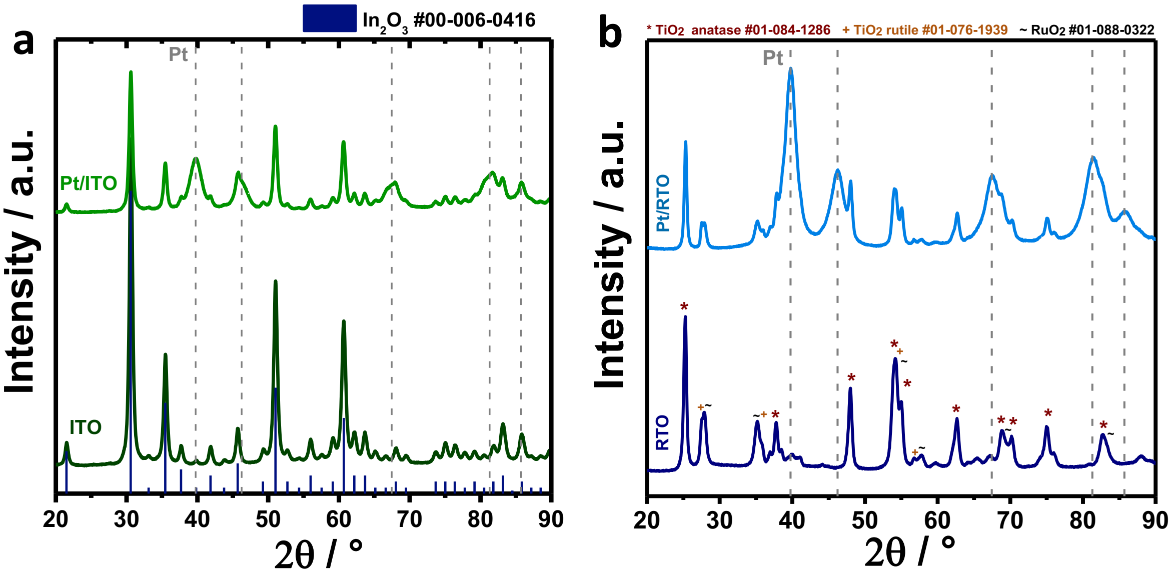

**Figure A14** X-ray diffractograms of (a) ITO and Pt/ITO with solid blue lines indicating $In_2O_3$ reference pattern and (b) RTO and Pt/RTO with symbols indicating $TiO_2$ anatase and rutile and $RuO_2$. Vertical dashed lines denote reference powder diffraction patterns of fcc Pt (PDF#00-004-0802). XRDs were obtained using Cu $K_\alpha$ radiation.

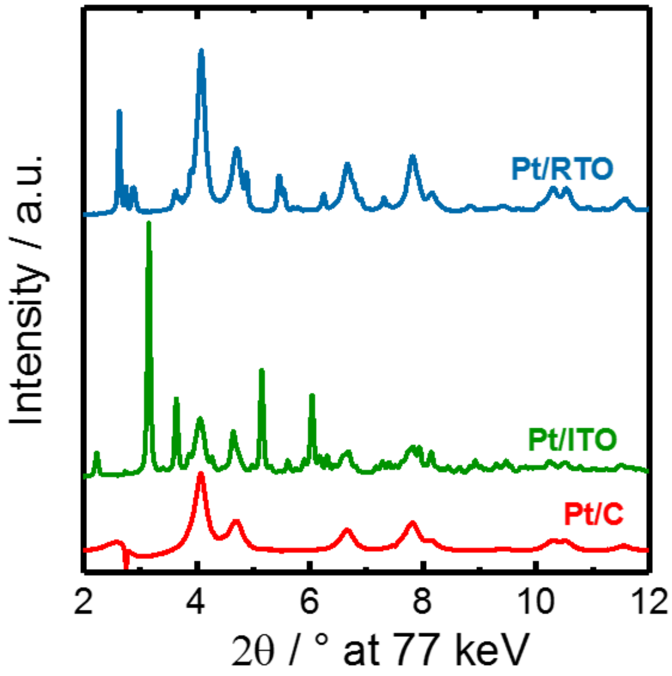

**Figure A15** High energy XRD patterns for Pt/RTO, Pt/ITO and Pt/C in the as-prepared state.

**Table A7** Crystallite diameter ($D_x$, $D_y$ and $D_z$) for ellipsoidal Pt particles on RTO and C support and for spherical particles on ITO as determined by Rietveld refinement of HE-XRD.

| | **crystallite diameter / nm** | | |
|---|---|---|---|
| | **$D_x$** | **$D_y$** | **$D_z$** |
| Pt/ITO | 4.06±0.09 | | |
| Pt/RTO | 3.28±0.05 | 4.54±0.11 | 2.44±0.02 |
| Pt/C | 2.32±0.04 | 2.46±0.05 | 1.78±0.02 |

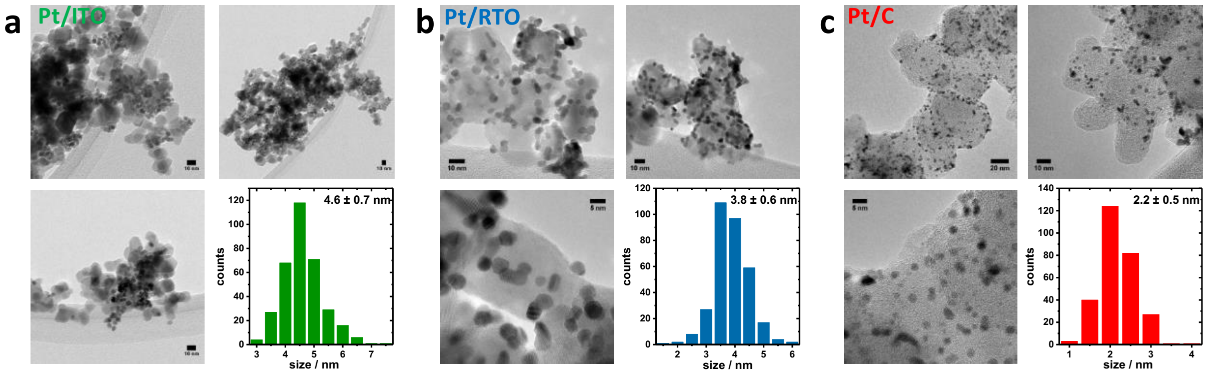
a
Pt/ITO
4.6 ± 0.7 nm
counts
size / nm
b
Pt/RTO
3.8 ± 0.6 nm
counts
size / nm
c
Pt/C
2.2 ± 0.5 nm
counts
size / nm

**Figure A16** Morphology of Pt nanoparticles on a) ITO (green), b) RTO (blue) and c) carbon (red) support and corresponding histograms showing mean particle diameter as determined by transmission electron microscopy. The particle size histogram was determined from analyzing > 200 particles along their shortest particle axes.

**Table A8** Structural parameters of Pt on ITO, RTO and C: $O_{td}$-incorporation and lattice constant by Rietveld refinement of HE-XRD.

| | **$O_{Td}$-incorporation** | **lattice parameter / Å** |
|---|---|---|
| Pt/ITO | 0.15±0.02 | 3.9301±E-4 |
| Pt/RTO | 0.000±0.016 | 3.9199±E-4 |
| Pt/C | 0.000±0.018 | 3.9136±E-4 |

**Table A9** Comparison of ECSA values based on the integration in the $H_{upd}$ region or the CO Oxidation peak area.

| **ECSA/ $m^2$ $g^{-1}$** | **$H_{upd}$** | **CO** |
|---|---|---|
| Pt/C | 63.1 | 67.5 |
| Pt/ITO | 17.8 | 25.6 |
| Pt/RTO | 19.0 | 16.7 |

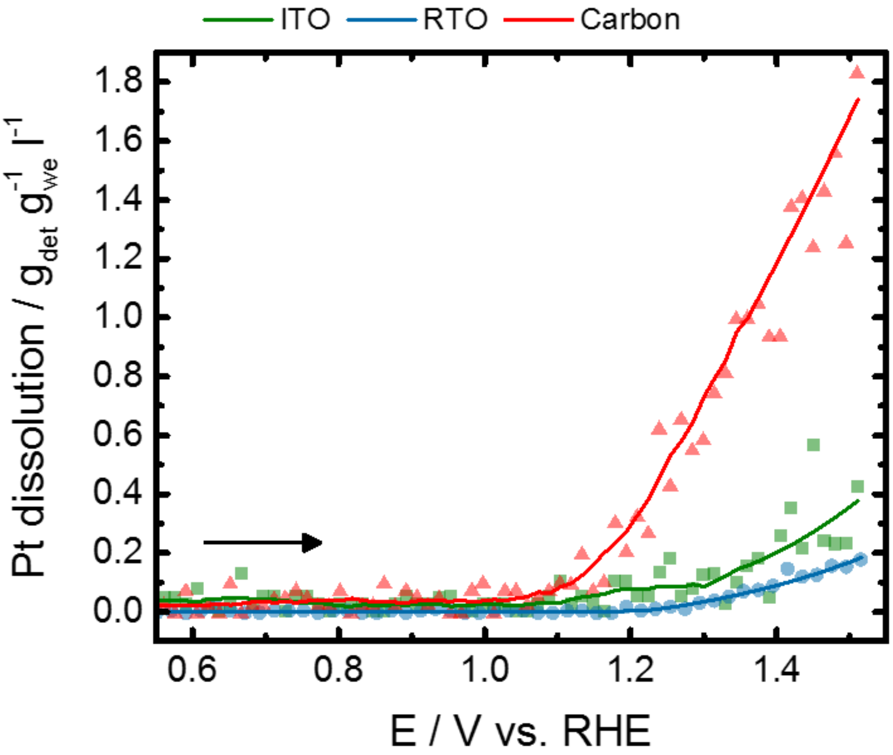

**Figure A17** Evolution of mass-normalized Pt dissolution rate as determined by SFC ICP-MS measurements during the initial anodic potential sweep from 0.05-1.5 V for Pt nanoparticles supported on ITO (green), RTO (blue), and carbon (red).

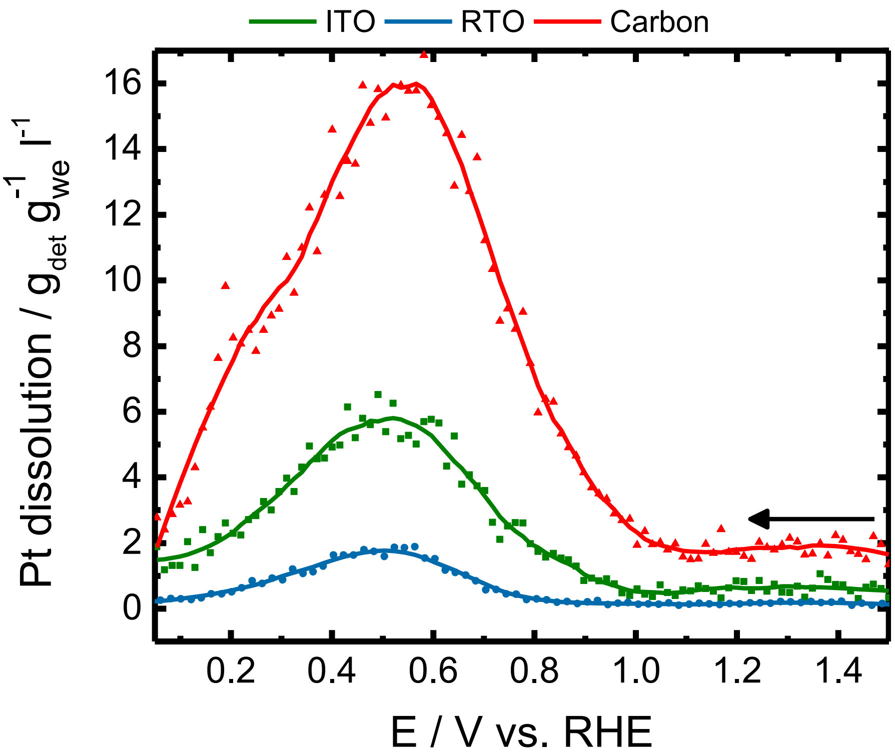

**Figure A18** Evolution of mass-normalized Pt dissolution rate of electrochemically-oxidized Pt nanoparticles supported on ITO (green), RTO (blue), and carbon (red) as determined by SFC ICP-MS measurements during the cathodic potential sweep from 1.5-0.05V after initial anodic potential sweep up to 1.5V.

# List of Acronyms

| **Abbreviation** | **Definition** |
|---|---|
| AFC | Alkaline fuel cell |
| ASAXS | Anomalous small angle X-ray scattering |
| AST | Accelerated stress test |
| at% | atomic % |
| BE | Binding energy |
| BET | Brunauer Emmett Teller |
| CNF | Carbon nanofibre |
| CNT | Carbon nanotube |
| CV | Cyclic Voltammetry |
| DFT | Density functional theory |
| DI | Deionized |
| DOE | Department of energy |
| ECSA | Electrochemical active surface area |
| EDX | Energy dispersive X-ray spectroscopy |
| ESRF | European Synchrotron Radiation Facility |
| fcc | face centered cubic |
| FWHM | Full width half maximum |
| GC | Glassy carbon |
| GDE | Gas diffusion electrode |
| GDL | Gas diffusion layer |
| HAADF | High-angle annular dark field |
| HE-XRD | Hiigh energy X-ray diffraction |
| HOR | Hydrogen oxidation reaction |
| HP | High potential |
| HRTEM | High resolution transmission electron mictroscopy |
| HT-DEMS | High temperature-differential electrochemical mass spectroscopy |
| $H_{upd}$ | Hydrogen under potential deposition |
| HZB | Helmholtz Zentrum Berlin |
| ICP-OES | Inductively coupled plasma mass spectroscopy |
| ITO | Indium tin oxide |
| LP | Low potential |
| LSV | Linear sweep voltammetry |
| MCFC | Molten carbonate fuel cell |
| MEA | Membrane electrode assembly |
| MMS | Mercury/mercury sulfate reference electrode |
| MS | Mass spectrometer |
| MWCNT | Multi-walled carbon nanotube |
| OCP | Open circuit potential |
| OER | Oxygen evolution reaction |
| ORR | Oxygen reduction reaction |
| PANI | Polyaniline |
| PDF | Powder diffraction file |
| PEFC | Polymer electrolyte fuel cell |
| PEIS | Potentiostatic electrochemical impedance spectroscopy |
| PEMFC | Proton exchange membrane fuel cell |

| **Abbreviation** | **Definition** |
|---|---|
| PSD | Particle size distribution |
| PTFE | Polytetrafluorethylene |
| RDE | Rotating disc electrode |
| RHE | Reversible hydrogen electrode |
| rpm | Rounds per minute |
| RT | Room temperature |
| RTO | Ruthenium Titanium Oxide |
| SAXS | Small angle X-ray scattering |
| SFC ICP-MS | Scanning flow cell inductively coupled plasma-mass spectroscopy |
| SMSI | Strong metal support interaction |
| SOFC | Solid oxide fuel cell |
| STEM | Scanning transmission electron mictroscopy |
| Td | Tetrahedral |
| TEM | Transmission electron mictroscopy |
| UHV | Ultra-high vacuum |
| UPD | Under potential deposited/deposition |
| WL | White line |
| wt% | weight % |
| XAS | X-ray absorption spectroscopy |
| XPS | X-ray photoelectron spectroscopy |
| XRD | X-ray diffraction |
| YSZ | Yttria-stabilized zirconia |
| ZIF | Zeolitic imidazolate framework |
| ZP | Zeta potential |
| yr | year |

# List of Chemicals

| Name | Abbreviation | Concentration / Purity | Supplier |
|---|---|---|---|
| 1,2-tetradecanediol | - | 90 % | Sigma Aldrich |
| Acetone | - | 100 % | VWR Chemicals |
| Ammonia | $NH_3$ | 99.98 % | Air Liquide |
| Carbon monoxide | CO | 99.997 % | Air Liquide |
| Dibenzylether | $Bn_2O$ | 98.0 % | Fluka |
| Ethanol | EtOH | 100 % | VWR Chemicals |
| Formic Acid | - | ~98 %, | Fluka |
| Hexachloroplatinic(II) acid hexahydrate | $H_2PtCl_6 \cdot 6H_2O$ | Pt 37.5 % min | Alfa Aesar |
| Hydrochloric acid | HCl | 37 % | VWR Chemicals |
| Hydrogen/Argon | $H_2/Ar$ | 4% $H_2/Ar$ | Air Liquide |
| Indium(III) chloride | $InCl_3$ | - | Strem Chemicals |
| Isopropanol | iPrOH | 100 % | VWR Chemicals |
| Nitric acid | $HNO_3$ | 69 % | Merck |
| Nitrogen | $N_2$ | 99.999 % | Air Liquide |
| Nafion | - | 5 wt% | Sigma Aldrich |
| Oxygen | $O_2$ | 99.998 % | Air Liquide |
| Oleic acid | - | 90.00 % | Alfa Aesar |
| Oleylamine | - | 70.0 % | Sigma Aldrich |
| Perchloric acid | $HClO_4$ | 99.999 % | Sigma Aldrich |
| Polytetrafluorethylene | PTFE | 60 wt% | ElectroChem Inc. |
| Propylene epoxide | PE | - | Sigma Aldrich |
| Platinum(II) acetylacetonate | $Pt(acac)_2$ | Pt 48 % min. | Alfa Aesar |
| Ruthenium(III) chloride hydrate | $RuCl_3 \cdot xH_2O$ | Ru 35-40 % | Acros Organics |
| Sulphuric acid | $H_2SO_4$ | 95 % | VWR Chemicals |
| Tin(IV) chloride | $SnCl_4$ | - | Acros Organics |
| Titanium dioxide powder | $TiO_2$ | - | Acros Organics |
| Ultrapure water | miliQ | 16.8 MΩcm | - |

# List of Figures

**Figure 1.1** Schematic illustration of the use of Hydrogen for energy conversion and storage. In here, hydrogen is produced by water electrolysis powered by renewable energy sources. Hydrogen is stored and distributed and can be used on demand in a fuel cell to generate electricity. .................................. **1**
**Figure 1.2** Schematic illustration of the general principle of a proton exchange membrane fuel cell (PEMFC). At the anode the fuel (hydrogen) is oxidized to form protons and electrons. Protons travel through the membrane to the cathode to form water by reacting with oxygen and electrons. The electrons travel through an external electric circuit and can be used as power supply. ......................................... **3**
**Figure 1.3** Schematic illustration of proposed degradation mechanisms for Pt nanoparticles supported on carbon including Pt dissolution, Ostwald ripening, agglomeration, detachment and carbon corrosion. Reprinted with permission from Ref. [26] from Beilstein Journal of Nanotechnology under the terms of the Creative Commons Attribution License (http://creativecommons.org/licenses/by/2.0). ................... **8**
**Figure 3.1** Schematic illustration of the Bragg equation. .................................................................. **23**
**Figure 3.2** Schematic illustration of the sequence of an electrochemical activity and stability measurement, including conditioning by cyclic voltammetry (CV), impedance measurement by potentiostatic electrochemical impedance spectroscopy (PEIS), activity determination by linear sweep voltammetry (LSV), accelerated stress test (AST) in two different potential windows (low potential (LP) and high potential (HP)) and activity determination after the AST. CO stripping, as applied in chapter 4, was performed directly before and after the AST. ......................................................................... **29**
**Figure 3.3** Schematic illustration of the setup and electrochemical in situ cell as used at a synchrotron facility, showing the incident and scattered X-rays, the 2D detector and the in situ transmission cell. Distance between sample and detector is defined as working distance. .............................................. **34**
**Figure 3.4** Schematic illustration of the elastic scattering as the basis of SAXS. ............................... **37**
**Figure 4.1** X-ray diffraction patterns of the bare ITO support material (black, bottom) and Pt/ITO catalyst (dark red, top) obtained using Cu Kα radiation. Solid lines denote pure $In_2O_3$ reference powder diffraction pattern (PDF#00-006-0416). Vertical dashed lines denote reference patterns of fcc Pt (PDF#00-004-0802). ............................................................................................................ **44**
**Figure 4.2** Morphology of Pt/ITO in the initial state: (a) showing overview HAADF-STEM image, (b) TEM and (c) HR-TEM images. ............................................................................................ **44**
**Figure 4.3** a,b) TEM images of the as prepared Pt nanoparticles on the ITO support, after electrochemical cycling for 5k times in d,e) lower potential region and in g,h) the higher potential region, as well as the corresponding histograms showing c,f,i) the particle size distribution. Histograms were obtained by measuring the diameter of at least 200 particles with errors obtained from standard deviation of mean particle diameter. ........................................................................................................ **45**
**Figure 4.4** Cyclic voltammograms of Pt/ITO catalyst before and after potential cycling in (a) lower and (c) higher potential region. CVs were recorded in nitrogen saturated electrolyte from 0.05–1 V with a scan rate of 100 mV $s^{-1}$. b,d) LSVs of the particular states with the bar plots in the inlets representing the mass activity ($j_m$) evaluated at 0.9 V. LSVs were recorded in oxygen-saturated electrolyte from 0.05–1 V with a scan rate of 5 mV $s^{-1}$ and 1600 rpm. All electrode potentials have been corrected for iR drop. ........................................................................................................................................ **46**
**Figure 4.5** Comparison of ECSAs based on the integration in the $H_{upd}$ and the CO oxidation potential range. CO-ECSAs were determined by integrating the CO oxidation peak area from the first cycle of the CO stripping experiment after subtraction of the second cycle representing the bare CO-free Pt surface. $H_{upd}$-ECSA was determined by subtracting the first from the second cycle of the CO stripping experiment. ........................................................................................................................ **47**
**Figure 4.6** X-ray photoelectron spectroscopy measurements. (a) and (b) are showing the Pt 4f depth profiling accessed by the kinetic energy of the photoelectrons of 210, 550 and 1200 eV at the initial (a) and the state after LP-AST (b) Dotted lines represent measured data and solid lines the fits and

component peaks. (c) and (d) are showing the 3d core levels for In and Sn, respectively, each at the initial and the cycled state. ........ **49**

**Figure 4.7** HAADF-STEM images and EDX mapping of a) Pt/ITO initial and b) after LP-AST. Platinum is depicted in light blue, indium in green, and tin in red........ **50**

**Figure 4.8** In situ HE XRD measurements depicted as the evolution of diffraction patterns from the initial state to the end of the electrochemical cycling for the LP-AST (a) and the HP-AST (b)........ **51**

**Figure 4.9** Results from in situ HE-XRD for LP-AST. Weight fractions of a) crystalline phases and b) their crystallite size as determined by Rietveld refinement........ **51**

**Figure 4.10** Evolution of normalized scale factors for Pt and $In_2O_3$ from fits of HE-XRD patterns over the cycle number for (a) LP-AST and (b) HP-AST. ........ **52**

**Figure 4.11** In situ ASAXS measurements for LP-AST: background subtracted, Pt element specific scattering curves for selected cycle numbers (a), particle size distribution (PSD) as a function of rel. intensity over the mean particle diameter for selected cycle numbers (b), mean Pt particle diameter (c) and the evolution of monodispersity as a function of σ over the cycle number (d). ........ **53**

**Figure 4.12** Results from in situ HE-XRD measurements for HP-AST. Weight fractions of (a) crystalline phases and (b) their crystallite size as determined by Rietveld refinement........ **54**

**Figure 4.13** In situ ASAXS measurements for HP-AST: background subtracted, Pt element specific scattering curves for selected cycle numbers (a), particle size distribution (PSD) as a function of rel. intensity over the mean particle diameter for selected cycle numbers (b), mean Pt particle diameter (c) and the evolution of monodispersity as a function of σ over the cycle number (d). ........ **55**

**Figure 4.14** In situ scanning flow cell ICP-MS measurements. Depicted are the Sn, In and Pt dissolution rates and the applied electrochemical protocols from the bottom to the top for (a) LP-AST and (b) HP-AST. The respective dissolution rates in detected (det) metal in µg per volume electrolyte ($\mu g_{det}\ L^{-1}$) are plotted against the time. A Pt/C reference sample was measured and therefore, the Pt dissolution rate was also normalized to the Pt mass loading on the working electrode (WE) ($\mu g_{det}\ L^{-1}\ \mu g_{WE}^{-1}$). The electrochemical protocol was conducted as follows: Beginning with 100 CVs (activation regime) from 0.05-1 V, followed by potential cycling in the LP regime (0.6-0.95 V, 40 CVs, 100 mV $s^{-1}$) or in the HP regime (1.0-1.5 V, 200 CVs, 500 mV $s^{-1}$) and followed by another 3 cycles from 0.05-1 V, all CVs were recorded with a scan rate of 100mV/s. The first contacts between catalyst and electrolyte (cell contact) are denoted with arrows. Breaks at the time axis of (a) and (b) have been implemented between 500 and 1700 s. Graphs with complete time axis can be found in Figure A5 and Figure A6........ **56**

**Figure 4.15** Results from in situ SFC ICP-MS of the integration of the peaks arising from Pt dissolution over time of the measurement (in $\mu g_{det}$) detected by the ICP-MS per mass loading Pt on the working electrode (in $\mu g_{WE}$) for LP- and HP-AST. ........ **57**

**Figure 5.1** Schematic illustration of the carbon modification procedure including oxidation step in concentrated nitric acid resulting in O-Vulcan, and ammonolysis in pure $NH_3$ at 400 and 800°C resulting in N-Vulcan. ........ **67**

**Figure 5.2** Surface and compositional analysis of the carbon materials: content of nitrogen (from elemental analysis) and oxygen (from hot gas extraction) for the modified carbons (a), physical BET surface area (b) and zeta potential (c) for modified carbons in comparison to the unmodified Vulcan.**68**

**Figure 5.3** (a) XPS N 1s spectra and individual peak deconvolution for modified carbons and Pt/N-Vulcan 400°C and (b) schematic illustrastion of different N-functionalities (green: graphitic N, blue: quaternary N, yellow: pyrrolic N and red: pyridinic N) in graphene-like plane. ........ **70**

**Figure 5.4** Fractions of the different N-moieties from deconvolution of the N 1s spectra in the modified carbons and in Pt/N-Vulcan 400°C. ........ **71**

**Figure 5.5** High Temperature-DEMS measurements from 0.06-1.05 V at 140 °C for modified carbons and the Vulcan reference carbon with respect to the resulting current j normalized to mass loading of carbon (a) and the ion current for $CO_2$ (m/z = 44) from the MS normalized to mass loading of carbon (b). HCl-Vulcan represents a HCl-treated Vulcan (1M HCl, RT, 24h) in order to remove metal traces from the unmodified Vulcan. ........ **72**

**Figure 5.6** X-ray powder diffraction patterns of the modified and unmodified carbon supports and the respective Pt electrocatalysts. Vertical blue lines represent the reference pattern for fcc Pt (PDF#00-004-0802)........ **73**
**Figure 5.7** TEM images (a) and ORR specific activity ($j_{spec}$) for the four catalysts (b) for Pt/Vulcan, Pt/O-Vulcan, Pt/N-Vulcan 400°C and Pt/N-Vulcan 800°C. See Figure A9 in the Appedix section A2 for more TEM overview images. ........ **74**
**Figure 5.8** Results from AST for 5k, 10k and 30k cycles from 0.6-0.95 V in Nitrogen-saturated 0.1 M $HClO_4$ for Pt/Vulcan, Pt/O-Vulcan, Pt/N-Vulcan 400°C and Pt/N-Vulcan 800°C as a function of mass activity at 0.9 V $j_{mass}$(a,d,g,j), ECSA (b,e,h,k) and specific activity $j_{spec}$ (c,f,i,l)........ **75**
**Figure 5.9** In situ high energy X-ray diffraction patterns over 5k cycle of the AST for Pt/Vulcan (a), and Pt/N-Vulcan 400°C (b). A full set of in situ HE-XRD patterns for all samples can be found in the Appendix section A2, Figure A10........ **76**
**Figure 5.10** Crystallite sizes obtained from Rietveld Refinement of the in situ HE-XRD patterns over 5k cycles of the AST for Pt/N-Vulcan 400°C (a) and Pt/Vulcan (b). Inlets in both graphs showing the mass activity up to 30k cycles between 0.6-0.95 V of the AST in nitrogen-saturated 0.1 M $HClO_4$. A full set evolution of crystallite size for all samples can be found in the Appendix section A2, Figure A11. ........ **77**
**Figure 5.11** In situ small angle X-ray scattering curves and mean particle diameter from SAXS fitting over 5k cycle of the AST for Pt/Vulcan (a,b) and Pt/N-Vulcan 400°C (c,d). A full set of in situ SAXS curves and evolution of mean particle diameters for all samples can be found in the Appendix section A2, Figure A12 and Figure A13........ **78**
**Figure 6.1** Structure and morphology of Pt nanoparticles supported on RTO (blue), ITO (green) and carbon (red) as determined by powder X-ray diffraction pattern (a) and transmission electron microscopy images (b,c,d). The Pt particle sizes as depicted in the histograms in (e,f,g) were determined from analyzing > 200 Pt particles along their shortest principal axes........ **84**
**Figure 6.2** Histograms of mean particle diameter for Pt supported on (a) ITO (green), (b) RTO (blue) and (c) carbon (red) support. Top row shows the average particle diameter measured along their shortest particle axis and bottom row along their longest particle axes........ **85**
**Figure 6.3** Morphology of Pt nanoparticles on (a) RTO (blue) and (b) carbon (red) support in a TEM tilting study from 0-30°. ........ **86**
**Figure 6.4** Electrochemical characterization of Pt nanoparticles on RTO (blue), ITO (green) and carbon (red) support by the evolution of cyclic voltammogram with increasing upper potential limit in $N_2$-saturated 0.1 M $HClO_4$ from 0.5-1.4 V (a-c) and from CO stripping experiments (d)........ **87**
**Figure 6.5** In situ high-energy X-ray diffraction patterns of Pt nanoparticles supported on ITO (green, a), RTO (blue, b) and carbon (red, c) on stepwise electrochemical oxidation of Pt (potential hold for 10 min each). ........ **89**
**Figure 6.6** Structural response of crystalline Pt nanoparticles supported on ITO (green circles), RTO (blue triangles) and carbon (red squares) on stepwise electrochemical oxidation (potential hold for 10 min each; reducing step to 1.0 V represented by open symbols) with respect to the change of Pt lattice parameter (a), normalized change of the Pt scale factor (b) as determined by Rietveld refinement of in situ high-energy X-ray diffraction pattern. The solid lines are shown to guide the eyes of the reader. **90**
**Figure 6.7** Evolution of the number of unit cells ($2R/a_{Pt}$) of the metallic Pt domains for Pt/C along the x,y and z-axes. The solid lines are shown to guide the eyes of the reader. ........ **91**
**Figure 6.8** Normalized in situ Pt $L_3$–edge X-ray near-edge absorption spectra for Pt nanoparticles supported on ITO (green, a), RTO (blue, b) and carbon (red, c) for potentials from 0.6 – 1.4 V of electrochemical oxidation of Pt. The positions of the Pt $L_3$ resonances applied in the fit procedure are denoted. ........ **92**
**Figure 6.9** Structural response of Pt nanoparticles supported on ITO (green circles), RTO (blue triangles), and carbon (red squares) on stepwise electrochemical oxidation (potential hold for 10 min each) with respect to the white line area (a) the integrated areas as the resonances 1 (Pt $L_3$-Res 1) at ~11566 eV and Pt $L_3$-Res 2 at ~11570 eV (b) and Pt $L_3$-Res 3 at ~11580 eV (c) as determined by peak

fitting of in situ Pt $L_3$–edge X-ray near-edge absorption spectra. The solid lines are shown to guide the eye of the reader. ........ **93**

**Figure 6.10** Pt dissolution profiles from in situ SFC ICP-MS measurement in $g_{det}$ Pt per volume electrolyte in l and electrochemical surface area (ECSA) in $m^2_{ECSA}$. (a) shows the whole electrochemical measurement (100 CVs of activation with a scanrate 100 mV $s^{-1}$ and 4 CVs of Pt Oxidation from 0.05-1.5 V with a scanrate 10 mV $s^{-1}$) and the corresponding dissolution profiles for Pt on carbon (red), ITO (green) and RTO (blue) support and (b) the four oxidation cycles from 0.05-1.5 V........ **96**

**Figure 6.11** Evolution of ECSA-normalized Pt dissolution rate for Pt nanoparticles supported on ITO (green), RTO (blue), and carbon (red) during the initial anodic potential sweep from 0.05-1.5 V with a scanrate of 10 mV $s^{-1}$ as determined by SFC ICP-MS measurements. ........ **97**

**Figure 6.12** Evolution of ECSA-normalized Pt dissolution rate of electrochemically-oxidized Pt nanoparticles supported on ITO (green), RTO (blue), and carbon (red) as determined by SFC ICP-MS measurements during the cathodic potential sweep from 1.5-0.05 V with a scanrate of 10 mV $s^{-1}$ after initial anodic potential sweep up to 1.5 V. ........ **98**

**Figure 7.1** Schematic illustration of degradation phenomena as found to occur in Pt/ITO electrocatalyst during two different simulated degradation protocols: low potential AST and high potential AST (denoted as LP-AST and HP-AST). Reproduced from Ref [52] (Adv. Energy Mat., **2018**, 8 (4), 1701663) with permission from John Wiley and Sons, Copyright 2018........ **102**

**Figure 7.2** Schematic illustration of the process of support functionalization by ammonolysis at 400°C and introduction of surface abundant pyrrolic-N. In the second step, Pt deposition on modified support and the improved ORR long-term stability is illustrated. Reprinted with permission from Ref[71] (Chem. Mat., **2018**, doi: 10.1021/acs.chemmater.8b03612). Copyright (2018) American Chemical Society. **103**

**Figure 7.3** Schematic illustration of potential-dependent responses of Pt nanoparticles on carbon, RTO and ITO support on electrochemical oxidation with respect to lattice expansion, formation of $PtO_x$ and $Pt^{n+}$ dissolution. ........ **105**

**Figure A1** TEM images of as prepared Pt nanoparticles on the ITO support which was used for the HP-AST experiments with a weight loading of 29.9 wt% (a,b) and the corresponding histogram showing particle size distribution (c). Histograms were obtained by measuring the diameter of at least 200 particles with errors obtained from standard deviation of mean particle diameter. ........ **119**

**Figure A2** Cyclic voltammograms of Pt/C reference catalyst (weight loading 20 wt% Pt on carbon) before and after potential cycling in lower (a) and higher (c) potential region. CVs were recorded in nitrogen saturated electrolyte from 0.05-1 V with a scan rate of 100 mV $s^{-1}$. Figure b and d are showing LSVs of the particular states LSVs were recorded in oxygen saturated electrolyte from 0.05-1 V with a scan rate of 5 mV·$s^{-1}$and 1600 rpm. All electrode potentials have been corrected for iR drop. ........ **119**

**Figure A3** Electrochemical CO stripping experiments for Pt/ITO electrocatalyst. For the two different stability tests in low (a) and high (b) potential regime three different points in the characterization protocol were chosen for CO stripping: initial, after CV+LSV and after 5k CV+LSV. ........ **120**

**Figure A4** In situ HE XRD measurements depicted as the evolution of diffraction patterns from the initial state to the end of the electrochemical cycling for the LP-AST (a) and the HP-AST (b). The inlet in (a) is showing the Pt (200) diffraction peak superimposed by an $In_2O_3$ peak (denoted with dashed vertical lines). ........ **121**

**Figure A5** In situ scanning flow cell ICP-MS measurements. Depicted are the Sn, In and Pt dissolution rates and the applied electrochemical protocols from the bottom to the top for LP-AST. The respective dissolution rates in detected metal per volume electrolyte (µ$g_{det}$ $l^{-1}$) are plotted against the time. A Pt/C reference sample was measured and therefore, the Pt dissolution rate was also normalized to the Pt mass loading on the working electrode (WE) (µ$g_{det}$ $l^{-1}$µ$g_{WE}^{-1}$). The electrochemical protocol was conducted as follows: Beginning with 100 CVs (activation regime) from 0.05-1 V, followed by potential cycling in the LP regime (0.6-0.95 V, 40 CVs, 100 mV·$s^{-1}$) and followed by another 3 cycles from 0.05-1 V, all CVs were recorded with a scan rate of 100mV $s^{-1}$. The first contacts between catalyst and electrolyte (cell contact) are denoted with arrows. ........ **121**

**Figure A6** In situ scanning flow cell ICP-MS measurements. Depicted are the Sn, In and Pt dissolution rates and the applied electrochemical protocols from the bottom to the top for HP-AST. The respective dissolution rates in detected metal per volume electrolyte ($\mu g_{det}\ l^{-1}$) are plotted against the time. A Pt/C reference sample was measured and therefore, the Pt dissolution rate was also normalized to the Pt mass loading on the working electrode (WE) ($\mu g_{det}\ l^{-1} \mu g_{WE}^{-1}$). The electrochemical protocol was conducted as follows: Beginning with 100 CVs (activation regime) from 0.05-1 V, followed by potential cycling in the HP regime (1.0-1.5 V, 200 CVs, 500 $mV \cdot s^{-1}$) and followed by another 3 cycles from 0.05-1 V, all CVs were recorded with a scan rate of 100mV $s^{-1}$. The first contacts between catalyst and electrolyte (cell contact) are denoted with arrows. **122**

**Figure A7** Evolution of Pt lattice constant as extracted from Rietveld Refinement from in situ HE-XRD measurements over the cycle number for (a) LP-AST and (b) HP-AST. **123**

**Figure A8** XPS C 1s spectra and individual peak deconvolution for unmodified Vulcan (a), O-Vulcan (b), N-Vulcan 400° (c), N-Vulcan 800°C (d) and for Pt/N-Vulcan 400°C (e). **125**

**Figure A9** TEM images for Pt on unmodified Vulcan (a), O-Vulcan (b), N-Vulcan 400°C (c), and N-Vulcan 800°C (d). **126**

**Figure A10** In situ high energy X-ray diffraction patterns over 5k cycle of the AST for Pt/Vulcan (a), Pt/O-Vulcan (b), Pt/N-Vulcan 400°C (c) and Pt/N-Vulcan 800°C (d). **127**

**Figure A11** Crystallite size from Rietveld refinement of the in situ high energy X-ray diffraction patterns over 5k cycle of the AST for Pt/Vulcan (a), Pt/O-Vulcan (b), Pt/N-Vulcan 400°C (c) and Pt/N-Vulcan 800°C (d). **128**

**Figure A12** In situ small angle X-ray scattering curves over 5k cycle of the AST for Pt/Vulcan, Pt/O-Vulcan, Pt/N-Vulcan 400°C and Pt/N-Vulcan 800°C (a,c,e,g) and scattering curves at start of the AST including the individual fit curves (b,d,f,h). **129**

**Figure A13** Mean particle diameter from fit of the in situ small angle X-ray scattering curves over 5k cycle of the AST for Pt/Vulcan (a), Pt/O-Vulcan (b), Pt/N-Vulcan 400°C (c) and Pt/N-Vulcan 800°C (d). **130**

**Figure A14** X-ray diffractograms of (a) ITO and Pt/ITO with solid blue lines indicating $In_2O_3$ reference pattern and (b) RTO and Pt/RTO with symbols indicating $TiO_2$ anatase and rutile and $RuO_2$. Vertical dashed lines denote reference powder diffraction patterns of fcc Pt (PDF#00-004-0802). XRDs were obtained using Cu $K_\alpha$ radiation. **131**

**Figure A15** High energy XRD patterns for Pt/RTO, Pt/ITO and Pt/C in the as-prepared state. **132**

Figure A16 Morphology of Pt nanoparticles on a) ITO (green), b) RTO (blue) and c) carbon (red) support and corresponding histograms showing mean particle diameter as determined by transmission electron microscopy. The particle size histogram was determined from analyzing > 200 particles along their shortest particle axes. **132**

**Figure A17** Evolution of mass-normalized Pt dissolution rate as determined by SFC ICP-MS measurements during the initial anodic potential sweep from 0.05-1.5 V for Pt nanoparticles supported on ITO (green), RTO (blue), and carbon (red). **133**

**Figure A18** Evolution of mass-normalized Pt dissolution rate of electrochemically-oxidized Pt nanoparticles supported on ITO (green), RTO (blue), and carbon (red) as determined by SFC ICP-MS measurements during the cathodic potential sweep from 1.5-0.05V after initial anodic potential sweep up to 1.5V. **134**

# List of Tables

**Table 3.1** Overview over different materials used in this work with the corresponding chapters in which their characterization is discussed. .......... **19**
**Table 3.2** Overview of Methods for physicochemical characterization used in this work with reference to the sections in which they are described. x indicates the the application of the method for the corresponding result chapter. .......... **22**
**Table 3.3** Details on Ink preparation and composition depending on the different supports used in this work.......... **28**
**Table 3.4** Overview of ASTs performed in this with work for Pt/ITO and Pt/(un)modified carbon with respect to the applied cycle numbers.......... **31**
**Table 4.1** Near-surface composition of Pt/ITO before and after LP-AST in the lower potential regime as obtained from XPS measurements. The molar ratios Pt, In, and Sn were determined from the peak areas of the Pt 4f as well as In and Sn 3d spectra recorded with a kinetic energy of the photoelectrons of 550 eV. The number in brackets denotes the composition at a second beam position of each sample. **50**
**Table 5.1** Assignment of binding energy (BE) for different N-functionalities from individual deconvolution of the N 1s XP spectra. .......... **69**

**Table A1** Comparison of ECSAs based on the integration in the $H_{upd}$ and the CO oxidation potential range. CO-ECSAs were determined by integrating the CO oxidation peak area from the first cycle of the CO stripping experiment after subtraction of the second cycle representing the bare CO-free surface. $H_{upd}$-ECSAs were determined by subtracting the first from the second cycle of the CO stripping experiment.......... **120**
**Table A2** Comparison of $j_m$ and ECSA before and after LP- and HP-AST for Pt/C reference catalyst. $j_m$ was determined at 0.9 V. ECSAs were determined by integrating the H-desorption and adsorption area between 0.05-0.4 V and subtracting the capacitive current.......... **120**
**Table A3** Results from in situ SFC ICP-MS of the integration over time of the measurement of the peaks arising from Pt dissolution in Pt/ITO and Pt/C reference and In and Sn from ITO support. Pt dissolution in µg is normalized to Pt mass loading on the working electrode in $\mu g_{Pt}$ and In and Sn dissolution in µg is normalized to In+Sn mass loading on the working electrode in $\mu g_{(In+Sn)}$.Potential dissolution peaks are arising from cell contact, program start and distinct dissolution peaks during the electrochemical cycling (1st and 2nd peak).Additionally, dissolution values are listed each without (wo/) and with (w/) contribution of metal dissolution at cell contact. .......... **122**
**Table A4** Elemental bulk and surface composition in at% of unmodified Vulcan, O-Vulcan and N-Vulcan 400°C and 800°C from elemental analysis, hot gas extraction and XPS.......... **124**
**Table A5** Pt weight loading (wt%) from ICP-OES for Pt/Vulcan, Pt/O-Vulcan, Pt/N-Vulcan 400°C and Pt/N-Vulcan 800°C. .......... **124**
**Table A6** Pt weight loading (wt%) for Pt on ITO, RTO and C as determined by ICP-OES analysis. **131**
**Table A7** Crystallite diameter ($D_x$, $D_y$ and $D_z$) for ellipsoidal Pt particles on RTO and C support and for spherical particles on ITO as determined by Rietveld refinement of HE-XRD. .......... **132**
**Table A8** Structural parameters of Pt on ITO, RTO and C: $O_{td}$-incorporation and lattice constant by Rietveld refinement of HE-XRD.......... **133**
**Table A9** Comparison of ECSA values based on the integration in the $H_{upd}$ region or the CO Oxidation peak area.......... **133**

# List of Publications

### *Publications as part of this thesis*

**Schmies, H.**; Bergmann, A.; Drnec, J.; Wang, G.; Teschner, D.; Kühl, S.; Sandbeck, D. J. S.; Cherevko, S.; Gocyla, M.; Shviro, M.; Heggen, M.; Ramani, V.; Dunin-Borkowski, R. E.; Mayrhofer, K. J. J.; Strasser, P., Unravelling Degradation Pathways of Oxide-Supported Pt Fuel Cell Nanocatalysts under In Situ Operating Conditions. *Advanced Energy Materials* **2018**, *8* (4), 1701663.

**Schmies, H.**; Hornberger, E.; Anke, B.; Jurzinsky, T.; Nong, H. N.; Dionigi, F.; Kühl, S.; Drnec, J.; Lerch, M.; Cremers, C.; Strasser, P., The Impact of Carbon Support Functionalization on the Electrochemical Stability of Pt Fuel Cell Catalysts. *Chemistry of Materials* **2018**, *30* (20), 7287-7295.

### *Other publications*

Gorlin, M.; de Araujo, J. F.; **Schmies, H.**; Bernsmeier, D.; Dresp, S.; Gliech, M.; Jusys, Z.; Chernev, P.; Kraehnert, R.; Dau, H.; Strasser, P., Tracking Catalyst Redox States and Reaction Dynamics in Ni-Fe Oxyhydroxide Oxygen Evolution Reaction Electrocatalysts: The Role of Catalyst Support and Electrolyte pH. *Journal of the American Chemical Society* **2017,** *139* (5), 2070-2082.

Beermann, V.; Gocyla, M.; Kuhl, S.; Padgett, E.; **Schmies, H.**; Goerlin, M.; Erini, N.; Shviro, M.; Heggen, M.; Dunin-Borkowski, R. E.; Muller, D. A.; Strasser, P., Tuning the Electrocatalytic Oxygen Reduction Reaction Activity and Stability of Shape-Controlled Pt-Ni Nanoparticles by Thermal Annealing - Elucidating the Surface Atomic Structural and Compositional Changes. *Journal of the American Chemical Society* **2017,** *139* (46), 16536-16547.

Sun, Y. Y.; Sinev, I.; Ju, W.; Bergmann, A.; Dresp, S.; Kuhl, S.; Spori, C.; **Schmies, H.**; Wang, H.; Bernsmeier, D.; Paul, B.; Schmack, R.; Kraehnert, R.; Cuenya, B. R.; Strasser, P., Efficient Electrochemical Hydrogen Peroxide Production from Molecular Oxygen on Nitrogen-Doped Mesoporous Carbon Catalysts. *ACS Catalysis* **2018,** *8* (4), 2844-2856.

Hornberger, E.; Bergmann, A.; **Schmies, H.**; Kühl, S.; Wang, G.; Drnec, J.; Sandbeck, D. J. S.; Ramani, V.; Cherevko, S.; Mayrhofer, K. J. J.; Strasser, P., In Situ Stability Studies of Platinum Nanoparticles Supported on Ruthenium−Titanium Mixed Oxide (RTO) for Fuel Cell Cathodes. *ACS Catalysis* **2018**, *8* (10), 9675-9683.